COPPE
Instituto Alberto Luiz Coimbra de Pós-Graduação e Pesquisa de Engenharia
UFRJ

DESIGN AND PERFORMANCE TUNING OF K-Co-Cu-Al CATALYSTS FOR SELECTIVE CO_2 HYDROGENATION TO HIGHER ALCOHOLS

Vitor Duarte Lage

Tese de Doutorado apresentada ao Programa de Pós-graduação em Engenharia Química, COPPE, da Universidade Federal do Rio de Janeiro, como parte dos requisitos necessários à obtenção do título de Doutor em Engenharia Química.

Orientador: Fabio Souza Toniolo

Rio de Janeiro

Dezembro de 2023

DESIGN AND PERFORMANCE TUNING OF K-Co-Cu-Al CATALYSTS FOR SELECTIVE CO_2 HYDROGENATION TO HIGHER ALCOHOLS

Vitor Duarte Lage

TESE SUBMETIDA AO CORPO DOCENTE DO INSTITUTO ALBERTO LUIZ COIMBRA DE PÓS-GRADUAÇÃO E PESQUISA DE ENGENHARIA DA UNIVERSIDADE FEDERAL DO RIO DE JANEIRO COMO PARTE DOS REQUISITOS NECESSÁRIOS PARA A OBTENÇÃO DO GRAU DE DOUTOR EM CIÊNCIAS EM ENGENHARIA QUÍMICA.

Orientador: Fabio Souza Toniolo

Aprovada por: Prof. Fabio Souza Toniolo

Prof. Carlos Andres Ortiz Bravo

Dr. Nicolas Bion

Dra. Neuman Solange de Resende

Profa. Sibele Berenice Castellã Pergher

RIO DE JANEIRO, RJ, BRASIL
DEZEMBRO DE 2023

Lage, Vitor Duarte

Design and Performance Tuning of K-Co-Cu-Al Catalysts for Selective CO_2 Hydrogenation to Higher Alcohols / Vitor Duarte Lage. – Rio de Janeiro: UFRJ/COPPE, 2023.

X, 66 p.: il.; 29,7 cm.

Orientador: Fabio Souza Toniolo

Tese (doutorado) – UFRJ/ COPPE/ Programa de Engenharia Química, 2023.

Referências Bibliográficas: p. 105-123.

1. Hidrogenação de CO_2. 2. Catálise Heterogênea. 3. Álcoois Superiores. I. Toniolo, Fabio Souza *et al.* II. Universidade Federal do Rio de Janeiro, COPPE, Programa de Engenharia Química. III. Título.

A maior riqueza do homem
é a sua incompletude.
Nesse ponto sou abastado.
Palavras que me aceitam como sou - eu não aceito.

Não aguento ser apenas um sujeito que abre portas,
que puxa válvulas, que olha o relógio,
que compra pão às 6 horas da tarde,
que vai lá fora, que aponta lápis,
que vê a uva etc. etc.

Perdoai
Mas eu preciso ser Outros.
Eu penso renovar o homem usando borboletas.

— Manoel de Barros (1998).

Agradecimentos

Gostaria de expressar minha gratidão ao meu orientador, Prof. Fabio Toniolo, por acreditar em mim e me acompanhar nesta jornada desde 2016 durante o meu mestrado, e me fazer ser otimista quando achei que nada daria certo.

Quero estender meus agradecimentos ao Prof. Nicolas Bion por me receber em Poitiers e orientar-me durante este período. Também agradeço ao Dr. Anthony Le Valant por sua assistência e paciência nos testes catalíticos.

Expresso meu agradecimento à UFRJ (Universidade Federal do Rio de Janeiro), à Université de Poitiers e ao CNRS (Centre National de la Recherche Scientifique) por permitirem o desenvolvimento desta pesquisa em suas instalações.

Agradeço aos laboratórios e às pessoas envolvidas nas análises, à equipe do NUCAT e do IC2MP (Institut de Chimie des Milieux et Matériaux de Poitiers); ao LabTecH2 (Laboratório de Tecnologia do Hidrogênio) na UFRJ pelas análises iniciais de XRD; ao INT (Instituto Nacional de Tecnologia) pelas análises de STEM-in-SEM; ao CBPF (Centro Brasileiro de Pesquisa em Física) pelas análises de HRTEM e EDS; à pesquisadora Carla Moreira (INT) por conduzir e auxiliar ambas as análises de microscopia, ao IC2MP pelas análises de in situ XRD; e ao pesquisador Alexander Caytuero pela assistência na implementação do refinamento de Rietveld.

Agradeço ao LNLS (Laboratório Nacional de Luz Síncrotron) do CNPEM (Centro Nacional de Pesquisa em Energia e Materiais) pelas análises de XPS e XANES na linha IPÊ. Estendo meus agradecimentos a toda a equipe do LNLS. Um agradecimento especial à equipe que me acompanhou nos experimentos no LNLS: Prof. Fabio Toniolo, Prof. Henrique Pacheco, Prof. Carlos Ortiz-Bravo e Dra. Débora Bezerra.

Expresso minha gratidão à CAPES (Coordenação de Aperfeiçoamento de Pessoal de Nível Superior – Brasil) – Código Financeiro 001 pelo apoio financeiro e ao COFECUB (Comitê Francês de Avaliação da Cooperação Universitária com o Brasil – Ph-C 912/18) pelo também apoio financeiro durante o meu doutorado sanduíche.

Gostaria de agradecer, agora em tom mais pessoal, a todos os meus amigos que estiveram comigo durante essa jornada, oferecendo apoio e escutando meus

anseios e reclamações, que não foram poucos. Estendo meu agradecimento aos amigos e colegas do NUCAT. Obrigado por tudo. Vocês fizeram essa jornada mais leve.

Agradeço a todos os professores que, de alguma forma, me inspiraram e incentivaram.

Por fim, expresso minha profunda gratidão à minha família, especialmente à minha mãe, por ter batalhado para me proporcionar acesso às ferramentas que me trouxeram até aqui, por estar sempre comigo mesmo quando distante; e ao meu avô, por todo apoio e inspiração.

Resumo da Tese apresentada à COPPE/UFRJ como parte dos requisitos necessários para a obtenção do grau de Doutor em Ciências (D.Sc.)

DESIGN E AJUSTE DE DESEMPENHO DE CATALISADORES DE K-Co-Cu-Al PARA HIDROGENAÇÃO SELETIVA DE CO_2 PARA ÁLCOOIS SUPERIORES

Vitor Duarte Lage

Dezembro/2023

Orientador: Fabio Souza Toniolo

Programa: Engenharia Química

A conversão catalítica de CO_2 e H_2 em produtos químicos diversos é uma solução promissora para os desafios contemporâneos de energia e meio ambiente. No entanto, desenvolver um catalisador capaz de converter seletivamente CO_2 em produtos desejados ainda é um desafio. Neste contexto, esta tese desenvolveu uma série de catalisadores K-Co-Cu-Al por coprecipitação para a síntese de álcoois superiores (HAs) por meio da hidrogenação do CO_2. Diferentes razões Co:Cu, temperaturas de redução e condições de reação, incluindo temperatura, velocidade espacial e razão H_2/CO_2, foram exploradas para aumentar o rendimento a HAs. O catalisador $Co_{1.8}Cu_{0.9}AlO_x$ (1% K m/m), reduzido a 400 °C, destaca-se dentre os testados, com alta seletividade para HAs de 44,8% (20,8% para etanol) e rendimento de 5,54 $mmol \cdot g_{cat}^{-1} \cdot h^{-1}$ (3,08 para etanol) em condições otimizadas (250 °C, 30 bar, razão H_2/CO_2 de 1,5 e 14200 $mL \cdot g_{cat}^{-1} \cdot h^{-1}$). O desempenho catalítico posiciona-o como um dos catalisadores mais eficazes já reportados destacando seu potencial para avançar o campo de conversão catalítica de CO_2 em produtos de valor agregado. A caracterização estrutural das amostras de $Co_{1.8}Cu_{0.9}AlO_x$ indicou a coexistência das fases CoO, Co^0, Cu^0 e potencialmente espinélio na amostra reduzida a 400 ºC. Cada fase desempenhando um papel distinto na reação, como reportado na literatura. A composição de superfície revelou a presença de espécies Co^0 e $Co^{\delta+}$ na amostra pós-reação, sendo a interface Co^0–$Co^{\delta+}$ considerada um sítio ativo, e uma possível concentração de superfície de Co sugerindo a adsorção preferencial de CO* (intermediário de reação) nos sítios de Co.

Abstract of Thesis presented to COPPE/UFRJ as a partial fulfillment of the requirements for the degree of Doctor of Science (D.Sc.)

DESIGN AND PERFORMANCE TUNING OF K-Co-Cu-Al CATALYSTS FOR SELECTIVE CO_2 HYDROGENATION TO HIGHER ALCOHOLS

Vitor Duarte Lage

December/2023

Advisor: Fabio Souza Toniolo

Department: Chemical Engineering

The catalytic conversion of CO_2 and H_2 into valuable chemicals stands as a promising solution to contemporary energy and environmental challenges. However, designing an earth-abundant catalyst capable of selectively converting CO_2 into desired products remains a significant challenge. In this context, this thesis developed a series of K-Co-Cu-Al catalyst via coprecipitation for the synthesis of higher alcohols (HAs) via CO_2 hydrogenation. Different Co:Cu ratios, reduction temperatures, and reaction conditions, including temperature, space velocity, and H_2/CO_2 ratio, were explored to enhance the yield of higher alcohols. The $Co_{1.8}Cu_{0.9}AlO_x$ (1 wt.% K) catalyst, reduced at 400 °C, emerges as the best-tested catalyst, with high HAs selectivity of 44.8% (20.8% for ethanol) and space-time yield of 5.54 $mmol \cdot g_{cat}^{-1} \cdot h^{-1}$ (3.08 of ethanol) under optimized conditions (250 °C, 30 bar, H_2/CO_2 ratio of 1.5, and 14200 $mL \cdot g_{cat}^{-1} \cdot h^{-1}$). This catalytic performance positions it as one of the most effective catalysts in the field, particularly among Co and CoCu-based catalysts, showcasing its potential for advancing the field of the catalytic conversion of CO_2 into value-added products. Comprehensive structural characterization of $Co_{1.8}Cu_{0.9}AlO_x$ samples indicated the coexistence of CoO, Co^0, Cu^0, and potentially spinel phases coexisting in the sample reduced at 400 ºC. Each phase plays a distinct role in CO_2 hydrogenation, according to literature. Surface composition uncovered the presence of both Co^0 and $Co^{\delta+}$ species on the post-reaction sample, Co^0–$Co^{\delta+}$ interface is regarded as an active site, and a potential Co surface enrichment suggesting preferential adsorption of CO* (reaction intermediate) onto Co sites.

Summary

Chapter 01

Introduction

The six stages of climate denial are: it's not real. / It's not us. / It's not that bad. / It's too expensive to fix. / (…) here's a great solution (that actually does nothing). / And - oh no! Now it's too late. You really should have warned us earlier.

— Prof. Katharine Hayhoe, Texas Tech University
Climate Science Center Director (2020)

Climate change poses an ever-growing threat, emphasizing the urgent need to address escalating levels of carbon dioxide (CO_2) —an anthropogenic greenhouse gas— in the atmosphere. The imperative to find effective solutions for mitigating CO_2 emissions and transitioning toward a sustainable society has given rise to three main strategies: (i) restraining emissions; (ii) capturing and storing; and (iii) utilizing or transforming (LI *et al.*, 2018a; WANG *et al.*, 2011).

Transitioning toward a sustainable energy system and reducing CO_2 emissions across all sectors is a key aspect of the first strategy. However, the challenge lies in developing suitable energy storage technologies due to the natural fluctuations in renewable sources (SCHEMME *et al.*, 2018). Hydrogen (H_2) production via electrolysis stands out as a promising storage option in this regard (KOMMOSS *et al.*, 2017). The second strategy involves the relatively well-established process of CO_2 capture and storage, representing a quick way of cutting down CO_2 emissions but presenting potential leakage risks (LI *et al.*, 2018a; WANG *et al.*, 2011). The third strategy explores the utilization of captured CO_2 in industrial processes or its transformation into valuable chemicals (SCHEMME et al., 2018).

In this context, CO_2 hydrogenation combines those three strategies. By utilizing H_2 from sustainable sources and CO_2 captured from high-emission economic sectors, this reaction can produce a wide array of products, such as fuel and feedstock chemicals. This not only addresses the challenge of CO_2 emissions but also reduces dependency

on fossil fuels. Among the products of interest, higher alcohols, particularly ethanol, have garnered significant attention due to their versatile applications, higher energy density, sustainability, and reduced environmental impact compared to other alternatives (ALI *et al.*, 2022; HE *et al.*, 2022; KAMKENG *et al.*, 2021; ZENG *et al.*, 2021).

Despite the potential of CO_2 hydrogenation, challenges persist, especially in tailoring catalysts and optimizing process conditions (ALI *et al.*, 2022; ISAHAK; SHAKER; AL-AMIERY, 2023). Various catalysts have been reported, with Co-based and Cu-based catalysts standing out due to their relative cost advantages (LI, X. *et al.*, 2023).

Co-based catalysts generally exhibit higher CO_2 conversion rates, but they often lead to predominant methane production, especially in their metallic form (Co^0). However, recent research has shown that it's possible to modify their surface composition to create hetero sites ($Co^{\delta+}$–Co^0) and/or tailor their structure (such as forming Co-Al spinel-like compounds), to reduce their propensity for breaking the C-O bond (LIU *et al.*, 2023; ZENG *et al.*, 2021). Cu-based catalysts are widely recognized for methanol synthesis, characterized by non-dissociative activation of CO_2. Interestingly, Cu has emerged as a promising addition to Co-based alloys, facilitating CO-insertion and impeding C-O bond cleavage. Additionally, alkali metals have been explored as promoters to enhance basicity by donating electrons to active metal sites (LI, X. *et al.*, 2023; XU *et al.*, 2021a; ZENG *et al.*, 2021).

Regarding the reaction conditions, determining the optimal temperature, H_2/CO_2 ratio, and space velocity, among other parameters, is crucial to improving the HAs synthesis. Yet it was not significantly explored in the past (LIU *et al.*, 2023; ZENG *et al.*, 2021).

In response to the call for sustainable technologies, this Ph.D. thesis delves into catalyst design and performance tuning for the selective hydrogenation of CO_2 to higher alcohols. The proposed investigation focuses on K-Co-Cu-Al catalysts, aiming to achieve the following objectives:

1. **To prepare K-Co-Cu-Al catalysts through a facile and scalable method**, which involves identifying suitable synthesis parameters and optimizing the procedure.
2. **To tune the catalyst characteristics to favor higher alcohol production**. The chosen parameters for this stage were the Co/Cu ratio and pretreatment condition (i.e., reduction temperature).
3. **To investigate the effect of various reaction parameters on the catalytic performance of K-Co-Cu-Al catalysts**, including reaction temperature, space

velocity, and H_2/CO_2 ratio, on the selectivity and conversion of CO_2 to HAs. The goal is to optimize the reaction conditions to achieve the highest yield of HAs while minimizing by-product formation.

4. **To gain an understanding of the structure-activity relationships governing the catalytic behavior of K-Co-Cu-Al catalysts**. This involves employing characterization techniques to elucidate the catalyst's structure, active sites, and surface properties, enabling rational catalyst design and further optimization.

The subsequent chapters will unfold as follows: **Chapter 02 - Literature Overview**: A comprehensive review of existing literature, elucidating the current state of knowledge and gaps in the field of CO_2 hydrogenation to higher alcohols; **Chapter 03 - Methodology**: A detailed exposition of the experimental methods employed in catalyst synthesis, characterization, and reaction studies; **Chapter 04 - Results and Discussion I**: In-depth exploration of the tuning of Co-Cu-Al catalysts and the impact of various reaction conditions on their performance; **Chapter 05 - Results and Discussion II**: Investigation into the behavior of Co-Cu-Al catalysts during the CO_2-to-higher alcohols reaction, shedding light on their underlying mechanisms; and **Chapter 06 - Conclusion**: A synthesis of the findings, implications, and potential avenues for future research.

Chapter 02

Literature Overview

We have the capacity and ability to create a remarkably different economy, one that can restore ecosystems and protect the environment while bringing forth innovation, prosperity, meaningful work, and true security.

— Paul Hawken (2010)

2.1 Carbon Dioxide

Carbon dioxide is a linear covalent molecule featuring two strong C=O bonds with a bond energy of up to 799 kJ/mol, a bond length of 116.3 pm, and a bond dissociation energy of 531.72 kJ/mol. As the final oxidation product of carbon, CO_2 exhibits high thermodynamic stability, presenting challenges for activation. The electron clouds in CO_2 are concentrated on the oxygen atoms, endowing carbon with strong electrophilicity and Lewis acid properties, activatable by alkali. Simple CO_2 activation and conversion are achieved through catalysts containing electron-donating ligands, often involving transition metal elements. Despite its stability, CO_2 poses challenges for value-added product synthesis due to the need for substantial energy input from carbon-neutral sources, active catalysts to lower activation energy, and high temperatures or pressures to overcome CO_2 stability (KAMKENG *et al.*, 2021; LI, X. *et al.*, 2023).

2.1.1 Problematics and Prospects

In 2022, global energy-related CO_2 emissions increased by 0.9% (321 Mt), reaching over 36.8 Gt, a slower growth compared to 2021's rebound of over 6%, as depicted in **Figure 2.1**. Emissions from energy combustion rose by 423 Mt, while industrial processes decreased by 102 Mt. Despite energy price shocks and disruptions, emissions growth was lower than feared, with clean energy technologies preventing an

additional 550 Mt in CO_2 emissions. Notably, oil emissions increased by 2.5% (268 Mt), driven partly by aviation rebound, while industry emissions declined by 1.7% to 9.2 Gt. Renewables, mainly solar photovoltaic (PV), and wind, met 90% of global growth in electricity generation (FRIEDLINGSTEIN *et al.*, 2022; HANNAH RITCHIE; MAX ROSER; PABLO ROSADO, 2020; IEA, 2023a).

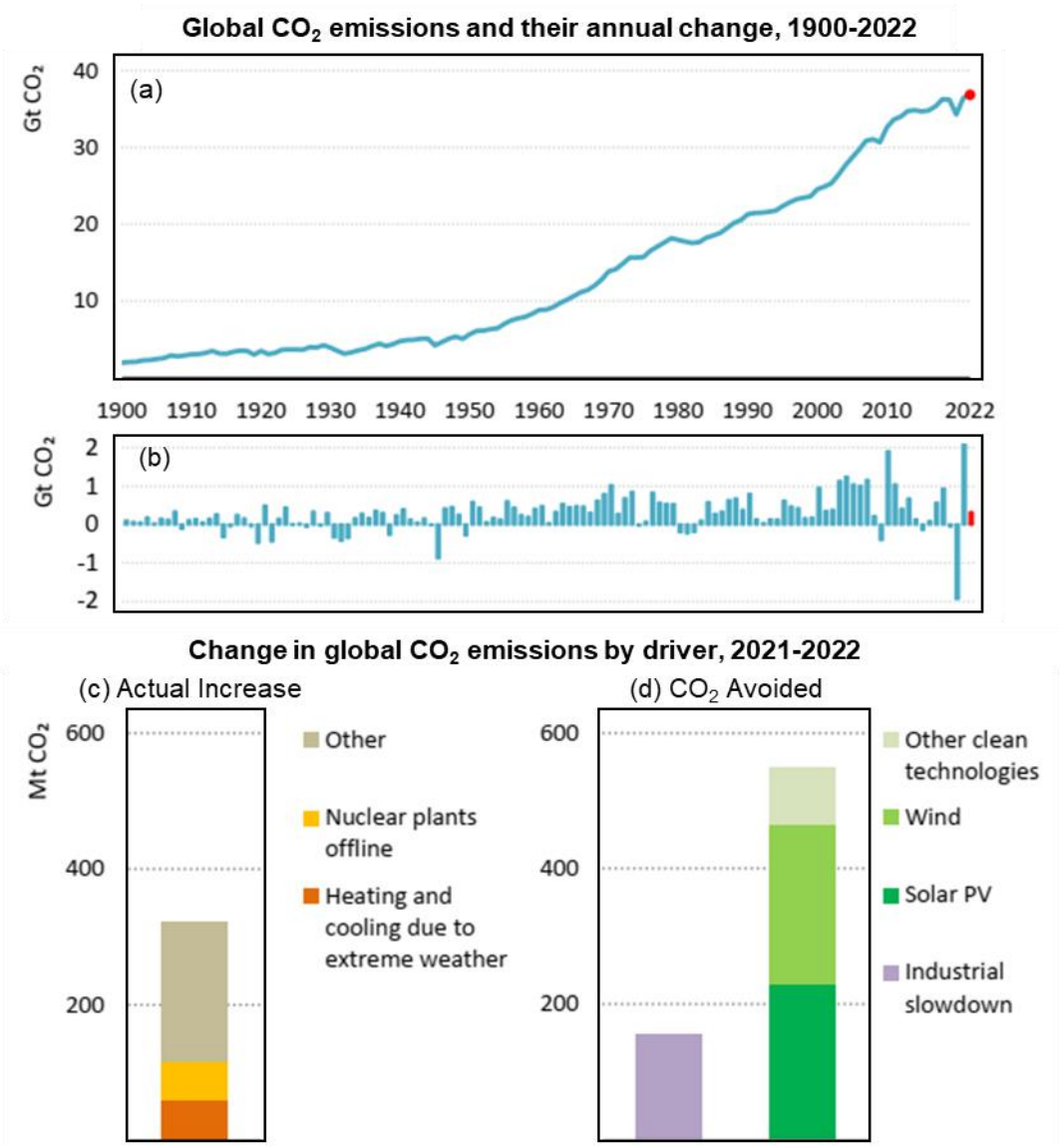

Figure 2.1 - *Global CO_2 emissions from energy combustion and industrial processes (a) and their annual change (b) from 1900 to 2022. Change in global CO_2 emissions from 2021 to 2022, by driver (c, d). (Adapted from* IEA, 2023a*).*

China's emissions remained relatively flat, declining by 0.2%, while the European Union reduced CO_2 emissions by 2.5% (70 Mt) despite market disruptions and hydro shortfalls. In the US, emissions grew by 0.8% (36 Mt), with the buildings sector experiencing the highest growth due to extreme temperatures. Asia's emerging markets

and developing economies, excluding China, surpassed other regions in emissions growth in 2022 (IEA, 2023a).

Despite the easing of immediate pressures from the global energy crisis, markets, geopolitics, and the global economy remain unsettled, with ongoing volatility in fossil fuel prices. The global average surface temperature is already 1.2 °C above pre-industrial levels, leading to increased extreme weather events, and greenhouse gas emissions have yet to peak (IEA, 2023a, 2023b).

Amid this complexity, the rise of a new clean energy economy brings hope. Clean energy investment has surged by 40% since 2020, driven by the imperative to reduce emissions, economic viability, energy security concerns, industrial strategies, and job creation. While not all clean technologies are thriving, notable progress is seen. The renewable energy sector, for instance, is flourishing, with over 500 gigawatts (GW) of capacity projected for this year (2023), marking a new record. Investment in solar deployment exceeds USD 1 billion per day, and manufacturing capacity for key clean energy components is rapidly expanding (IEA, 2023b).

2.1.2 CO_2 Conversion Technologies

The motivation for harnessing CO_2 for a sustainable future, driven by the pressing concerns of global warming and climate change, is evident. Moreover, recognizing the economic advantages, the concept of Carbon Capture, Utilization, and Storage (CCUS) has become an economically viable approach to meet CO_2 reduction targets. CO_2 utilization encompasses direct and indirect uses, where direct use involves utilizing pure or solution-suspended CO_2, such as in enhanced oil recovery, carbonated drinks, food preservation, and fire extinguishers. In contrast, indirect CO_2 utilization transforms CO_2 into chemicals, materials, and fuels through diverse chemical and biological processes (KAMKENG *et al.*, 2021).

According to **Table 2.1**, which outlines estimates for CO_2 utilization through both direct and indirect methods, the current global consumption of CO_2 for direct applications stood at 42.4 Mt in 2016, constituting approximately 18% of the total CO_2 utilized for indirect purposes (ARESTA; DIBENEDETTO; QUARANTA, 2016; KAMKENG *et al.*, 2021; NAIMS, 2016). While the demand for CO_2 in direct uses is expected to remain steady due to its stable industrial applications (NAIMS, 2016; NORHASYIMA; MAHLIA, 2018), the potential for efficient CO_2 utilization as a feedstock is projected to surge to over 332 Mt per year by 2030 (ARESTA; DIBENEDETTO; QUARANTA, 2016). Despite the challenges associated with transforming CO_2, the prospect of mitigating climate

change while simultaneously repurposing waste emissions into valuable products creates momentum for advancing CO_2 transformation technologies (KAMKENG *et al.*, 2021).

Table 2.1 – Current estimates of CO_2 utilization.

Utilization	Application/Product	CO_2 used ($Mt \cdot year^{-1}$)	Production ($Mt_{product} \cdot year^{-1}$)
Direct uses	Enhanced oil & gas recovery	25.0	25.0
	Food preservation	8.2	8.2
	Industrial gases	6.3	6.3
	Carbonated drinks	2.9	2.9
	Total	**42.4**	--
Indirect uses	Urea	132.0	180.0
	Inorganic carbonates	70.0	250.0
	Methanol	10.0	60.0
	Formaldehyde	5.0	25.0
	Dimethyl ether (DME)	5.0	20.0
	Tertiary butyl methyl ether	3.0	40.0
	Algae	2.0	1.0
	Polymers	1.5	15.0
	Acrylates	1.5	3.0
	Carbamates	1.0	6.0
	Formic acid	0.9	1.0
	Organic carbonates	0.5	5.0
	Total	**232.4**	**--**

(Adapted from KAMKENG *et al.*, 2021)

As portrait in **Figure 2.2**, CO_2 transformation technologies are often classified as into two categories, biological and chemical routes.

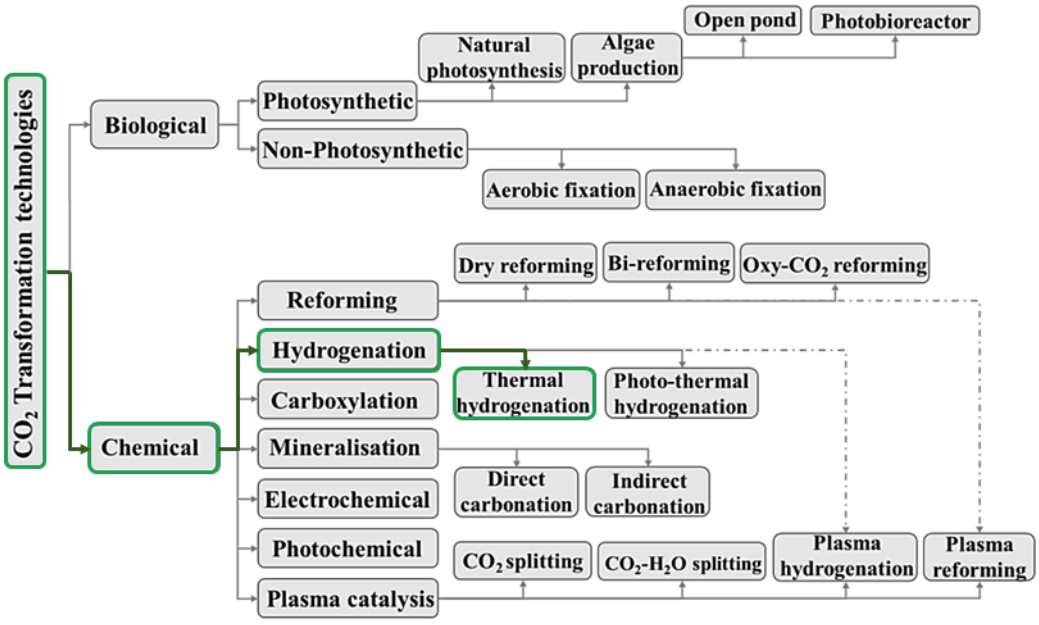

Figure 2.1 - *CO_2 transformation technologies*. (Adapted from KAMKENG *et al.*, 2021)

The biological route encompasses two sub-categories: photosynthetic and non-photosynthetic technologies. Photosynthetic technologies involve CO_2 fixation in plants or algae, while non-photosynthetic technologies utilize microorganisms (such as methanogens and acetogens) along with a high-energy electron source for CO_2 reduction into valuable bio-products (KAMKENG *et al.*, 2021).

The chemical route is further classified into seven sub-categories. Reforming technologies, including dry reforming, bi-reforming, and Oxy-CO_2 reforming, are catalytic processes that transform CO_2 and methane into syngas (CO + H_2). CO_2 hydrogenation, the primary focus of this thesis, is discussed separately (**section 2.3**). Carboxylation involves coupling CO_2 with another reactant to produce organic carbonates, urea, carbamates, polymers (polymerization), and carboxylic acids. CO_2 mineralization or carbonation produces inorganic carbonates from corresponding alkaline earth oxides. In CO_2 electrochemical reduction, the molecule is converted to chemicals and fuels in an electrolytic cell. CO_2 photochemical reduction is an artificial photosynthesis process using a catalyst that absorb light to convert CO_2 into value-added products. Plasma catalysis involves ionizing CO_2, leading to processes such as CO_2 splitting or, when accompanied by other molecules like CH_4 (plasma reforming), H_2 (plasma hydrogenation), and H_2O (CO_2-H_2O splitting), conversion into desired chemicals (CHAUVY *et al.*, 2019; CUÉLLAR-FRANCA; AZAPAGIC, 2015; KAMKENG *et al.*, 2021).

2.1.2.1 CO_2 Hydrogenation Initiatives

Kamkeng and coworkers utilized the Smart CO_2 Transformation (SCO_2T) database in 2020 to assess the status of CO_2 conversion projects. Their study revealed that approximately 53% of these projects are in the laboratory phase, while those at the pilot, demonstrative, and commercial scales account for 23%, 10%, and 14% of all initiatives, respectively. Notably, North America and Europe have emerged as primary hubs for these projects, constituting 29% and 65% of the initiatives, respectively (KAMKENG *et al.*, 2021).

Among the technologies studied, CO_2 catalytic hydrogenation is considered one of the most significant chemical conversions of CO_2 (CHAUVY *et al.*, 2019) representing about 35 projects and ranking as the second technology with the highest number of initiatives (KAMKENG *et al.*, 2021). The Technology Readiness Level (TRL) of CO_2 hydrogenation varies based on the specific technology and process. For instance, the production of renewable methanol via catalytic CO_2 hydrogenation is classified as TRL 8-9, at commercial scale, while CO_2-to-ethanol technologies, as of 2019, is at TRL 2, transitioning from theoretical to applied experiments (CHAUVY *et al.*, 2019).

TRL is employed to estimate the maturity of technologies during the acquisition phase, with TRL 1-3 indicating basic technology research, TRL 4-6 representing development scale, and TRL 7-9 signifying the transition from demonstration to full system qualification and successful operation (CHAUVY *et al.*, 2019). From a different perspective, TRL 1-4 corresponds to laboratory scale, 4-6 to pilot projects, 6-8 to demonstration projects, and 8-9 to commercial projects (KAMKENG *et al.*, 2021).

Furthermore, several companies have played a prominent role in implementing CO_2 hydrogenation projects for potential fuel production. Carbon Recycling International (CRI), for instance, initiated pilot projects for methanol production between 2006 and 2011, with commercialization beginning in 2020. The company has been involved in demonstrative and commercial-scale projects, including the "George Olah Renewable Methanol Plant" project in Iceland (2011), the "Shunli CO_2-to-methanol" (2022), and "Sailboat CO_2-to-methanol" (2023) projects in China. Additionally, CRI is planning the "Finnfjord E-Metanol" project in Norway (2024). The company aims to mitigate approximately 160,000 tons of CO_2 annually from various industrial sources (oil and gas, electricity, metallurgy, chemical industry, and cement). The hydrogen used in these processes comes from water electrolysis (CARBON RECYCLING INTERNATIONAL, 2023).

SeeO_2 Energy, based in Canada, claims to convert CO_2 into syngas, which is subsequently transformed into various fuels, as well as industrial and medical oxygen. Similar to CRI, this company also uses CO_2 from industrial emissions (SEEO2 ENERGY, 2023).

Also located in Canada, Carbon Engineering, founded in 2009, asserts that it converts CO_2 captured from the atmosphere with its proprietary technology into various fuels using hydrogen from water electrolysis. The company's first pilot plant was inaugurated in 2020, and in 2022, it began constructing its first commercial plant in Texas called "1PointFive" (CARBON ENGINEERING, 2023).

Two notable partnerships are worth mentioning. The first, established in 2021, is between the University of Cape Town (UCT) in South Africa and the company Sasol, aiming to produce green chemicals by combining CO_2 from biogenic or unavoidable industrial sources with hydrogen from water electrolysis (SASOL, 2021). The second partnership, formed in 2022, is between the company Larsen & Toubro and NTPC, a branch of India's Ministry of Energy. This collaboration aims to produce methanol from CO_2 captured from the atmosphere and hydrogen obtained through water electrolysis (THE HINDU BUSINESSLINE, 2022).

2.1.3 Brazilian Context

2.1.3.1 CO_2 Emissions in Brazil

Over the past 30 years, the waste, industry, and energy sectors in Brazil have witnessed a significant two to threefold increase in CO_2 emissions. This alarming trend is particularly concerning as industry and energy generation proportionally represent the primary sources of CO_2 emissions growth. In 2021, the Brazilian industrial sector contributed 108 million tons of CO_2 to the atmosphere, while the energy sector was responsible for 435 million tons of carbon dioxide as depicted by **Figure 2.2**. Notably, the metallurgical and cement production sectors within the industrial segment are intrinsic sources of CO_2 emissions, arising from manufacturing processes rather than fuel combustion to meet energy demands.

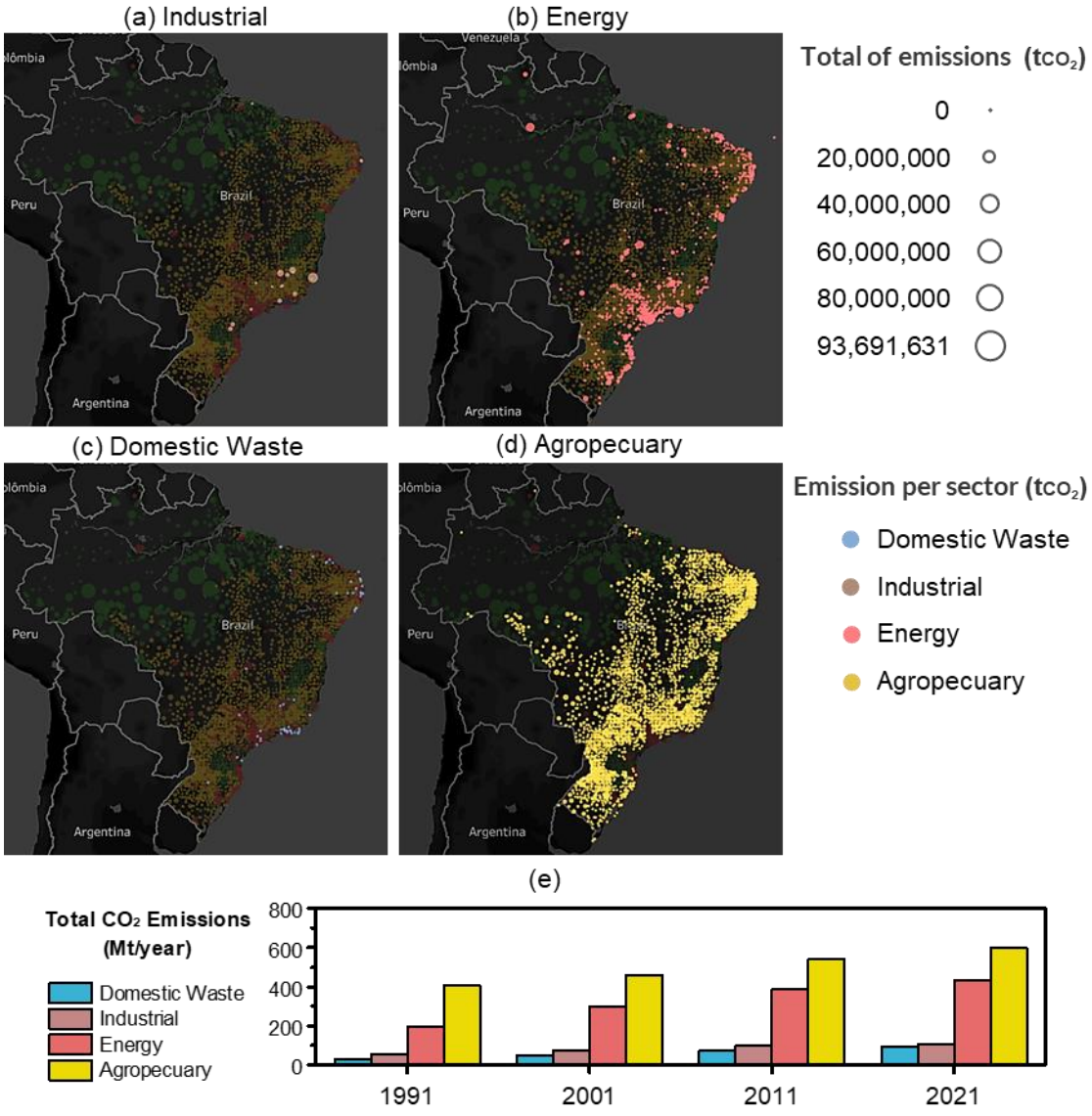

Figure 2.2 – *Distribution of emission per sector in 2019 (a-d), and their contribution to total of CO_2 emissions in Brazil over the years (e).* (Adapted from SEEG, 2022)

According to the latest survey from Greenhouse Gas Emissions and Removals Estimation System (SEEG), emissions from agricultural activities are dispersed nationwide, while emissions from industrial activities and energy generation are concentrated in specific regions. Energy production tends to concentrate in densely populated areas, while industrial activities are centralized in industrial hubs, predominantly in the Southeast region of Brazil. Regarding CO_2 emissions in the waste sector, it is noteworthy that they particularly concentrate in the state capitals of São Paulo and Rio de Janeiro, emphasizing these areas as significant emission hotspots (SEEG, 2022). In 2021, Brazil ranked 12th globally in CO_2 emissions, contributing 1.32% to the world's total emissions (FRIEDLINGSTEIN *et al.*, 2022).

2.1.3.1 Opportunities in Brazil

In the Brazilian context, the economic viability of CO_2 hydrogenation presents a compelling opportunity, driven by the convergence of two important factors: low-cost hydrogen production and the potential for generating valuable carbon credits. First, Brazil's efficient onshore wind projects contribute to its world-leading potential for low-cost, zero-carbon hydrogen production, ranging from \$2.01 to \$4.05·kg^{-1} (BLOOMBERG, 2023).

The introduction of carbon pricing mechanisms adds another layer of economic viability to CO_2 hydrogenation in Brazil. Carbon pricing, achieved through mechanisms like carbon taxes or cap-and-trade systems, serves as a policy tool addressing climate change by assigning a monetary value to carbon emissions. This policy creates economic incentives for businesses and individuals to transition to cleaner alternatives, fostering innovation and guaranteeing emission reduction targets. The key benefits of carbon pricing are as follows: cost-effectiveness; incentives for innovation; guaranteeing emission targets; intrinsic value and co-ownership of nature's gifts (BOYCE, 2018).

In the Brazilian context, carbon pricing can lead to a reduction in carbon-intensive infrastructure, particularly in the energy and transport sector, by promoting the use of biomass and e-fuels (GARAFFA *et al.*, 2021). Moreover, the removal of CO_2 can be strategically targeted across various economic sectors. Biogenic sources, given the prominence of the agricultural sector in Brazil, provide considerable flexibility. Conversely, for non-biogenic sources, the focus would be on metropolitan regions. Within the industrial sector, notable candidates include the metallurgy and cement industries, serving as significant sources of unavoidable CO_2 emissions and constituting a substantial portion of Brazil's industrial activities (SEEG, 2022).

This synergy between low-cost hydrogen production and carbon credit generation positions CO_2 hydrogenation as a promising avenue for economic development and climate mitigation in Brazil. On a side note, Brazil's rich environmental assets, notably the Amazon rainforest, provide a unique opportunity for the country to capitalize on carbon credits. Carbon revenue could contribute to the financing social, environmental and research expenses, and income distribution in Brazil (BOYCE, 2018; CALDEIRA; SEKULA; SCHABIB, 2020; GARAFFA et al., 2021).

2.2 CO_2 Hydrogenation

Carbon dioxide has emerged as a promising renewable carbon source, with its utilization as a feedstock for chemical production playing a crucial role in mitigating emissions and addressing global climate change. This area of research presents a compelling scientific challenge that necessitates the exploration of novel concepts and the development of catalytic and process breakthroughs (WANG *et al.*, 2011).

Carbon dioxide's industrial application is, however, limited by its thermodynamic stability, making its activation and subsequent conversion energy-intensive. Hence, an additional substance with higher Gibbs energy is required to enhance the thermodynamic feasibility of CO_2 transformation. For that reason, CO_2 hydrogenation has garnered considerable attention in recent years as an alternative method to produce fuels and chemicals, including lower olefins, higher hydrocarbons, formic acid, methanol, and higher alcohols (LI *et al.*, 2018a; WANG *et al.*, 2011), as illustrated by **Figure 2.3**.

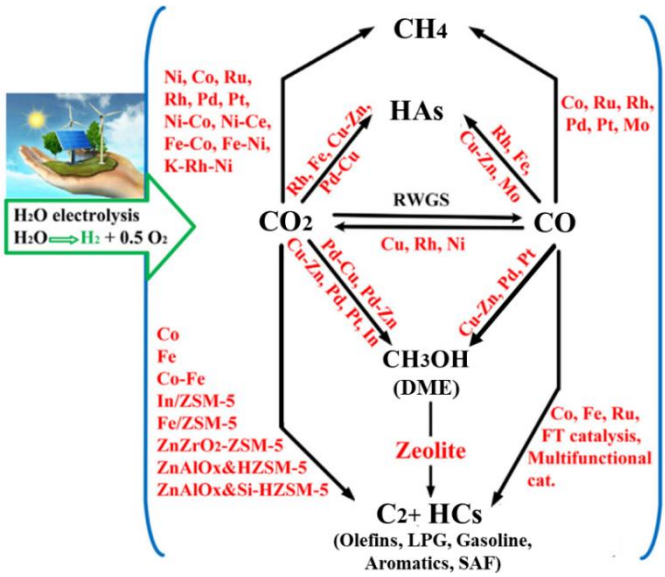

Figure 2.3 - *Various products of CO_2 hydrogenation*. (Adapted from SAEIDI *et al.*, 2021))

The concept of CO_2 hydrogenation dates to 1902 when Paul Sabatier reported the first CO_2 hydrogenation reaction, leading to the formation of methane (HASHIMOTO *et al.*, 2002). This reaction, commonly known as the Sabatier reaction or CO_2 methanation, and it exhibits exothermic behavior and a high equilibrium yield between 25 °C and 400 °C, reaching up to 99% selectivity towards CH_4 over suitable catalysts (KOSCHANY; SCHLERETH; HINRICHSEN, 2016). Notably, this process can serve as a valuable means of storing solar and wind energy (THAMPI; KIWI; GRÄTZEL, 1987). For instance, there were some “power-to-gas” pilot or commercial scale plants for CO_2 methanation in Germany (2009–2013, capacity: 25–6500 kW) (RÖNSCH *et al.*, 2016), and Denmark (2016, capacity: 1000 kW) (YOUNAS *et al.*, 2016). However, CO_2 methanation faces challenges due to its high H_2 consumption, lower energy density, and storage difficulties when compared to oxygenates and C_{2+} hydrocarbons (CENTI; PERATHONER, 2009).

While CO_2 methanation is noteworthy, the production of C_{2+} hydrocarbons is of greater interest due to their higher energy density and broader applicability in the fuel and chemical industries. Moreover, the Fischer–Tropsch synthesis, which involves converting syngas into hydrocarbons, is an established process, both academically and industrially (CHENG *et al.*, 2016; MULEJA *et al.*, 2017). However, substituting CO for CO_2 in this reaction introduces thermodynamic challenges (ZHENG *et al.*, 2017), as CO_2's inertness and lower adsorption compared to hydrogen, leads to a low C/H ratio, favoring methane and preventing chain-growth (GAO *et al.*, 2017; KATTEL *et al.*, 2016; LI *et al.*, 2017; WANG *et al.*, 2011; WEI *et al.*, 2017). Despite these challenges, the production of hydrocarbons via CO_2 hydrogenation remains appealing, as it aligns well with existing industrial infrastructure. On the other hand, when compared to oxygenates, hydrocarbons produced through CO_2 hydrogenation require more intensive use of resources, that is, energy, hydrogen, and reaction steps (CENTI; PERATHONER, 2009).

An alternative to hydrocarbons is methanol, which finds use as a solvent, fuel, and platform chemical (WANG *et al.*, 2011). Although CO_2 hydrogenation for methanol synthesis is reaching commercial viability (CHAUVY *et al.*, 2019), its kinetics often limits its large-scale application. Some authors propose focusing on small-scale local plants in the "Methanol Economy" while continually enhancing catalyst performance (CENTI; PERATHONER, 2009; LIU; YANG; WHITE, 2013). Alternatively, methanol can be dehydrated to dimethyl ether (DME) over acid catalysts, offering a clean-burning diesel substitute with attractive qualities, such high cetane number, low NOx emission, and near-zero smoke. However, CO_2 hydrogenation to DME faces similar kinetic and

thermodynamic limitations as methanol (CENTI; PERATHONER, 2009; WANG *et al.*, 2011).

Lastly, Higher alcohols (HAs) have garnered considerable attention as desirable products of CO_2 hydrogenation. Owning to their higher energy densities and diverse applications across industries, higher alcohols are a sustainable, safer, and easier-to-store fuel, platform chemical, and hydrogen carrier (CENTI; PERATHONER, 2009; HE *et al.*, 2015; LIU; YANG; WHITE, 2013). These alcohols, usually referred to as a group of C_2–C_4 (WANG *et al.*, 2011) or C_{2+} (LUK *et al.*, 2017) alcohols, serve as feedstock and intermediates in the chemical, polymer, and pharmaceutical industries, reagents in the preparation of plasticizers and detergents, and fuel sources (HE *et al.*, 2022; LUK *et al.*, 2017).

Currently, lighter alcohols, such as ethanol and isobutanol, are largely produced via starch or sugarcane-derived sugar fermentation, with the drawbacks are the high energy demand for the separation of the fermentation products. Heavier alcohols arise from the petrochemical industry, more specifically the hydration of alkene over acid catalysts, with a low single-pass conversion (~5%) (LUK *et al.*, 2017).

The exploration of CO_2 hydrogenation has involved both homogeneous and heterogeneous catalysts. Heterogeneous catalysts stand out for their stability, ease of handling, separation, and reuse. Furthermore, their lower cost makes them preferable for large-scale production (CENTI; PERATHONER, 2009; LI *et al.*, 2018a; WANG *et al.*, 2011).

2.2.1 Methane

The methanation of CO_2 has been extensively studied, predominantly employing transition metals, including Ni, Ru, Rh, Pt, Pd, Co, and Fe, supported on various oxide materials, such as Al_2O_3, TiO_2, SiO_2, ZrO_2, and CeO_2 (LI *et al.*, 2018a; WANG *et al.*, 2011), as depicted by **Figure 2.4.** Furthermore, the landscape of carbon dioxide methanation has witnessed the rise of novel catalysts, with structured catalysts and Metal-Organic Frameworks (MOFs) taking center stage (FAN; TAHIR, 2021).

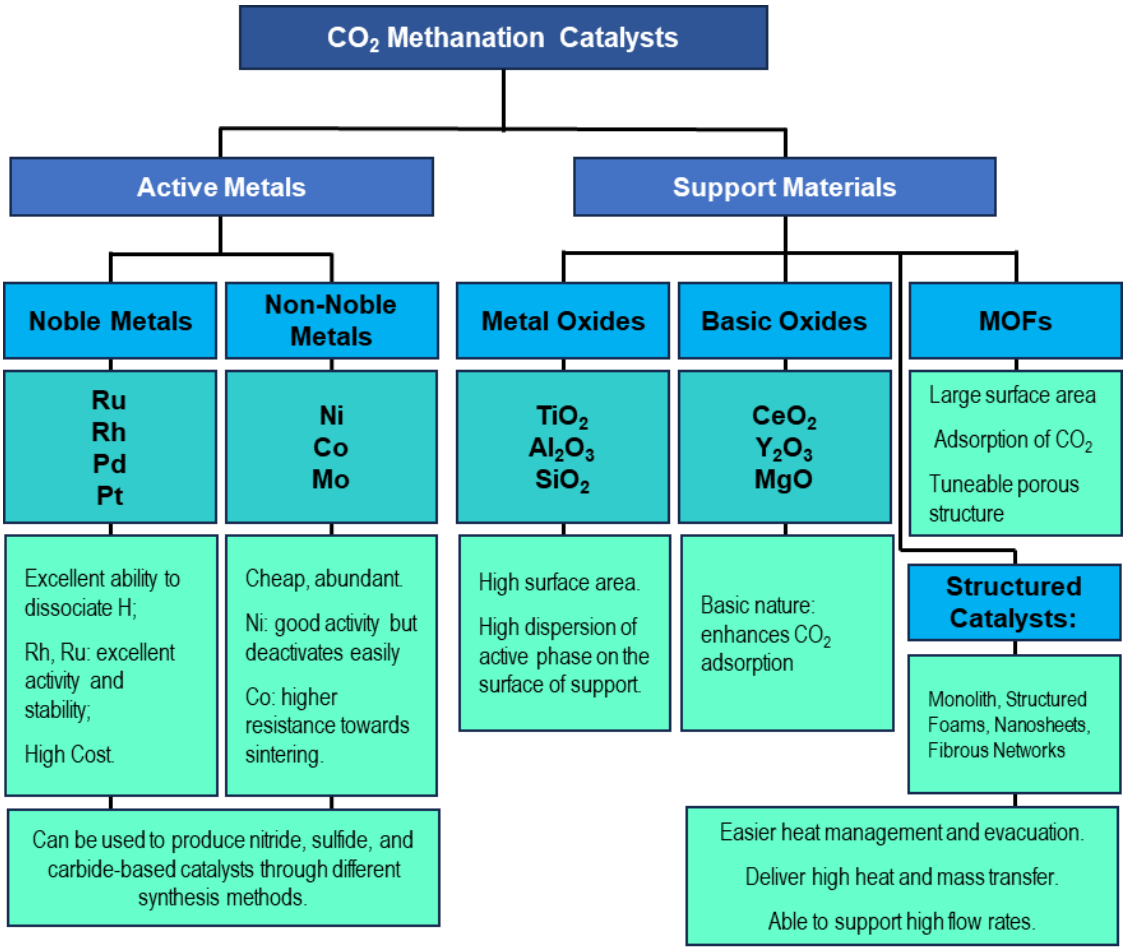

Figure 2.4 - *Overview of active metals and supports used for methanation.* (Adapted from FAN; TAHIR, 2021)

Through an analysis of previous literature, the activity and selectivity of various metals in carbon dioxide methanation have been ranked as follows: In terms of activity, the order is Ru > Rh > Ni > Fe > Co > Os > Pt > Ir > Mo > Pd. Conversely, the selectivity ranking, from highest to lowest, is Pd > Pt > Ir > Ni > Rh > Co > Fe > Ru > Mo. In summary, noble metals like Ru and Rh exhibit high activity and stability, but their cost remains a drawback. Consequently, non-noble metals, particularly Ni, have become a favored choice owing to their significant catalytic performance, abundance, and cost-effectiveness. Additionally, secondary metals like Ru, Fe, and Co enhance catalytic performance and stability when compared to supported monometallic Ni catalysts. The use of nitride, sulfide, and carbide-based catalysts further improves CO_2 methanation by enhancing metal-support interactions, resisting deactivation (e.g., sulfur poisoning and sintering), and augmenting surface basicity (FAN; TAHIR, 2021).

Over the years, several researchers explored different catalysts, preparation methods, and reaction conditions to produce methane through CO_2 hydrogenation. Some of the most relevant catalysts are summarized in **Table 2.2**.

Table 2.2 - *Summary of CO_2 methanation catalysts.*

Catalyst	GHSV ($mL \cdot g^{-1} \cdot h^{-1}$)	P (bar)	T (ºC)	X_{CO_2} (%)	S_{CH_4} (%)
$NiO–MgO@SiO_2$	90000	1	300	80	97
$Ni\text{-}W\text{-}MgO_x$	40000	1	300	83	99
Ni/CeO_2	22000	1	240	91.1	100
Ni-Ce /USY	43000	1	400	68.3	95.1
Ni/MOF-5	2000	1	320	75.1	100
$Ni/\gamma\text{-}Al_2O_3–ZrO_2–TiO_2–CeO_2$	20000	1	300	85	98
Ni–Al hydrotalcite	20000	1	300	86	98
$Ce–Ni/Al_2O_3$	7200	1	400	74	98
Ni/Al_2O_3	1500	1	350	85	98
Ni/TiO_2	60000	1	350	73.2	99
Rh/CeO_2	60000	1	350	46	89
$Ni\text{-}Ru/Al_2O_3$	40000	1	350	82	100
$Pd\text{-}Mg/SiO_2$	45000	1	450	59.2	95.3
$Pt–Co/Al_2O_3$	36000	1	400	70	98
Co/PC-600	72000	30	270	59	99
Co/ZrO_2	3600	30	400	92.5	99
Co/KIT-6	22000	1	260	46	99
Ru/P25	6000	1	200	27.4	100

(FAN; TAHIR, 2021; LI *et al.*, 2018a)

The choice of active metal and support material greatly influences the catalytic activity and stability of the reaction (FAN; TAHIR, 2021). Moreover, numerous factors influence the selection of an optimal catalyst support. For instance, ZHOU et al. (2017) prepared a series of ceria-supported nickel catalysts and attributed the best CO_2 methanation activity to the catalyst with a mesoporous structure and high surface area. Oxygen vacancies present in some supports also play a role in the activation of CO_2 into reaction intermediates (ZHOU *et al.*, 2016). Surface basicity is also a compelling feature as it can improve the catalyst CO_2 adsorption capability (LI *et al.*, 2018a).

The metal-support interaction is said to play an important role in CO_2 methanation by providing metal-support interface sites (WANG *et al.*, 2011). Moreover, along with the preparation method, metal-support interaction influences active metal particle size, in turn impacting the C/H ratio. Smaller clusters favor CO production, while larger particles favor CH_4 yield. This phenomenon could be explained by the types of reaction sites available for CO_2 adsorption (i.e., kink and step sites) and H_2 (i.e., terrace sites), but also by the particle oxidation state (LI *et al.*, 2018a). In other words, bigger particles are

composed mostly of zerovalent atoms, which favors the methanation reaction. On the other hand, smaller particles are usually more positively charged, favoring the reverse water-gas shift (rWGS) reaction (LI *et al.*, 2017).

Catalyst deactivation, which is one of the biggest challenges in CO_2 methanation, can occur chemically due to water leading to structural changes, or physically due to carbon deposition or metal sintering. Strategies to combat deactivation include modifying specific reaction sites (LI *et al.*, 2018a), enhancing metal-support interaction (LI *et al.*, 2018b), adding catalyst promoters (LI *et al.*, 2015), developing novel materials (LI; LU; MA, 2014), and using advanced synthesis methods (SCHUBERT *et al.*, 2016).

2.2.2 Hydrocarbons

Catalysts to produce C_{2+} hydrocarbons (HCs) via CO_2 hydrogenation can be divided into two types, the CO-mediated or modified Fischer-Tropsch (MFT) route and the methanol-mediated route (FUJIMOTO; SHIKADA, 1987; LEE *et al.*, 1992). Some relevant catalysts are summarized in **Table 2.3**.

***Table** Erro! Nenhum texto com o estilo especificado foi encontrado no documento.**.3** – Summary of some catalysts for CO_2 hydrogenation to hydrocarbons.*

Catalyst	GHSV ($mL \cdot g^{-1} \cdot h^{-1}$)	P (bar)	T (ºC)	X_{CO_2} (%)	S_{CH_4} (%)	$S_{C_{2-4}}$ (%)	$S_{C_{2-4}^{=}}$ (%)	$S_{C_{5+}}$ (%)
1Fe-1Zn-K	1000	5	320	51	34.8	7.8	53.6	3.7
10Fe4.8K	560	25	300	35.2	7.4	3.9	14.9	64.8
84Fe6.7K9.3Co	560	25	300	57.2	22.4	8.7	23.5	43.8
5Mn-Na/Fe	2040	30	320	38.1	11.8	4	30.2	42.1
Fe-Cu-K-Al	2000	10	275	32.4	7.7	5.4	11.5	70.4
Fe/Al_2O_3	32	10	300	22.8	38.3	42.4	0.3	7.8
$ZnZrO_x@Al_2O_3@$ SAPO-34	3500	30	380	21	1.7	11	41.2	1.1
$ZnZrO_x$/SAPO-34	3600	20	380	12.6	1.5	1.6	42.4	7.4
ZnAl/HZSM-5	2000	30	320	9.1	0.2	2.9	4.6	34.2
ZS-HPB-500	3500	30	380	21	8.5	51.3	10.1	3.1
In_2O_3/HZSM-5	9000	30	340	13.1	0.6	7.2		43.2
FeZnZr@HZSM-5 @Hβ	3000	80	340	14.9	0.9	43.6		16.3

(LI *et al.*, 2018a; OJELADE; ZAMAN, 2021; SAEIDI *et al.*, 2021)

For the synthesis of alkanes and alkenes via MFT, CO_2 is first hydrogenated to CO via rWGS, followed by Fischer-Tropsch synthesis (FTS) (SAEIDI *et al.*, 2021; WANG

et al., 2011). This route can be achieved by either a standalone catalyst or a tandem catalyst. In this context, a tandem catalyst indicates a combination of either an FTS catalyst or a methanol synthesis (MS) catalyst and zeolites (OJELADE; ZAMAN, 2021). For MFT, modified Fe-based catalysts have been extensively explored for CO_2 hydrogenation (LI *et al.*, 2018a; OJELADE; ZAMAN, 2021; SAEIDI *et al.*, 2021).

The presence of Fe on the catalyst surface enhances C-C coupling, a critical rate-determining step (NIE *et al.*, 2017). Furthermore, various facets of Fe-based catalysts can undergo electronic modification, leading to the formation of new phases with catalytic properties that facilitate the reaction. For example, certain studies have identified Fe_3O_4 as the active phase for the rWGS step, and iron carbide (Fe_5C_2) for the FTS step (OJELADE; ZAMAN, 2021).

Like in CO_2 methanation catalysts, the metal-support interaction plays a pivotal role in CO_2-to-HCs catalysis. Thus, the choice of support significantly influences the product distribution (WANG *et al.*, 2011). Support materials for the MFT pathway encompass a range of materials such as metal oxides, MOFs, and nitrogen-doped carbon. These materials exhibit beneficial structures that enhance heat and mass transfer properties (OJELADE; ZAMAN, 2021).

For instance, ZrO_2-supported catalysts exhibit superior selectivity and yield for lower olefins when compared to SiO_2, Al_2O_3, TiO_2, and carbon-based materials, due to the oxygen vacancies and basic sites on the zirconia support (LI *et al.*, 2018a; WANG *et al.*, 2013). In contrast, alumina effectively prevents sintering of active particles due to strong metal-support interaction, often attributed to its hydroxyl-rich surface (WANG *et al.*, 2011).

Additionally, promoters can be incorporated into catalysts to enhance HC product distribution. For example, potassium acts as an electronic promoter to the supported metal and functions as a reversible H_2 storage, effectively suppressing side hydrogenation reactions of the products. Thus, K-doing can tune the C/H ratio and enhance CO_2 conversion, olefin yield, and C-C coupling (DORNER *et al.*, 2010; SATTHAWONG *et al.*, 2015). Other alkali metals, particularly Na, also exhibit promising promotional effects for iron-based catalysts in CO_2 hydrogenation (LI *et al.*, 2018a; LIANG *et al.*, 2018; LIU et al., 2018b; WANG *et al.*, 2011).

Similarly, manganese suppresses methanation reactions and enhances the olefin/paraffin ratio (DORNER *et al.*, 2010). Other positive effects of Mn include improving supported metal reducibility and dispersion, as well as increasing surface basicity (HERRANZ *et al.*, 2006; LI *et al.*, 2007; LIU et al., 2018b) while promoting the

rWGS and FT reactions (AL-DOSSARY et al., 2015). Likewise, copper enhances catalyst reducibility and provides a dissociative site for hydrogen adsorption (HERRANZ *et al.*, 2006). Cu-doped catalysts show performance similar to Mn-doped ones (ANDO *et al.*, 1998; NING; KOIZUMI; YAMADA, 2009). However, excessive copper doping can have a reverse promotional effect, leading to a reduction in HC selectivity (DORNER *et al.*, 2010).

Additionally, the introduction of zinc can lead to the formation of a spinel structure with iron ($ZnFe_2O_4$), thereby modifying CO_2 adsorption behavior. Consequently, the addition of Zn has the potential to improve both CO_2 conversion and olefin yield, at the expense of inhibiting the production of heavier hydrocarbons. It's worth noting that an excessive amount of Zn can hinder conversion (WITOON *et al.*, 2021; ZHANG *et al.*, 2015).

One of the primary challenges in the CO-mediated approach lies in the broad product distribution, adhering to the Anderson-Schulz-Flory (ASF) distribution (ZHANG; KANG; WANG, 2010). To address this limitation and gain better control over the production of lower olefins or gasoline-range hydrocarbons, the methanol-mediated approach is suggested (LI *et al.*, 2018a). In this pathway, CO_2 is initially converted into methanol using a methanol-directed catalyst, usually a combination of metal oxides (In_2O_3, ZrO_2, ZnO, Ga_2O_3), and then transformed into hydrocarbons, often over zeolites (OJELADE; ZAMAN, 2021; SAEIDI *et al.*, 2021). Among the zeolites studied in the literature, HZSM-5 has demonstrated notable selectivity towards C5-C11 high-octane hydrocarbons (GAO et al., 2017). Conversely, modified hydrophilic Hβ and SAPO-34 zeolites have exhibited superior selectivity for C2-C4 hydrocarbons (CHENG *et al.*, 2016; FUJIWARA *et al.*, 2015b, 2015a; LIU, X. *et al.*, 2017).

Additionally, structured catalysts can be used to favor specific products (LI *et al.*, 2018a; OJELADE; ZAMAN, 2021; SAEIDI *et al.*, 2021). For example, isoalkanes can be favored in the CO_2 hydrogenation reaction through confinement effect of a core-shell structure (e.g., Fe-Zn-Zr@zeolites), HZSM5-Hβ being the most extensively explored zeolite (WANG *et al.*, 2016). More so, the nature of the metal oxide surface in tandem catalysts play a crucial role in controlling the confinement of hydrocarbons within zeolite pores. Different metal oxides exhibit different abilities to activate CO_2 and adsorb CO for the formation of methoxy/methanol intermediates that later are converted into HCs. The geometry and topology of the zeolite, in turn, determine hydrocarbon distribution (OJELADE; ZAMAN, 2021).

2.2.3 Methanol

In general, the catalysts employed for CO_2 hydrogenation into methanol are similar to those used for methanol production via CO hydrogenation. However, during CO_2 hydrogenation, the formation of by-products can occur. Consequently, the demand for highly selective catalysts in this process is essential (WANG *et al.*, 2011). The primary catalytic materials employed for methanol production are illustrated in **Figure 2.5**.

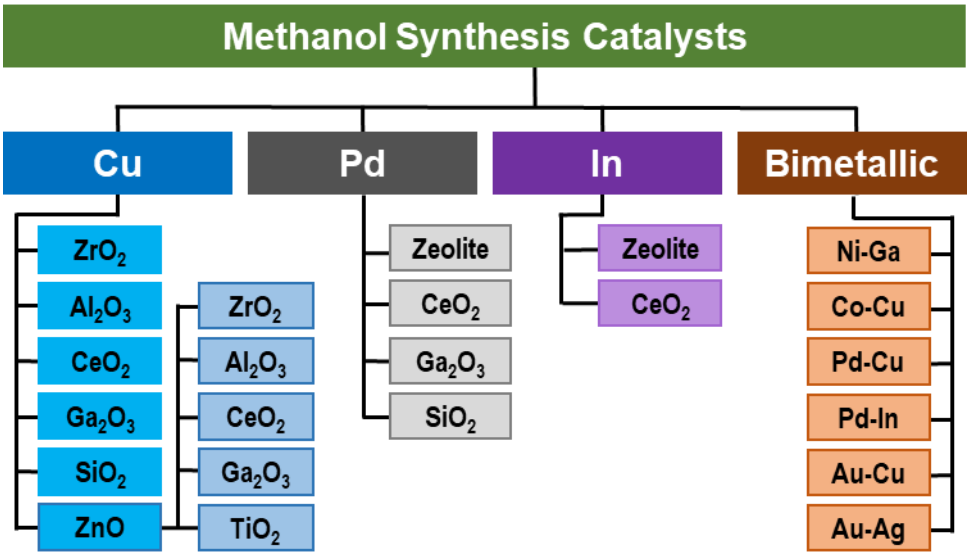

Figure 2.5 – *Types of CO_2-to-methanol catalysts. (Adapted from* SAEIDI *et al.*, 2021)

Among all the metal-based catalysts studied for methanol synthesis, Cu-based catalysts exhibit the highest activity. Cu-based catalysts are frequently combined with modifiers such as Zn, Zr, and Ga, among others (ARENA *et al.*, 2007; LIAW; CHEN, 2001). Additionally, noble metals like Au and Pd can be introduced to facilitate hydrogen activation and enhance surface reducibility through the hydrogen-spillover mechanism (FIERRO; MELIÁN-CABRERA; LÓPEZ GRANADOS, 2002a, 2002b; LIANG *et al.*, 2009; SŁOCZYŃSKI *et al.*, 2004). Similarly to hydrocarbons, the choice of support can influence and stabilize the active phase, determine surface basicity and/or acidity, and adjust the interaction between the catalyst's main components, specifically the metal and its modifiers (LIU *et al.*, 2003). In this respect. Al_2O3 and ZrO_2 are the most used supports and Cu-ZnO-Al_2O_3 is the most widely used catalyst for methanol synthesis (SAEIDI *et al.*, 2021).

Despite the extensive research on Cu-based catalysts, the issues regarding deactivation, sintering, and phase segregation during the CO_2 hydrogenation reaction

have prompted the search for alternative materials. In this context, indium oxide (In_2O_3) has emerged as a promising candidate for methanol synthesis via CO_2 hydrogenation due to its exceptional selectivity and stability. Palladium (Pd) and bimetallic catalysts also demonstrate promising results (SAEIDI *et al.*, 2021). Some catalysts investigated over the years for methanol synthesis via CO_2 hydrogenation are depicted in **Table 2.4**.

Table 2.4 *- Summary of some catalysts for CO_2 hydrogenation to methanol.*

Catalyst	**GHSV** ($mL \cdot g^{-1} \cdot h^{-1}$)	**P** (bar)	**T** (ºC)	**X_{CO_2}** (%)	**S_{CO}** (%)	**S_{CH_3OH}** (%)
$Cu/ZnO/Al_2O_3$	18000	40	250	11.1	45.2	54.8
$Cu/Zn/Al/ZrO_2$	9800	40	240	18.8	52.8	47.2
$Au/Zn/ZrO_2$	3300	80	220	1.5	-	100
$Cu/Zn/ZrO_2$	3600	30	220	12	-	71.1
$Cu/ZnO/Ga_2O_3$	3600	45	240	27	-	50
Cu/CeO_2	10000	30	280	10	16	74
$Cu\text{-}Ni/CeO_2$	6000	30	260	18	17	73
$0.5Pd\text{-}Zn/CeO_2$	2400	30	220	7.7	0	100
$Pd/In_2O_3/SBA\text{-}15$	15000	10	260	12.4	16	84
Pd/In_2O_3	21000	50	300	20	-	70
$Pd\text{-}Cu/CeO_2$	3600	41	250	9.9	71.6	28.4
$Pd\text{-}Cu/ZrO_2$	3600	41	250	15.8	73.2	26.8
$Pd\text{-}Cu/Al_2O_3$	3600	41	250	12.4	68.7	31.4
$Pd\text{-}Cu/SiO_2$	3600	41	250	6.6	66	34
In_2O_3/ZrO_2	20000	50	300	5.2	0.2	99.8
$Cu\text{-}In/In_2O_3$	7500	30	280	11.4	-	80.5
Cu@ZnO	18000	30	250	2.3	0	100
$Cu\text{-}ZnO/Al_2O_3$ ($H_2:CO_2 = 10$)	182000	360	260	65.8	-	77.3

(Adapted from KANURI *et al.*, 2022; SAEIDI *et al.*, 2021; ZHONG *et al.*, 2020)

As aforementioned, In-based catalysts have garnered considerable interest for their remarkable selectivity towards methanol and their stability across a broad range of reaction conditions (10-50 bar, 16000-48000 $mL \cdot g^{-1} \cdot h^{-1}$, and 200-300 °C) (MARTIN *et al.*, 2016). DFT calculation revealed In_2O_3 provides oxygen vacancies on which CO_2 is adsorbed and converted to methanol (GAO *et al.*, 2017).

Zinc and zirconium are used as both promoters and supports for methanol-directed catalysts (WANG *et al.*, 2011). ZnO enhances particle dispersion and stability (OVESEN *et al.*, 1997; YOSHIHARA; CAMPBELL, 1996), and introduces oxygen vacancies, i.e., lattice electron pairs that activate CO_2 (LIU *et al.*, 2003). Meanwhile, ZrO_2

exhibits stability in both reductive and oxidative atmospheres and contributes to particle dispersion, thereby enhancing catalytic activity and selectivity towards methanol (AN *et al.*, 2007; ARENA *et al.*, 2007; GUO *et al.*, 2009; LIU *et al.*, 2001; RAUDASKOSKI; NIEMELÄ; KEISKI, 2007).

Additionally, CeO_2 is another potential catalyst support that exhibits effects similar to zirconia (KANURI *et al.*, 2022). Methanol-catalyst activity can also be improved by the addition of Ga_2O_3 and Y_2O_3, as they improve Cu dispersion, reducibility, and metal-support interaction. Moreover, La-insertion in the support structure increases oxygen vacancies and promotes basicity, in general, improving methanol selectivity (ZHONG *et al.*, 2020).

Furthermore, water adsorption on the catalyst surface can hinder methanol formation, necessitating the addition of other components to mitigate this process. For instance, the inclusion of Ga, B, and Al not only reduces water adsorption but also enhances copper dispersion, thereby boosting catalyst activity (KANURI *et al.*, 2022; LIU; LU; YAN, 2005; SŁOCZYŃSKI *et al.*, 2006; ZHONG *et al.*, 2020).

2.3 CO_2 Hydrogenation to Higher Alcohols

The CO_2 conversion to higher alcohols (HAs), encompassing C_{2+} alcohols, has gained significant attention due to their diverse applications as energy carriers and feedstock chemicals. While the exploration of CO_2-to-HAs synthesis is a relatively new research area, recent geopolitical conflicts causing uncertainties in the chemical sector and soaring gasoline and natural gas prices underscore the need for intensified efforts in chemical production. In the current landscape, there is a particular emphasis on higher alcohols as alternative fuel additives (LATSIOU *et al.*, 2023). Compared to extensively studied alternatives like methanol, higher alcohols offer advantages such as lower toxicity, reduced volatility, enhanced solubility in fuel, and higher energy density (HE *et al.*, 2022).

2.3.1 Reaction Thermodynamics

In recent decades, researchers have devoted significant attention to studying the thermodynamic and mechanistic aspects of CO_2 and CO hydrogenation reactions to several products, such as hydrocarbons, dimethyl ether, and methanol. Yet, CO_2 conversion into higher alcohols has only received focus in recent years (ATSONIOS; PANOPOULOS; KAKARAS, 2016; CENTI; PERATHONER, 2009; LUK *et al.*, 2017; PRIETO, 2017; STANGELAND; LI; YU, 2018-; YOUNAS *et al.*, 2016). The intricacies of the CO_2 hydrogenation reaction, constrained by both thermodynamics and kinetics, pose

significant challenges in developing catalysts for commercial applications (JIA *et al.*, 2016).

Understanding the thermodynamic and theoretical aspects of CO_2 hydrogenation is of paramount importance. It aids in selecting optimal reaction conditions and designing catalysts with selectivity for higher alcohols. Thermodynamic calculations serve as valuable tools for comprehending and predicting complex catalytic processes, offering insights into the impact of various reaction parameters (GAO *et al.*, 2012; LIMA DA SILVA; MALFATTI; MÜLLER, 2009; SWAPNESH; SRIVASTAVA; MALL, 2014; TANG; KITAGAWA, 2005).

(JIA *et al.*, 2016) conducted systematic thermodynamic analyses of CO_2 hydrogenation reaction using the total Gibbs free energy minimization method, a widely employed approach for complex reaction systems (GAO *et al.*, 2012; LIMA DA SILVA; MALFATTI; MÜLLER, 2009; TANG; KITAGAWA, 2005). Their study considered multiple products in the calculation and explored the relationship between product distribution and reaction conditions. It is essential to note that the analysis focused on thermodynamics, omitting considerations of reaction kinetics and transport phenomena. Data validation was carried out in well-designed catalytic experiments targeting CO_2 hydrogenation to CO and CH_4 over ceria-supported Ni and Cu catalysts. The data related to Gibbs free energy changes ($\Delta G^{\ominus}_{298\,K}$), enthalpy changes ($\Delta H^{\ominus}_{298\,K}$), and standard equilibrium constant ($K^{\ominus}_{298\,K}$) for some of the products are summarized below in **Table 2.5**.

Table 2.5 - *Gibbs free energy changes, enthalpy changes, and standard equilibrium constants in hydrogenation reactions of CO_2 to some products.*

No.	Reaction	$\Delta G^{\ominus}_{298\,K}$ (kJ.mol^{-1})	$\Delta H^{\ominus}_{298\,K}$ (kJ.mol^{-1})	$K^{\ominus}_{298\,K}$
1	$CO_2 + H_2 \leftrightarrow CO + H_2O$	28.6	41.2	$9.67 \cdot 10^{-6}$
2	$CO + 3H_2 \leftrightarrow CH_4 + H_2O$	-141.9	-206.0	
3	$CO_2 + 4H_2 \leftrightarrow CH_4 + 2H_2O$	–113.5	–165.0	$7.79 \cdot 10^{19}$
4	$CO + 2H_2 \leftrightarrow CH_3OH$		–90.4	
5	$CO_2 + 3H_2 \leftrightarrow CH_3OH + H_2O$	3.5	–49.3	$2.45 \cdot 10^{-1}$
6	$2CO_2 + 6H_2 \leftrightarrow CH_3OCH_3 + 3H_2O$	–4.9	–61.3	*7.15*
7	$2CO + 4H_2 \leftrightarrow C_2H_5OH + H_2O$	–221.1	–253.6	

8	$2CO_2 + 6H_2 \leftrightarrow C_2H_5OH + 3H_2O$	–32.4	–86.7	$4.70 \cdot 10^5$
9	$3CO_2 + 9H_2 \leftrightarrow n\text{-}C_3H_7OH + 5H_2O$	–39.9	–94.6	$9.82 \cdot 10^6$
10	$4CO_2 + 12H_2 \leftrightarrow n\text{-}C_4H_9OH + 7H_2O$	–43.2	–98.3	$3.73 \cdot 10^7$
11	$CO_2 + 4H_2 \leftrightarrow CH_4 + 2H_2O$	–113.5	–165.0	$7.79 \cdot 10^{19}$
12	$2CO_2 + 7H_2 \leftrightarrow C_2H_6 + 4H_2O$	–78.7	–132.1	$6.26 \cdot 10^{13}$
13	$3CO_2 + 10H_2 \leftrightarrow C_3H_8 + 6H_2O$	–70.9	–125.0	$2.64 \cdot 10^{12}$
14	$4CO_2 + 13H_2 \leftrightarrow n\text{-}C_4H_{10} + 8H_2O$	–66.9	–121.6	$5.28 \cdot 10^{11}$

(JIA *et al.*, 2016; ZENG *et al.*, 2021)

According to Jia's calculations, for the CO_2 hydrogenation reaction, CO_2 conversion increases with temperature and H_2/CO_2 ratio. In contrast, CO and CH_4 selectivity exhibit opposed responses to changes in temperature. As temperature increases, CO formation, an endothermic reaction, is favored over CH_4, which is an exothermic reaction, as depicted in **Figure 2.6**.

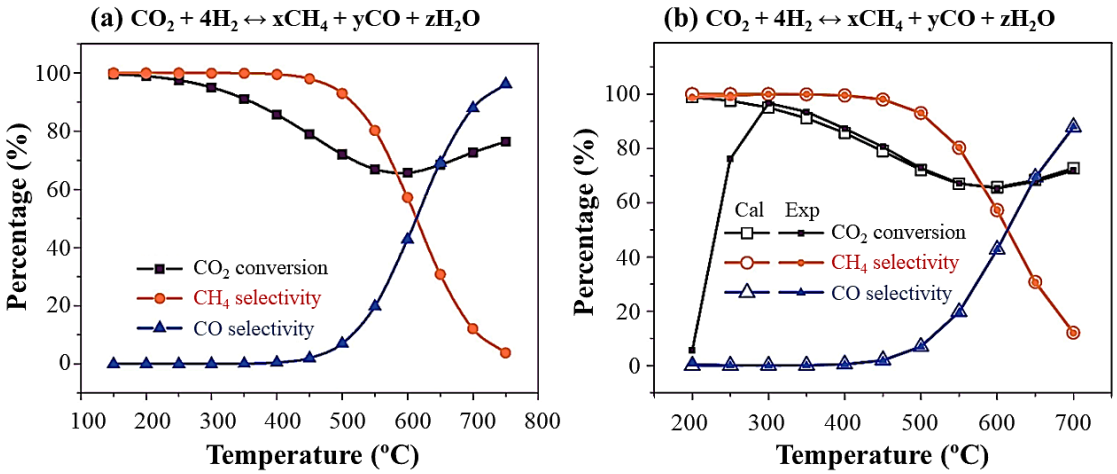

Figure 2.6 - *CO_2 hydrogenation to CO and CH_4 at 0.1 MPa and H_2/CO_2 ratio of 4: conversion at equilibrium state (a); comparison of calculated data and experimental data over Ni/CeO_2 catalyst (b).* (JIA *et al.*, 2016)

However, it's important to recognize that the methanation reaction exhibits a high equilibrium up to 400 ºC (GAO *et al.*, 2012; KOSCHANY; SCHLERETH; HINRICHSEN, 2016). This equilibrium effect contributes to one of the significant challenges in CO_2 hydrogenation reactions aimed at producing valuable chemicals, as it inhibits the formation of CH_4 (LI *et al.*, 2018a). It's worth noting that Jia and coworkers' experimental data for CO_2 conversion below 300 ºC exhibit deviations from their calculated values (Figure 2.Y1b). These discrepancies were attributed to the poor activity of the catalyst at lower temperatures.

In the context of CO_2 hydrogenation towards alcohols, it's crucial to consider the exothermic nature of the reaction, which has significant implications for its

thermodynamics. The equilibrium CO_2 conversion is inversely proportional to temperature. Conversely, CO_2 hydrogenation to produce alcohols (methanol, ethanol, and C_{3+} alcohols) is a volume-reducing reaction. As a result, an increase in pressure has a direct and positive impact on CO_2 conversion, as shown in **Figure 2.7**. In essence, the reaction benefits from higher pressure conditions.

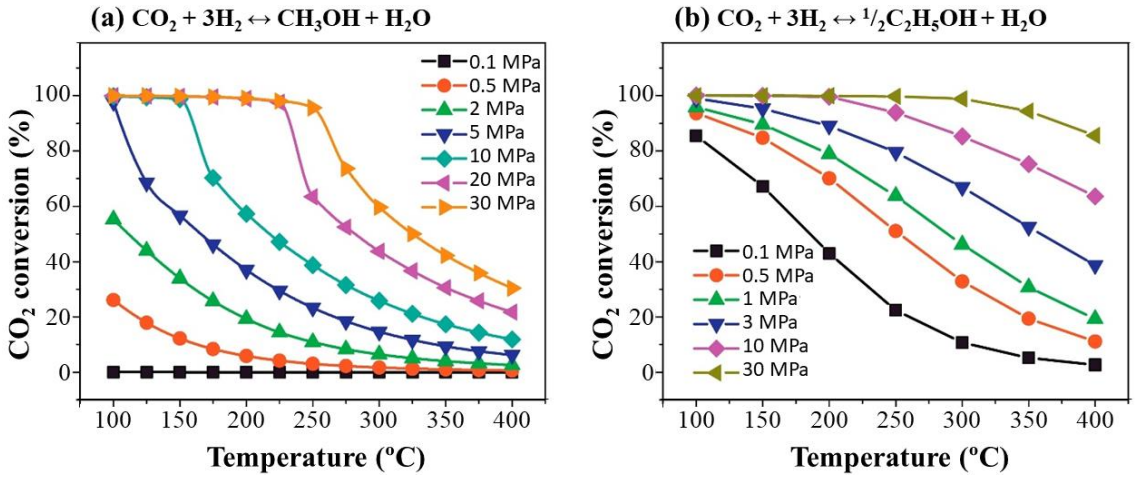

Figure 2.7 - *Equilibrium CO_2 conversion for the hydrogenation reaction to (a) methanol, and (b) ethanol.* (JIA *et al.*, 2016)

From a thermodynamic perspective, it becomes evident that maintaining low-to-moderate temperatures and operating under high pressures presents distinct advantages for enhancing alcohol production. Moreover, when compared under the same reaction conditions, ethanol emerges as the more favorable product over methanol (JIA *et al.*, 2016).

(JIA *et al.*, 2016) applied the same method considering methanol, ethanol, propanol, and butanol as products from CO_2 hydrogenation, illustrated by **Figure 2.8**. According to their calculation, butanol would be the dominant product under a wide range of reaction conditions.

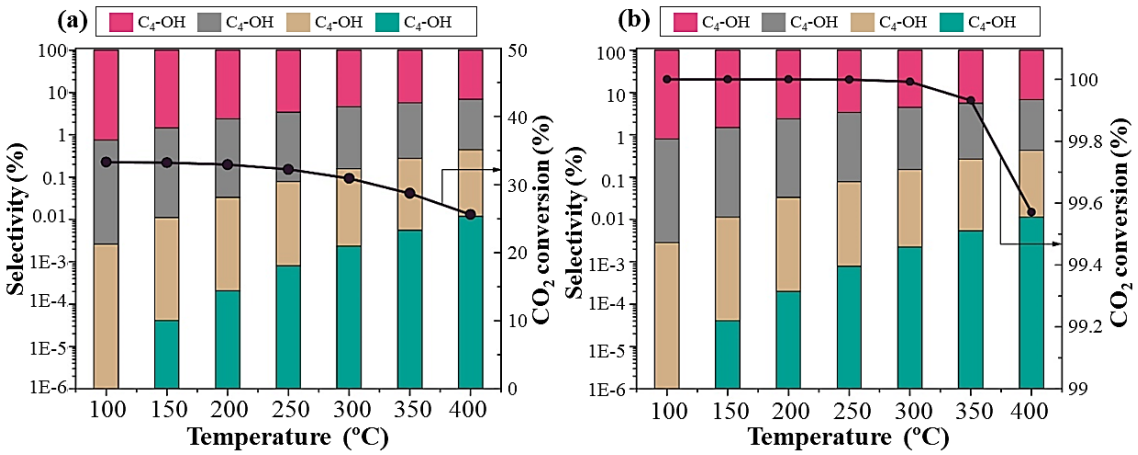

Figure 2.8 *- CO_2 hydrogenation performance towards a mixture of alcohols: (a) under H_2/CO_2 ratio of 1 and 5 MPa; and (b) under H_2/CO_2 ratio of 5 and 20 MPa. (JIA* et al.*, 2016)*

These findings align with the changes in Gibbs free energy and lend support to the hypothesis that the formation of higher alcohols is more thermodynamically favorable than methanol in CO_2 hydrogenation (JIA *et al.*, 2016; PRIETO, 2017). A similar conclusion arises when CO is considered. Across all studied scenarios ($C_{1\text{-}2}$OH/CO, $C_{1\text{-}3}$OH/CO, or $C_{1\text{-}4}$OH/CO), the longest-chain alcohol was favored over methanol (STANGELAND; LI; YU, 2018-). However, it's essential to note that this method does not account for other potential by-products. For instance, the CO_2 hydrogenation to ethanol is considerably limited at 0.1 to 3 MPa, since CH_4 is formed preferentially. In other words, in practice, selectivity toward alcohols is usually low (YANG *et al.*, 2019).

As a matter of fact, taking into consideration the equilibrium constants ($K^{\ominus}_{298\ K}$) (**Table 2.5**) for different products of the CO_2 hydrogenation reaction, it becomes evident that hydrocarbons, particularly methane, would be predominant under typical conditions (XU *et al.*, 2021a; ZENG *et al.*, 2021). Thus, this observation underlines the significance of designing efficient CO_2-to-HAs catalysts capable of imposing a high kinetic barrier for methanation to reduce CH_4 selectivity and increase the selectivity towards alcohols (ZENG *et al.*, 2021).

In summary, the CO_2 hydrogenation reaction to alcohols demonstrates thermodynamic favorability (JIA *et al.*, 2016; STANGELAND; LI; YU, 2018-). Contrarily to CO_2 hydrogenation reaction to C_{2+} hydrocarbons, the Gibbs free energy for this reaction decreases logarithmically with product chain growth (PRIETO, 2017). Furthermore, the CO_2 hydrogenation to higher alcohols is an exothermic and volume-reducing reaction, making it more favorable at low temperatures and high pressures (HE *et al.*, 2022; JIA *et al.*, 2016; LATSIOU *et al.*, 2023; XU *et al.*, 2021a). The influence of these reaction parameters is further discussed in **section 2.3.5**. Nevertheless, despite its thermodynamic favorability, the complexity of this reaction system presents a significant challenge, namely, the formation of other byproducts such as CO, CH_4, and various hydrocarbons.

2.3.2 Reaction Mechanisms

The mechanism of HAs synthesis via the CO_2 hydrogenation reaction is complex and remains a subject of debate due to the coexistence of various surface species at different concentrations. In that sense, more *in situ* or *operando* studies are required to gain clarity (XU *et al.*, 2021a).

In general, the mechanism for HAs synthesis involves the activation of CO_2, controlled hydrogenation, C-C coupling, and, in some cases, hydroxylation (LI, X. *et al.*, 2023). A simplification of this mechanism is depicted in **Figure 2.9**, where the activation and hydrogenation of CO_2 generate C_1 surface or gas-phase intermediates, including CO, CO_3, COOH, HCOH, and CH_x (ZENG *et al.*, 2021).

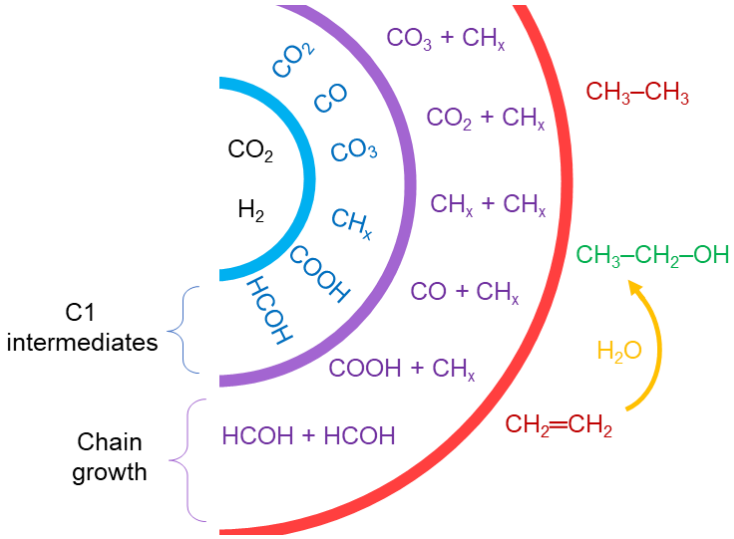

Figure 2.9 - *Schematic representation of the several possible pathways in higher alcohol synthesis by CO_2 hydrogenation.* (Adapted from ZENG *et al.*, 2021)

Subsequently, C_2 species can be formed through the coupling of C_1 species, such as $CO/CO_2/CO_3-CH_x$ coupling, $COOH-CH_x$ coupling, $HCOH-HCOH$ coupling, and CH_x-CH_x coupling, all illustrated in **Figure 2.10**. These C_2 species are further hydrogenated to C_2 hydrocarbons or oxygenates. The C_{3+} species are formed via propagation of the coupling stage (ZENG *et al.*, 2021).

i) $\mathbf{CO/CO_n^* + CH_x^* \longrightarrow CO_nCH_x^* \xrightarrow{H_2} CH_3CH_2OH}$ (n = 1, 2, or 3)

ii) $\mathbf{CH_x^* + CH_x^* \longrightarrow CH_xCH_x^* \longrightarrow CO_nCH_xCH_x^* \xrightarrow{H_2} CH_3CH_2CH_2OH}$

$\mathbf{CH_2CH_2 \xrightarrow{H_2O} CH_3CH_2OH}$

iii) $\mathbf{HCOH^* + HCOH^* \xrightarrow{-H_2O} CHCOH^* \xrightarrow{H_2} CH_3CH_2OH}$

iv) $\mathbf{HCOO^* + CH_x^* \longrightarrow CH_3COO^* \xrightarrow{H_2} CH_3CH_2OH}$

Figure 2.10 - *Schematic representation of the several possible pathways for chain growth and alcohol formation.* (Adapted from (ZENG *et al.*, 2021))

Understanding the reaction mechanism of ethanol synthesis is crucial for guiding the design and preparation of catalysts (LI, X. *et al.*, 2023). In that sense, this literature review provides an overview of the proposed reaction mechanisms and explores the role of key factors in the conversion of CO_2 into higher alcohols. The proposed reaction mechanisms can be simply divided into two groups, CO-mediated and direct CO_2 activation.

Also referred to as CO_2-FTS (Fischer-Tropsch Synthesis), the CO-mediated pathway was proposed by Kusama (Kusama et al., 1996) and it is still the most widely accepted for the hydrogenation of CO_2. They argued CO species can be found in FTIR analysis and that usually CO is detected as effluent in the CO_2 hydrogenation reaction to ethanol over Rh-based catalysts.

This mechanism involves first the CO_2 to CO conversion via the rWGS reaction. Then, CO can be stabilized by the catalyst. Conversely, it can also be hydrogenated to stable CH_x* (LI, X. *et al.*, 2023; XU *et al.*, 2021a). DRIFTS data strongly supports the existence of CO dissociative activation and non-dissociative activation. According to authors, the catalyst's ability to promote both CO* activation (dissociative and non-dissociative) is detrimental to the final HAs yield (WANG, G. *et al.*, 2019). The pathway is followed by C-C coupling to form C_xH_y, non-dissociated CO insertion reactions, and subsequent hydrogenation to higher alcohols (LI, X. *et al.*, 2023; XU *et al.*, 2021a).

Furthermore, CO–insertion plays a crucial role in this mechanism and its effectiveness depends on the electron density of the transition metals involved (AO *et al.*, 2018; WANG, G. *et al.*, 2019; XU *et al.*, 2021a). Electron-donating metals, such as alkali or early *3d* transition metals like V and Fe, enhance CO–insertion reactions. However, excessive electron density can reduce the favorability of CO-alkyl migratory insertions and encourage direct CO dissociation. The optimal pathway varies depending on the specific metals, surface type, and the presence of promoters (KUSAMA *et al.*, 1996; WANG, G. *et al.*, 2019; XU *et al.*, 2021a; YANG *et al.*, 2019).

Some Co-based catalysts are reported to follow this mechanism. Liu et al. (2018) found that small amounts of CO formed were gradually consumed and eventually depleted among the products. Zhang et al. (2020) detected CO* and CHx* via *in situ* DRIFTS experiments on CO_2 hydrogenation to ethanol over Co_2C. Meanwhile, An et al. (1996) investigated $CoGaAl/SiO_2$ catalyst and concluded that the CoGaAl spinel structure is responsible for the adsorption of CO_2 and rWGS reaction, Co^0-$Co^{\delta+}$, for the

molecular activation of CO and H_2, and Co^0 for CH_x*. In short, they observed that $Co^{\delta+}$ tends to retain C-O bonds, leading to *CO and CH_xO* intermediates. Efficient ethanol synthesis results from the coupling of CHx* on Co^0 and CO*/HCO* on $Co^{\delta+}$, following a tandem reaction mechanism.

More recently, Liu et al. (2022) researched CoCu alloy catalysts for their potential to produce ethanol via CO_2 hydrogenation. They combined computational and experimental data to study the effects of Co surface segregation and CO surface coverage, demonstrating that moderate surface segregation, accompanies an increased CO coverage, and promotes CO_2 hydrogenation to ethanol. Deep insights were gained from density functional theory (DFT) analyses, revealing that this moderate surface segregation promoted C–O scission of CH_2O*, pivotal step, and C–C coupling of formed CO* and CH_x*.as demonstrated by **Figure 2.11**.

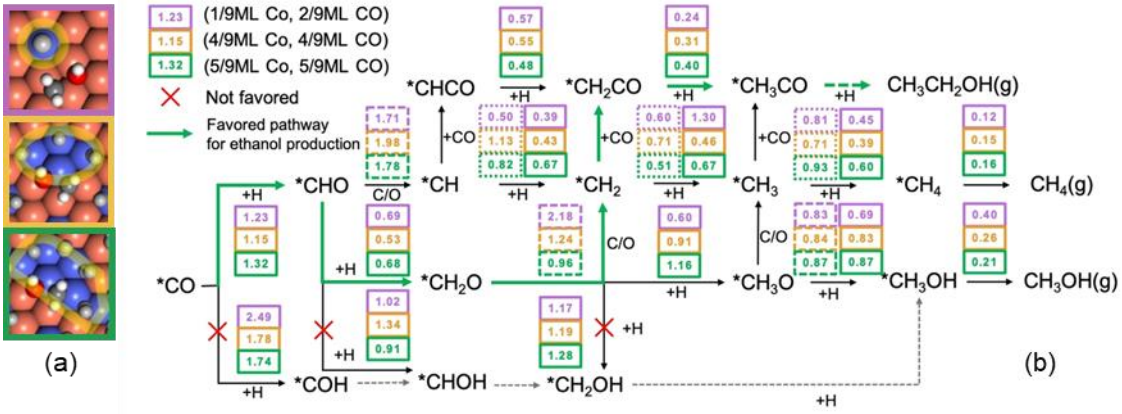

Figure 2.11 - *The transition states of C–O bond scission of CH_2O* on three surfaces (a). DFT-calculated reaction networks of *CO hydrogenation towards methanol, methane, and ethanol (b). Barriers of hydrogenation are in boxes with a solid line, barriers of C–O scission are in boxes with a long-dashed line, and barriers of CO insertion are in boxes with a short-dashed line. All values are in eV.* (LIU *et al.*, 2022)

Other theoretical studies with Co or Cu-based catalysts suggest that at the metal/oxide interface, CH_xO* hydrogenation accelerates the dissociation of C-O bonds, leading to the principal formation of CH_x, rather than CO (FAN *et al.*, 2021; KATTEL; LIU; CHEN, 2017; LI, K. *et al.*, 2023). Some authors dubbed this pathway as a methoxy/methanol-mediated mechanism. It involves the formation of CO* and its hydrogenation to a methoxy/methanol intermediate, which later suffers C–O scission generating CH_x*. Upon the formation of methyl intermediate, it undergoes chain growth and CO–insertion (LI, X. *et al.*, 2023; XU *et al.*, 2021a). This mechanism was first proposed in studies involving Pt/Co_3O_4 catalysts in batch reactors using water as solvent.

The author speculated that water could protonate methanol leading to its dissociation into CH_3* species (HE *et al.*, 2016).

In contrast to the CO-mediated pathway, the formate-mediated mechanism proposes that CO_2 directly hydrogenates to form formate (HCOO*) intermediates (LI, X. *et al.*, 2023; XU *et al.*, 2021a). A few studies have explored this mechanism, for example, Wang et al. characterized CoAlOx and CoNiAlOx catalysts, detecting the formation of HCOO* intermediates during CO_2 hydrogenation. These catalysts were able to both stabilize HCOO* and perform dissociation-hydrogenation to form CH_x. This mechanism involves the coupling of HCOO* and CH_x*, ultimately leading to the formation of ethanol as a precursor of C_2 intermediates (WANG *et al.*, 2018; WANG, L. *et al.*, 2019). Formate is also detected as key intermediate in some methanol synthesis pathways (KATTEL *et al.*, 2017).

Zheng and coworkers also found that CO_2 follows the formate-mediated mechanism on a Co/La_2O_3-$La_4Ga_2O_9$ catalyst, and implied that the coupling of *HCOO and *CH_3 represents a critical step in ethanol synthesis in this context (ZHENG *et al.*, 2019). Yang and coworkers also detected the formation of formate over RhFeLi/TiO_2-NR, attributing both the stabilization and the C–O scission to the hydroxyl-rich surface of this catalyst (YANG *et al.*, 2019).

In summary, the hydrogenation of CO_2 to higher alcohols involves various mechanisms, with CO-mediated, methanol-mediated, and formate-mediated pathways, as illustrated by **Figure 2.12,** playing distinct roles in the formation of ethanol. These mechanisms depend on the nature of the catalyst and reaction conditions, highlighting the complexity of this conversion process (LI, X. *et al.*, 2023; XU *et al.*, 2021a).

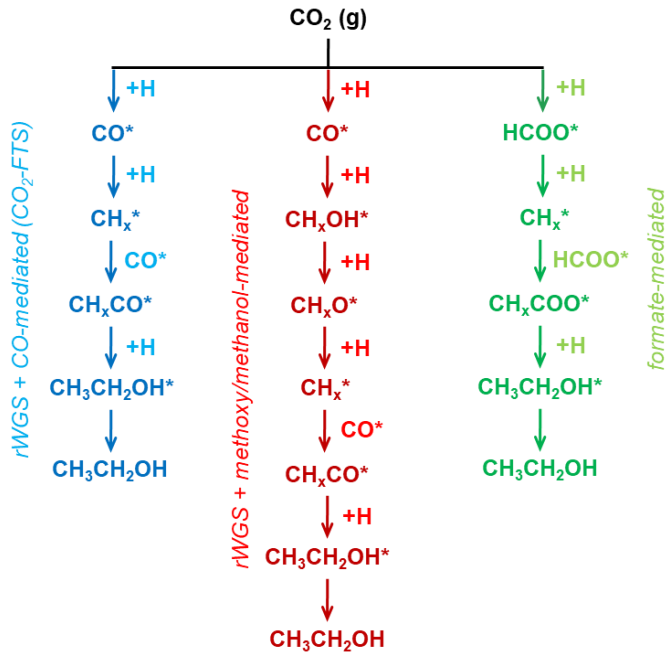

Figure 2.12 - *Reaction pathways of catalytic hydrogenation of CO_2 to ethanol.* (Adapted from LI, X. *et al.*, 2023)

In conclusion, based on critical analyses of work such Xu et al. (2021a), Zeng et al. (2021), Zhao et al. (2021), Ali et al. (2022), Wang et al. (2022), Li et al. (2023), and other researchers, several key conclusions regarding the mechanisms governing CO_2 hydrogenation to higher alcohols can be drawn.

Firstly, it has been identified that certain steps, such as C–C coupling, C–O scission, CO-insertion, and hydrogenation are detrimental steps for this reaction. Evidence suggests that HAs synthesis happens at the interface of two active metal centers, such as Co–CoO or Co–Co_2C interfaces in the case of Co-based catalysts, and Cu-Fe_xC interfaces for Fe-modified Cu-based catalysts.

Furthermore, to enhance HAs synthesis, it is imperative to maintain a balance between non-dissociative and dissociative activations of CO*/CO_2. Maintaining the surface coverage of key species, including CO*, H*, and CH_3*, in equilibrium is vital. The introduction of promoters, such as alkali metals and select transition metals, offers a common approach to modulating the adsorption of these key species and fine-tuning catalytic centers.

In addition, it is essential to kinetically inhibit undesirable product formation like hydrocarbons and methanol. Strong H* activators, exemplified by Ni and Ru, can facilitate the termination of CH_3*, favoring the production of methane. Hydrogenation of CH_3* to CH_4 competes with CO-insertion, key to the formation of higher alcohols.

Consequently, it is crucial to raise the energy barrier for CH_3* hydrogenation and/or lower it for CO-insertion to promote the formation of ethanol and C_2 intermediates.

Moreover, the choice of catalyst supports can significantly influence the catalytic performance in the CO_2 hydrogenation reaction to HAs. Supports can stabilize and/or create new active sites through mechanisms such as the strong-metal-support interaction (SMSI) effect, confinement effect, or by providing a unique coordination environment.

2.3.3 Catalysts

As aforementioned, CO_2 hydrogenation leads to a wide range of products, thus it is necessary to adjust the catalyst properties to favor the yield of one product over another. Therefore, the first step in determining a suitable catalyst design for the CO_2 hydrogenation to higher alcohols (HAs) is to thoroughly examine the literature for relevant catalyst properties for this reaction. In this regard, four main groups of CO_2-to-HAs catalysts have been reported, namely noble metal-based, Cu-based, Mo-based, and Co-based materials (ALI *et al.*, 2022; LATSIOU *et al.*, 2023; LI, X. *et al.*, 2023; XU *et al.*, 2021a; ZENG *et al.*, 2021). The key examples of these catalysts are summarized below in **Table 2.6**.

Table 2.6 *- Summary of some catalysts for CO_2 hydrogenation to higher alcohols (HAs).*

Catalyst	**T** (°C)	**P** (bar)	**GHSV** ($mL \cdot g_{cat}^{-1} \cdot h^{-1}$)	**H_2/CO_2 Ratio**	**XCO_2** (%)	**Selectivity** (%)				**Y_{HAs}** [b] (%)	**Ref.**
						CO	CH_4	HAs			
								C_2	C_{3+}		
KFeRh-SiO_2	250	75	7000	3	18.4	--	46	15.9	--	2.92	(GORYACHEV *et al.*, 2021)
RhFeLi/TiO_2-NRs	250	30	6000	3	21.4	5.1	53.9	31.3	0.1	6.70	(YANG *et al.*, 2019)
Pd/Fe_2O_3	300	1	60000	4	0.3	--	--	97.5	--	0.29	(CAPARRÓS *et al.*, 2018)
Pd_2/CeO_2	240	30	3000	3	15.1	--	0.8	99.2	--	15.0	(LOU *et al.*, 2021)
KMoCoS/AC	320	50	3000	3	8.1	69.8	12.2	4.8 [a]		0.39	(LIU, M. *et al.*, 2019)
sp-CuNaFe	310	30	28800	3	32.3	16.0*	10.0*	9.0*	--	2.91	(SI *et al.*, 2022)
K-CuMgZnFe	320	50	6000	3	30.4	30.6	--	15.9 [a]		4.83	(XU *et al.*, 2020a)
CuZnAl / K-CMZF	320	50	6000	3	42.3	13.8	11.5*	17.4 [a]		7.36	(XU *et al.*, 2021b)
Cu-CoGa	220	30	6000	3	17.8	2.3	33.4*	23.8	--	4.24	(ZHANG *et al.*, 2022)
Na-CuCo	330	10	2000	1	21.7	22.3	20.0*	8.0	19.2	5.90	(IRSHAD *et al.*, 2024)
$CoGaAlO_4$/SiO_2	270	30	3000	3	4.4	27.3	--	20.1	--	0.88	(AN *et al.*, 2022)
Na-Co/SiO_2	310	50	6000	3	53.2	3	61.8	6.8*	5.1*	6.33	(ZHANG *et al.*, 2021)
K-Co-In_2O_3	380	40	2250*	3	36.6	80.8	--	11.1* [a]		4.06	(WITOON *et al.*, 2022)

* Value calculated based on the data provided by the authors.
[a] HAs ($C_{2+}OH$) selectivity or STY.
[b] Yield of higher alcohols.

2.3.3.1 Noble Metal-based Catalysts

Among noble metal-based materials, rhodium (Rh) and palladium (Pd) based catalysts stand out in performance. Nonetheless, platinum (Pt), ruthenium (Ru), Iridium (Ir), and gold (Au) based catalysts are also reported (ALI *et al.*, 2022; LATSIOU *et al.*, 2023; LI, X. *et al.*, 2023; ZENG *et al.*, 2021).

One of the earliest works on HAs synthesis through CO_2 hydrogenation was published in 1996 by Kusama and coworkers (LATSIOU *et al.*, 2023). They experimented with Rh-based catalysts associated with 28 additives (Li, Na, K, Mg, Ca, Sr, Ba, Fe, Co, Ni, Ru, Pd, Ir, Pt, Cu, Ag, Ti, V, Mn, Zr, Nb, Mo, Re, Zn, Sn, La, Ce, and Sm) with Rh:M molar ratios of one, supported over SiO_2. In general, the addition of promoters led to increased CO_2 conversion, yet only Li, Fe, Sr, and Ag promoter HAs formation, leading to ethanol selectivities of 15.5%, 3.2%, 2.5%, and 1.8%, respectively. As for CO_2 conversion, Li and Fe also had the best results, namely 7% and 10.4%, in that order (KUSAMA *et al.*, 1996). Kusama's work also helped the understanding of reaction mechanisms, as depicted in **section 2.3.2.**

Later works of the same group, associated both Fe and Li on Rh-based catalysts. Rh-Fe-Li supported on titania nanorods (TiO_2-r). They inferred that the addition of Fe had the role of increasing the selectivity toward ethanol. Meanwhile, Li-doping was necessary to countereffect losses in CO_2 conversion due to Fe-doping. They also proved that hydroxyl groups played a role in the CO_2 hydrogenation to ethanol, favoring CO-insertion (YANG *et al.*, 2019).

In short, recent literature shows Rh as a popular noble metal for higher alcohol synthesis due to its C-C coupling. Nonetheless, the addition of alkali promoters and/or transition metals is required to make viable such catalysts. These catalysts are usually prepared by supporting Rh on metal oxides such as TiO_2, SiO_2, CeO_2, and zeolites, and adding promoters like Li, Mn, Fe, and Ce. Typical reaction conditions include temperatures of 240-270 °C, pressures of 20-50 bar, and a GHSV of approximately 7000 $mL \cdot g_{cat}^{-1} \cdot h^{-1}$, with H_2/CO_2 ratios of 1-3. Optimized catalysts show CO_2 conversions of 7-27% and ethanol selectivity of 1-83%. Most Rh-based materials exhibit low selectivity for methanol (<10%), with CO and hydrocarbons being the primary products, achieving selectivity of up to 80% (ALI *et al.*, 2022; ZENG *et al.*, 2021). Despite optimization efforts, the maximum yield of higher alcohols remains low, with the highest yield of 4.9% achieved using a Rh/TiO_2-r catalyst promoted with Fe and Li (YANG *et al.*, 2019).

Pd-based catalysts became an objective of attention due to their high ethanol selectivity, reaching approximately 99% (ALI *et al.*, 2022). Studies indicate that low Pd contents (≤ 0.2% w/w) promote selectivity to ethanol, as seen in Pd/Fe_3O_5 (CAPARRÓS *et al.*, 2018) and Pd_2/CeO_2 (LOU *et al.*, 2021), two of the most relevant studies on Pd-based CO_2-to-HAs catalysts. However, in excess, this metal promotes CO formation at the expense of ethanol (ALI *et al.*, 2022).

The work of Caparrós and coworkers reported on Pd single atoms (0.1 wt.%) over Fe_3O_4 reaching 97.5% selectivity for ethanol at ambient pressure and high GHSV (60000 $mL \cdot g_{cat}^{-1} \cdot h^{-1}$), yielding 413 $mmol \cdot g_{Pd}^{-1} \cdot h^{-1}$ (or 4.13 $mmol \cdot g_{cat}^{-1} \cdot h^{-1}$), one the highest yet reported. They also observed that increasing the temperature could favor propanol formation at the cost of decreasing ethanol selectivity and increasing CO selectivity. No methane was observed, even at higher temperatures. According to them, the support promotes rWGS reaction, helping activate CO_2 to CO*, while Pd promotes C-C coupling (CAPARRÓS *et al.*, 2018).

Lou and coworkers displayed even higher ethanol selectivity (99.2%) using Pd dimers supported over CeO_2. They also performed DFT calculations to propose a reaction mechanism, centered around the formation of CHO* intermediate (LOU *et al.*, 2021), in agreement with the methanol-mediated pathway explored in **section 2.3.2**. On the other hand, both these highly selective catalysts deactivate after a few hours of reaction due to Pd single-atoms (Pd/Fe_3O_4) or dimers (Pd_2/CeO_2) sintering to nanoparticles, drastically reducing their ethanol yield (CAPARRÓS *et al.*, 2018; LOU *et al.*, 2021).

For Pd-based catalysts, reactions are typically carried out at temperatures between 240-300 °C, pressures of 1-30 bar, and gas hourly space velocity (GHSV) ranging from 3000-6000 $mL \cdot g_{cat}^{-1} \cdot h^{-1}$, with CO_2 conversions ranging from 1-9% and C_2H_5OH selectivity of 80-99% (ALI *et al.*, 2022). Pd can often be used as a promoter in Cu and CO-based catalysts (ALI *et al.*, 2022; LATSIOU *et al.*, 2023; LI, X. *et al.*, 2023; ZENG *et al.*, 2021).

2.3.3.2 Molybdenum-based Catalysts

Mo-based catalysts find applications in both the rWGS and FTS. Over the past four decades, various Mo-based materials, such as MoS_2, Mo_2C, MoO_x, and MoP, have been extensively investigated as catalysts for converting syngas into alcohols. More recently, these materials have gained recognition for their potential in CO_2 hydrogenation. However, the activity of monometallic Mo-based catalysts in CO_2-to-HAs reaction is very low, predominantly yielding methane. To overcome this limitation, it has

become imperative to introduce alkali promoters, along with transition metals (Fe, Co, and Ni), as well as explore different supporting methods (LATSIOU *et al.*, 2023; LI, X. *et al.*, 2023).

One of the earliest reports on modified Mo-based catalysts for CO_2 hydrogenation to HAs belongs to Nieskens and coworkers, reporting on CoMoS catalyst prepared by precipitation method, displaying CO_2 conversion of 32% at 340 ºC. However, it yielded mainly methanol and CO, with minor presence of ethanol (NIESKENS *et al.*, 2011). Similarly, Liu and coworkers investigated the influence of K/Mo and Co/Mo ratios and the support on a series of Mo-Co-K sulfide-based catalysts. First, regarding K/Mo and Co/Mo ratios, by increasing the K/Mo ratio up to 0.6 and the Co/Mo ratio up to 1.0, alcohol production was favored over hydrocarbons, increasing HAs selectivity. Second, changing the support helped to tune the selectivity. Activated carbon (AC) was the only capable of reducing the selectivity towards CO and promoting the selectivity towards ethanol and propanol, at the cost of decreasing CO_2 conversion. Al_2O_3, SiO_2, and TiO_2 suppressed the formation of HCs, but favored methanol formation (LIU, S. *et al.*, 2017). Another work from the same group explored the $Mo_1Co_1K_{0.6}$/AC catalyst under wider reaction conditions (LIU *et al.*, 2019).

Mo-based catalysts for HAs synthesis are reported in the form of sulfides, oxides, and carbides, with the addition of promoters such as K, Na, Co, Fe, and Ir. The CO_2 hydrogenation reaction is typically carried out at temperatures between 200-340 °C, pressures between 20-100 bar, H_2/CO_2 ratios of 1-5, and GHSV between 1200-9000 $mL \cdot g_{cat}^{-1} \cdot h^{-1}$. CO_2 conversions were found in the range of 3-32%, with CO and hydrocarbons typically being the major products. The reported selectivity to higher alcohols is relatively low, for instance, generally below 15% (ALI *et al.*, 2022; ZENG *et al.*, 2021) The highest reported yield of higher alcohols to date is only 3.6% using K-Co-MoS_2 (LIU, S. *et al.*, 2017).

2.3.3.3 Copper-based Catalysts

Cu/ZnO-based catalysts exhibit exceptional activity in a range of reactions, including methanol-reforming, methanol synthesis, and the rWGS reaction. The key to their effectiveness lies in zinc's role as a reservoir for hydrogen atoms, facilitating the reduction of copper. This enables the conversion of inert CuO species into active metallic Cu, Cu_2O, and other low oxidation state Cu species, thus activating CO_2 to form other carbon products (LATSIOU *et al.*, 2023; LI, X. *et al.*, 2023).

It is widely accepted that Cu favors the non-dissociative type of hydrogenation of CO* to CH_xO*, thus facilitating alcohol production. However, to enable the synthesis of

C2+OH compounds, additional sites or promoters are often incorporated to facilitate the formation of CHx* species (XU *et al.*, 2021a). For example, researchers have utilized compounds like ethylenediamine tetra-acetic acid (EDTA) and triethanolamine (TEA) to modify the CuZnAl structure, leading to enhanced ethanol selectivity in CO_2 hydrogenation. These additives promoted Cu^{2+} reduction, induced morphological changes, and increased the number of basic sites, ultimately favoring ethanol production (CHENG *et al.*, 2018). Other structurally complex Cu-based materials, including metal-organic frameworks (MOFs) and core-shell like Cu@Zeolite catalysts, have also shown potential for HAs synthesis (LI, X. *et al.*, 2023)

Nonetheless, Single Cu-based catalysts face limitations in the synthesis of C2+OH compounds, particularly in terms of hydrogenation ability and carbon chain growth. To promote the shift from C_1OH production to $C_{2+}OH$, Cu-based catalysts have been combined with transition metals (Co and Fe) and alkali promoters (K or Na) to regulate the amount of CO and alkyl species produced (LATSIOU *et al.*, 2023; LI, X. *et al.*, 2023).

Takagawa and coworkers are regarded as the pioneers in publishing works on K/Cu-Zn-Fe (0.08:1:1:3) catalysts for HAs synthesis via CO_2 hydrogenation. Their catalyst achieved ethanol selectivity of 19.5% at 300 °C (70 bar, $H_2/CO_2 = 3$), with CO_2 conversion of 44.2%. Moreover, the product followed the ASF distribution, suggesting it follows a mechanism like FTS. The major drawback of this catalyst was deactivation, primarily caused by the segregation of elements (TAKAGAWA *et al.*, 1998), later overcome by the addition of a fifth element to the structure, Cr, into the catalyst structure (HIGUCHI *et al.*, 1998).

Another research group delved into this catalyst formulation years later and specifically explored the role of Fe by varying its content. They identified the optimal molar ratio as $Cu_1Zn_1Fe_{0.5}K_{0.15}$, resulting in a remarkable CO_2 conversion of 42.3% and HAs selectivity of 31.9%, ultimately achieving a significant HAs yield of 13.5% (300 °C, 60 bar, $H_2/CO_2 = 3$). The study revealed a distinctive relationship between HAs selectivity and the Cu/Fe ratio, resembling a volcano-shaped curve (LI *et al.*, 2013).

Furthermore, the addition of a moderate amount of Fe was found to enhance the interaction between Cu-Fe and Zn-Fe, resulting in the formation of dispersed CuO, $CuFe_2O_4$, and $ZnFe_2O_4$ spinel phases. During the CO_2 hydrogenation reaction, CuO and $CuFe_2O_4$ were reduced to Cu species, while $ZnFe_2O_4$ was reduced to FeC_x, with the extent of reduction dependent on the Fe (low or high Fe concentrations resulting in incomplete reduction) (LI *et al.*, 2013). As it is well-established, FeC_x promotes CO

dissociation, C-C coupling, and the hydrogenation reaction, while Cu promotes the non-dissociation of CO (LATSIOU *et al.*, 2023).

Recent studies have explored CuZnFe-based catalysts with various approaches, including altering the weight contents of potassium, introducing promoters such as Zr (GUO *et al.*, 2013) and Mg (XU *et al.*, 2020a), and changing the alkali promoter (XU *et al.*, 2020b). Xu and coworkers found that the relationship between the weight content of K and HAs selectivity also follows a volcano-shaped curve. HAs selectivity increased in K content up to a maximum of 4.6 wt.%, at the cost of CO_2 conversion (XU *et al.*, 2020a).

In another investigation, Xu explored substituting K with Cs in CuZnFe-based catalysts and optimizing the Cu/Fe ratio. Cs demonstrated a similar effect to K in influencing the catalyst's performance. As for the Cu/Fe ratio, they proposed that as it increased, the production of non-dissociative CO increased, and CH_4 (dissociative CO) declined, up to an optimal ratio. In essence, peak performance (apex of the volcano) is achieved when there is a balance between the active sites responsible for the dissociation (FeC_x) and non-dissociation (Cu) of CO, allowing the desired coverage of CO and alkyl species to (LATSIOU *et al.*, 2023; XU *et al.*, 2020b).

In summary, Cu-based materials are widely investigated as promising catalysts to produce HAs via CO_2 hydrogenation and are associated with promoters such as Zn, Fe, K, Cs, Zr, Pa, Ga, and Co. Typical reaction conditions for CO_2 hydrogenation to HAs include temperatures of 300-350 °C, pressures of 30-80 bar, GHSV of 3600-20000 $mL \cdot g_{cat}^{-1} \cdot h^{-1}$, and H_2/CO_2 ratio of 3. These materials often exhibit high selectivity for CO or hydrocarbons ($\%S_{CO + hydrocarbons}$ = 52-94%), with low selectivity for methanol (<18%) and HAs ranging from 1-32%. The yield of HAs varies between 1-13.5% (ALI *et al.*, 2022; ZENG *et al.*, 2021), with CuZnFeK bulk-catalyst showing the most promising results (LI *et al.*, 2013).

2.3.3.4 Cobalt-based Catalysts

Cobalt (Co) is a well-known element in Fischer-Tropsch synthesis (FTS), widely employed to produce heavy hydrocarbons and higher alcohols. However, substituting CO_2 for CO reorients its function to, primarily, a methanation catalyst (LATSIOU *et al.*, 2023; XU *et al.*, 2021a). Both experimental observations and theoretical calculations have substantiated the fact that Co readily breaks C-O bonds and subsequently hydrogenates them to produce hydrocarbons (LI, X. *et al.*, 2023). However, it has been discovered that the ability of Co to break the C-O bond can be tuned to fit the intended product (LIU *et al.*, 2023). For instance, Co in different oxidation states exhibits distinct properties and capabilities (LI, X. *et al.*, 2023).

It is postulated that each Co species plays a distinct role in the CO_2 hydrogenation reaction. Metallic Co (Co^0), for instance, is more active in dissociating H_2 providing active H* species (LIU *et al.*, 2023). Nonetheless, experimental evidence suggests that Co^0 also generates CO* species (HAVE *et al.*, 2022) and promotes chain growth (ZHAO *et al.*, 2021). In contrast, the presence of CoO is often associated with a decrease in the availability of active H*, thereby facilitating C-C coupling. Notably, carbonates (CO_x*), formate (HCOO*), and formyl (CHO*) species have been detected over CoO, supporting formate-mediated pathways (WANG *et al.*, 2022). Some researchers have also observed the formation of carboxylate (COOH*) intermediates on the oxygen vacancies on CoO, suggesting a carboxylate-intermediated route (LIU *et al.*, 2023; WANG *et al.*, 2022).

Partially oxidized Co sites ($Co^{\delta+}$) are acknowledged for their activity in CO_2 hydrogenation, with these sites being conducive to the formation of stable yet active oxygenate intermediates (AN *et al.*, 2022; ZHENG *et al.*, 2019). Notably, the Co-CoOx (Co-$Co^{\delta+}$) phase has been recognized as an excellent active site for CO_2-to-HAs catalysts (LI, X. *et al.*, 2023; LIU *et al.*, 2023). Additionally, Co_2C, previously considered a methanation director, has been shown to, under specific conditions, such as stabilized by an alkali promoter or metal-support interaction, inhibit methanation and promote CO_2 conversion (GNANAMANI *et al.*, 2016; LATSIOU *et al.*, 2023; ZHANG *et al.*, 2021).

In that sense, there are several potential approaches to fine-tune the activity of Co-based catalysts, including tailoring the reduction process, incorporating alkali promoters, or leveraging Co-support-promoter interactions by forming metal alloys or interacting with oxide supports (LIU *et al.*, 2023).

For instance, Wang and coworkers synthesized Co-Al from layered double hydroxides (LDH), leading to the formation of $CoAlO_x$ upon calcination. The samples were then reduced with H_2 at various temperatures to create Co^0-CoO hetero sites, adjusting their structure. At a reduction temperature of 300 °C, only Co_3O_4 was obtained. At 400 °C, Co_3O_4 was reduced to CoO, and at 600 °C, both Co^0 and CoO coexisted. Further increasing the reduction temperature reduced CoO content, while Co0 content increased. Catalytic tests were conducted in a batch reactor (T = 140-200 ºC, P = 40 bar, H_2:CO_2 = 3) using H_2O as a solvent. The optimal calcination temperature was observed at 600 ºC, where a balanced content between Co^0 and CoO was achieved. At this reduction temperature, $CoAlO_x$ exhibited ethanol selectivity of 92.1% and an STY of 0.44 $mmol \cdot g_{cat}^{-1} \cdot h^{-1}$ at 140 ºC. The catalyst's performance was also influenced by the Co/Al ratio, with the catalyst at a ratio of 2.72 being the most active. FTIR evidence

suggested a formate-mediated pathway, where CH_x* and HCOO* coupled to form CH_3COO*, which is further hydrogenated to ethanol (WANG *et al.*, 2018).

In a subsequent study, the same research group explored the formation of alloys with other metals ($CoMAlO_x$), namely Ni, Pd, and Pt, to modulate the production of CH_x* and HCOO* intermediates. The catalysts were evaluated under the same conditions as in the previous research. All alloys resulted in increased ethanol STY in the following order: Ni (1.32 $mmol \cdot g_{cat}^{-1} \cdot h^{-1}$) > Pt (0.93 $mmol \cdot g_{cat}^{-1} \cdot h^{-1}$) > Pd (0.87 $mmol \cdot g_{cat}^{-1} \cdot h^{-1}$), albeit at the expense of ethanol selectivity. The enhanced ethanol yield with Ni was attributed to its acceleration of CH_x* formation, regarded as a rate-determining reaction step (WANG, L. *et al.*, 2019).

In a study by Zheng and coworkers Co-support-promoter interactions and reductive treatments were explored to create hetero sites. They synthesized $LaCo_{1-x}Ga_xO_3$ perovskite and later reduced to form, at optimum Co/Ga ratio, to Co/La_2O_3-$La_4Ga_2O_9$. Such catalysts exhibited a CO_2 conversion of 8.1% and ethanol selectivity of 62.1% (240 °C, 30 bar, H_2/CO_2 = 3, 3000 $mL \cdot g_{cat}^{-1} \cdot h^{-1}$). The addition of Ga to the structure increased the content of $Co^{\delta+}$ in the catalyst, inhibited methanation, and facilitated ethanol formation (ZHENG *et al.*, 2019).

Building on this, An and coworkers also prepared $Co/La_4Ga_2O_9$ catalyst by reducing LaCoGa perovskite. The interaction of Co nanoparticles with $La_4Ga_2O_9$ resulted in the formation of a Co^0-$Co^{\delta+}$ active phase at their interface. The author proposed that $La_4Ga_2O_9$ catalyzed rWGS conversion of CO_2 to CO, with CO* stabilized on the Co^0-$Co^{\delta+}$ interface. Subsequently, CO* is hydrogenated to CH_x* over Co^0, and both intermediates are coupled to form ethanol, as illustrated by **Figure 2.13**. Nevertheless, as reaction time was prolonged, ethanol selectivity decreased significantly, which was caused by the increase of Co^0 and the decrease of $Co^{\delta+}$ (AN *et al.*, 2021).

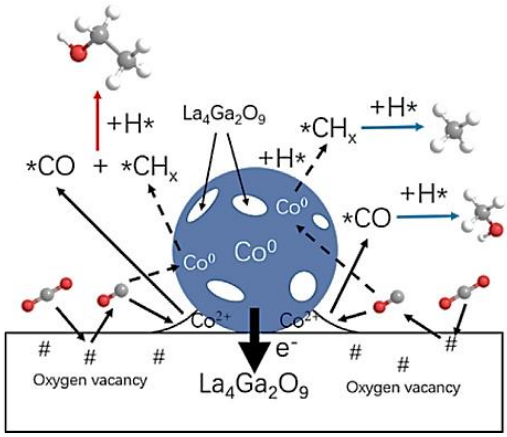

Figure 2.13 - *Proposed reaction mechanism* (Adapted from AN *et al.*, 2021).

To address the deactivation observed in the previous study, An and coworkers investigated the formation of a Co-Al spinel to stabilize $Co^{\delta+}$ species. In that sense, they prepared SiO_2-supported CoGaAl, and $CoGa_1Al_1O_4/SiO_2$ catalyst achieved an ethanol selectivity of 20.1%. The study suggests that Ga inhibits the excessive reduction of Co, and the electron donation from Co^0 to Ga^{3+} results in the formation of Co^0-$Co^{\delta+}$ active pairs. Moreover, CO_2 is converted to CO over the reduced CoGaAl spinel, followed by CO hydrogenation to HAs. Associative CO adsorption (CO*) occurs on $Co^{\delta+}$, and dissociative CO adsorption, forming CH_x*, over Co^0 sites. The optimized $Co^0/Co^{\delta+}$ ratio enhances the CH_x*-CO* coupling for ethanol synthesis (AN *et al.*, 2022).

Zhang and coworkers delved into the influence of different alkali promoters (Li, Na, K), and various supports (Al_2O_3, ZnO, AC, TiO_2, SiO_2, and Si_3N_4) on Co_2C catalyst for the CO_2 hydrogenation to ethanol. Among the alkali promoters, only Na and K yielded alcohols, with Na exhibiting higher selectivity. Optimized Na-Co/SiO_2 catalyst demonstrated an ethanol selectivity of 62.8% (250 ºC, 50 bar, 6000 $mL \cdot g_{cat}^{-1} \cdot h^{-1}$) displaying high catalytic stability over 300 h. Through characterization, the team proposed a stability mechanism: during reduction with CO flow and reaction, the CoO transforms into Co_2C phase, stabilizing only over SiO_2 and Si_3N_4. Electron charge transfer to the support from Co^{2+} forms stabilized Co−O−Si bonds, enhancing Co−C bond strength and stabilizing Co_2C. During the reaction, the Co-support interface provides active sites for rWGS and hydrogenation of CO* to CH_xO*, a key intermediate for ethanol synthesis. Ethanol is then produced through the coupling of CH_3O* and CO. CO generated during the reaction helps regenerate decomposed Co species back into Co_2C, ensuring prolonged catalyst stability (ZHANG *et al.*, 2021).

Witoon and coworkers studied K-Co/In_2O_3 CO_2-to-HAs catalysts, which upon reduction in H_2, Co/In_2O_3 forms a mixture of Co^0 and CoO. The author concluded that the oxygen vacancies on the surface of In_2O_3 facilitate CO_2 to CO conversion. Co^0 participates in the dissociative adsorption of C-O, C-C bond formation, and hydrogenation of adsorbed carbon intermediates to form C_xH_y*. CoO stabilizes CO*, which migrates and inserts into the adjacent C_xH_y* species at Co^0 sites, forming $C_{2+}OH$. However, hydrocarbons exhibited higher selectivity than oxygenated products over Co/In_2O_3 due to the rapid hydrogenation of C_xH_y* species compared to CO* insertion, attributed to weakly adsorbed H*. Upon adding K as an alkali promoter, K-O-Co species are generated, reducing weakly adsorbed H* and enhancing H* adsorption. This suppresses alkyl intermediate hydrogenation, favoring CO* insertion and C-C bond formation, ultimately boosting higher alcohol formation (WITOON *et al.*, 2022).

To sum it up, Co-based and Co-promoted catalysts have shown remarkable activity in CO_2 hydrogenation to higher alcohols often in collaboration with elements like K, Ga, Pt, Pd, Ni, and Fe. Operational conditions typically involve temperatures of 200-250 °C, pressures of 12-50 bar, GHSV of 3000-6000 $mL \cdot g_{cat}^{-1} \cdot h^{-1}$, and H_2/CO_2 ratio of 3. CO_2 conversions range from 7-29%, with significant alcohol formation. Selectivity to methanol varies from 0.7-29%, while selectivity to higher alcohols ranges from 4-63%. CO selectivity ranges from negligible to 46%, while hydrocarbon selectivity varies from 24-81% (ALI *et al.*, 2022; LIU *et al.*, 2023; ZENG *et al.*, 2021). The highest reported ethanol yields are 6.5% for LaGaCo perovskite-type catalysts (ZHENG *et al.*, 2019) and 6.9% for Na-Co catalysts supported on SiO_2 (ZHANG *et al.*, 2021).

2.3.4 Effect of the Addition of Promoters

Promoters play a pivotal role in CO_2 hydrogenation catalysts, falling into two categories: alkali metal and transition metal promoters. Alkali metal promoters, known as basicity promoters, enhance the catalytic surface's basicity, fostering improved CO_2 adsorption and conversion. Conversely, transition metal promoters serve various functions, contingent on the primary active metal in the catalyst. The impact of each promoter group can vary, influencing the catalyst's activity and selectivity in the CO_2 hydrogenation to ethanol reaction (ALI *et al.*, 2022; LIU *et al.*, 2023; ZENG *et al.*, 2021).

2.3.4.1 Alkali Promoters

Alkali and alkaline earth metals, classified as basicity promoters, play a crucial role by leveraging their low electronegativity to donate electrons to active metals. This electron donation increases the electron density around active metals, strengthening the bonds formed during CO_2 activation. This, in turn, enhances the activation and stabilization of CO, ultimately improving catalytic performance. The introduction of alkali and alkaline earth metals (such as Li, Na, K, Mg, Ca, and Sr) can modify the adsorption modes of reagents, intermediates, and products. Additionally, these promoters may block specific active sites involved in H_2 activation, reducing hydrogenation activity and enhancing selectivity for oxygenates. Basicity promoters are also capable of generating active species in the reaction and stabilizing active metal particles. Notably, sodium (Na) and potassium (K) are particularly effective in facilitating CO_2 conversion, promoting selectivity towards oxygenates, and inhibiting the formation of methane and other hydrocarbons (ALI *et al.*, 2022; XU *et al.*, 2021a; ZENG *et al.*, 2021).

The relationship between the synthesis of HAs and the content of alkali promoters such as Na and K follows a volcano-shaped pattern. This implies that there exists an optimum concentration at which both CO_2 conversion and selectivity are maximized.

Deviating from this optimal concentration may lead to a shift in reaction pathways. The specific optimal concentration varies depending on the catalyst material. Typically, optimum content ranges from 2-7 wt.%, for Cu-based catalysts, and from 0.5-5%, for Co-based catalysts. Na is commonly reported for Co-based catalysts, but relatively fewer studies explore it as a promoter in Cu-based catalysts. The reported optimum Na content revolves around 0.5-2 wt.% (ALI *et al.*, 2022; LI, X. *et al.*, 2023; LIU *et al.*, 2023; WANG *et al.*, 2022; WITOON *et al.*, 2022; ZENG *et al.*, 2021; ZHANG *et al.*, 2021).

2.3.4.2 Effect of Transition Metals Promoters

The introduction of various elements, including iron (Fe), cerium (Ce), manganese (Mn), iridium (Ir), cobalt (Co), zinc (Zn), gallium (Ga), and palladium (Pd), plays a crucial role in influencing both CO_2 conversion and the selectivity of products generated in the hydrogenation reaction. Fe and Co, in particular, facilitate C-C coupling reactions, promoting chain growth. Metallic Fe^0 tends to enhance methane formation by aiding the dissociation of surface CO (CO*), while $Fe^{\delta+}$ stabilizes CO* and increases selectivity toward CO, methanol, and ethanol. The addition of Co as a promoter generally enhances selectivity to alcohols (methanol, ethanol, and propanol) while suppressing the formation of CO and hydrocarbons (ALI *et al.*, 2022; LIU *et al.*, 2023; ZENG *et al.*, 2021).

Ce contributes to increased CO_2 adsorption, dispersion of active metals, and the formation of surface CO intermediates, thereby promoting the synthesis of CH_4 and ethanol. Mn is known to enhance CO_2 conversion, while Ir serves to encourage the formation of higher alcohols. Zn, particularly in copper catalysts, aids in active metal dispersion, enhances the redox character of the catalyst, activates CO_2, and increases selectivity toward higher alcohols. Ga and Pd play crucial roles in hydrogenation, preventing the conversion of alcohols into hydrocarbons. They are associated with hydrogen spillover (Pd) and inverse spillover (Ga), and by altering Pd particle size and Ga content, the hydrogenation step can be controlled. They act as fine-tuning promoters, added in the final stages of CO_2 hydrogenation to ethanol catalyst formulation. In summary, each element fulfills a specific function in influencing the catalyst's activity and selectivity during the conversion of CO_2 into alcohols (ALI *et al.*, 2022; ZENG *et al.*, 2021).

2.3.5 Effect of Reaction Parameters

Another step in tailoring a catalyst activity is to tune the reaction parameters to optimize conversion and selectivity. These reaction conditions are intricately associated with the nature of the catalyst. Conditions such as reaction temperature, pressure, feed

ratio, space velocity, and reactor type, have a significant impact on the CO_2 hydrogenation to ethanol.

For instance, pressure, when increased, enhances CO_2 conversion and HAs formation, especially at pressures above 10 bar. At higher pressures, selectivity for alcohols increases, while selectivity for methane decreases (ALI *et al.*, 2022; HE *et al.*, 2022; ZENG *et al.*, 2021). In terms of chemical equilibrium dynamics, CO_2 hydrogenation to higher alcohols is a volume-reducing reaction. Thus, by itself, increasing pressure will move the equilibrium toward C_{2+} generation and is beneficial to increase the yield of HAs. However, the positive impact of increasing pressure tends to plateau within a certain range. It becomes particularly critical when considering the practical constraints of high-pressure conditions in the production process, the sensible selection of an appropriate pressure range emerges as a crucial factor for optimizing conversion rates and cost-effectiveness (HE *et al.*, 2022; LI, X. *et al.*, 2023).

Conversely, temperature introduces a trade-off dynamic; as the temperature rises, there is a simultaneous increase in CO_2 conversion; however, at elevated temperatures, selectivity for ethanol tends to decrease (HE et al., 2022; STANGELAND; LI; YU, 2018). The optimal temperature range varies depending on the active metal employed: 150-200 °C for Co, 200-240 °C for Rh, 250-300 °C for Cu, and 300-320 °C for Mo (ALI *et al.*, 2022; ZENG *et al.*, 2021). It is essential to consider the influence of temperature on the deactivation or sintering of the active phase as well (LI, X. *et al.*, 2023).

The space velocity parameter is crucial in determining the duration that the gas mixture spends interacting with the catalyst (LI, X. *et al.*, 2023). It is commonly represented by the Gas Hourly Space Velocity (GHSV), and its relationship with catalyst performance is inherently linked to material characteristics. In Mo catalysts, CO_2 conversion tends to remain nearly constant as GHSV increases up to a certain threshold, while both alcohol and CO selectivity experience an uptick. Pd catalysts, on the other hand, exhibit an inverse correlation between GSHV and CO_2 conversion, with product selectivity showing relative independence from the conversion. In Cu catalysts, an increase in GHSV slightly reduces CO_2 conversion but maintains constant selectivity for CO and HAs. However, high GHSV significantly reduces methanol selectivity (ALI *et al.*, 2022; ZENG *et al.*, 2021).

Overall, a discernible volcano curve emerges for HAs production concerning GHSV, indicating that an increase in this variable enhances the yield of ethanol production (a product of conversion and selectivity) up to a certain point. Beyond this

threshold, other products become favored due to the competition of surface reactions such as hydrogenation, C-C coupling, and CO* coupling (SI *et al.*, 2022; XU *et al.*, 2020a, 2021a).

The influence of the feed mixture, or H_2/CO_2 ratio, has not been extensively explored and only has been given attention in the past few years (ALI *et al.*, 2022; ZENG *et al.*, 2021). An and coworkers observed a decline in both CO_2 conversion and ethanol selectivity as the H_2/CO_2 ratio increased (AN *et al.*, 2021). In contrast, it is commonly reported that a higher H_2/CO_2 ratio promotes CO_2 conversion, often favoring hydrocarbons due to excess hydrogen availability (LATSIOU *et al.*, 2023). A recent study on Na-CoCu catalysts described a trade-off relationship where CO_2 conversion decreased with a lower H_2/CO_2 ratio but HAs selectivity increased. Ultimately, a H_2/CO_2 ratio of 1 was identified as the optimum condition (IRSHAD *et al.*, 2024). Lastly, reducing the required amount of H_2 could also positively impact the overall cost of the process.

2.4 LDH-derived materials

Layered double hydroxides (LDHs), also known as hydrotalcite-like compounds (HTlc), are composed of positively charged lamellas and interlayer charge-compensation anions. LHDs are represented as $[M_{(1-x)}^{2+}M_{(x)}^{3+}(OH)_2]^{x+}[A_{x/n}]^{n-}\cdot mH_2O$, where divalent metal cations (e.g., Mg^{2+}, Fe^{2+}, Co^{2+}, Cu^{2+}, Ni^{2+}, or Zn^{2+}) are partially replaced by trivalent metal cations (e.g., Al^{3+}, Ga^{3+}, In^{3+}, Mn^{3+} or Fe^{3+}). The $M^{2+}/(M^{2+} + M^{3+})$ molar ratio (x) is typically in the range of 0.2–0.33, and interlayer galleries contain water and exchangeable inorganic or organic anions, as depicted by **Figure 2.14**. LDHs exhibit weak interlayer bonding, allowing for easy expansion (CHAILLOT; BENNICI; BRENDLÉ, 2021; FAN *et al.*, 2014; FANG *et al.*, 2021).

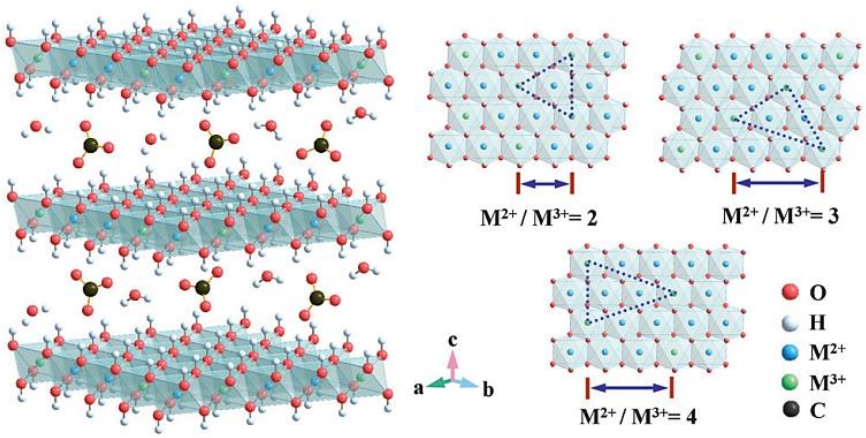

Figure 2.14 - *The idealized structure of carbonate-intercalated LDHs with different M^{2+}/M^{3+} molar ratios.* (FAN *et al.*, 2014)

The versatility of LDHs, attributed to their tunable metal cations, M^{2+}/M^{3+} ratios, and interlayer compensating anions, results in a broad range of materials with diverse physical and chemical properties, and drives increasing interest in these materials (FAN *et al.*, 2014). LDH-derived catalysts can be synthesized using various methods, including co-precipitation, urea hydrolysis, and sol-gel techniques (CHAILLOT; BENNICI; BRENDLÉ, 2021), with co-precipitation being the most widely employed, particularly in the context of CO_2 hydrogenation (FANG *et al.*, 2021).

LDHs, being synthesized through established methods, offer simplicity and scalability, making them suitable for industrial production (CHAILLOT; BENNICI; BRENDLÉ, 2021; FAN *et al.*, 2014). Furthermore, LDH properties have been tailored for various practical applications over the past three decades (FAN *et al.*, 2014). In catalysis, LDHs, many structures can be obtained depending on the synthetic pathways (CHAILLOT; BENNICI; BRENDLÉ, 2021; FAN *et al.*, 2014; FANG *et al.*, 2021), as illustrated by **Figure 2.15**.

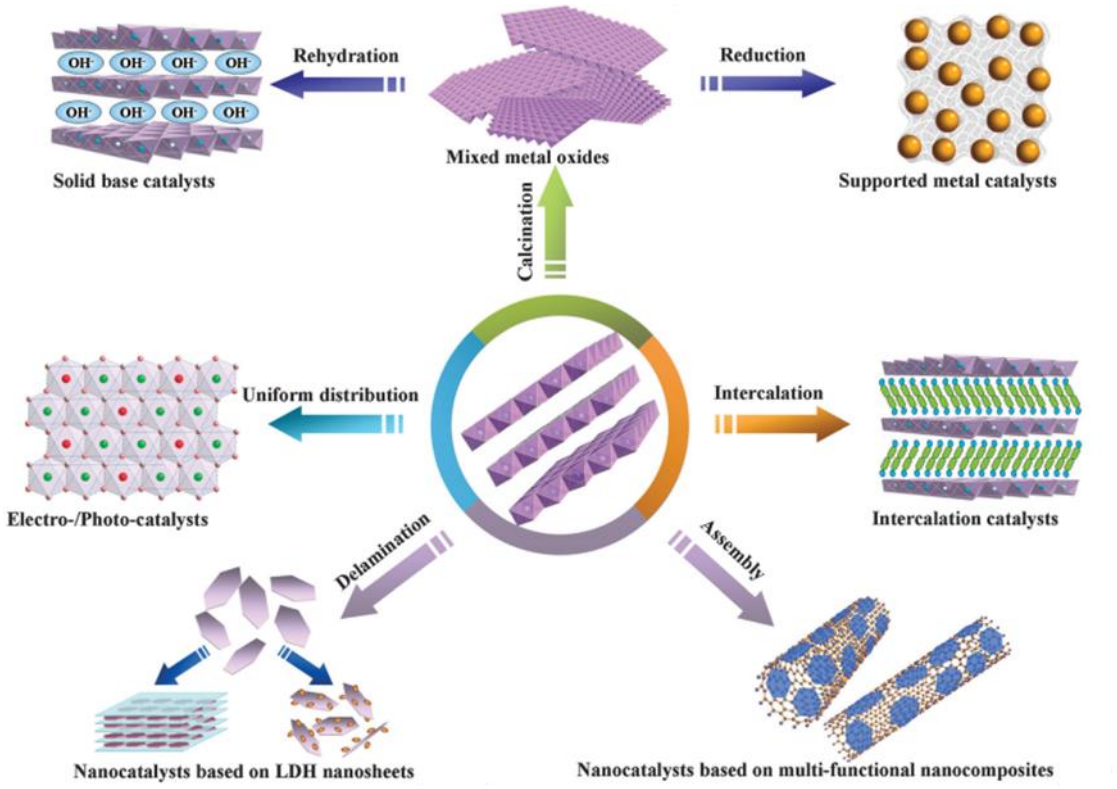

Figure 2.15 - *Summary of the synthetic pathways for preparation of the LDH-based catalysts*. (Adapted from FAN *et al.*, 2014)

LDHs serve as precursors for mixed metal oxides (MMOs) through controlled thermal decomposition. The transformation from LDHs to MMOs leads to materials with large surface areas, basic properties, and homogeneous dispersion of metal ions—ideal

for catalysts. The resulting multi-metal MMOs, particularly those with transition metals, exhibit higher activities and lifetimes than traditionally prepared catalysts. Furthermore, LDHs are also excellent precursors for metal catalysts offering advantages over traditional methods. Both nanoparticles (NPs) and MMO support can formed upon calcination and subsequent reduction. LHDs facilitate the formation of highly dispersed and stable metallic species; prevent sintering/aggregation of the metal NPs via strong metal–support interactions; allow the control *in situ* of particle size and specific morphology of metal NPs (CHAILLOT; BENNICI; BRENDLÉ, 2021; FAN *et al.*, 2014; FANG *et al.*, 2021).

In summary, LDHs, with their tunable composition and versatile properties, serve as excellent precursors for various catalytic applications, offering advantages in terms of synthesis simplicity, scalability, and performance compared to traditional methods. This type of material has been recently reported for CO and CO_2 hydrogenation (DIAS; PEREZ-LOPEZ, 2023; FANG *et al.*, 2021; LIM; YEO; ZENG, 2023; LYU *et al.*, 2023; SUN *et al.*, 2018, 2021, 2023; XU *et al.*, 2023; YUAN *et al.*, 2023).

2.5 Final Remarks: Defining Gaps and Relevance

Recent reviews on CO_2 hydrogenation to higher alcohols, based theoretical studies, have identified CoCu-based catalysts as potential materials (LI, X. *et al.*, 2023; LIU *et al.*, 2023), as these catalysts have continuously demonstrated efficacy inCO hydrogenation to HAs (GÖBEL *et al.*, 2020; SUBRAMANIAN *et al.*, 2009; SUN *et al.*, 2018, 2021, 2023). However, a crucial gap existed—insufficient experimental evidence on the applicability of CoCu-based catalysts when substituting CO with CO_2. The understanding of catalyst characteristics and the impact of reaction conditions was also limited.

As a matter of fact, recently published studies have begun to address these gaps (IRSHAD *et al.*, 2024; LIU *et al.*, 2022; SHAO *et al.*, 2023; WANG *et al.*, 2023; ZHANG *et al.*, 2022), with our contribution stemming from the research presented in this thesis (LAGE *et al.*, 2023). Our work has contributed by exploring different reaction conditions, notably higher space velocities and lower H_2/CO_2 ratios, diverse pretreatment conditions, and varying Co:Cu ratios, and their effects on product yield.

In our exploration of various pretreatment conditions, we delved into a contemporary trend—tuning the surface composition of Co-based catalysts to create hetero-sites ($Co^{\delta+}$–Co^0) to enhance activity towards higher alcohols (LIU *et al.*, 2023; WANG *et al.*, 2022). Additionally, we investigated LDH-derived catalysts, a burgeoning

material in the field, known for its favorable features for CO_2 hydrogenation catalysts, including surface basicity and a tunable structure. Notably, these catalysts offer synthesis simplicity, scalability, and usually above-average durability, making them suitable for industrial production (CHAILLOT; BENNICI; BRENDLÉ, 2021; FAN *et al.*, 2014; FANG *et al.*, 2021).

Furthermore, among CO_2 hydrogenation pathways, he synthesis of higher alcohols was among the least developed, rated at TRL 2 in 2019 (CHAUVY *et al.*, 2019). As emphasized by Kamkeng and coworkers, prioritizing research in underexplored technologies with low TRLs is crucial for establishing early good practices and effective techniques (KAMKENG *et al.*, 2021).

The significance of our research extends beyond the academic realm, finding resonance in the prospectives offered by the low-cost of hydrogen production in Brazil and the impending of carbon pricing policies. This positions CO_2 hydrogenation as a promising avenue for economic development and climate mitigation in Brazil, aligning with global efforts to address pressing environmental challenges.

Chapter 03

Methodology

First Principle: never to let one's self be beaten down by persons or events.

— Marie Curie.

3.1 Preparation of mixed Co-Cu catalysts

The $Co_{(2.8-n)}Cu_nAlO_x$ samples were derived from the calcination of LDH, which were prepared by a modified coprecipitation method (BENHITI *et al.*, 2020; GÖBEL *et al.*, 2020). The alkaline solution was formed by 2 M NaOH (Sigma-Aldrich, ≥98%) and 0.5 M Na_2CO_3 (Sigma-Aldrich, ≥99.5%). The precursor solution (1 M) was prepared by dissolving $Co(NO_3)_2{\cdot}6H_2O$ (Sigma-Aldrich, ≥98%), $Cu(NO_3)_2{\cdot}2.5H_2O$ (Sigma-Aldrich, ≥98%), and $Al(NO_3)_3{\cdot}9H_2O$ (Sigma-Aldrich, ≥98%), in deionized water, with the desired Co:Cu:Al molar ratio. The chosen M:Al ratio (M: active metals, i.e., Co and Cu) was 2.8, based on other works reporting similar materials (BENHITI *et al.*, 2020; GÖBEL *et al.*, 2020; JIRÁTOVÁ *et al.*, 2016; KUPKOVÁ *et al.*, 2023; OBALOVÁ *et al.*, 2009). The selected molar ratios of Co and Cu, expressed by the Co/(Co+Cu), were 0, 0.5, 0.66, and 1.

Both the precursor and alkaline solutions were added drop-wise to a recipient under agitation, maintaining pH 10 by regulating the flow of the alkaline solution. The pH was continuously monitored using a pH meter. Following the addition of the precursor solution, the resulting solution was aged overnight, filtered, and washed thoroughly in deionized water to remove excess sodium (BENHITI *et al.*, 2020; GÖBEL *et al.*, 2020). The resulting filtered cake was suspended in a K_2CO_3 with concentration adjusted to obtain approximately 1 wt.% K in the catalyst (AO *et al.*, 2020; KARÁSKOVÁ *et al.*, 2020; OBALOVÁ *et al.*, 2009). Finally, the resulting sludge was filtered and washed 3 times

with deionized water. The filtered caked was calcined in a muffle in static air at 500 °C for 3 h (KEFIF *et al.*, 2019; OBALOVÁ *et al.*, 2009).

The preparation methodology outlined above was refined through a trial-and-error approach to ensure the proper formation of crystalline phases and achieve the desired surface area while eliminating excess sodium. Any issues encountered and the specific solutions employed in previous methodologies are briefly discussed in **Appendix A – Figure A.2**.

3.2 Characterization of Physical Chemical Properties

3.2.1 Elemental Analysis

Elemental analysis of metal content was conducted using Inductively Coupled Plasma Optical Emission Spectroscopy (ICP-OES) on a Perkin Elmer Optima 2000DV spectrometer. The analyses were carried out at the Institut de Chimie des Milieux et Matériaux de Poitiers (IC2MP - Université de Poitiers) in France. ICP-OES can analyze more than 70 elements from the periodic table, with very low detection limits that vary depending on the specific element under examination.

Prior to analysis, the samples underwent acid digestion. For this, circa 5 mg of samples was dissolved in 50 mL of an acidic solution containing HNO_3 (3 mL) and HCl (5 mL) and heated by microwave. The solution was then injected into the plasma as an aerosol generated by a nebulizer.

In ICP-OES, upon introducing the sample into the plasma, it undergoes vaporization and induced plasma processes, enabling atomization, ionization, and thermal excitation of all present elements. Optical spectroscopy matches emitted light wavelengths to the sample's elements. Emission intensity is compared to a known reference sample, facilitating precise element quantification in the analyzed sample.

3.2.2 X-Ray Diffraction

The identification of the crystalline phases and crystallographic properties of the prepared samples was investigated via X-ray diffraction (XRD) collected on a Rigaku Miniflex II diffractometer at *Laboratório de Tecnologias do Hidrogênio* (LabTecH – UFRJ). The equipment operated with an X-ray tube Cu target (CuKα, λ=1,5418 Å) generated at 30 kV, and 15 mA, and with graphite monochromator. The diffractograms were collected with Bragg angles ranging from 10º to 80º, using a continuous scan mode with a step size of 0.05º and a collection time of 1 s per step.

3.2.3 N_2 Physisorption

The textural properties such as specific surface area (A_{BET}), pore volume (V_{pore}), and pore diameter (d_{pore}) of the calcined catalysts were determined by N_2 physisorption. Prior to the adsorption-desorption experiments, the samples were heated to 200 °C and degassed overnight under vacuum before the N_2 adsorption. The experiments were conducted at liquid nitrogen temperature (~ -196 °C) using a Micromeritics Tristar II instrument at IC2MP (Université de Poitiers, France).

Textural properties were assessed using the proprietary Tristar II software. The surface area was determined via the multipoint Brunauer, Emmet and Teller (BET) method. The pore diameter was obtained using the Barrett-Joyner-Halenda (BJH) equation, focusing on the desorption branch. Pore volume measurements were conducted at P/P^0=0.98, specifically on the adsorption branch of the isotherms.

3.2.4 Temperature-Programmed Reduction

The catalyst reduction profiles were analyzed through temperature-programmed reduction (TPR) experiments employing a Micromeritics Autochem II 2920 apparatus equipped with a thermal conductivity detector (TCD). These experiments were conducted at IC2MP (Université de Poitiers, France).

For each analysis, approximately 125 mg of the sample was pretreated at 200 °C with an Argon flow (30 mL·min^{-1}) for 1 h. Subsequently, the sample was cooled down to room temperature, and the TPR experiment was carried out with the pretreated catalyst in a 10% H_2/Ar flow (30 mL·min^{-1}) over a temperature range of 30 to 1000 °C (10 °C·min^{-1}) using a programmable temperature controller. The reduction degree was then determined by dividing the actual H_2-intake by the theoretical H_2-intake, the latter calculated based on the ICP-OES results.

3.2.5 CO_2 Temperature-Programmed Desorption

The basicity profile of the catalysts was analyzed via CO_2 temperature-programmed desorption (CO_2-TPD) experiments, conducted in a multipurpose testing unit equipped with an online quadrupole mass detector QUADSTAR 422 (QMS 200, BALZERS). These experiments took place at *Núcleo de Catálise* (NUCAT – COPPE/UFRJ, Brazil).

For that, 100 mg of the sample was loaded into a quartz tube reactor, which was heated (10 °C·min^{-1}) to the desired temperatures (250, 400, and 500 °C) under pure H_2 flow (60 mL·min^{-1}) for 30 min, and then cooled to room temperature in ultra-high purity

He flow (60 mL·min^{-1}). Following the pretreatment, the CO_2 adsorption step was performed by passing pure CO_2 (30 mL·min^{-1}) for 30 min and then flushing the reaction with He (60 mL·min^{-1}) for 60 min. The TPD was then performed by heating (20 °C·min^{-1}) the sample to 800 °C. The effluent gases were continuously monitored by an online mass detector (m/z = 2, 4, 28, 30, 32, 44, and 46).

3.3 Catalytic Test

3.3.1 Reaction System

The CO_2 hydrogenation catalytic tests for the $Co_{(2.8-n)}Cu_nAlO_x$ samples were executed in a continuous fixed-bed stainless steel reactor (L = 400 mm, $Ø_{ext}$ = 17.2 mm $Ø_{int}$ = 12.5 mm), as illustrated by **Figure 3.1**. These tests were performed at IC2MP (Université de Poitiers, France).

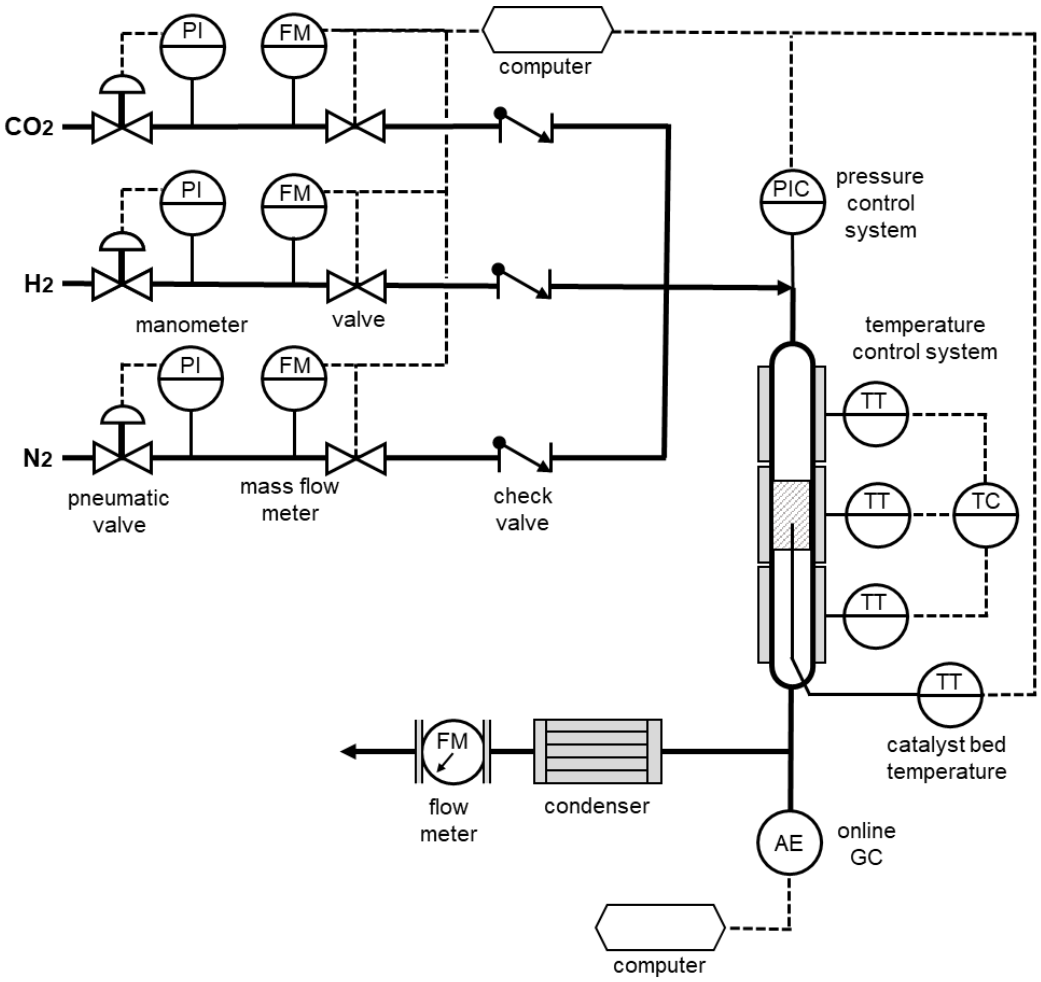

Figure 3.1 – *Schematics of the reaction system.*

The supply of gases (N_2, H_2, CO_2) was regulated by mass flow meters (model 5850TR by Brooks). Control of feed gas flow and reactor pressure was managed by

computer software. The heating system employed three pairs of VINCI heating half-shells equipped with thermocouples connected to a proportional-integral-derivative (PID) controller that managed the desired setpoints. The lower section of the reactor included a thermowell to allow the immersion of a thermocouple into the catalyst bed's center for real-time temperature measurements during the reaction. All lines in this system are heated to 200°C to avoid condensation.

A condenser is placed following the analysis system to trap the reagents and condensable products. The temperature within the condenser is regulated by a cryostat (Hubert) and set at 0°C. A gas meter (Ritter) is placed following the condenser to measure the gas flow every second.

During regular tests, 300 mg of catalysts (0.160-0.100 mm, sieved fraction) is placed between two layers of carborundum (SiC), as demonstrated in **Figure 3.2**, enough to ensure a 10 cm height reaction bed and to maintain the fluid dynamic conditions between different samples and ensure temperature homogeneity within the catalytic bed. The outer-most layer is composed of 1 cm of SiC with 0.250 mm granulometry, named SiC-I. Followed by SiC with 0.125 mm granulometry, named SiC-II, whose mass was regulated to ensure 8 cm when summed to the height of the catalyst. For that, the apparent density of each component is considered. The density of each catalyst is summed in **Table A.1** in **Appendix A**.

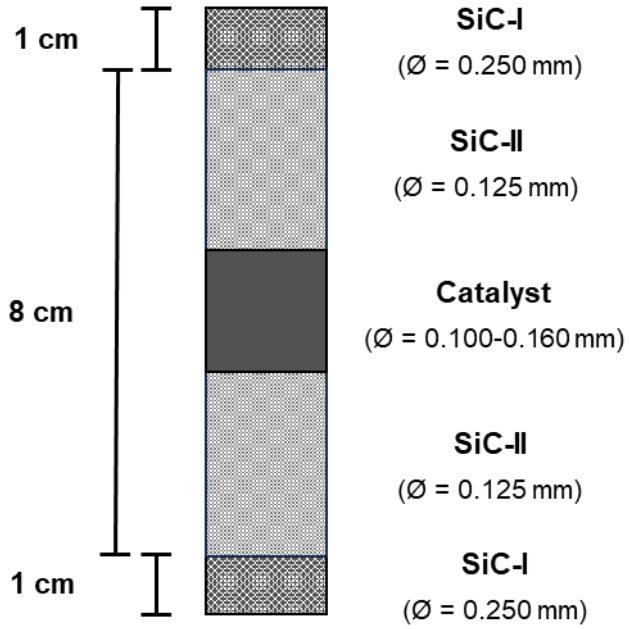

Figure 3.2 – *Representative image of catalytic bed.*

Prior to the reaction, the samples undergo *in situ* reduction at the desired

temperature for 30 min, with a heating ramp of 5 °C.min^{-1}, under pure H_2 flow (30 ml·min^{-1}). Following the reduction, the reactor is brought back to reaction temperature under N_2 flow (30 ml·min^{-1}). The reactor is then flushed with the gas mixture used for the reaction while increasing the pressure. It takes approximately 90 min to reach a pressure of 30 bar in this system, after which, the reactor outlet is open. Periodic injections were made to a gas chromatograph (GC) connected online.

3.3.2 Reaction Conditions

The initial tests were conducted with samples reduced at 250 °C, at a reaction temperature of 250 °C, pressure of 30 bar, and gas-hourly space velocity (GHSV) of 14200 mL·g_{cat}^{-1}·h^{-1} (300 mg of catalyst), for 24 h. The reaction mixture was fed to the reactor at an H_2:CO_2:N_2 ratio of 3:1:0.25.

For subsequent tests, we evaluated four different reduction temperatures, namely 250, 300, 400, and 500 °C, while keeping reaction temperature, pressure, GHSV, and H_2:CO_2 ratio constant. After determining the optimum reduction temperature, we tested different reaction temperatures (200, 250, and 300 °C), while keeping all other parameters unchanged. Following the determination of the optimum reaction temperature, we also studied the isolated effect of changing the GHSV to 10625 mL.g_{cat}^{-1}.h^{-1} (H_2:CO_2 = 3:1) and reducing the H_2:CO_2 ratio from 3:1 to 3:2 (maintaining the GHSV at 14200 mL·g_{cat}^{-1}·h^{-1}).

3.3.3 Analytical System

The outlet products of each experiment were analyzed online (each 36 min) in an Agilent 7890A online GC. The gas products (CO, CH_4, CO_2, H_2, and N_2) were detected by a thermal conductivity detector (TCD) using two chromatography columns in tandem, HP-Plot SA (N_2, H_2, and CO) and HP-Plot Q (CH_4, CO_2, and H_2O). Hydrocarbons and condensable liquid products were analyzed by two flame ionization detectors (FID), one for general quantification (GSQ column) and the other to confirm the presence of oxygenates (HP-Innovax column).

3.3.4 Catalytic Performance Calculation

The catalytic performance was expressed by CO_2 conversion (X_{CO_2}), C-based product selectivity (S_i), and the product space-time yield (STY_i), calculated by the equation as follows:

$$X_{CO_2} = \frac{[CO_2]_{in} - [CO_2]_{out}}{[CO_2]_{in}} \times 100\% \quad (1)$$

$$S_i = \frac{n_i \times C_i}{\sum(n_i \times C_i)} \times 100\% \quad (2)$$

$$STY_i = \frac{F_{CO_2,in} \times X_{CO_2} \times S_i}{m_{cat}} \quad (3)$$

where $[CO_2]_{in}$ and $[CO_2]_{out}$, respectively, are the molar concentration of CO_2 in the inlet and outlet flow; C_i refers the concentration of products (CO, CH_4, C_xH_n, CH_3OH, C_2H_5OH, C_3H_7OH, among others) in the outlet flow; n_i represents the number of carbon atoms for product C_i; $F_{CO_2,in}$ stands for the molar flow of CO_2; and m_{cat} is the mass of catalyst. The concentration of CO_2 and the products was calculated based on their respective areas on the chromatograms, using N_2 as an internal standard.

3.4 Structural and Surface Characterizations

In this section, the main catalyst, $Co_{1.8}Cu_{0.9}AlO_x$, was comprehensively characterized, along with its monometallic counterparts, $Co_{2.6}AlO_x$ and $Cu_{2.6}AlO_x$, to provide better understanding of its activity.

3.4.1 In Situ X-Ray Diffraction

To investigate the structural changes in the catalysts during the reduction pretreatment, in situ XRD experiments were carried out on a Bruker D8-Advance diffractometer using the Co-Kα radiation (1.79 Å) equipped with VANTEC detector (aperture 3°). The in situ XRD analysis involved heating the sample from room temperature (RT) to 500 °C (5 °C·min^{-1}) under 3% H_2 flow (50 mL·min^{-1}). Upon reaching the desired temperature, the reduction proceeded at a constant temperature for 1 hour. The sample was positioned on a Kanthal (FeCrAl alloy) sample support. XRD patterns were recorded at different temperatures, including RT, 250, 400, and 500 °C. After the reduction at 500 °C, samples were cooled down to RT under inert atmosphere (Ar, 50 mL·min^{-1}). The 2θ range analyzed was 10 to 80°, with a step size of 0.05° and step times of 2 s for spectra collected at RT and 1 s for spectra collected at higher temperatures.

3.4.1.1 Rietveld Refinement

The Rietveld method is a refinement technique capable of determining structural parameters of almost all crystalline materials by constructing a theoretical model that fits the experimentally observed diffraction pattern using the least-squares method. The

calculated pattern, when adjusted to the experimental data (observed pattern), provides information on the material's structural parameters and diffraction profile. Refinement in the Rietveld method involves adjusting the model parameters obtained from the calculation of atomic distribution in a crystalline structure and an experimentally obtained XRD pattern. This adjustment aims to accommodate the calculated pattern to the experimental results, respecting the exact peak positions and the profile behavior concerning baseline broadening (MCCUSKER *et al.*, 1999).

The refinement process enables the definition of the positions and intensities of Bragg reflections, allowing for accurate evaluation even in the presence of peak overlap. The use of all diffraction patterns enhances precision in quantitative analysis compared to traditional methods relying on isolated reflections (MCCUSKER *et al.*, 1999). The refinement was conducted using the free software Maud (Materials Analysis Using Diffraction), featuring a user-friendly interface for comparing the calculated (from the Crystallographic Information File, CIF) and observed (experimental) diffractograms. Maud also facilitates real-time visualization of the refinement graph and reliability indices (WENK, 2023). The “goodness-of-fit” (χ^2 = Rwp / Rexp) index is an easy way to confirm the fit of the model (Rwp) and the quality of experimental data (Rexp), χ^2 value should be close to 1 (MCCUSKER *et al.*, 1999).

Lanthanum hexaboride (LaB_6) was used a standard sample or reference material to calibrate the equipment parameters of the refinement. To obtain a better peak definition for calibration the XRD acquisition parameters were: 2θ range of 10 to 130°, step size of 0.024° and step times of 2.5 s. The collect XRD pattern for LaB6 is displayed on **Figure C.1** at **Appendix C**.

3.4.2 Electron Microscopy

The investigation of surface morphology, first, employed a field emission gun scanning electron microscope (FE-SEM), specifically a FEI Helios Nanolab Dual Beam G3 CX. This system was complemented by an Edax energy dispersive X-ray detector (EDX) and featured a transmission mode detector. Enhanced resolution was achieved through scanning transmission electron mode (STEM-in-SEM) under low-voltage SEM operating conditions at 30 kV.

The STEM-in-SEM configuration utilized a dedicated sample holder designed for conventional copper TEM grids. A scanning transmission electron (STEM) detector positioned below the sample holder operated in three different modes: annular bright

field (STEM-BF), annular dark field (STEM-DF), and high angular annular dark field (STEM-HAADF).

Additionally, surface morphology investigations were conducted via high-resolution transmission electron microscopy (HRTEM). HRTEM images and selected area electron diffraction (SAED) patterns were captured using a 200 kV Jeol 2100F instrument, coupled with an Oxford energy dispersive X-ray (EDX) detector, for Energy Dispersive X-ray Spectroscopy (EDXS or EDS).

For both SEM and TEM analyses, samples were prepared by suspending them in ethanol and subjecting them to ultrasonic dispersion for 15 minutes. Subsequently, droplets of the dispersed samples were deposited onto a 200 mesh (100 nm) copper grid coated with a holey carbon film.

3.4.2 X-ray Photoelectron Spectroscopy

XPS experiments were conducted at the IPÊ beam-line at the Brazilian Synchrotron Light Laboratory (LNLS) in Campinas. The powder sample was meticulously prepared by depositing it onto a carbon tape (30×30 mm), which was then placed in the sample holder. Then, the sample holder was placed in the pre-chamber to achieve vacuum and transferred to the Ultra-High Vacuum (UHV) chamber. During the experiments, XPS data was collected using a SPECS Phoibos 150 electron analyzer equipped with a 9-channeltron detector.

To ensure consistent penetration in each scan, the energy of the X-ray beam (hv) was set to maintain constant kinetic energy (KE = 600 eV). Specifically, the settings for various scans were as follows: survey (1543 eV), Cu 2p (1543 eV), Cu 2p (1385 eV), O 1s (1131 eV), C 1s (884 eV), Al 2p (673 eV). For high-resolution or detailed spectra of specific bands, the pass energy was configured at 15 eV, while for the survey, it was set at 40 eV. To mitigate surface charging effects, a flood gun was employed (150 eV; 50 μA).

The XPS data analysis was performed using CasaXPS. Spectra alignment was conducted by referencing the C 1s band at a binding energy (BE) of 284.8 eV and verifying the fermi level edge (E_F) at 0 eV. Both methodologies produced consistent outcomes. Prior to analysis, peaks were fitted with a Shirley background.

Chapter 04

Results and Discussion I

Tuning Co-Cu-Al Catalysts and Their Reaction Conditions

Estamos condenados à civilização. Ou progredimos ou desaparecemos.

— Euclides da Cunha (1998)

The data presented in this chapter was published in the peer-reviewed journal Chemical Engineering Science (LAGE *et al.*, 2023), as elucidated by **Annex A**.

4.1 Physical-Chemical Properties

First, to confirm the success of catalyst synthesis, we characterized the samples, assessing their metallic content, crystalline phases, and textural properties through ICP-OES, XRD, and N_2 physisorption, respectively. The metallic weight content (wt.%), the calculated molar ratio between Co:Cu:Al, and the textural properties of the samples are summarized in **Table 4.1**. Henceforth the catalysts are referred to as $Cu_{2.6}AlO_x$, $Co_{1.3}Cu_{1.3}AlO_x$, $Co_{1.8}Cu_{0.9}AlO_x$, and $Co_{2.6}AlO_x$, based on their Co:Cu:Al molar ratios. We verified that the Co/(Co+Cu) ratios agreed with expected nominal values and that obtaining an M-Al ratio close to 2.8 was possible, as desired. The samples did not present any detectable amounts of Na, confirming that the treatment with K_2CO_3 solution efficiently removed the excess Na. The K content for $Cu_{2.6}AlO_x$, $Co_{1.3}Cu_{1.3}AlO_x$, $Co_{1.8}Cu_{0.9}AlO_x$, and $Co_{2.6}AlO_x$ was 0.8, 0.7, 0.8 and 0.9 wt.%, respectively, close to the expected 1 wt.%.

Table 4.1 - *Content of Co, Cu, Al, and K, Surface area (A_{BET}), pore volume (V_{pore}), and pore diameter (d_{pore}) of the prepared catalysts after calcination at 500 °C.*

Catalyst	Metallic content (wt%)				Co:Cu:Al	A_{BET}	V_{pore}	d_{pore}
	Al	Co	Cu	K	Ratio	($m^2 \cdot g^{-1}$)	($cm^3 \cdot g^{-1}$)	(nm)
$Cu_{2.6}AlO_x$	9.3	0.0	57.5	0.8	0:2.6:1	56	0.18	9
$Co_{1.3}Cu_{1.3}AlO_x$	9.3	27.3	29.3	0.7	1.3:1.3:1	85	0.44	19
$Co_{1.8}Cu_{0.9}AlO_x$	9.0	34.9	18.7	0.8	1.8:0.9:1	69	0.37	18
$Co_{2.6}AlO_x$	9.1	52.2	0.0	0.9	2.6:0:1	78	0.35	13

Regarding the N_2 physisorption isotherms for $Cu_{2.6}AlO_x$ (blue), $Co_{1.3}Cu_{1.3}AlO_x$ (light purple), $Co_{1.8}Cu_{0.9}AlO_x$ (dark purple), and $Co_{2.6}AlO_x$ (red) are shown in **Figure 4.1**. Based on the N_2 physisorption analysis, the calculated BET surface area for $Cu_{2.6}AlO_x$, $Co_{1.3}Cu_{1.3}AlO_x$, $Co_{1.8}Cu_{0.9}AlO_x$, and $Co_{2.6}AlO_x$ was 56, 85, 69, and 78 $m^2 \cdot g^{-1}$, in that order. The values agree with the expected area (50-150 $m^2 \cdot g^{-1}$) for mixed oxides prepared by the modified coprecipitation method (BENHITI *et al.*, 2020; KEFIF *et al.*, 2019). Moreover, the hysteresis at high relative pressure indicates the formation of a mesoporous material (SULMONETTI *et al.*, 2017), which is consistent with similar previously reported materials (KUPKOVÁ *et al.*, 2023; LIMA; DIAS; PEREZ-LOPEZ, 2020; SULMONETTI *et al.*, 2017; TEIXEIRA *et al.*, 2018; WAN *et al.*, 2022) and with the values of pore diameter (Table 4.1).

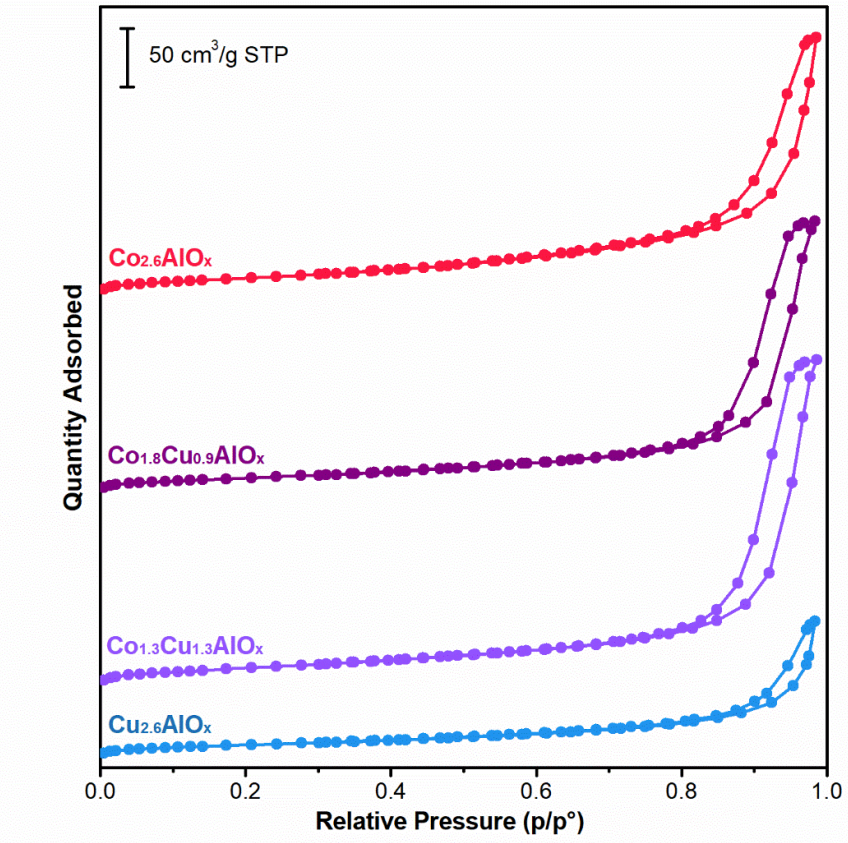

Figure 4.1 - *Nitrogen adsorption isotherms of $Cu_{2.6}AlO_x$ (blue), $Co_{1.3}Cu_{1.3}AlO_x$ (light purple), $Co_{1.8}Cu_{0.9}AlO_x$ (dark purple), and $Co_{2.6}AlO_x$ (red).*

Powder XRD patterns for the catalysts calcined at 500 °C are presented in **Figure 4.2**. For $Cu_{2.6}AlO_x$ (blue), a CuO (tenorite, PDF#48-1548) phase was identified. The presence of small and poorly defined peaks could be attributed to $CuAl_2O_4$ spinel (PDF#44-0106) or diffraction noise. For $Co_{2.6}AlO_x$ (red), the Co_3O_4 (PDF#43-1003) and the Co_2AlO_4 inverse spinel (PDF#38-0814) phases were compatible with the XRD pattern. It is also possible to infer the presence of $CoAl_2O_4$ spinel (PDF#44-0106), as it presents the same position of diffraction lines only slightly shifted to a lower angle. From the XRD patterns, it is difficult to distinguish Co_3O_4 from spinel-like structures, as their lattice parameters are very similar (WAN *et al.*, 2022).

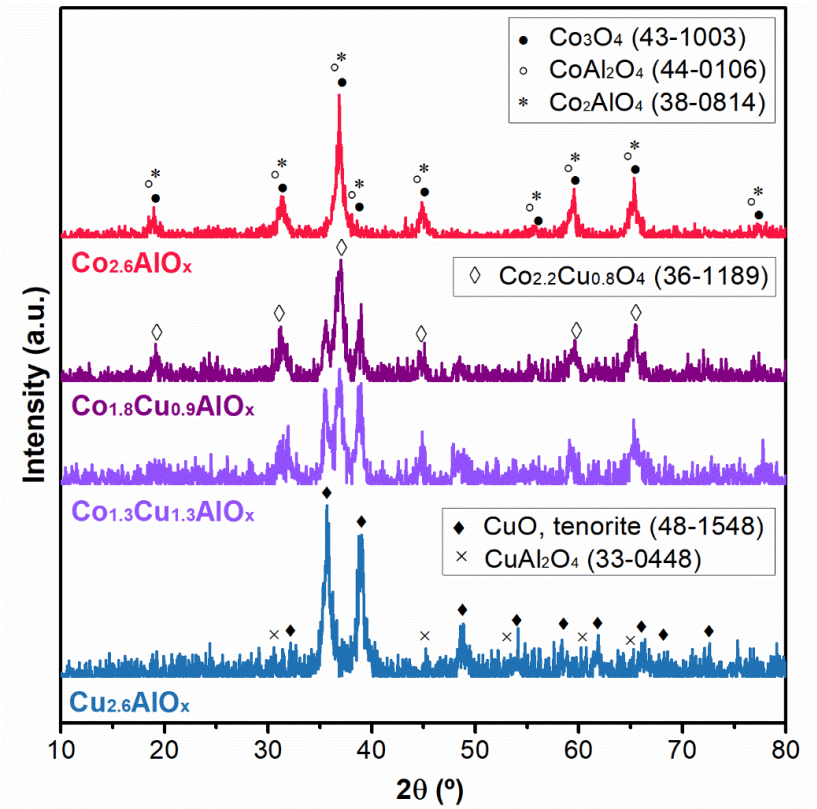

Figure 4.2 - *$Cu_{2.6}AlO_x$ (blue), $Co_{1.3}Cu_{1.3}AlO_x$ (light purple), $Co_{1.8}Cu_{0.9}AlO_x$ (dark purple), and $Co_{2.6}AlO_x$ (red) XRD patterns (CuKα, λ=1.5418 Å).*

As for $Co_{1.3}Cu_{1.3}AlO_x$ (light purple) and $Co_{1.8}Cu_{0.9}AlO_x$ (dark purple), it appears that a mixture of CuO, Co_3O_4, and the Co-Al spinel-like structures is the likely case. It is also reported that Co-Cu mixed oxides, such as $Co_{2.2}Cu_{0.8}O_4$ (PDF#36-1189), $Co_{2.05}Cu_{0.95}O_4$ (PDF#36-1189), and $Co_{2.84}Cu_{0.15}O_4$ (PDF#36-1189), display the same diffraction pattern as Co_3O_4, with a slight or no shift in angle due to the small difference in Co and Cu cationic radii. Consequently, via XRD analysis, distinguishing whether the pattern corresponds to Co_3O_4 or a Co-Cu spinel becomes a challenging task (CHEN *et al.*, 2020; KUPKOVÁ *et al.*, 2023). Recent works reported similar materials containing a mixture of different phases and spinel structures (GÖBEL *et al.*, 2020; JIRÁTOVÁ *et al.*, 2016; KUPKOVÁ *et al.*, 2023; SULMONETTI *et al.*, 2017; WAN *et al.*, 2022).

Subsequently, we evaluated the reduction and basicity profiles of the catalysts. The reduction profiles of the samples calcined at 500 °C were obtained using H_2-TPR and are presented in **Figure 4.3**. For $Cu_{2.6}AlO_x$ (blue), we observed a single reduction region around 200 and 300 °C, marking the reduction of Cu^{2+} to Cu^0 (WEI *et al.*, 2019). Similar reduction profiles for Cu-Al catalysts derived from LDHs are reported in the literature (CORRÊA *et al.*, 2017; KIM *et al.*, 2017; PRAKRUTHI *et al.*, 2018; TEIXEIRA *et al.*, 2018).

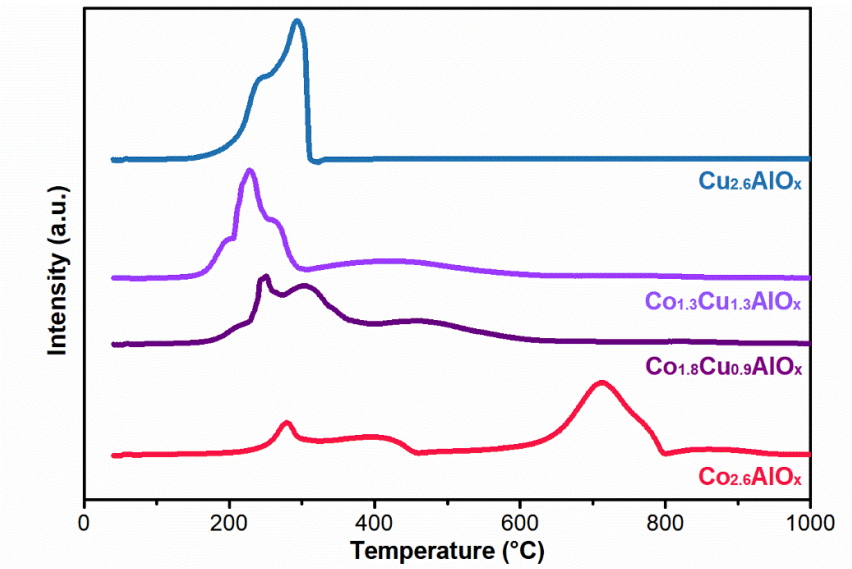

Figure 4.3 - *H_2 TPR profile of $Cu_{2.6}AlO_x$ (blue), $Co_{1.3}Cu_{1.3}AlO_x$ (light purple), $Co_{1.8}Cu_{0.9}AlO_x$ (dark purple), and $Co_{2.6}AlO_x$ (red) under 10% H_2 flow (30 mL.min^{-1}).*

In the case of $Co_{2.6}AlO_x$ (red), we can ascribe at least three distinct reduction regions: a peak at 250 °C, a broad region from 350 to 450 °C, and a broad peak around 700 °C. The first peak and region are commonly attributed to the reduction of Co^{3+} to Co^{2+}, and the reduction of Co^{2+} to Co^0, whereas reduction peaks above 450 °C were previously attributed to the reduction of spinel-like structures (KARÁSKOVÁ *et al.*, 2020; LIMA; DIAS; PEREZ-LOPEZ, 2020; ZHAO *et al.*, 2018). Furthermore, Co-Al catalysts derived from LDHs have been reported with two distinct reduction regions, one around 250-450 °C, attributed to the reduction of Co^{3+} to Co^{2+}, and other one around 550-700 °C, assigned to the reduction of Co^{2+} to Co^0 (AIDER *et al.*, 2018; RAMOS *et al.*, 2017; TEODORESCU *et al.*, 2020; WANG *et al.*, 2018; ZHAO *et al.*, 2018).

As for $Co_{1.3}Cu_{1.3}AlO_x$ (light purple) and $Co_{1.8}Cu_{0.9}AlO_x$ (dark purple), we observed two distinct regions: one from 200 to 400 °C, which could be attributed to, first, the reduction of Cu^{2+} to Cu^0, along with the reduction of Co^{3+} to Co^{2+} (GÖBEL *et al.*, 2020; KUPKOVÁ *et al.*, 2023; SULMONETTI *et al.*, 2017); and a second broad region above 400 °C, ascribed to the two-step reduction of bulk Co^{3+} to Co^0, the reduction of Co^{2+} to Co^0, and the reduction of spinel-like structures (GÖBEL *et al.*, 2020; SULMONETTI *et al.*, 2017). It is worth mentioning that adding Cu to the Co-Al structure significantly reduced its reduction temperature. Moreover, when comparing $Co_{1.3}Cu_{1.3}AlO_x$ and $Co_{1.8}Cu_{0.9}AlO_x$, the reduction profile of $Co_{1.3}Cu_{1.3}AlO_x$ is slightly shifted to a lower temperature. This shift to lower reduction temperatures of Co-containing catalysts can be explained by hydrogen spillover from Cu metallic particles (BERENGUER *et al.*, 2019; GÖBEL *et al.*, 2020; KUPKOVÁ *et al.*, 2023; PAKNAHAD; ASKARI; GHORBANZADEH,

2015; SULMONETTI *et al.*, 2017).

From the TPR analysis and the elemental analysis of Co and Cu, we calculated the degree of reduction of the samples This measure is expressed as the experimental H_2 consumption (determined by the peak area of the TPR profiles) divided by the theoretical H_2 consumption (based on the nominal molar content of Co and Cu in the samples, assuming all Co exists as Co_3O_4, and all Cu as CuO) in percentage. This information is summarized in **Table 4.2**. The degree of reduction ranged from 88% to 99% with the increase in Cu content in the samples. The measured H_2 consumption was lower than the expected or theoretical H_2 consumption, suggesting that not all Co is present as Co_3O_4, likely due to the presence of spinel-like structures.

Table 4.2 - *Calculated experimental and theoretical H_2 consumption, and degree of reduction based on the 10% H_2-TPR profiles of the catalysts.*

Catalyst	Experimental H_2 consumption ($mmol \cdot g^{-1}$)	Theoretical H_2 consumption ($mmol \cdot g^{-1}$)	Degree of Reduction (%)
$Cu_{2.6}AlO_x$	8.97	9.05	99
$Co_{1.3}Cu_{1.3}AlO_x$	9.62	10.79	89
$Co_{1.8}Cu_{0.9}AlO_x$	9.70	10.84	89
$Co_{2.6}AlO_x$	10.44	11.81	88

Regarding surface basicity, an essential aspect of CO_2 hydrogenation catalysts, it was assessed through CO_2-TPD experiments and is shown in **Figure 4.4**. All samples reduced at 250 °C displayed a sharp peak around 110 °C and a sinusoidal pattern from 150 to 350 °C due to the re-adsorption of CO_2 (DELGADO *et al.*, 2007; DELGADO; GÓMEZ, 2005; KREITZ *et al.*, 2021; XU; IGLESIA, 1998) $Co_{1.3}Cu_{1.3}AlO_x$ and $Co_{1.8}Cu_{0.9}AlO_x$ also displayed a broader peak around 250 and 300 °C.

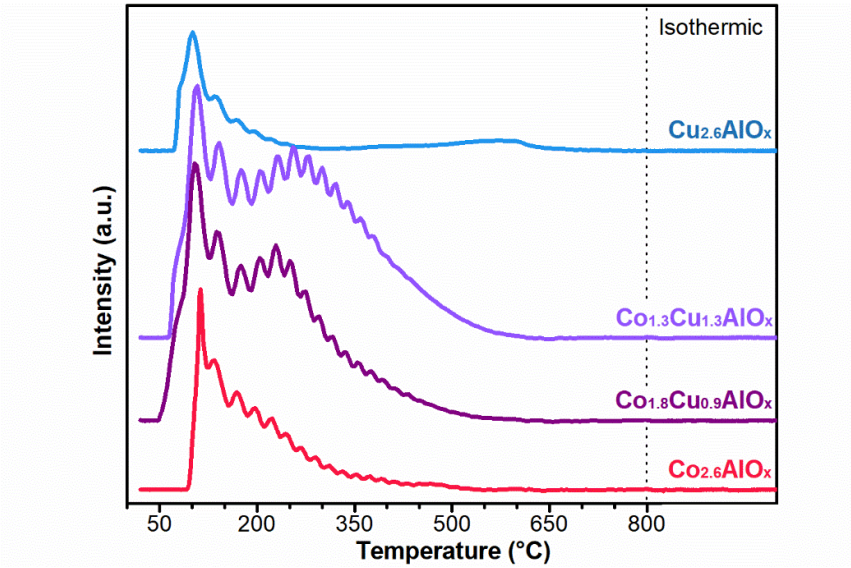

Figure 4.4 - *CO_2-TPD curves for $Cu_{2.6}AlO_x$ (blue), $Co_{1.3}Cu_{1.3}AlO_x$ (light purple), $Co_{1.8}Cu_{0.9}AlO_x$ (dark purple), and $Co_{2.6}AlO_x$ (red) reduced at 250 °C.*

According to the literature, it is possible to divide the CO_2-TPD profile into three regions according to the strength of the adsorption site. Below 200 °C, the desorption is ascribed to weakly adsorbed CO_2 (AN *et al.*, 2022; NGUYEN; KIM; PARK, 2022; SHI *et al.*, 2018; WANG *et al.*, 2022, 2023; ZHANG *et al.*, 2021). This region can be assigned to Bronsted basicity sites, i.e., surface hydroxyl (-OH) (AN *et al.*, 2022; LIU *et al.*, 2016; RONDUDA *et al.*, 2021; TURSUNOV; KUSTOV; TILYABAEV, 2017). Peaks at this region were identified in all four catalysts.

The second desorption region, from 200 to 500 °C, is attributed to moderately adsorbed CO_2 (AN *et al.*, 2022; LIU *et al.*, 2016; WANG *et al.*, 2023; ZHANG *et al.*, 2021) and associated with Lewis basicity, ergo oxygen sites (RONDUDA *et al.*, 2021), more specifically metal-oxygen pairs (M-O) (LIU *et al.*, 2016). It is reported that these moderate basic sites contribute to ethanol formation (AN *et al.*, 2021) and the activity of catalysts on the CO_2 hydrogenation reaction at that range of temperature (AN *et al.*, 2022). Peaks at this second region were identified in both mixed CoCu catalysts.

The last region, above 500 °C, is attributed to strong basic sites (WANG *et al.*, 2022, 2023), also associated with Lewis basicity (RONDUDA *et al.*, 2021), more specifically to low coordination oxygen atoms (LIU *et al.*, 2016). Strong CO_2 adsorption sites are reported to favor CO_2 methanation (LE *et al.*, 2017) and, in the case of Co-based catalysts, are associated with Co^0 species (WANG *et al.*, 2022).

Based on the catalytic test results (section 4.2.2), CO_2-TPD experiments were carried out at different reduction temperatures for $Co_{2.6}AlO_x$ and $Co_{1.8}Cu_{0.9}AlO_x$, which are displayed in **Figure 4.5**.

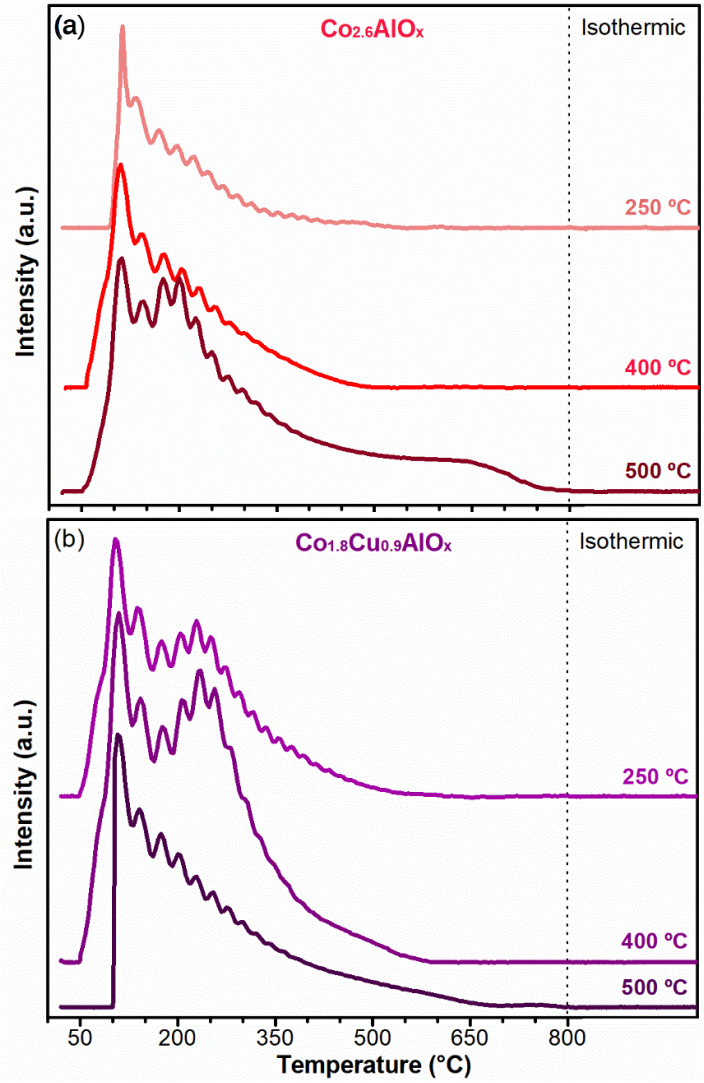

Figure 4.5 - *CO_2-TPD curves for $Co_{2.6}AlO_x$ (a), $Co_{1.8}Cu_{0.9}AlO_x$ (b) after different reduction temperatures*.

$Co_{2.6}AlO_x$, after reduction at 500 °C, changed its profile, displaying a sharp at 200 °C and a tail indicating CO_2 desorption up until 700 °C (Figure 4.5a). The presence of CO_2 desorption at such high temperatures indicates the presence of strong basicity sites (RONDUDA *et al.*, 2021; WANG *et al.*, 2022, 2023), and indicates the presence of Co^0 species (WANG *et al.*, 2022) upon reduction. As for $Co_{1.8}Cu_{0.9}AlO_x$, upon reduction at 400 °C, the peak attributed to moderate basicity sites became more prominent (Figure 4.5b), indicating an increase in moderate basicity sites (AN *et al.*, 2022; LIU *et al.*, 2016; WANG *et al.*, 2023; ZHANG *et al.*, 2021), which disappeared when the sample was reduced at 500 °C.

In general, we can see that the combination of Co and Cu resulted in an enhanced CO_2 adsorption capacity. This observation becomes especially pronounced when comparing the calculated CO_2 uptake of the bimetallic catalysts, $Cu_{2.6}AlO_x$ and $Co_{2.6}AlO_x$, to the trimetallic catalysts, $Co_{1.3}Cu_{1.3}AlO_x$ and $Co_{1.8}Cu_{0.9}AlO_x$, which is summarized in **Table 4.3**.

Table 4.3 - Calculated CO_2 uptake based on the CO_2-TPD results for the samples.

Catalyst	Reduction Temperature (°C)	CO_2 uptake ($\mu mol \cdot g^{-1}$)
$Cu_{2.6}AlO_x$	250	10.1
$Co_{1.3}Cu_{1.3}AlO_x$	250	57.2
$Co_{1.8}Cu_{0.9}AlO_x$	250	43.4
	400	84.5
	500	42.9
$Co_{2.6}AlO_x$	250	17.8
	400	31.1
	500	55.5

Furthermore, both $Co_{1.3}Cu_{1.3}AlO_x$ and $Co_{1.8}Cu_{0.9}AlO_x$ (Figure 4.4) exhibited a desorption peak in the moderately basic region at around 250 °C, which is commonly associated with CO_2 hydrogenation activity. Notably, the peak representing moderate basicity in the TPD profile of $Co_{1.8}Cu_{0.9}AlO_x$ increased significantly when the sample underwent reduction at 400 °C (Figure 4.5b), leading to nearly double CO_2 uptake. On the other hand, upon reducing $Co_{1.8}Cu_{0.9}AlO_x$ at 500 °C, the CO_2 uptake decreased by half, and the peak at 250 °C vanished. For $Co_{2.6}AlO_x$, the CO_2 uptake increased with the increase in the reduction temperature. At a reduction temperature of 500 °C, all three desorption regions were identified: two sharp peaks corresponding to weakly and moderately adsorbed CO_2, and a broad region spanning from 500 to 700 °C, attributed to strongly adsorbed CO_2. The effect of reduction temperature on $Co_{2.6}AlO_x$ and $Co_{1.8}Cu_{0.9}AlO_x$ activity is further elaborated upon in the subsequent discussion of catalytic tests (section 4.2.2).

4.2 Tuning Catalyst Performance

We initially tested the catalysts, namely $Cu_{2.6}AlO_x$, $Cu_{1.3}Co_{1.3}AlO_x$, $Cu_{1.8}Co_{0.9}AlO_x$, and $Co_{2.6}AlO_x$, in the CO_2 hydrogenation reaction at 30 bar, 250 °C, H_2/CO_2 ratio of 3, gas-hourly space velocity (GHSV) of 14200 $mL \cdot g_{cat}^{-1} \cdot h^{-1}$. Henceforth, the products are coded as CH_4 (methane), CO (carbon monoxide), C_{2-5} alkanes and alkenes (HCs), methanol, ethanol, and $C_{3+}OH$ (propanol, isopropanol, and other C_{3+} oxygenates).

We evaluated their CO_2 conversion, product selectivity (HCs and oxygenates,

CO, and CH_4), HCs and oxygenates (methanol, ethanol, and $C_{3+}OH$) distribution, and space-time yield (STY). In the initial test, each sample was pretreated in a pure hydrogen atmosphere at the reaction temperature of 250 °C to evaluate the effect of combining Co and Cu (section 4.2.1). Subsequently, we examined the impact of altering the reduction temperature (section 4.2.2) and various reaction parameters, including the reaction temperature (section 4.2.3), GSHV (section 4.2.4), and H_2/CO_2 ratio (section 4.2.5). Additionally, we assessed the stability of the most effective catalyst (section 4.2.6). This top-performing catalyst was then compared to existing literature (section 4.2.7). The outcomes of all these investigations are succinctly presented in **Appendix B**, in **Table B1**, **Table B2**, and **Table B3**.

4.2.1 Effect of Co-Cu Ratio

The effect of combining Co and Cu was evidenced by the increase in CO_2 conversion and selectivity towards products of interest. For that, the molar ratios between cobalt and copper in the catalysts can be expressed by the Co/(Co+Cu) ratio. The Co/(Co+Cu) ratios for the samples $Cu_{2.6}AlO_x$, $Cu_{1.3}Co_{1.3}AlO_x$, $Co_{1.8}Cu_{0.9}AlO_x$, and $Co_{2.6}AlO_x$ are, respectively, 0, 0.5, 0.66, and 1. The changes in CO_2 conversion and selectivity towards the different products are expressed in **Figure 4.6**.

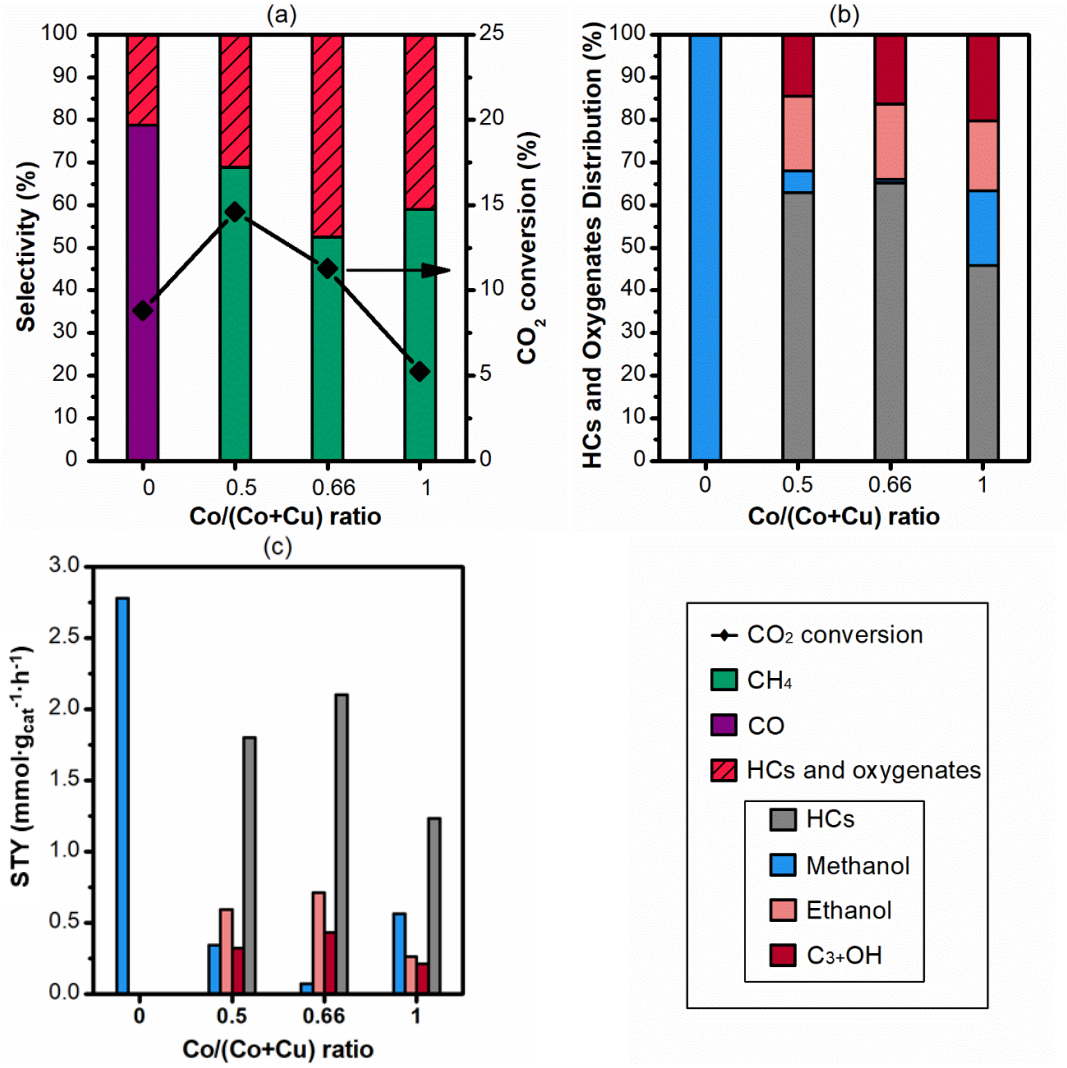

Figure 4.6 - *Effect of Co/(Co+Cu) ratio on the selectivity and CO_2 conversion (a), HCs and oxygenates distribution (b), and the STY of products of interest (c) (250 °C, 30 bar, H_2/CO_2 = 3, GHSV = 14200 mL·g_{cat}^{-1}·h^{-1}).*

We observed an increase in CO_2 conversion and selectivity towards products of interest, i.e., hydrocarbons and oxygenates (striped, red), when combining cobalt and copper (Figure 4.6a). Both mixed Co-Cu catalysts, $Cu_{1.3}Co_{1.3}AlO_x$ and $Cu_{1.8}Co_{0.9}AlO_x$, displayed CO_2 conversion above 10%, whereas the values of conversion for the single metal catalysts, $Cu_{2.6}AlO_x$ and $Cu_{2.6}AlO_x$, were below 10%. When comparing the HCs and oxygenates distribution (Figure 4.6b), $Cu_{2.6}AlO_x$ displayed 100% selectivity towards methanol, whereas $Cu_{1.3}Co_{1.3}AlO_x$, $Cu_{1.8}Co_{0.9}AlO_x$, and $Co_{2.6}AlO_x$ produced HCs (gray), ethanol (light red), $C_{3+}OH$ (dark red) and methanol (blue).

Our observations indicate that the combination of Co and Cu results in an increased production of higher alcohols and hydrocarbons, suggesting that the Co-Cu combination favors chain growth. Notably, $Cu_{1.8}Co_{0.9}AlO_x$, with a Co/(Co+Cu) ratio of 0.66, displayed the lowest selectivity towards undesired products, i.e., CH_4 (green) and

CO (purple), and the higher yield of both ethanol and $C_{3+}OH$, specifically 0.71 and 0.43 $mmol.h^{-1}.g^{-1}$ (Figure 4.6c).

This “synergic” effect between Co and Cu has been previously reported for enhancing HAs selectivity from syngas (GÖBEL *et al.*, 2020; SUBRAMANIAN *et al.*, 2009; SUN *et al.*, 2018, 2021, 2023) and CO_2 hydrogenation (LIU *et al.*, 2022; WANG *et al.*, 2023; ZHANG *et al.*, 2022). For example, Subramanian et al. (2009) observed that mixed CoCu particles exhibited greater selectivity towards HAs than CoCu core-shell particles, suggesting that both Co and Cu sites need to be present on the surface. Sun et al. (2018) concluded that each metal played a role in the synthesis of HAs, with Cu facilitating the activation of surface CO*; and Co contributing to hydrogenation and chain growth, identifying an ideal Co/(Co+Cu) ratio of 0.33 for CO-to-HAs reaction.

As for CO_2-to-HAs reaction, both DFT data and experimental results have revealed that an optimal Co/(Co+Cu) is needed to maintain an ideal CO* surface coverage for ethanol production (LIU *et al.*, 2022). Both Liu *et al.* (2022) and Wang *et al.* (2023) observed the highest ethanol selectivity and STY at Co/(Co+Cu) ratios of 0.5 and 0.66. Zhang and coworkers achieved a high ethanol STY with said ratio of 0.5 on Cu-CoGa catalysts (ZHANG *et al.*, 2022). In contrast, obtained high HAs selectivity, specially C_{3+}, with Co/(Co+Cu) ratio of 0.1 on Na-CoCu catalysts (IRSHAD *et al.*, 2024). A common thread across these studies is the consensus that achieving equilibrium between CH_x* and oxygenated C_1 intermediates is possible by controlling the Co:Cu ratio to favor the desired product.

In light of these findings, $Cu_{1.8}Co_{0.9}AlO_x$ exhibited the highest STY for HAs and the second-highest CO_2 conversion of all four catalysts. Hence, we opted to explore the influence of reduction temperature on this particular sample. Additionally, we chose to draw a comparison between the outcomes of $Cu_{2.6}AlO_x$ and $Co_{2.6}AlO_x$ to emphasize the unique characteristics of the Co-Cu catalyst.

4.2.2 Effect of Reduction Temperature

First, we evaluated the influence of the reduction temperature (pure H_2, 30 $ml.min^{-1}$) on the activity of $Co_{2.6}AlO_x$ and $Cu_{1.8}Co_{0.9}AlO_x$. Based on the TPR results and the literature (CORRÊA *et al.*, 2017; KIM *et al.*, 2017; PRAKRUTHI *et al.*, 2018; TEIXEIRA *et al.*, 2018), $Cu_{2.6}AlO_x$ was not tested with different reduction temperatures, since 250 °C is sufficient for the reduction and activation of copper.

The effect of different reduction temperatures on $Co_{2.6}AlO_x$ catalytic performance in the CO_2 hydrogenation towards higher alcohols is graphically represented in

Figure 4.7. Elevating the reduction temperature resulted in an increase in CO_2 conversion, with a concurrent reduction in CH_4 selectivity up to 400 °C (Figure 4.7a). Reducing $Co_{2.6}AlO_x$ at 500 °C led to a noticeable boost in CO_2 conversion, accompanied by a rise in CH_4 selectivity. The HCs and oxygenates distribution remained largely consistent between 400 to 500 °C (Figure 4.7b). However, the yield of HAs and HCs was hindered by the reduction at 500 °C (Figure 4.7c).

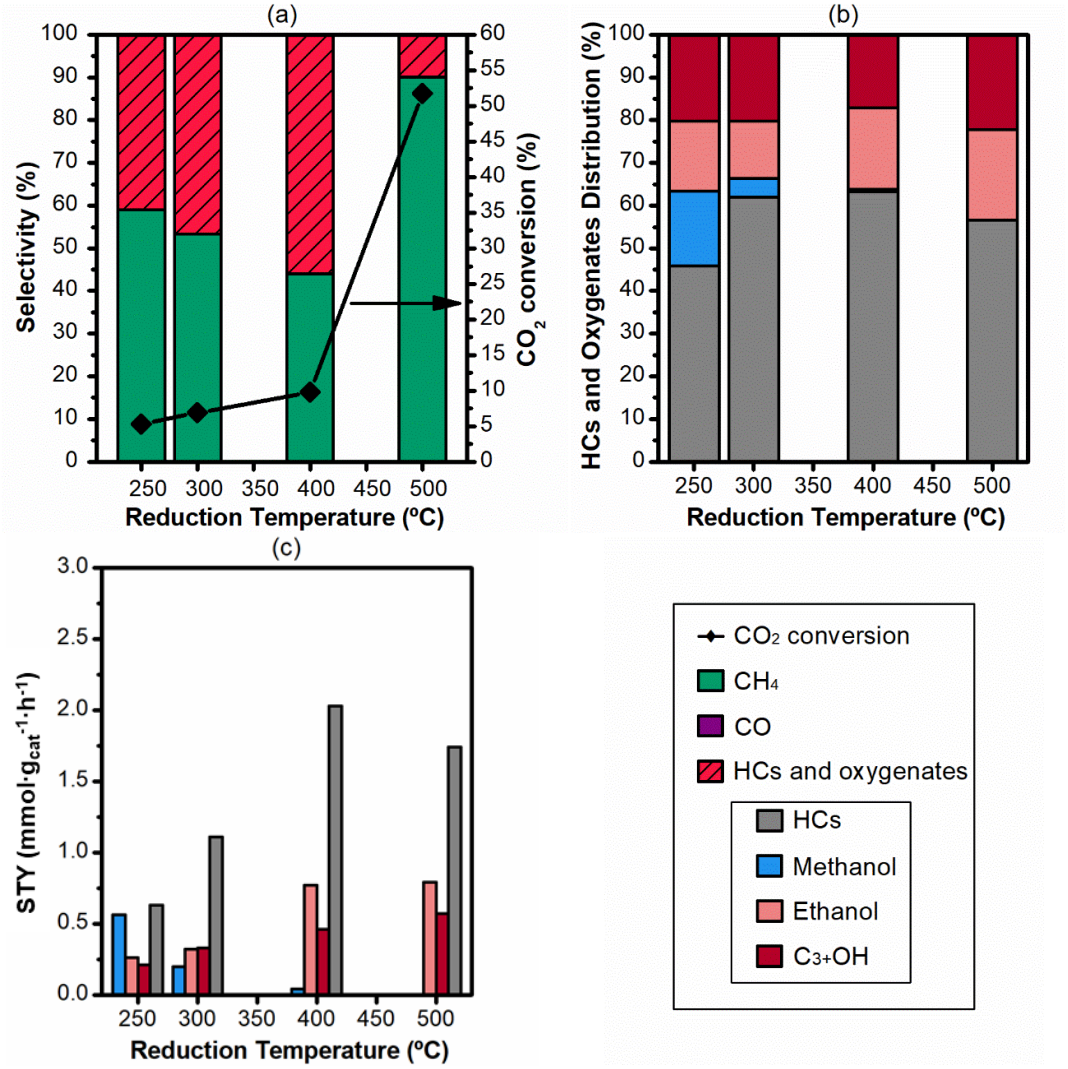

Figure 4.7 - *Effect of the reduction temperature on the selectivity and CO_2 conversion (a), HCs and oxygenates distribution (b), and the STY of products of interest (c) of $Co_{2.6}AlO_x$ (250 °C, 30 bar, H_2/CO_2 = 3, GHSV = 14200 mL·g_{cat}^{-1}·h^{-1}).*

As elaborated in the earlier discussion of the TPR analysis, at temperatures above 400 °C, it is likely that the reduction at temperatures exceeding 400 °C results in the reduction of bulk Co and the transformation of spinel-like structures (GÖBEL *et al.*, 2020; KARÁSKOVÁ *et al.*, 2020; LIMA; DIAS; PEREZ-LOPEZ, 2020). The presence of excess Co^0 and larger metallic particles can favor methanation reaction (LI *et al.*, 2018a;

WANG *et al.*, 2011), thereby justifying the observed increase in CO_2 conversion and CH_4 selectivity. Additionally, in the CO_2-TPD analyses, the profile of $Co_{2.6}AlO_x$ reduced at 500 °C exhibited remarkable desorption up until 700 °C, marking strong basicity sites, which promote methanation (LE *et al.*, 2017).

Furthermore, $Co_{1.8}Cu_{0.9}AlO_x$ underwent testing following the same reduction temperatures (250, 300, 400, and 500 °C), and its catalytic performance is presented in **Figure 4.8**.

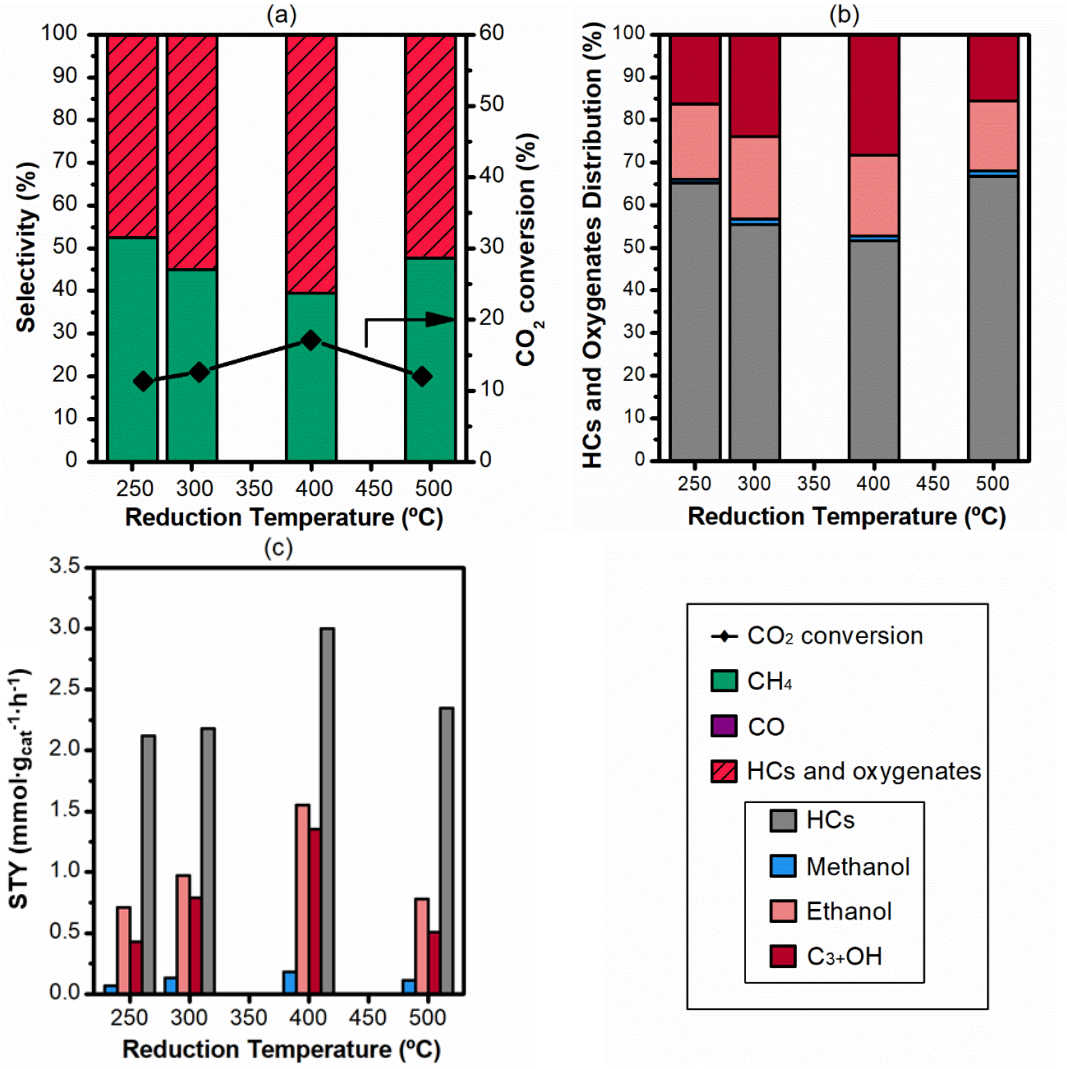

Figure 4.8 - *Effect of the reduction temperature on the selectivity and CO_2 conversion (a), HCs and oxygenates distribution (b), and the STY of products of interest (c) of $Co_{1.8}Cu_{0.9}AlO_x$ (250 °C, 30 bar, H_2/CO_2 = 3, GHSV = 14200 mL·g_{cat}^{-1}·h^{-1}).*

Similar to $Co_{2.6}AlO_x$, increasing the reduction temperature resulted in a decrease in CH_4 selectivity for $Co_{1.8}Cu_{0.9}AlO_x$ and an increase in CO_2 conversion up to 400 °C. Contrastingly, reducing $Co_{1.8}Cu_{0.9}AlO_x$ at 500 °C led to a decline in CO_2 conversion (Figure 4.8a) without any notable change in the distribution of HCs and oxygenates

(Figure 4.8b).

The highest STY of HAs achieved by the sample reduced at 400 °C, specifically 1.55 and 1.35 $mmol.h^{-1}.g^{-1}$, in that order, for ethanol and $C_{3+}OH$. This represents a substantial increase of approximately 2 and 3 times, respectively, in the yield of both higher alcohols (Figure 4.8c).

It is probable that the reduction process at temperatures exceeding 400 °C leads to an increased $Co^0/Co^{\delta+}$ ratio on the surface, which can hinder the catalyst activity (BAI *et al.*, 2017; WANG *et al.*, 2018; ZHENG *et al.*, 2019). As reported, achieving an optimal $Co^0/Co^{\delta+}$ ratio is necessary for tuning the activity and selectivity of cobalt-based catalysts in the CO_2 hydrogenation reaction (LIU *et al.*, 2023; WANG *et al.*, 2018, 2022; ZHAO *et al.*, 2020).

Moreover, these catalytic test results align with the CO_2-TPD profile for the different reduction temperatures of $Co_{1.8}Cu_{0.9}AlO_x$ (Figure 4.5). Reduction at 500 °C resulted in a halving of the calculated CO_2 uptake and the disappearance of the peak associated with moderate basicity, which is linked to ethanol selectivity (AN *et al.*, 2021) and CO_2 hydrogenation activity (AN *et al.*, 2022).

A comparison between $Cu_{2.6}AlO_x$, $Co_{1.8}Cu_{0.9}AlO_x$, and $Co_{2.6}AlO_x$ catalytic test results is shown in **Figure 4.9**, each catalyst after its best-tested pretreatment, i.e., $Co_{2.6}AlO_x$ and $Co_{1.8}Cu_{0.9}AlO_x$ reduced at 400 °C, and $Cu_{2.6}AlO_x$ reduced at 250 °C. Comparatively, the CO_2 conversions for $Cu_{2.6}AlO_x$, $Co_{1.8}Cu_{0.9}AlO_x$, and $Co_{2.6}AlO_x$ at the optimal reduction temperature were 8.8%, 17.2%, and 9.8%, in that order (Figure 4.9a). $Co_{1.8}Cu_{0.9}AlO_x$ reduced at 400 °C converted nearly twice as much CO_2 as the other two compared catalysts. Moreover, mixing Co-Cu increased the HAs selectivity (28.5%) and hydrocarbons (31.3%).

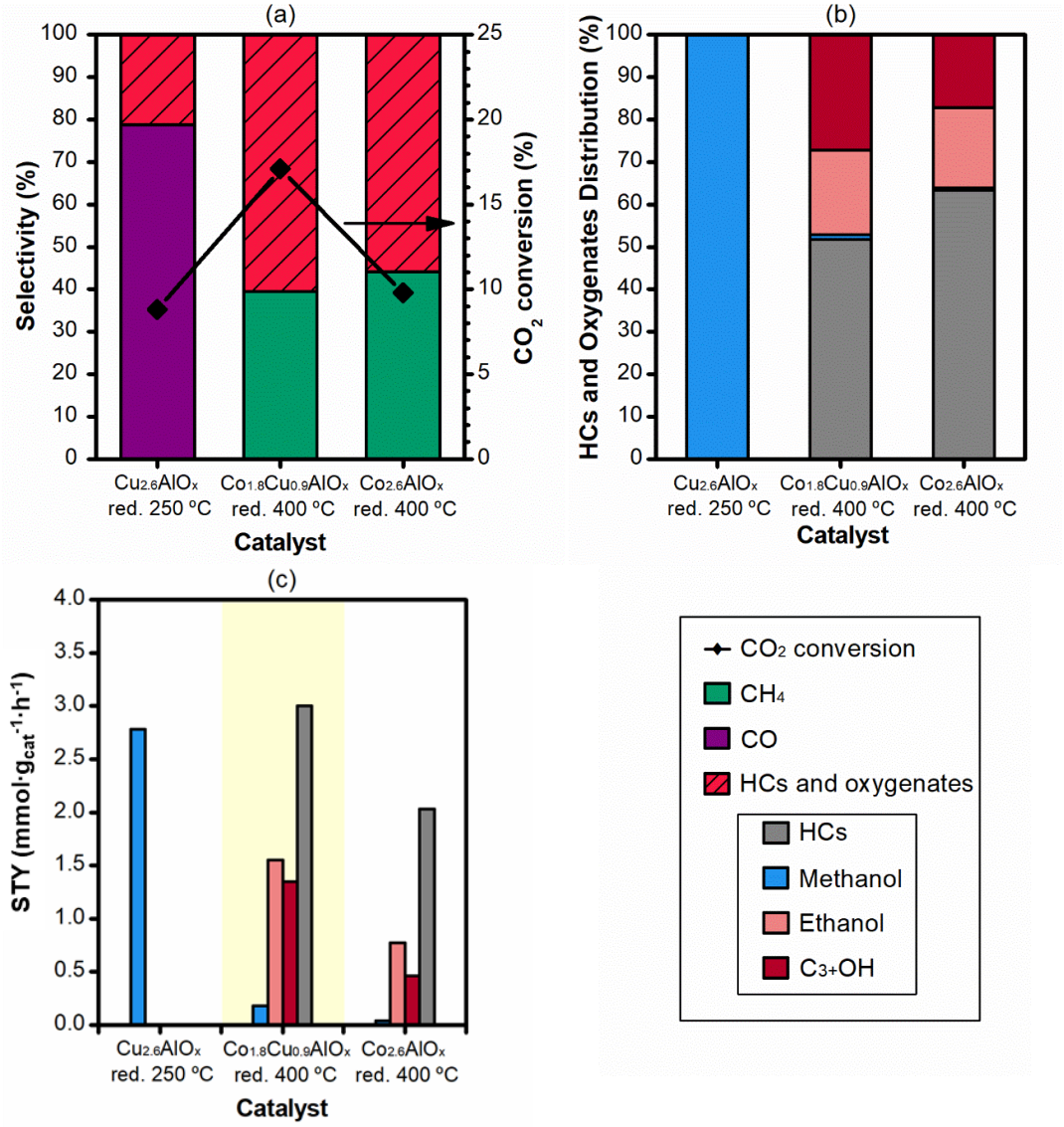

Figure 4.9 - *Comparison of the selectivity and CO_2 conversion (a), HCs and oxygenates distribution (b), and the STY of products of interest (c) of the catalysts after the best reduction pretreatment: $Cu_{2.6}AlO_x$ (250 °C), $Co_{1.8}Cu_{0.9}AlO_x$ (400 °C), and $Co_{2.6}AlO_x$ (400 °C), on the CO_2 hydrogenation reaction (250 °C, 30 bar, H_2/CO_2 = 3, GHSV = 14200 mL·g_{cat}^{-1}·h^{-1}).*

Regarding the yield of products of interest (Figure 4.9b), $Cu_{2.6}AlO_x$ reduced at 250 °C produced only methanol, circa 2.78 mmol.h^{-1}.g_{cat}^{-1}, while the Co-containing catalysts also yielded HAs (C_{2-3}) and HCs (C_{2-5}). The yield of HAs and HCs for $Co_{1.8}Cu_{0.9}AlO_x$, reduced at 400 °C, was approximately 2.90 and 3.00 mmol.h^{-1}.g_{cat}^{-1}, respectively. In that sense, $Co_{1.8}Cu_{0.9}AlO_x$ produced as much higher alcohols as $Cu_{2.6}AlO_x$ produced methanol. Henceforth, we evaluated the effect of reaction conditions of $Co_{1.8}Cu_{0.9}AlO_x$ reduced at 400 °C. Additionally, we chose to evaluate the effect of the reaction temperature on $Co_{2.6}AlO_x$ to further highlight the effect of combining Co-Cu.

4.2.3 Effect of the Reaction Temperature

To optimize HAs production, we investigated the impact of varying the reaction temperature by 50 °C, both above and below the previously used temperature of 250 °C, on the activity of Co-Al and Co-Cu-Al samples on the CO_2 hydrogenation reaction. First, we submitted the $Co_{2.6}AlO_x$ to the catalytic test, as it is shown in **Figure 4.10**.

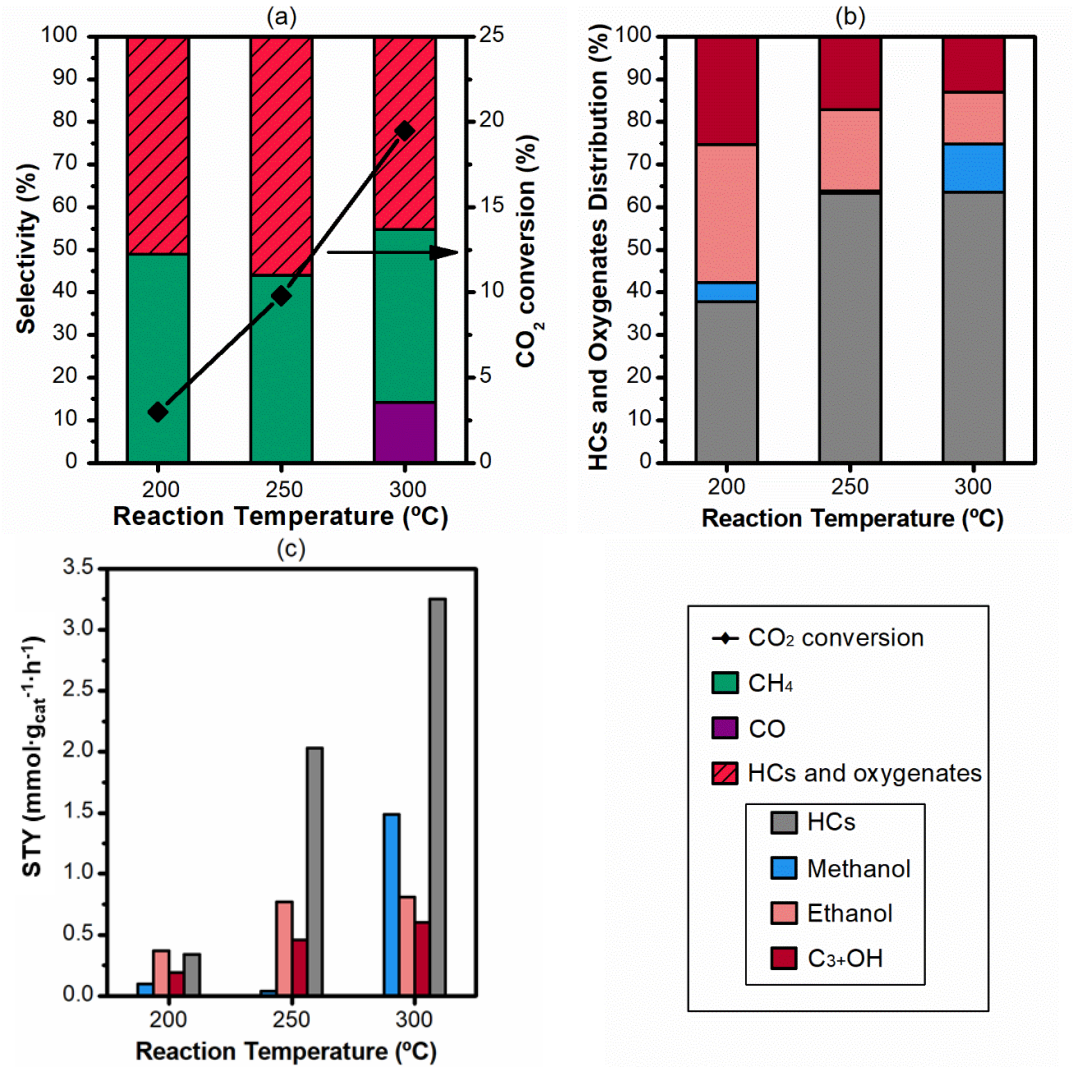

Figure 4.10 - *Effect of the reaction temperature on the selectivity and CO_2 conversion (a), HCs and oxygenates distribution (b), and the yield of products of interest (c) of $Co_{2.6}AlO_x$ reduced at 400 °C (30 bar, H_2/CO_2 = 3, GHSV = 14200 mL·g_{cat}^{-1}·h^{-1}).*

For the Co-Al catalyst, we observed an almost linear increase in CO_2 conversion as the reaction temperature was raised, going from 3% at 200 °C to 9.8% at 250 °C and further to 19.5% at 300 °C with each 50 °C increment (Figure 4.10a). However, at the highest temperature tested, $Co_{2.6}AlO_x$ displayed a decrease in selectivity towards products of interest, going from 55.9% (250 °C) to 45.2% (300 °C). The undesirable products, CH_4 and CO, constituted 40.6% and 14.2%, respectively, of the product distribution. This is noteworthy because it marks the first appearance of CO as a product

for Co-containing catalysts in our experiments, suggesting that other CO_2 conversion routes are favored at 300 °C. A notable example is the substantial increase in the yield of methanol (Figure 4.10c), which surged from 0.04 (250 °C) to 1.49 $mmol \cdot h^{-1} \cdot g_{cat}^{-1}$ (300 °C). This points to a preference for the reverse water-gas shift (rWGS) and methanol routes over direct CO_2 activation at the highest tested temperature (IRSHAD *et al.*, 2024; WANG *et al.*, 2023; ZENG *et al.*, 2021). Conversely, reducing the temperature to 200 °C favored the production of higher alcohols over C_{2+} hydrocarbons (Figure 4.10b), but the decrease in conversion makes operating at this temperature less advantageous. Consequently, for $Co_{2.6}AlO_x$, 250 °C appears to be the optimal temperature for HAs production.

Subsequently, $Co_{1.8}Cu_{0.9}AlO_x$ underwent catalytic testing at 50 °C below and above the previously employed temperature of 250 °C, as presented in **Figure 4.11**.

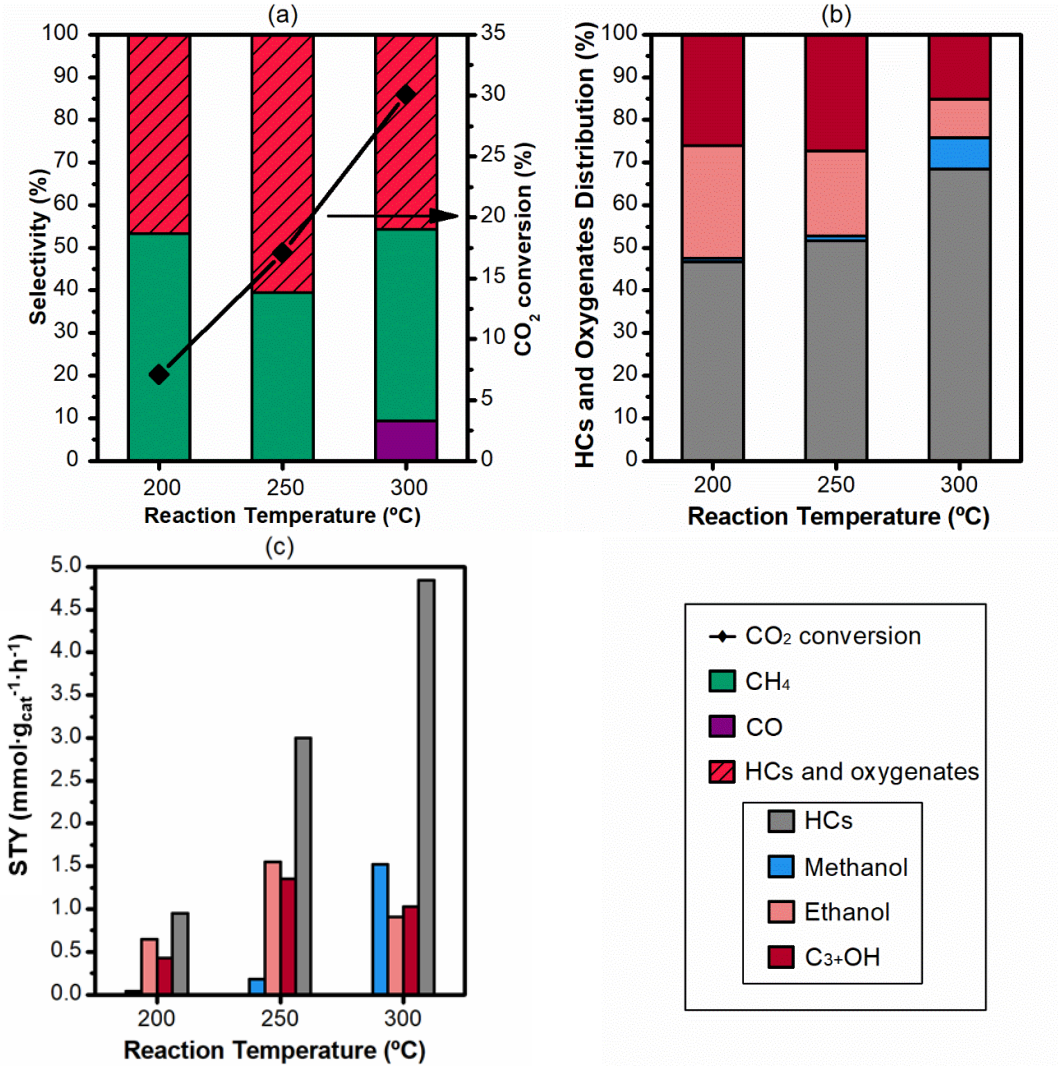

Figure 4.11 - *Effect of the reaction temperature on the selectivity and CO_2 conversion (a), HCs and oxygenates distribution (b), and the yield of products of interest (c) of $Co_{1.8}Cu_{0.9}AlO_x$ reduced at 400 °C (30 bar, H_2/CO_2 = 3, GHSV = 14200 $mL \cdot g_{cat}^{-1} \cdot h^{-1}$).*

Similar to $Co_{2.6}AlO_x$, the Co-Cu-Al catalyst displayed a direct increase in CO_2 conversion as the reaction temperature was elevated. It went from 7.1% at 200 °C to 17.1% at 250 °C and further to 30.1% at 300 °C with each 50 °C increment (Figure 4.11a). For $Co_{1.8}Cu_{0.9}AlO_x$, we also observed CO formation at 300 °C. This higher temperature favored HCs and methanol production (Figure 4.11b) but hindered HAs yield, despite the increase in conversion.

On the other hand, lowering the reaction temperature from 250 to 200 °C led to an increase in ethanol selectivity and a decrease in HCs selectivity (Figure 4.11c) at the expense of a nearly 60% reduction in CO_2 conversion. Therefore, the highest STY for ethanol and $C_{3+}OH$ was at 250 °C. In other words, much like $Co_{2.6}AlO_x$, 250 °C emerged as the optimal temperature for HAs production for $Co_{1.8}Cu_{0.9}AlO_x$.

The increase in reaction temperature can indeed lead to gains in CO_2 conversion, which may be accompanied by an increase in the yield of higher alcohols (BAI *et al.*, 2017; HE *et al.*, 2015) even when HAs selectivity is hindered by the increase in temperature (WANG *et al.*, 2018), here evidenced when reaction temperature increased from 200 to 250 °C. However, the increase in the reaction temperature can also favor the production of side products, such as CO (LIU, S. *et al.*, 2017), hydrocarbons (LIU, B. *et al.*, 2018), and methanol (HE *et al.*, 2016; ZHENG *et al.*, 2019). As reviewed by Zeng et al. (2021), most of the recently reported Co-based catalysts operate well from 140 to 250 °C, whereas the temperature for Mo-based, Rh-based, and Cu-based catalysts ranges from 200-340 °C, 240-270 °C, and 300-350 °C, respectively.

CoCu alloys (LIU *et al.*, 2022) and CoCu-supported catalysts (WANG *et al.*, 2023) prepared based on previous DFT studies were tested at 200 °C. The Cu-CoGa MMO catalyst operated at 220 °C (ZHANG *et al.*, 2022). All three studies did not explore different reaction temperatures. Irshad and coworkers, on the other hand, investigated the reaction temperature in the range of 300-350 °C on Na-CoCu catalysts and observed a volcano curve behavior with apex at 330 °C. They found that CO_2 conversion increased with temperature, while CO selectivity decreased. Interestingly, as the temperature deviated from 330 °C, the selectivity towards methane and C_{2+} HCs increased (IRSHAD *et al.*, 2024).

4.2.4 Effect of Space Velocity

In the following sections, we exclusively focused on assessing the impact of different reaction conditions on the catalytic performance of $Co_{1.8}Cu_{0.9}AlO_x$. First, we investigated the effect of space velocity on $Co_{1.8}Cu_{0.9}AlO_x$ catalytic performance by reducing the GHSV from 14200 to 10625 $mL \cdot g_{cat}^{-1} \cdot h^{-1}$, as displayed in **Figure 4.12**.

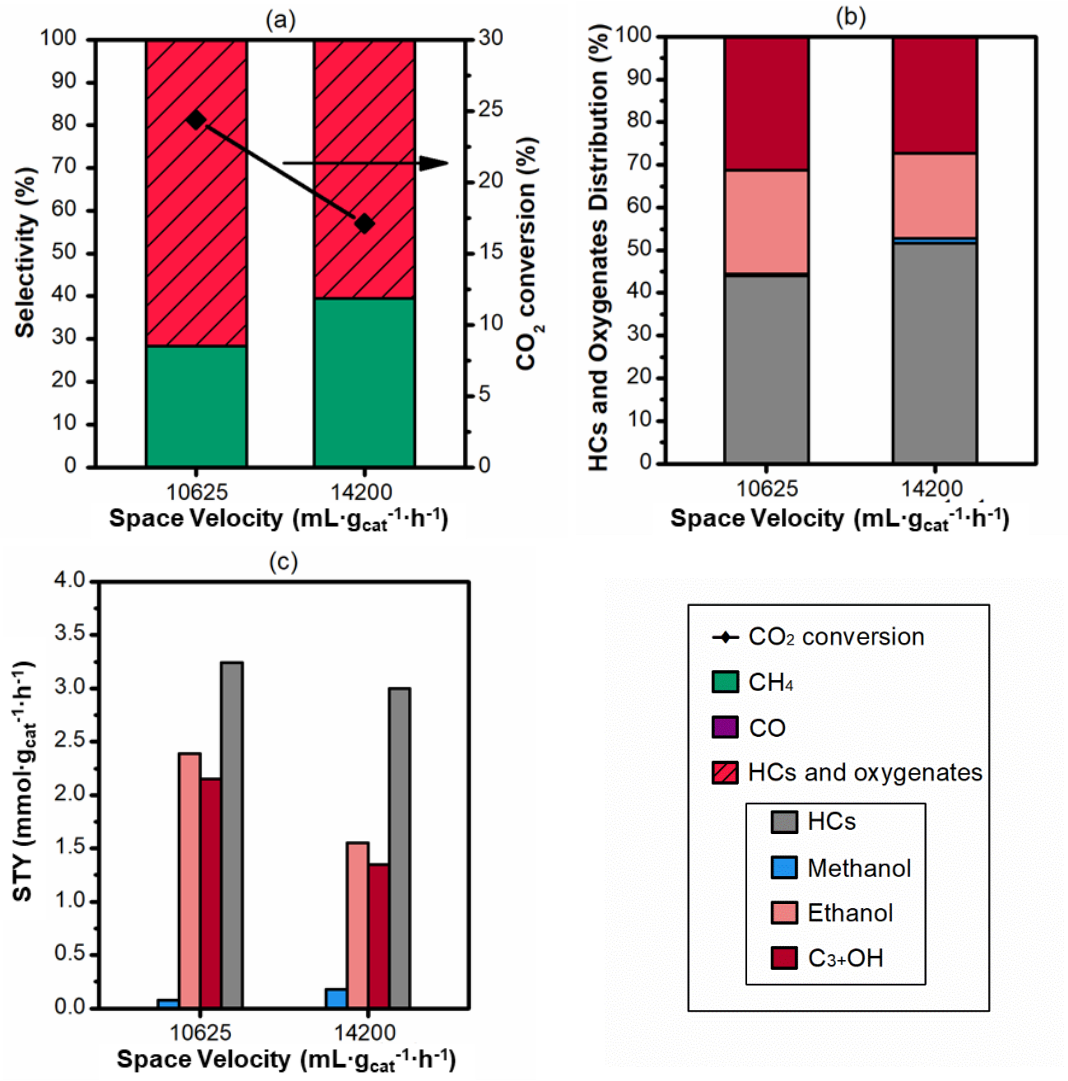

Figure 4.12 - *Effect of the space velocity on the selectivity and CO_2 conversion (a), HCs and oxygenates distribution (b), and the yield of products of interest (c) of $Co_{1.8}Cu_{0.9}AlO_x$ reduced at 400 °C (250 °C, 30 bar, H_2/CO_2 = 3).*

Overall, the decrease in space velocity was beneficial to the yield of HAs and resulted in an increase of roughly 40% in CO_2 conversion, which rose from 17.1% to 24.4% (Figure 4.12a). Additionally, this change inhibited the production of methane. Moreover, apart from the decrease in methanol selectivity, the oxygenates were favored by this reduction in GHSV, as observed in the HCs and oxygenates distribution (Figure 4.12b). It also promoted the formation of HAs, namely, the yield of ethanol and $C_{3+}OH$ increased approximately 1.5 times each, whereas HCs yield only grew 1.08 times (Figure 4.12c). In summary, the reduction in space velocity proved to be advantageous for enhancing the yield of higher alcohols.

As explained by Si et al., higher space velocity hinders CO insertion, which has slow reaction rate than the C-C coupling and hydrogenation reactions; hence lowering

the space velocity could benefit the HAs selectivity. On the other hand, lowering too much the space velocity could lead to a decrease in STY. Overall, HAs STY presents behavior similar to a volcano curve (SI *et al.*, 2022). Xu and workers also observed an increase in CO_2 conversion and a decrease in CO selectivity with the decrease in space velocity, implying that increasing the contact time further converts CO to HAs and HCs (XU *et al.*, 2021b). Irshad and coworkers reported similar trend with Na-CoCu, where a decrease in GHSV led to higher CO_2 conversion and lower CO selectivity, favoring alcohols, including methanol.

Noteworthy, $Co_{1.8}Cu_{0.9}AlO_x$ did not yield any CO at the space velocity tests and exhibited minimum selectivity towards methanol. This research, along with the study by Si et al. (2022), stands out as one of the few to successfully explore higher GHSV values maintaining high selectivity toward products of interest. This condition can be particularly interesting for practical application (SI *et al*., 2022), and to avoid deactivation, specially by water (WEBER *et al.*, 2021; YAN *et al.*, 2023).

4.2.5 Effect of H_2/CO_2 Ratio

Then, we evaluated the effect of changing the H_2/CO_2 ratio from 3 (3:1) to 1.5 (3:2) on the catalytic performance of $Co_{1.8}Cu_{0.9}AlO_x$, which can be seen on **Figure 4.13**.

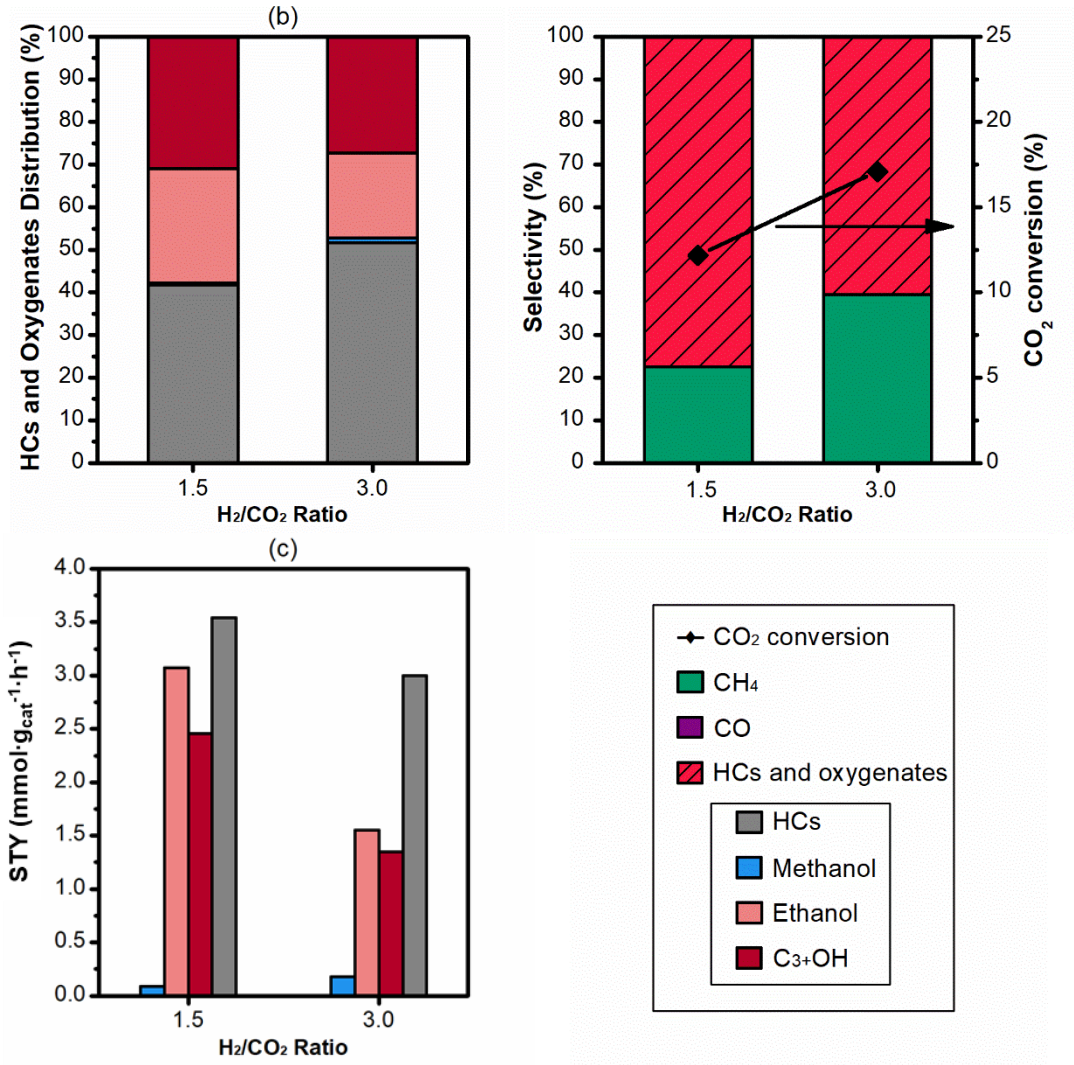

Figure 4.13 - *Effect of the H_2/CO_2 ratio on the selectivity and CO_2 conversion (a), HCs and oxygenates distribution (b), and the yield of products of interest (c) of $Co_{1.8}Cu_{0.9}AlO_x$ reduced at 400 °C (250 °C, 30 bar, GHSV: 14200 mL·g_{cat}^{-1}·h^{-1}).*

Reducing the H_2/CO_2 ratio from 3 (3:1) to 1.5 (3:2), we observed a reduction in the nominal value of CO_2 conversion from 17.1% to 12.2%, respectively (Figure 4.13a). However, decreasing the H_2/CO_2 ratio implies reducing the amount of H_2 and increasing the amount of CO_2; therefore, at an H_2/CO_2 ratio of 3:2, more CO_2 was fed to the reactor, namely 60%, more than at H_2/CO_2 ratio of 3:1. Hence, reducing the H_2/CO_2 ratio from 3 (3:1) to 1.5 (3:2) led to an increase in the amount of CO_2 converted, in terms of moles of CO_2 converted per hour at the same space velocity, here evaluated for both tests with different H_2/CO_2 ratio.

This reduction in the H_2/CO_2 ratio also inhibited methane production, decreasing CH_4 selectivity from 39.5% to 22.5%. and promoted the selectivity towards HAs, composing approximately 58% of the HCs and oxygenates distribution at H_2/CO_2 ratio of 3:2, compared to 47.1% at H_2/CO_2 ratio of 3:1 (Figure 4.13b). Furthermore, this

represents an increase of about 2 and 1.8 times, respectively, to the STY of ethanol and $C_{3+}OH$, whereas the yield of HCs increased by roughly 1.2 times (Figure 4.13c). It is reported that the increase in H_2/CO_2 ratio leads to a decrease in HAs selectivity (AN *et al.*, 2021).

However, very few works explore decreasing H_2/CO_2 ratio as it usually hinders conversion. Irshad and coworkers, similar to the present study, reported a positive effect of H_2/CO_2 ratio reduction on Na-CoCu catalysts. They found that reducing the H_2/CO_2 ratio to 1 resulted in improved HAs yield, albeit at the expense of decreased CO_2 conversion and increased CO selectivity (IRSHAD *et al.*, 2024). In turn, this behavior could be explained by the tuning of H/C species on the catalyst surface, which impacts product selectivity, for instance elevated presence of H* can favor hydrogenation of oxygenates to HCs (IRSHAD *et al.*, 2024; LI, X. *et al.*, 2023; LIU *et al.*, 2022; WANG *et al.*, 2023).

4.2.6 Stability of $Co_{1.8}Cu_{0.9}AlO_x$ Under Different Conditions

Finally, the 24 h stability profiles of $Co_{1.8}Cu_{0.9}AlO_x$ reduced at 400 °C are displayed in **Figure 4.14**.

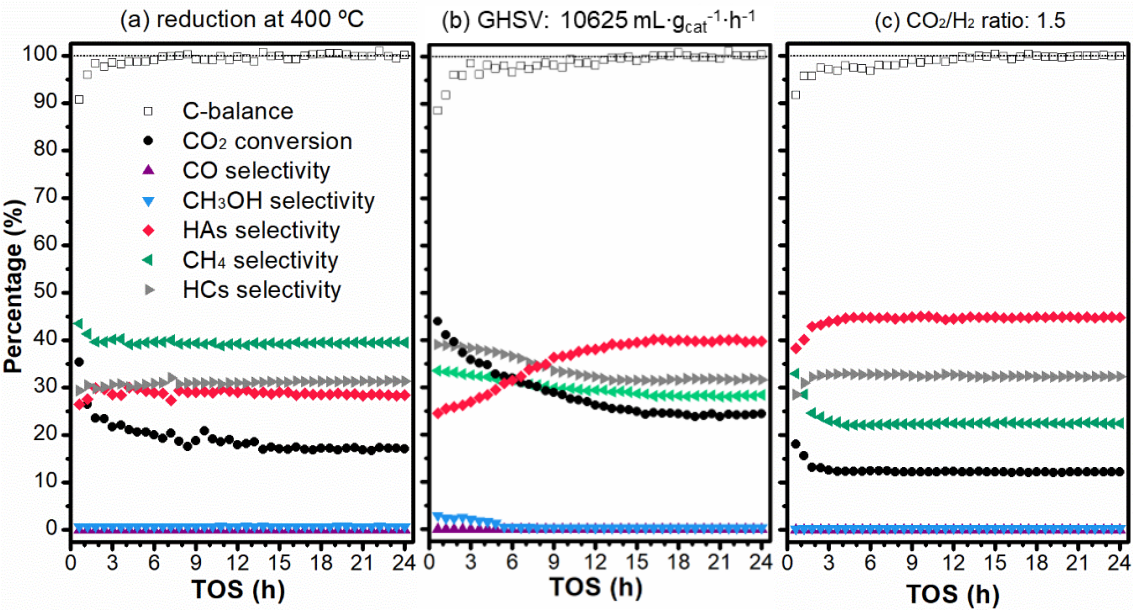

Figure 4.14 - *24 h-TOS of $Co_{1.8}Cu_{0.9}AlO_x$ reduced at 400 °C (250 °C, 30 bar) after (a) initial conditions (H_2/CO_2 = 3, GHSV = 14200 mL·g$_{cat}^{-1}$·h^{-1}); (b) decreasing GSHV (H_2/CO_2 = 3); and (c) changing H_2/CO_2 ratio (GHSV = 14200 mL·g$_{cat}^{-1}$·h^{-1}).*

In the first and last conditions, the carbon balance (C-balance) reaches 95-102% after the first 3 h of reaction, probably due to reactor wash-out after opening. $Co_{1.8}Cu_{0.9}AlO_x$, at the initial conditions (Figure 4.14a), achieves stability after 12 h of

reaction. Meanwhile, at GHSV of 10625 $mL \cdot g_{cat}^{-1} \cdot h^{-1}$ (Figure 4.14b), it took longer to reach stability. On the other hand, reducing the H_2/CO_2 ratio from 3 to 1.5 (Figure 4.14c) leads to the reactional system reaching stability right after the reactor wash-out. Additionally, after reaching stability, the CO_2 conversion and HAs selectivity did not change during the 24 h test at that condition, i.e., $Co_{1.8}Cu_{0.9}AlO_x$ did not deactivate. Considering the stability test and yield of products of interest, the H_2/CO_2 ratio change rendered the best catalytic performance for $Co_{1.8}Cu_{0.9}AlO_x$.

4.2.7 Comparison

Finally, the changes in catalytic performance resulting from each of the adjustments to enhance the HAs yield of $Co_{1.8}Cu_{0.9}AlO_x$ are depicted in **Figure 4.15**.

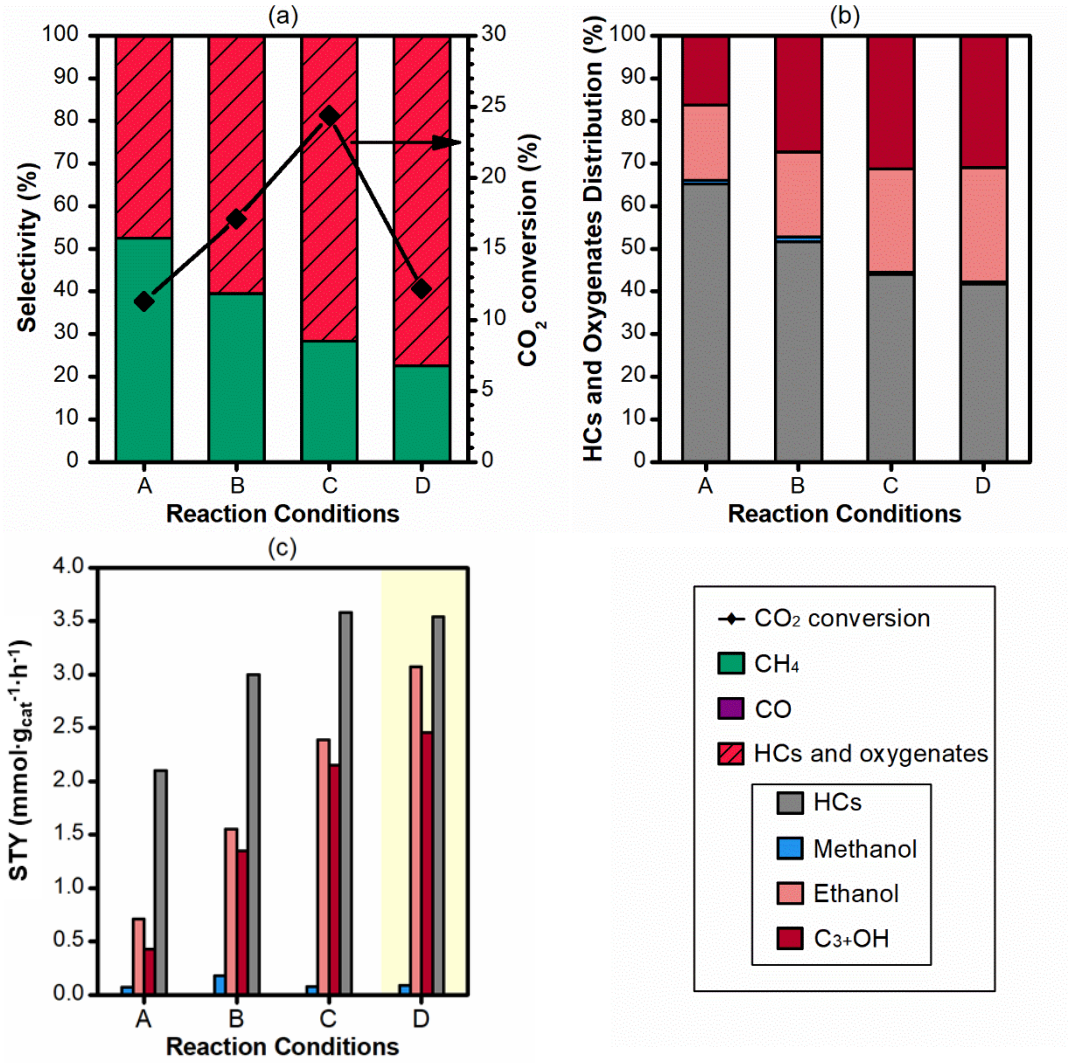

Figure 4.15 - *Comparison of $Co_{1.8}Cu_{0.9}AlO_x$ product selectivity and CO_2 conversion (a), HCs and oxygenates distribution (b), and STY (c), at 250 °C, 30 bar, H_2/CO_2 = 3, and GHSV = 14200 $mL \cdot g_{cat}^{-1} \cdot h^{-1}$ after: (A) reductive pretreatment at 250 °C; (B) reductive pretreatment at 400 °C; (C) decreasing GSHV to 10625 $mL.h^{-1}.g_{cat}^{-1}$ (H_2/CO_2 = 3); and (D) changing H_2/CO_2 ratio to 1.5 (GHSV: 14200 $mL \cdot g_{cat}^{-1} \cdot h^{-1}$).*

In short, there is a progressive decrease in the selectivity of undesired products with each adjustment made (**Figure 13a**). $Co_{1.8}Cu_{0.9}AlO_x$ reduced at 250 °C (reaction condition A) displays HCs and oxygenates selectivity of 47.5%, later increased to 60.5% by tunning the reduction temperature to 400 °C (reaction condition B). The decrease in space velocity from 14200 to 10625 mL·g_{cat}^{-1}·h^{-1} (reaction condition C) leads to HCs and oxygenates selectivity of 71.6%, whereas changing the H_2/CO_2 ratio from 3 to 1.5 (reaction condition D) raise it further to 77.5%. It is worth mentioning that very few of the reviewed works have worked with a space velocity above 6000 mL·g_{cat}^{-1}·h^{-1} (GORYACHEV *et al.*, 2021; SI *et al.*, 2022), which is usually done to minimize the selectivity of undesired products, such as CH_4 and CO and increase CO_2 conversion, yet we still managed to achieve HCs and oxygenates selectivity above 70% working above 10000 mL·g_{cat}^{-1}·h^{-1}.

Regarding the space-time yield of $Co_{1.8}Cu_{0.9}AlO_x$, after reduction at 400 °C, reaction condition B (250 °C, 30 bar, H_2/CO_2: 3, GHSV: 14200 mL·g_{cat}^{-1}·h^{-1}), the yield of ethanol was 1.55 mmol·g_{cat}^{-1}·h^{-1} (STY_{HCs}: 3.00; $STY_{C_{3+}OH}$: 1.35). After tuning the space velocity, reaction condition C (250 °C, 30 bar, H_2/CO_2: 3, GHSV: 10625 mL·g_{cat}^{-1}·h^{-1}), the ethanol STY reached 2.39 mmol·g_{cat}^{-1}·h^{-1} (STY_{HCs}: 3.24; STY_{C3+OH}: 2.15). Meanwhile, tuning the H_2/CO_2 ratio, reaction condition D (250 °C, 30 bar, H_2/CO_2: 1.5, GHSV: 14000 mL·g_{cat}^{-1}·h^{-1}), led to an ethanol STY of 3.08 mmol·g_{cat}^{-1}·h^{-1} (STY_{HCs}: 3.54; STY_{C3+OH}: 2.46).

The selectivity of $Co_{1.8}Cu_{0.9}AlO_x$ towards undesired products was one of the lowest in the current literature, meanwhile the HAs STY was one of the highest. Hence, we also compared our best results with the current CO_2 hydrogenation literature, summarized in **Table 4.4**.

Table 4.4 - *Comparison of the catalytic performance in the current literature for CO_2-to-HAs with the best results from $Co_{1.8}Cu_{0.9}AlO_x$.*

Catalyst	T (°C)	P (bar)	GHSV ([c])	R [a]	X_{CO_2} (%)	STY ($mmol \cdot g_{cat}^{-1} \cdot h^{-1}$)			Selectivity (%)						Ref.
						HCs (C_{2+})	HAs		CO	CH_4	HCs (C_{2+})	ROH			
							C_2	C_{3+}				C_1	C_2	C_{3+}	
sp-CuNaFe	310	30	28800	3	32.3	12.9*	3.32*	--	16.0*	10.0*	65.0*	--	9.0*	--	(SI *et al.*, 2022)
CZA/K-CMZF	320	50	6000	3	42.3	--	2.24 [b]		13.8	11.5*	56.1*	1.3	17.4 [b]		(XU *et al.*, 2021b)
K-Co-In_2O_3	380	40	2250*	3	36.6	--	0.49*	0.24*	80.8	4.2*	2.3*	1.6*	7.4*	3.7*	(WITOON *et al.*, 2022)
KFeRh-SiO_2	250	75	7000	3	18.4	--	0.79*	--	--	46	--	13.8	15.9	--	(GORYACHEV *et al.*, 2021)
Pd_2/CeO_2	240	30	3000	3	15.1	--	1.28*	--	--	--	--	0.8	99.2	--	(LOU *et al.*, 2021)
Cu-CoGa	220	30	6000	3	17.8	0.11*	1.35	0.06*	2.3	43.5	1.9	27.5	23.8	1.0	(ZHANG *et al.*, 2022)
$CoGaAlO_4/SiO_2$	270	30	3000	3	4.4	0.13*	0.30	--	27.3	33.4*	5.9*	13.3	20.1	--	(AN *et al.*, 2022)
Na-Co/SiO_2	310	50	6000	3	53.2	--	1.1 [b]		3.0	61.8	24.3	--	12.9 [b]		(ZHANG *et al.*, 2021)
Na-CuCo	330	40	2000	1	22.3	0.60*	0.55*	0.57*	22.3	20.0*	28.0*	2.0	8.0	19.2	(IRSHAD *et al.*, 2024)
$Co_{1.8}Cu_{0.9}AlO_x$	250	30	10625	3	24.4	3.24	2.39	2.15	0	28.4	31.6	0.3	17.3	22.4	This Work
$Co_{1.8}Cu_{0.9}AlO_x$	250	30	14200	1.5	12.2	3.54	3.08	2.46	0	22.5	32.3	0.4	20.8	24.0	This Work

* Value calculated based on the data provided by the authors.
[a] R: H_2/CO_2 ratio.
[b] HAs ($C_{2+}OH$) selectivity or STY.
[c] GHSV expressed in $mL.g_{cat}^{-1}.h^{-1}$.

Comparatively, Xu and coworkers reported a tandem catalyst composed of a CuZnAl (CZA) catalyst to favor CO formation and a K-CuMgZnFe (K-CMZF) catalyst to favor HAs formation achieving STY of 2.24 $mmol.h^{-1}.g_{cat}^{-1}$ (310 °C, 50 bar, H_2/CO_2: 3, GHSV: 6000 $mL \cdot g_{cat}^{-1} \cdot h^{-1}$) for higher alcohols (ethanol and C_{3+} oxygenates) (XU et al., 2021b). Even though the tandem catalyst displayed elevated CO_2 conversion (42.3%), the HAs selectivity (17.4%) was lower than the one displayed by of $Co_{1.8}Cu_{0.9}AlO_x$ (39.7% for reaction condition C and 44.8% for reaction condition D). Ultimately, the ethanol STY of $Co_{1.8}Cu_{0.9}AlO_x$ under both reaction conditions was similar or higher than the higher alcohol (ethanol and C_{3+} oxygenates) STY displayed by the tandem catalysts, even though it operated at a much higher pressure (50 bar).

Furthermore, Si et al. (2022) reported a sputtering CuNaFe catalyst with high STY of alkene of 680 $mg \cdot g_{cat}^{-1} \cdot h^{-1}$ and ethanol of 153 $mg \cdot g_{cat}^{-1} \cdot h^{-1}$ (310 °C, 30 bar, H_2/CO_2: 3, GHSV: 28800 $mL \cdot g_{cat}^{-1} \cdot h^{-1}$), which converts to 3.32 $mmol \cdot g_{cat}^{-1} \cdot h^{-1}$ ($MM_{ethanol}$: 46.07 $g \cdot mol^{-1}$). The ethanol STY of sp-CuNaFe was comparable to that displayed by $Co_{1.8}Cu_{0.9}AlO_x$ at reaction condition D (H_2/CO_2: 1.5). The sp-CuNaFe catalyst operates at double the GHSV of our experiments. It is also important to mention that, at reaction condition D, we reduced the amount of H_2 used in the process, thereby reducing its cost. Notably, $Co_{1.8}Cu_{0.9}AlO_x$, under certain conditions, exhibits one of the highest higher alcohols (ethanol and $C_{3+}OH$) STY of the literature, to the best of our knowledge.

Regarding catalyst with similar formulations, Zhang and coworkers conducted a study on Cu-Co-Ga-Al LDH-derived catalysts —Co/(Co+Cu) ratio of 0.5—, prepared via a co-precipitation method similar to the approach presented in this research. They focused on exploring the impact of different Ga:Co ratios and found that the catalyst with the best performance, Cu-CoGa-0.4, exhibited an ethanol selectivity of 23.8% at a CO_2 conversion of 17.8%. Additionally, this catalyst demonstrated an ethanol STY of 1.35 $mmol \cdot g_{cat}^{-1} \cdot h^{-1}$ (220 °C, 30 bar, 6000 $mL \cdot g_{cat}^{-1} \cdot h^{-1}$). Through comprehensive structural characterization and in situ FTIR data, they identified that CH_x* was formed at oxygen vacancies of defective $CoGaO_x$ species, while CO* was stabilized by Cu^+ species. The Cu^0/Cu^+–$CoGaO_x$ interfacial sites promoted the CH_x-CO* coupling and simultaneously inhibited alkylation reactions (ZHANG *et al.*, 2022).

Moreover, in a study conducted by Irshad *et al.* (2024), prepared (0.6 wt.%) Na-CoCu catalysts with a 0.6 wt.% Na content were prepared through co-precipitation, with variations in the Co/(Co+Cu) ratio. The optimal ratio was identified as 0.1. Under the optimized reaction conditions (330 °C, 40 bar, 2000 $mL \cdot g_{cat}^{-1} \cdot h^{-1}$)., the Na-CoCu catalyst achieved a CO_2 conversion of 22.3% and HAs selectivity of 27.2% ($\%S_{EtOH}$ = 8%;

$\%S_{C_{3+}OH}$ = 19.2%). HAs STY reached 1.12 $mmol \cdot g_{cat}^{-1} \cdot h^{-1}$. In-depth *in situ* characterization and DFT data unveiled that during the reaction, Co migrated to outermost surface forming NPs, CO_2 is converted to CO* via rWGS over Cu, followed by CH_x* formation and C-C coupling step over Co NPs.

Both the Cu-CoGa and Na-CoCu catalysts demonstrated notable activity in the production of HAs, with the former favoring ethanol and the latter showing a preference for C_{3+} alcohols. The CO_2 conversion and ethanol selectivity exhibited by Cu-CoGa were comparable to those of $Co_{1.8}Cu_{0.9}AlO_x$, but its methane (CH_4) selectivity was 1.5 times higher than the best result obtained in the present study. Moreover, $Co_{1.8}Cu_{0.9}AlO_x$ produced a broader range of desired products, including C2+ hydrocarbons (HCs) and C3+ alcohols. Na-CoCu overall performance, apart from conversion, was inferior to $Co_{1.8}Cu_{0.9}AlO_x$. Notably, the catalyst developed in this work demonstrated superior performance despite operating under GHSV, a condition typically associated with the generation of undesired products.

Additionally, investigations intoboth the Cu-CoGa and Na-CoCu catalysts revealed the presence of CO* and CH_x* as key intermediates, suggesting that they likely follow the CO-mediated or methanol-mediated pathway. In contrast, $Co_{1.8}Cu_{0.9}AlO_x$ only produced measurable amounts of CO at 300 °C, as the increase in temperature favors the rWGS reaction. This could be an indicative that either all the formed CO* is converted to other intermediates, or $Co_{1.8}Cu_{0.9}AlO_x$ follows a direct CO_2 activation route, such as the formate-mediated pathway.

4.3 Final Remarks

Lastly, it is essential to acknowledge that the CO_2 hydrogenation reaction to ethanol and other higher alcohols (HAs) is currently rated at TRL 2, indicating that it is transitioning from pure to applied research (CHAUVY *et al.*, 2019). Therefore, one should expect few reports on catalysts, especially non-noble-based ones, with high selectivity to ethanol or other HAs, due to the existing challenges in the CO_2 hydrogenation process. Achieving high yields of products is challenging due to the thermodynamic stability of CO_2, which often requires high temperatures, pressures, excess overpotentials, or the use of catalysts with low availability and high costs (HE *et al.*, 2023; KAMKENG *et al.*, 2021). However, progress is being made over time as new active materials demonstrate the potential to increase yield and selectivity to alcohols, making this process more feasible.

In this context, this work presents a non-noble-based catalyst that, under mild

conditions, displayed conversion rates comparable to current results while showing superior selectivity and yield towards higher alcohols, particularly ethanol. This achievement represents a significant advancement in the field and offers promising potential for the synthesis of higher alcohols from CO_2.

As we advance toward higher TRLs, it becomes crucial to consider implementation aspects, including addressing separation and recycling steps, and their impact on the process's cost and emission reduction efficiency. These factors play a significant role in ensuring the practical viability and sustainability of the CO_2 hydrogenation to higher alcohols, making it essential to explore efficient and cost-effective approaches for separation, recycling, and overall process optimization.

Chapter 05

Results and Discussion II

Understanding Co-Cu-Al Behavior in the CO_2-to-HAs Reaction

No book can ever be finished. While working on it we learn just enough to find it immature the moment we turn away from it.

— Karl Popper

The subsequent characterizations were pursued to improve the comprehension of $Co_{1.8}Cu_{0.9}AlO_x$ catalytic activity in CO_2 hydrogenation to higher alcohols. All characterizations that were acquired and analyzed within the timeframe of this thesis are presented. X-ray Absorption Spectroscopy (XAS) data is not included as additional time is required for compilation and interpretation. Further characterization efforts are essential for refining this understanding.

5.1 In Situ X-Ray Diffraction

The structural changes of the catalysts during the reduction pretreatment were investigated through *in situ* XRD experiments. Diffractograms were obtained for $Cu_{2.6}AlO_x$, $Co_{2.6}AlO_x$, and $Co_{1.8}Cu_{0.9}AlO_x$ at room temperature (RT) before reduction, after reduction at 250, 400 and 500 °C, and at room temperature after reduction at 500 °C (red. RT). The selection of reduction temperatures was based on the catalytic test results. The XRD patterns for all tested samples and temperatures are presented in **Figure 5.1**.

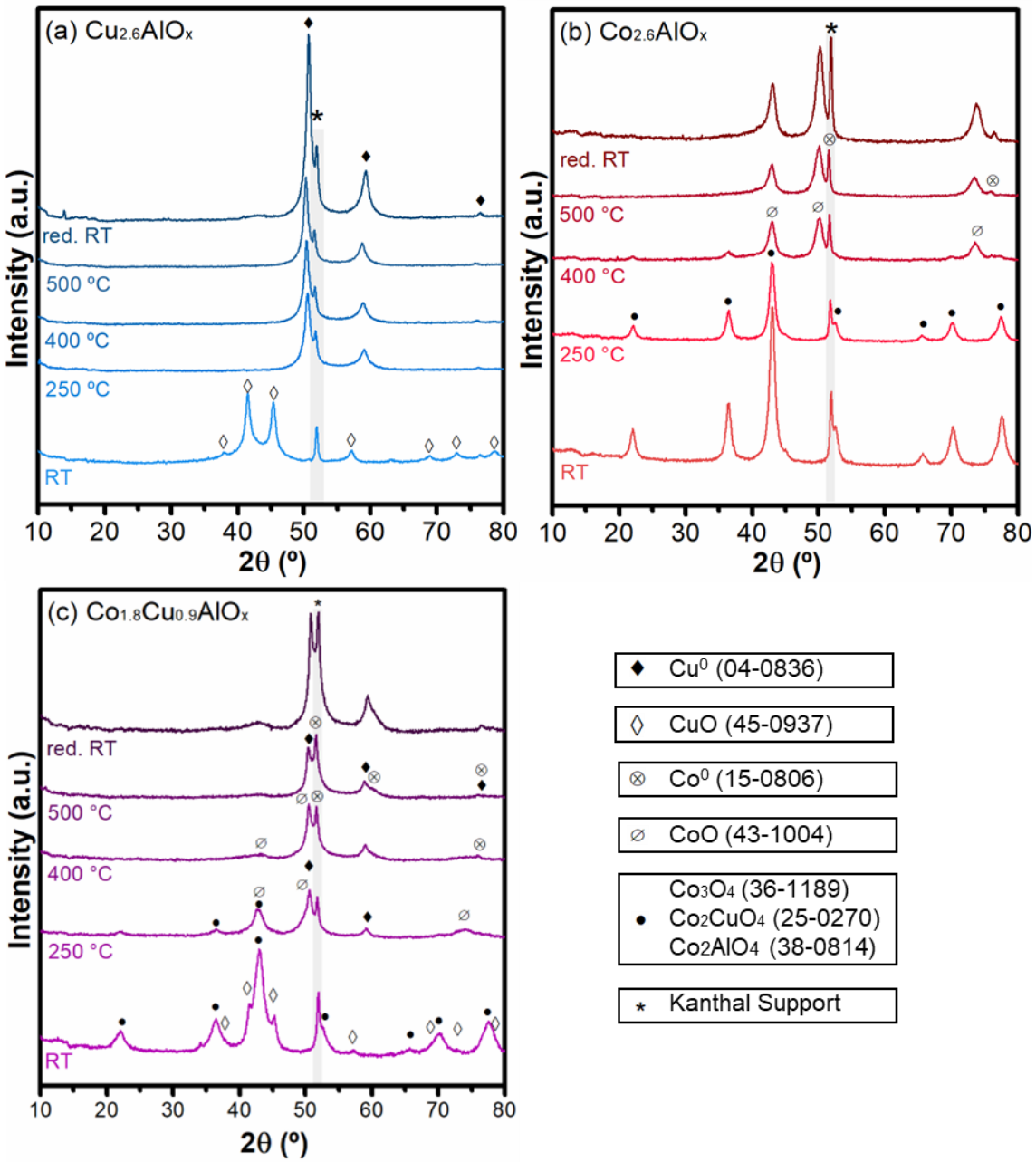

Figure 5.1 – *In situ XRD study of $Cu_{2.6}AlO_x$ (a), $Co_{2.6}AlO_x$ (b), and $Co_{1.8}Cu_{0.9}AlO_x$ (c) reduction (5 °C·min^{-1}, 3% H_2, 50 mL·min^{-1}).*

After reduction at 250 °C, only diffraction peaks attributed to Cu^0 (04-0836) are observed in $Cu_{2.6}AlO_x$ (Figure 5.1a), confirming the assumption from H_2-TPR (Figure 4.3) that the sample was fully reduced at this temperature. Beyond 250 °C, an increase in intensity in the diffraction peaks is observed, suggesting a higher degree of crystallinity or, more likely, a larger crystal size, indicating particle growth. A parallel interpretation was presented by Haddad et al. (2015) in their analysis of CuAl (Cu:Al = 1) LHD-derived catalysts reduced at 250 and 500 °C. However, there is a notable distinction: Haddad et al. observed a broad and very weak diffraction peak assigned to Al_2O_3 at 53-54°. $Cu_{2.6}AlO_x$ did not exhibit such a diffraction peak, possibly because of higher Cu:Al ratio.

For $Co_{2.6}AlO_x$ (Figure 5.1b), reduction is not apparent at 250 °C, as only one phase is identified in both RT and 250 ºC patterns. This diffraction pattern can be attributed to either Co_3O_4 (36-1189) or Co_2AlO_4 (38-0814). With the increase in temperature, the CoO (43-1004) phase becomes identifiable. The peak attributed to the Kanthal support coincides at the same position as the most significant peak from Co^0 (15-0806), making identification challenging. However, a lower intensity peak can be identified at around 74°, marking the presence of metallic Co. Wang et al. (2018) reported a similar behavior in their in situ XRD studies of the reduction of Co-Al layered double hydroxide (LDH) derived catalysts. They observed that metallic Co became the predominant phase only after the reduction at 600 °C. However, at the higher temperature tested (650 °C), a peak assigned to CoO was still present.

For $Co_{1.8}Cu_{0.9}AlO_x$ (Figure 5.1c), as discussed in the physical-chemical characterizations (section 4.1), the presence of Cu hinders the analysis as the insertion of Cu into Co structure does not shift peak position due to the similarity in atomic radii between Co and Cu. At RT, CuO (45-0937) is identified, suggesting the segregation of at least a part of Cu. Additionally, the diffraction pattern shows that either Co_3O_4 (36-1189), Co_2CuO_4 (25-0270), or Co_2AlO_4 (38-0814) could be identified, or a combination of them. At 250 °C, the latter is still present, CuO disappears giving rise to Cu^0 (04-0836), and CoO (43-1004) becomes identifiable. At 400 and 500 °C, a combination of CoO, $Cu^{0,}$ and Co^0 could be identified. The primary difference between the reduction at 400 °C and at 500 °C is in the intensity of the peaks associated with metallic Co and Cu, which increases, and CoO, which decreases. A similar interpretation was described by Göbel et al. (2020) when analyzing CoCuAl LHD-derived catalysts reduced at 350 °C.

Overall, the in situ XRD confirms that substituting Co for Cu improved the material reducibility, as observed in the TPR analysis (Figure 4.3). Unlike $Co_{2.6}AlO_x$, in $Co_{1.8}Cu_{0.9}AlO_x$, the phase attributed to Co_3O_4 (Co_2CuO_4 or Co_2AlO_4) undergoes changes after reduction at 250 °C. On the other hand, precise identification of each phase is impeded by the juxtaposition of some phases and the presence of a peak related to Kathan support. Thus, Rietveld refinement was applied to the XRD data, initially focusing on the calcined samples, as depicted in **Table 5.1** and **Figure 5.2**.

Table 5.1 – *Parameters obtained from Rietveld refinement.*

Catalyst	Identified Phase	Cell Parameters (Å)			Wt. %	Crystallite Size (Å)	χ^2
		a	b	c			
$Cu_{2.6}AlO_x$	CuO Monoclinic C2/c:b1	4.67	3.42	5.13	100 ±0.0	144.58 ±1.88	1.43
$Co_{2.6}AlO_x$	Co_3O_4 Cubic Fd-3m:2	8.08	8.08	8.08	100 ±0.0	152.11 ±1.98	1.98
$Co_{1.8}Cu_{0.9}AlO_x$	Co_2CuO_4 Cubic Fd-3m:2	8.07	8.07	8.07	97.32 ±0.0	69.47 ±0.90	1.67
	CuO Monoclinic C2/c:b1	4.69	3.41	5.14	2.68 ±0.1	2335.95 ±30.4	

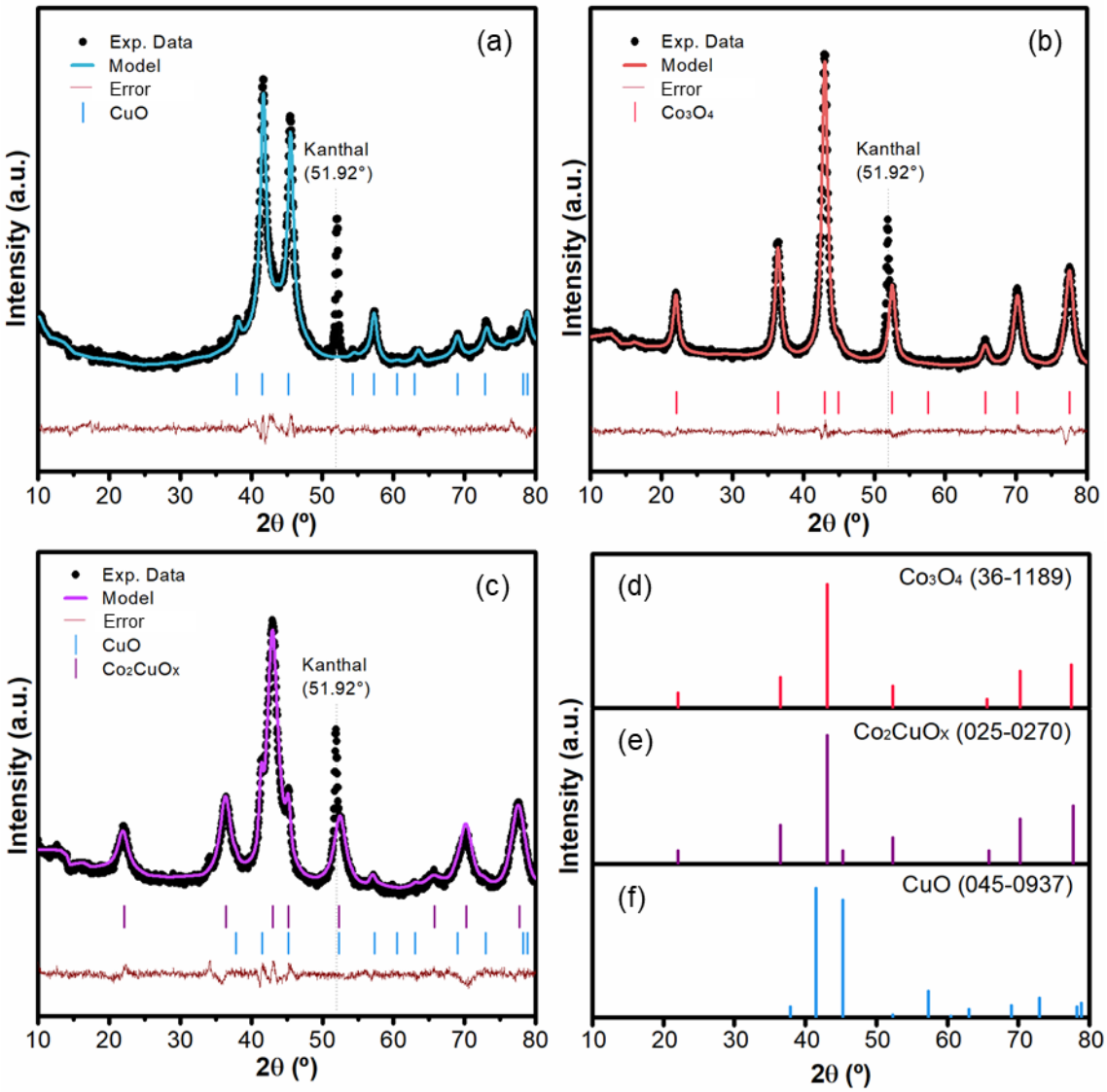

Figure 5.2 - *Rietveld refinement of XRD patterns from calcined $Cu_{2.6}AlO_x$ (a), $Co_{2.6}AlO_x$ (b), and $Co_{1.8}Cu_{0.9}AlO_x$ (c)*. Refraction pattern taken in account in the refinement (d-f).

Both $Cu_{2.6}AlO_x$ and $Co_{2.6}AlO_x$ data exhibited satisfactory fits with their respective refinement models. The Rietveld analysis confirmed the absence of a Cu-Al spinel phase in the $Cu_{2.6}AlO_x$ diffraction pattern, with only CuO (45-0937) being identified. The goodness-of-fit index (χ^2) for this sample was 1.43, indicating a good model fit. Conversely, for $Co_{2.6}AlO_x$, χ^2 was 1.98 for a fit with Co_3O_4 (36-1189) phase, and a similar result was obtained for Co_2AlO_4 (38-0814) (**Figure C.2**).

For $Co_{1.8}Cu_{0.9}AlO_x$, a favorable fit was achieved by considering Co_2CuO_4 (025-0270) and CuO (05-0937) phases, resulting in a χ^2 value of 1.67. In this iteration, the Co/(Co+Cu) ratio was 0.64 closely matching the measured ratio of 0.67 (section 4.1). The iteration considering Co_3O_4 (36-1189) and CuO (05-0937) phases (**Figure C.3**) did not display a similar fit (χ^2 = 4.71). This iteration resulted in a phase distribution of 95 wt.% Co_3O_4 and 5 wt.% CuO which contradicts the metallic content results (Table 4.1), unless Cu is predominantly amorphous. Moreover, the formation of Co-Cu MMO (Co_2CuO_4) aligns with the TEM-EDS results presented in the subsequent section.

Given that 400 °C emerged as the optimal reduction temperature in the catalytic tests for$Co_{1.8}Cu_{0.9}AlO_x$, a detailed examination of the XRD data for this specific reduction temperature is presented in **Figure 5.3**.

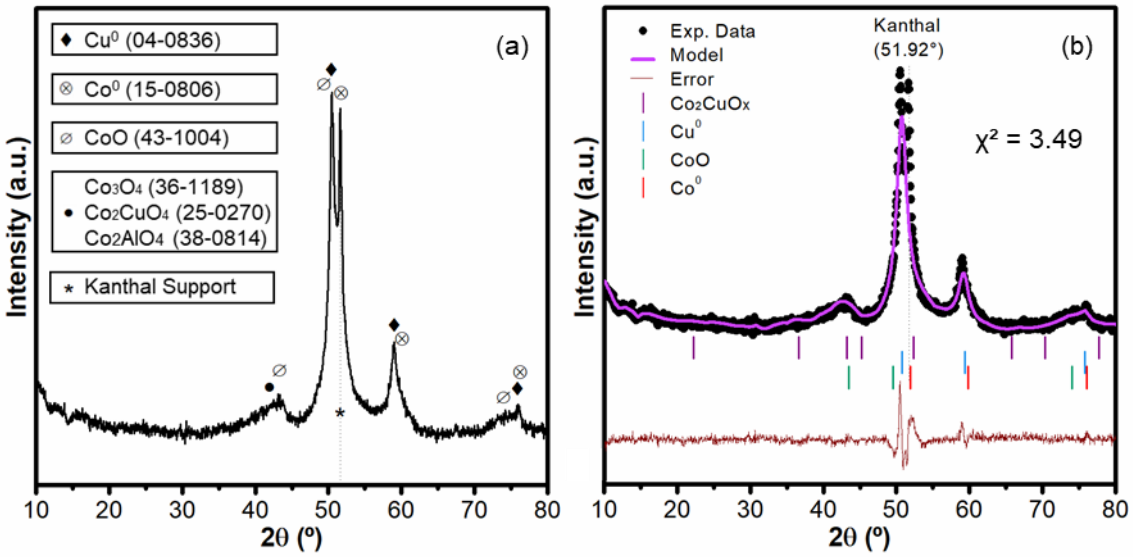

Figure 5.3 - *XRD patterns of $Co_{1.8}Cu_{0.9}AlO_x$ reduced at 400 °C (a) and its Rietveld refinement results (b).*

The analysis of the XRD data for $Co_{1.8}Cu_{0.9}AlO_x$ reduced at 400 °C posed significant challenges, as the diffraction pattern revealed multiple phases. In this iteration, we chose to fit the following phases: Co_2CuO_4 (25-0270), CoO (43-1004), Cu^0 (04-0836), Co^0 (15-0806). Based on the fit for the calcined sample and TPR analysis, we

hypothesized a sequential reduction pathway: (i) CuO would first be reduced to Cu^0; (ii) Co_2CuO_4 then undergo reduction to Cu^0 and CoO; (iii) CoO would subsequently experience partial reduction to Co^0.

This iteration resulted in a χ^2 value of 3.49, indicating a need to further refine the model. The phase distribution was 18.26 wt.% Co_2CuO_4, 25.35 wt.% CoO, 35.30 wt.% Cu^0, 21.09 wt.% Co^0, given a Co/(Co+Cu) ratio of 0.57, deviating from the original ratio. To enhance the model, the impact of temperature on the Kanthal peak should be considered. Additionally, the preferential reduction of Cu, leaving the $Co_{3-x}Cu_xO_4$ structure, must be considered. Further characterization is essential to comprehend this structure, specifically through XAS, which can provide insights into the charges involved and the chemical environment. A more comprehensive understanding of the relationship between these findings with catalytic activity, along with insights from TEM and XPS, are elaborated in section 5.4.

5.2 Electron Microscopy

First, the STEM-in-SEM analysis was exploratory in nature, and the outcomes are detailed in **Appendix C.3** (**Figure C.4 – Figure C.9**) . Herein, we delve into the scans collected using TEM. The HRTEM and EDS elemental mapping (Co, Cu, Al, and O) for $Co_{1.8}Cu_{0.9}AlO_x$ after calcination, reduction at 400 °C, and the reaction phases are presented in **Figures 5.4**, **Figure 5.5**, and **Figure 5.6**, respectively. Additional images from TEM analyses can be found in **Appendix C.4** (**Figure C.10 – Figure C.15**).

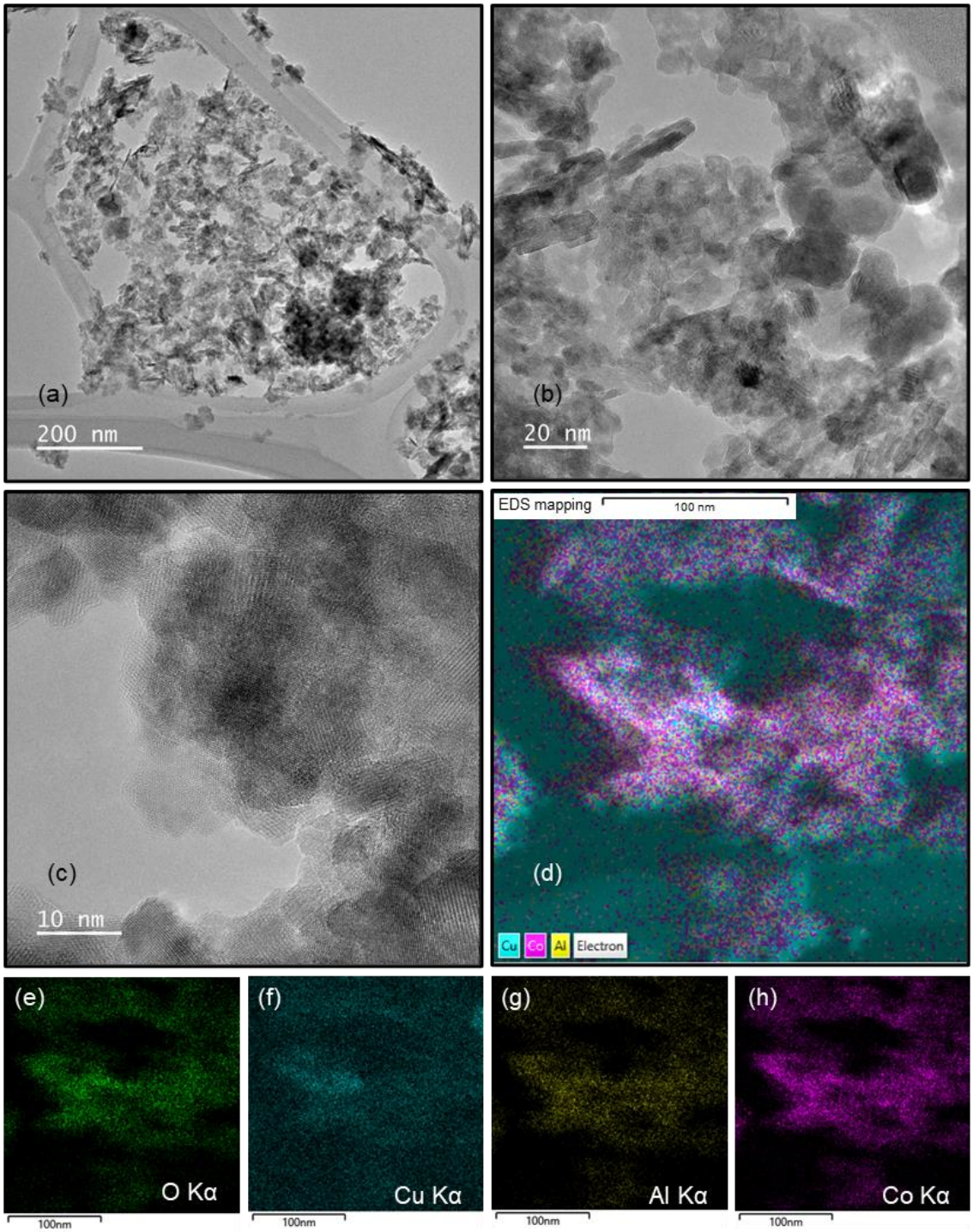

Figure 5.4 - *HRTEM imaging (a-c) and EDS elemental mapping (d-h) of calcined* $Co_{1.8}Cu_{0.9}AlO_x$.

According to electron microscope imagining, calcined $Co_{1.8}Cu_{0.9}AlO_x$ (Figure 5.4 and Appendix C.4) maintains the sheet-like shape characteristic of LHD lamellar structure, as reported for other LHD-derived oxides (FAN *et al.*, 2014; FANG *et al.*, 2021; OBEID *et al.*, 2023; SUN *et al.*, 2023; ZHANG, Z. *et al.*, 2023). Overall, at least two distinct regions were identifiable: one where the elements were more dispersed, forming

a CoCu alloy, and a second where Cu was segregated. This observation was consistent with the XRD results (Figure 5.2c).

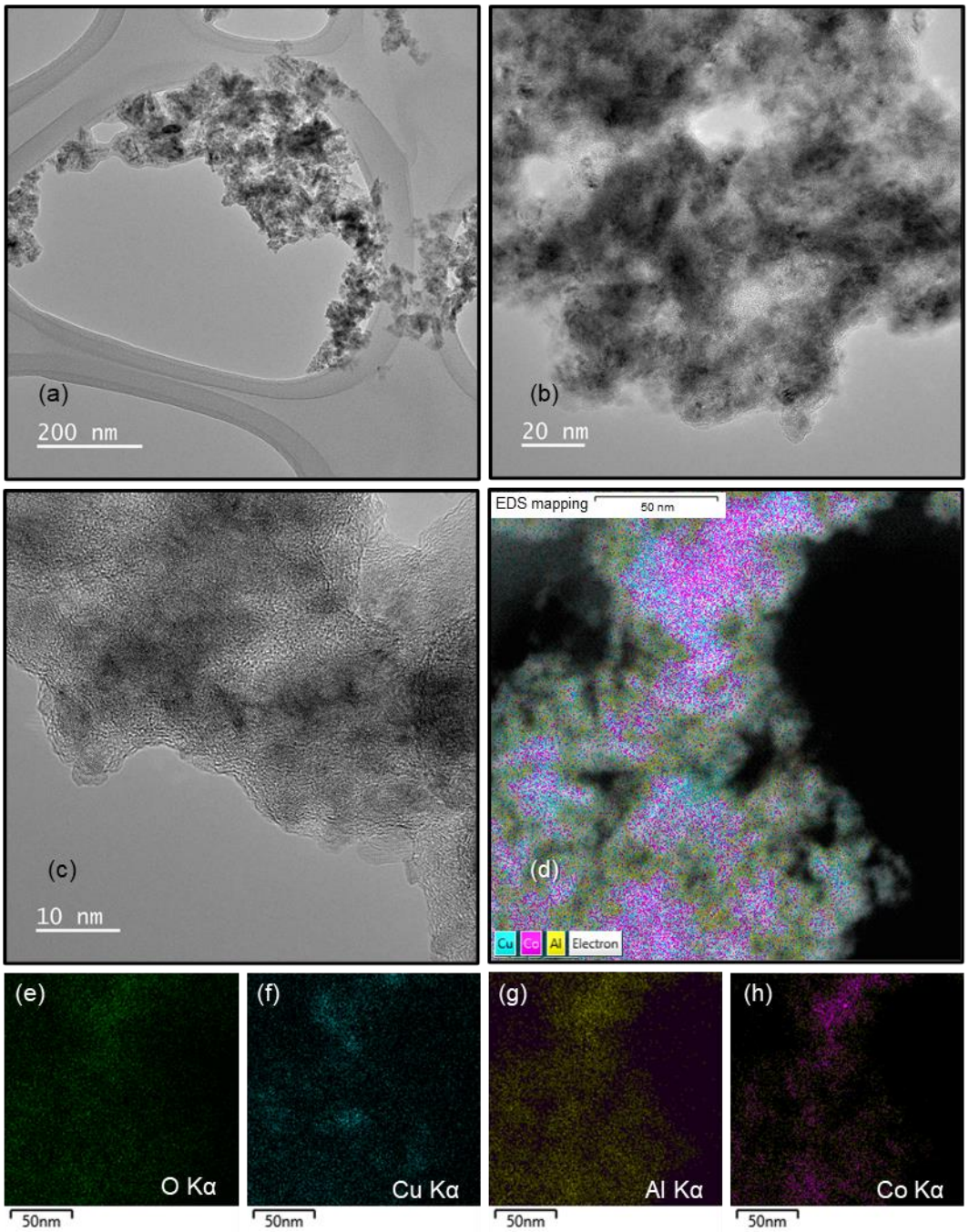

Figure 5.5 - *HRTEM imaging (a-c) and EDS elemental mapping (d-h) of $Co_{1.8}Cu_{0.9}AlO_x$ reduced at 400 °C.*

In the case of reduced $Co_{1.8}Cu_{0.9}AlO_x$, the TEM and EDS analyses (Figure 5.5 and Appendix C.4), reveal the presence of a denser region in Cu and another region where the elements are more blended.

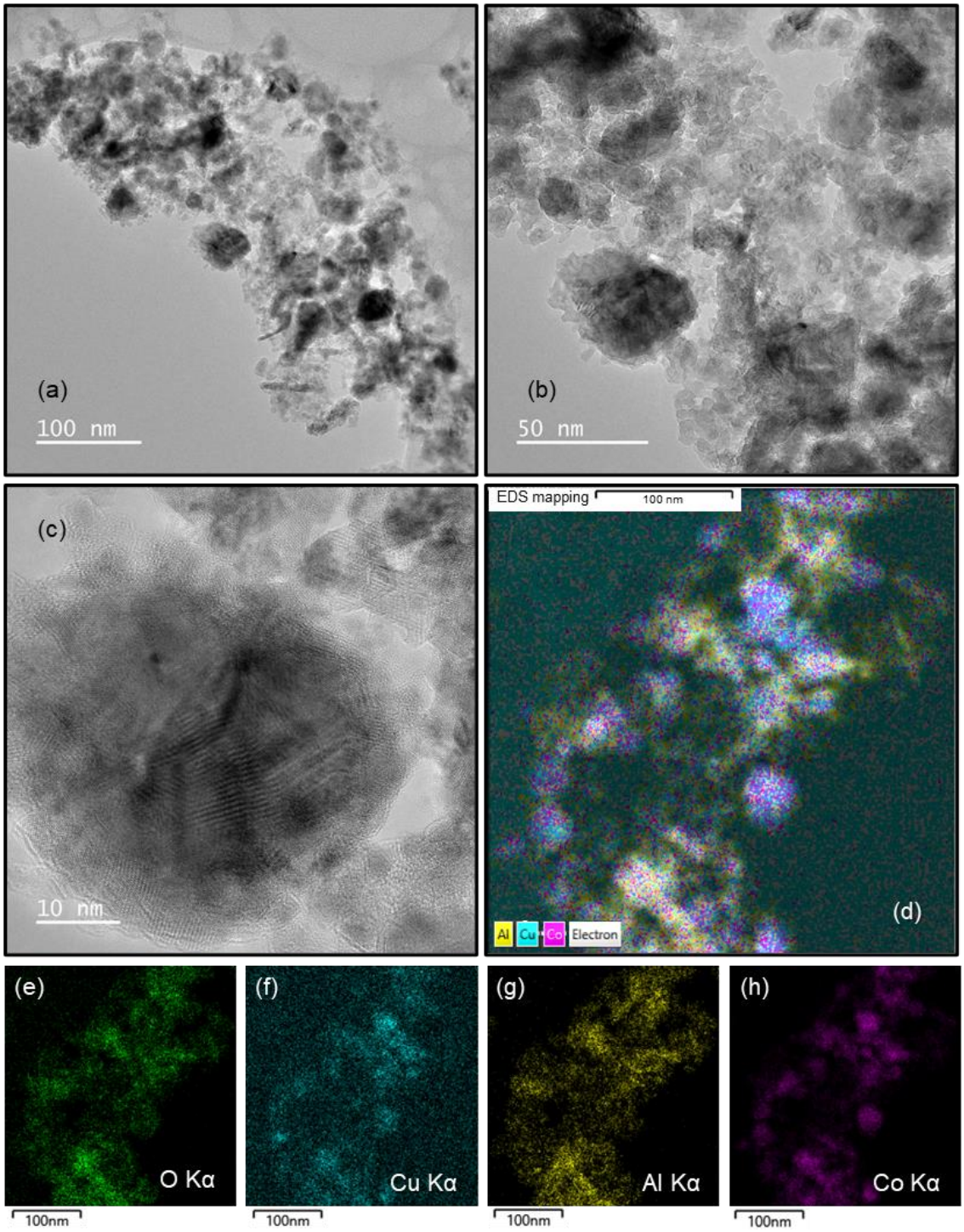

Figure 5.6 - *HRTEM imaging (a-c) and EDS elemental mapping (d-h) of $Co_{1.8}Cu_{0.9}AlO_x$ after reaction.*

Finally, the post-reaction $Co_{1.8}Cu_{0.9}AlO_x$ TEM and EDS analyses (Figure 5.6 and Appendix C.4) highlight the formation of regions or particles that are more densely populated by both Co and Cu. Interestingly, the EDS signal for Co appeared to be more intense than that for Cu, particularly when compared to the calcined and reduced samples. This suggests surface enrichment with Co, which is consistent with the XPS findings presented in the next section. This observation aligns with recently reported

CoCu catalysts used in CO_2 hydrogenation (IRSHAD *et al.*, 2024; LIU *et al.*, 2022). Moreover, the elucidation of this phenomenon is explored in the XPS section, and the implications of these results on the catalyst test outcomes are further discussed in Section 5.4.

5.3 X-Ray Photoelectron Spectroscopy

XPS experiments were carried out at the IPÊ beam-line at LNLS in Campinas, to assess and compare the surface composition of the optimal catalyst across various stages (calcined, reduced, and post-reaction) and correlate these findings with catalytic test results. However, conducting measurements under LNLS conditions posed significant challenges. As a result, the spectrum obtained from the reduced sample was deemed unreliable due to excessive charging.

5.3.1 Survey

Figure 5.7 illustrates XPS surveys of both calcined and post-reaction $Co_{1.8}Cu_{0.9}AlO_x$ samples. The depicted spectra provide insights into the elemental composition of the sample, except for K, for which no photoemission peak was detected. Each XPS band corresponding to the detected elements is accurately assigned for comprehensive analysis.

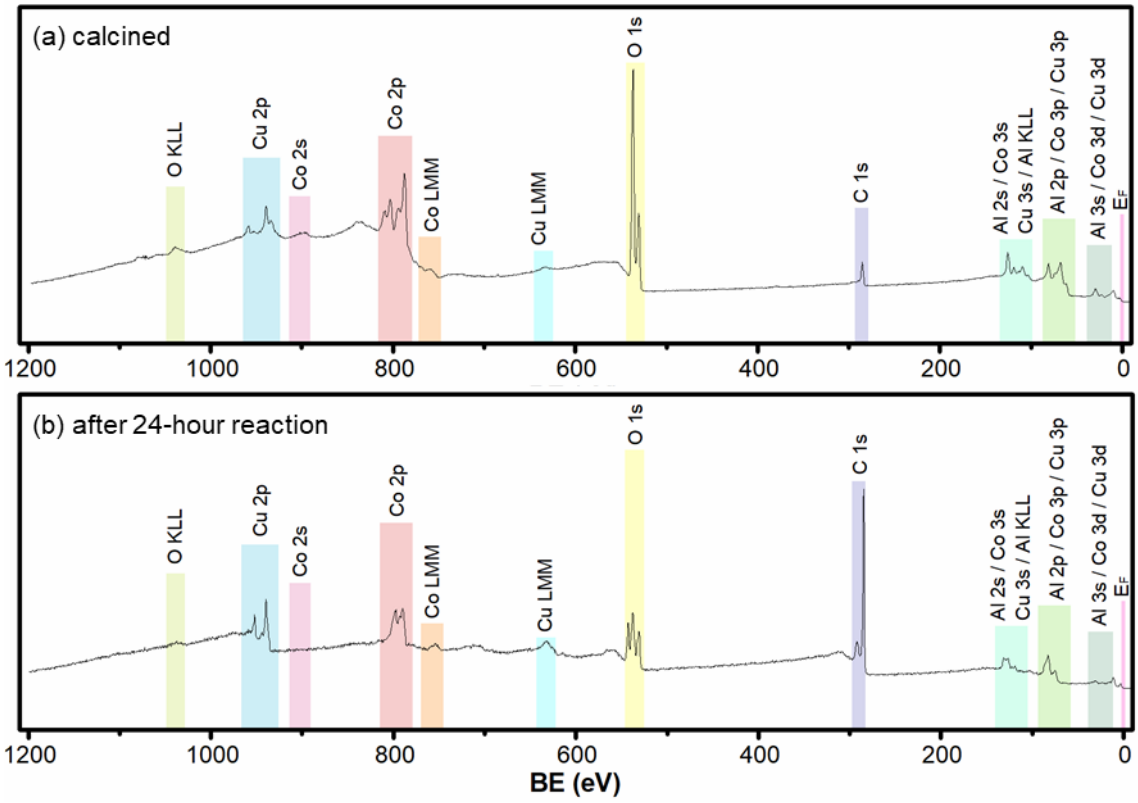

Figure 5.7 – *XPS survey of $Co_{1.8}Cu_{0.9}AlO_x$: calcined (a), and after reaction (b).*

The peak assigned to the C 1s band was expressive in both samples. However, the O 1s band exhibited noticeable differences between the two: the calcined catalyst displayed a highly intense peak, while the post-reaction band presented as a triplet. Due to issues with charging, the exploration of high-resolution spectrum for the O 1s band was ruled out. The C 1s band was absent of signals other than C-C (284.8 eV). Both spectra are presented in **Appendix C.5** for reference.

For surface composition, only Cu and Co were taken into consideration. This decision was taken due to the convolution of the Al-assigned band with other Co and Cu XPS bands. The surface composition was expressed as the Co/(Co+Cu) ratio for easy comparison with the bulk ratio (0.66). The calculation involved the 2p bands for Co (779 eV) and Cu (931 eV), considering relative sensitivity factors (R.S.F.) of 19.16 and 25.39, respectively. The resulting Co/(Co+Cu) ratio was 0.73 for the calcined catalyst and 0.83 for the post-reaction sample. This indicates an increase in cobalt concentration on the surface after the reaction, aligning with TEM-EDS imaging findings.

As reported by Kupková et al. (2023), the migration of Cu to the surface in CoCu mixed metal oxides (MMO) is commonly anticipated. Nonetheless, both Kupková and Irshad et al. (2024) identified segregation of Co on the surface through XPS and TEM imaging. In the former case, this occurred during the heat treatment of Cu-rich CoCu MMOs. In the latter case, Irshad and corwokers observed significant Cu migration during calcination and reduction, whereas a more pronounced Co migration occurred during CO_2 hydrogenation reactions. Similar phenomena were observed in this work with $Co_{1.8}Cu_{0.9}AlO_x$, as demonstrated by previously presented HRTEM imaging and XPS.

Irshad et al. (2024) attributed this behavior to the preferential adsorption of CO* (resulting from rWGS) onto Co sites, promoting Co surface enrichment, which as previously described by Liu et al. (2022). In their work, Liu and coworkers provided proof of Co surface segregation through both theoretical and experimental results. In their experimental approach, Co surface enrichment was induced via pretreatment with different partial pressures of CO.

5.3.2 Co 2p

The analysis of Cobalt via XPS is typically focused on the intense 2p region. However, like many first-row transition metals, the presence of a significant multiplet splitting complicates the deconvolution of Co compounds (BIESINGER *et al.*, 2011). In the Co 2p band, asymmetric-shaped doublet peaks are separated by 14.99 eV. Additionally, several satellite peaks emerge due to the interaction of the photoemitted

electron with others, typically positioned 3-8 eV apart from the original peak (MOULDER *et al.*, 1992).

Interpreting data from Co-based compounds exhibiting multiplet splitting poses challenges. The distinctive line shapes, however, enable fingerprint analysis, either through theoretical fits or reference spectra of standard materials (BIESINGER *et al.*, 2009, 2011; GROSVENOR *et al.*, 2005; KUMAR *et al.*, 2017). Reference spectra and the valued form theoretical fits are provided in Annex B.

Some studies on catalytic materials have adopted a simplified fit, assigning four doublets: (i) Co^0 at 778.2 eV, (ii) Co^{3+} (Co_3O_4) at 779.7 eV, (iii) Co^{2+} (CoO) at 780.1 eV, and (iv) Co^{2+} (Co_3O_4) at 782.6 eV. Deviations of ±0.2-0.3 eV from these values are common. Typically, a shake-up satellite is observed at 4±1 eV from the Co^{2+} (CoO) peak, while other satellites, often attributed to plasmon losses, are fitted at 7±1 eV from the original peak (AMRI *et al.*, 2013; BIESINGER *et al.*, 2011; GÖBEL *et al.*, 2020; IRSHAD *et al.*, 2024; KUPKOVÁ *et al.*, 2023; WAN *et al.*, 2022). This approach was adopted for the following interpretation and the Co 2p spectra of the catalyst fresh and after reaction are presented in **Figure 5.8**.

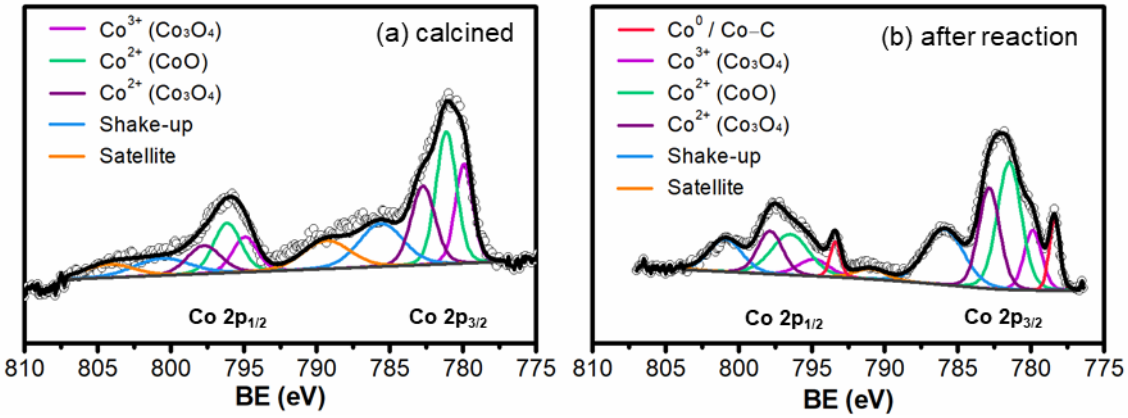

Figure 5.8 – *Co 2p spectra of $Co_{1.8}Cu_{0.9}AlO_x$: calcined (a), and after reaction (b).*

The line-shapes, or fingerprints, of the Co 2p band for $Co_{1.8}Cu_{0.9}AlO_x$ after calcination and after the reaction exhibit marked differences. The calcined sample's shape closely resembles that of other Co-containing mixed metal oxides (MMO), resembling a blend of Co_3O_4 and CoO fingerprints (IRSHAD *et al.*, 2024; KUPKOVÁ *et al.*, 2023; WEI *et al.*, 2019; ZHAO *et al.*, 2021). In fact, similar spectrum shapes have been reported for Co-Al LDH-derived catalysts (GÖBEL *et al.*, 2020; WAN *et al.*, 2022; ZHANG *et al.*, 2022).

Regarding the spectrum of the sample after the reaction, it is characterized by a more pronounced Co^{2+} (CoO) contribution and a lower binding energy peak commonly associated with Co^0. Moreover, similar profiles have been reported for spent Co-based catalysts in CO/CO_2 hydrogenation reactions (AN *et al.*, 2021; GÖBEL *et al.*, 2020; IRSHAD *et al.*, 2024; ZHANG, S. *et al.*, 2023). In essence, the catalyst after the reaction exhibits a surface enriched in Co^{2+} compared to the calcined sample. Additionally, a Co^0 component appeared in its spectrum.

It is noteworthy that the C 1s spectrum (**Appendix C.5**) does not show any component that could be attributed to C-Co, thus dismissing hypotheses of Co_2C formation leading to Co^{2+} rich surface (GÖBEL *et al.*, 2020; ZHANG, S. *et al.*, 2023). Similarly, it rules out the possibility of Co^0 peak being any type of Co-C (IRSHAD *et al.*, 2024).

5.3.3 Cu 2p

Like Co 2p, the interpretation of the Cu 2p XPS band can involve a more intricate deconvolution procedure. Alternatively, line-shape identification or other simplified deconvolution methods can be used (BIESINGER, 2017; BIESINGER *et al.*, 2007, 2010). In Annex B, reference material can be found.

For catalysts and other complex materials, the assignment of $2p_{3/2}$ peaks follows specific criteria: (i) Cu^0/Cu^+ at 932.4 eV; (ii) Cu^{2+} (CuO) at 933.6 eV; (iii) Cu^{2+} (Cu-OH) at 935.1 eV (GÖBEL *et al.*, 2020; IRSHAD *et al.*, 2024; KUPKOVÁ *et al.*, 2023; LI *et al.*, 2020; SUN *et al.*, 2021; WEI *et al.*, 2019). Notably, a pair of shake-up satellites may appear in the presence of Cu^{2+}, and their distances from the original peak and from each other often provide information about the material's structure or ligands. In general, Cu 2p has a doublet separation of 19.75 eV (BIESINGER, 2017; BIESINGER *et al.*, 2007, 2010). This approach was adopted for the following interpretation and the Cu 2p spectra of $Co_{1.8}Cu_{0.9}AlO_x$, both fresh and after the reaction, are depicted in **Figure 5.9**.

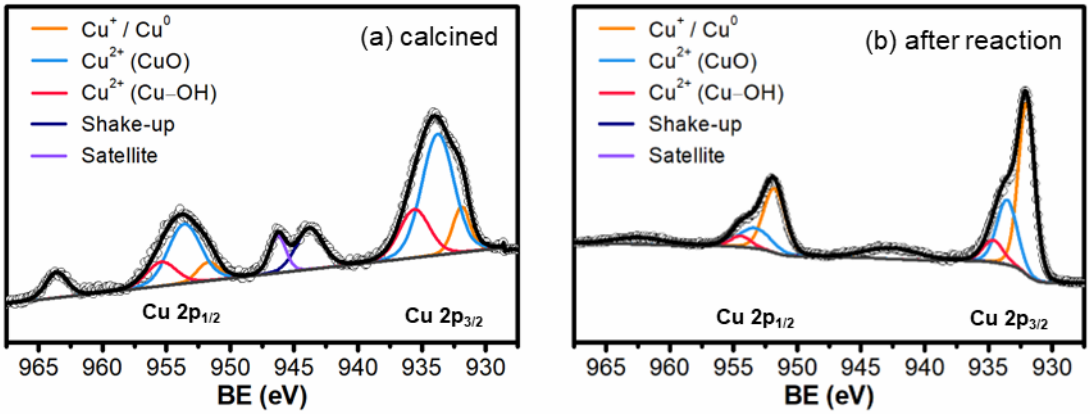

Figure 5.9 – *Cu 2p spectra of $Co_{1.8}Cu_{0.9}AlO_x$: calcined (a), and after reaction (b).*

Like Co 2p spectra, the line-shapes of the Cu 2p band exhibit significant distinctions between the calcined and post-reaction catalyst. The calcined sample revealed a prominent Cu^{2+} peak, consistent with findings in other reported Cu-containing catalysts (GÖBEL *et al.*, 2020; HADDAD *et al.*, 2015; IRSHAD *et al.*, 2024; KUPKOVÁ *et al.*, 2023; LI *et al.*, 2020; WEI *et al.*, 2019). Additionally, it displayed a shoulder at a lower binding energy (~932 eV), attributed to Cu^{+}/Cu^{0}. This presence could be associated with dispersed Cu, which is more prone to reduction to Cu_2O/Cu by the X-ray beam or other external sources (KUPKOVÁ et al., 2023).

In the post-reaction sample, an intense Cu^{+}/Cu^{0} peak was evident, while the shoulder at a higher binding energy (~938 eV) indicated the presence of some Cu^{2+}. Similarly, spent catalysts used in CO/CO_2 hydrogenation have shown an increase in the Cu^{+}/Cu^{0} peak and a decrease in Cu^{2+} (GÖBEL *et al.*, 2020; IRSHAD *et al.*, 2024; SI *et al.*, 2022). Overall, the comparison between the fresh and spent samples suggests partial reduction during the reaction. However, it is crucial to note that, according to the literature, the reduction of Cu-based catalysts happens during pretreatment, with partial reoxidation during the CO/CO_2 hydrogenation reaction (GÖBEL *et al.*, 2020; IRSHAD *et al.*, 2024).

5.4 Linking Findings and Catalytic Activity

The *in situ* XRD study revealed the presence of both CoO and Co^0 phases in $Co_{1.8}Cu_{0.9}AlO_x$ after reduction at 400 °C, and the Cu^0 was phase also detected. It is also likely that one or more non-reduced Cu/Co-depleted spinel phases ($Co_xCu_yO_4$, $Co_xCu_yAlO_4$, and Co_xAlO_4) coexist with the other detected phases. These findings are supported by TEM imaging and EDS mapping of the catalyst. After reduction at 500 °C, a decrease in the intensity of the diffraction peak at 44°, attributed to CoO, was observed. This finding substantiates the hypothesis that the change observed in product selectivity comparing $Co_{1.8}Cu_{0.9}AlO_x$ reduced at 400 and 500 °C (Figure 4.8) was due to a decrease in the $Co^{\delta+}$ content.

Recent studies have consistently highlighted a close relationship between the Co/CoO (Co^0/Co^{2+} or $Co^0/Co^{\delta+}$) ratio and the catalyst activity and selectivity in CO_2 hydrogenation. In fact, they point to the Co^0-$Co^{\delta+}$ interface as active sites for higher alcohol production (AN *et al.*, 2021, 2022; IRSHAD *et al.*, 2024; LIU *et al.*, 2023; WANG *et al.*, 2018; ZHANG *et al.*, 2022; ZHAO *et al.*, 2021). Spinel phases formed from Co and other metals have also been reported to participate in this reaction in varying roles (AN

et al., 2022; SHAO *et al.*, 2023; WANG *et al.*, 2018; WANG, L. *et al.*, 2019; ZHANG *et al.*, 2022).

The presence of Co^{2+} is further confirmed by XPS Co 2p analysis of the calcined and post-reaction $Co_{1.8}Cu_{0.9}AlO_x$ samples. In the post-reaction sample, a Co^0-related peak was also detected. The presence of Co^0 and $Co^{\delta+}$ may elucidate its activity. An et al. (2022) observed, for instance, that samples with low to moderate $Co^0/Co^{\delta+}$ ratios were more selective towards ethanol.

Regarding Cu 2p, the spectrum of the post-reaction sample indicates the presence of both Cu^0 and $Cu^{\delta+}$. However, the actual content of Cu^0 could not be determined, as Cu^+ and Cu^0 cannot be differentiated on the Cu 2p spectrum. The Cu Auger LMM spectrum should be referenced for this purpose. Zhang et al. (2022) identified partially reduced Cu NPs (Cu^+–Cu^0) as active sites for CO_2 hydrogenation to ethanol over LHD-derived Cu-Co-Ga-Al catalysts.

Finally, combining the findings from XPS surface composition and EDS elemental mapping, it was possible to infer Co surface enrichment during the reaction, likely related to surface CO* preferential adsorption onto Co sites (IRSHAD *et al.*, 2024; LIU *et al.*, 2022). Irshad and coworkers observed high segregation of Co decorating the Cu surface on a Cu-rich CoCu alloy catalyst, leading to $C_{3\text{-}4}$ alcohol production. In contrast, Liu and coworkers observed both theoretically and experimentally that moderate Co segregation is beneficial for ethanol production. Other studies have observed Co segregation from MMOs (AN *et al.*, 2021, 2022) and Cu segregation from CoCu MMO (ZHANG *et al.*, 2022) during CO_2 hydrogenation to HAs. All the above-cited studies emphasized that CO_2 conversion to higher alcohols should occur at the interface between Co–Cu or Co–MMO, balancing the CO* stabilization, C–O scission, CH_x* formation, and C–C coupling steps.

Chapter 06

Conclusion

If you want to have good ideas, you must have many ideas. Most of them will be wrong, and what you have to learn is which ones to throw away.

— Linus Pauling

6.1 Final Considerations

In summary, the partial substitution of Co for Cu, Cu improve MMO reducibility, decreasing the temperature of reduction (H_2-TPR). The combination of Co and Cu resulted in catalysts with more prominent moderate basicity pofile (CO_2-TPD), thereby rendering the Co-Cu MMO more active compared to their monometallic counterparts in the catalytic tests for CO_2 hydrogenation to higher alcohols. Notably, the $Co_{1.8}Cu_{0.9}AlO_x$ catalyst emerged as the most promising candidate for further investigation at this stage.

Similarly, the investigation into the effect of reduction temperature mirrored the trend observed with the Co-Cu substitution. The increase in moderate basicity profile up to 400 °C (CO_2-TPD) corresponded to improved CO_2 conversion and selectivity toward HAs in catalytic tests. Consequently, 400 °C was identified as the optimal reduction temperature for $Co_{1.8}Cu_{0.9}AlO_x$.

Exploring reaction conditions revealed that 250 °C represented the best-tested temperature, striking a balance between conversion and HAs selectivity within the tested range. That is, the increase in temperature is accompanied by increased conversion at the cost of HAs selectivity. The decrease in space velocity was found to favor both conversion and HAs selectivity, warranting further investigation. Additionally, a lower H_2/CO_2 ratio proved favorable to HAs yield.

Under the optimum conditions (250 °C, 30 bar, 14200 $mL \cdot g_{cat}^{-1} \cdot h^{-1}$, $H_2/CO_2 = 1.5$), $Co_{1.8}Cu_{0.9}AlO_x$ exhibited a CO_2 conversion of 12.2% and a selectivity toward products of interest of 77.5% ($\%S_{CH_4} = 22.5\%$). Notably, this represents one of the highest selectivity towards products of interest from a earth abundant metal-based catalyst. The HAs selectivity reached 44.8% ($\%S_{EtOH} = 20.8\%$ and $\%S_{C_{3+}OH} = 24\%$). This translates to a HAs STY of 5.54 $mmol \cdot g_{cat}^{-1} \cdot h^{-1}$ ($STY_{EtOH} = 3.08$ and $STY_{C_{3+}OH} = 2.46$) being on the highest reported HAs STY,to the best of our knowledge. The yield of C_{2+} HCs was not negligible, 3.54 $mmol \cdot g_{cat}^{-1} \cdot h^{-1}$, mainly C_2 and C_3.

The overall performance of $Co_{1.8}Cu_{0.9}AlO_x$ surpasses existing literature, in some level, positioning it as a catalyst with significant potential for future applications. This among the very few catalysts to operate with significant activity for CO_2-to-HAs at higher space velocities, which can be advantageous for practical applications leading to higher yield over time, and to avoid some types of deactivations. Furthermore, this is also among the very few works to explore a lower H_2/CO_2 ratio, which, not only can decrease the cost of the process associated but also helps balancing the ratio of H/C surface species to favor CO-insertion, C-C coupling over hydrogenation steps.

A more comprehensive investigation of $Co_{1.8}Cu_{0.9}AlO_x$ through *in situ* XRD, TEM imaging, EDS mapping, and XPS analyses has provided valuable insights into its structural evolution and surface composition after pretreatment and after CO_2 hydrogenation reaction. XRD analyses revealed the coexistence of CoO, Co^0, and Cu^0 phases, along with potential non-reduced spinel phases in the main catalyst after reduction at 400 °C. Subsequent reduction at 500 °C resulted in a decrease in the CoO phase and the potential spinel phases, aligning with the loss in higher alcohol selectivity observed in the catalytic test. The correlation between the Co^0–$Co^{\delta+}$ sites and catalyst performance, particularly in higher alcohol production, has been consistently emphasized in recent studies. Furthermore, $Co_{1.8}Cu_{0.9}AlO_x$ displays both Co^0 and $Co^{\delta+}$ species on their surface after reaction, as underlined by XPS.

Notably, XPS and TEM-EDS analyses revealed surface Co enrichment in the post-reaction $Co_{1.8}Cu_{0.9}AlO_x$ sample, hinting at preferential adsorption of surface CO* onto Co sites. This phenomenon aligns with observations from recent literature, emphasizing the intricate balance required at the Co–Cu or Co–MMO interface for efficient CO_2 conversion to higher alcohols. However, more in-depth characterization is required to close the gaps in understanding the behavior of K-Co-Cu-Al catalysts.

In conclusion, this research represents an advance in CO_2 hydrogenation to higher alcohols. Combining Co and Cu improves the catalyst's reducibility and results in

a more active MMO, as such, CoCu-based catalysts emerge a potential catalyst from HAs synthesis. At the identified optimal conditions, with $Co_{1.8}Cu_{0.9}AlO_x$ showcased exceptional HAs space-time yield, surpassing existing literature. The present study followed a recent trend in exploring higher space velocities and a lower H_2/CO_2 ratio, offering practical advantages, and revealing a catalyst with potential for future applications. The comprehensive structural analyses contribute to a deeper understanding of the structural and compositional dynamics governing the catalytic behavior of $Co_{1.8}Cu_{0.9}AlO_x$, providing a foundation for future advancements in catalyst design and optimization for CO_2 hydrogenation applications.

6.2 Recommendations for Future Work

As a natural progression from the findings of this study, a series of additional characterizations on $Co_{1.8}Cu_{0.9}AlO_x$ is recommended. Initiating with an in-depth analysis of X-ray Absorption Near Edge Structure (XANES) data obtained at the National Laboratory of Synchrotron Light (LNLS) will provide valuable insights into the chemical state and environment of the elements within the sample. The High-Resolution Transmission Electron Microscopy (HRTEM) and Selected Area Electron Diffraction (SAED) data presented in the Appendix should be thoroughly examined, as these datasets hold the potential to unveil intricate details about the localized crystalline structure of the catalyst. Although included or mentioned in this thesis, these datasets were not explored due to time constraints.

Additionally, Diffuse Reflectance Infrared Fourier Transform Spectroscopy (DRIFTS) experiments should be conducted to unravel the interaction of CO_2 and H_2 with $Co_{1.8}Cu_{0.9}AlO_x$ and the key reaction intermediates formed. A revisit to X-ray Photoelectron Spectroscopy (XPS) analysis is also recommended, considering that the previous experiments conducted at LNLS faced challenges due to the insulating nature of the samples and beam characteristics. Extended X-ray Absorption Fine Structure (EXAFS) analysis could also provide essential information concerning the structural aspects of $Co_{1.8}Cu_{0.9}AlO_x$.

As for catalyst synthesis and formulation, improvements in methodology are proposed, including the incorporation of hydrothermal treatment to augment crystallinity, or exploring alternative synthesis methods, such as sol-gel. Investigation into different interlayer charge-compensation anions and Co:Cu ratios is also suggested. A more in-depth exploration of basicity promoters (K and Na) is advised. Additionally, consideration should be given to exploring other promoters and active metals (e.g., Zn, Zr, Mn, Ni, Fe,

In, Ga, among others), and delving into different pretreatment strategies, including controlled reduction pretreatments with CO or H_2.

Exploring and understanding the effects of reaction conditions requires meticulous attention, given the sensitivity of product selectivity and CO_2 conversion to their variation.

Moving forward, operando and in situ characterizations should be integrated into the research approach. These techniques can provide real-time insights into catalyst behavior under reaction conditions, offering a deeper understanding of the specific effects of various parameters. Complementing experimental endeavors, computational studies are deemed essential to augment and validate the experimental research, contributing to a comprehensive and robust understanding of CO_2 hydrogenation to higher alcohols.

References

AIDER, N. *et al.* Improvement of catalytic stability and carbon resistance in the process of CO2 reforming of methane by CoAl and CoFe hydrotalcite-derived catalysts. **International Journal of Hydrogen Energy**, v. 43, n. 17, p. 8256–8266, 2018.

ALI, S. *et al*. A review on CO2 hydrogenation to ethanol: Reaction mechanism and experimental studies. **Journal of Environmental Chemical Engineering**, v. 10, n. 1, 2022.

AMRI, A. *et al.* Solar absorptance of copper–cobalt oxide thin film coatings with nano-size, grain-like morphology: Optimization and synchrotron radiation XPS studies. **Applied Surface Science**, v. 275, p. 127–135, 2013.

AN, X. *et al.* A Cu/Zn/Al/Zr fibrous catalyst that is an improved CO2 hydrogenation to methanol catalyst. **Catalysis Letters**, v. 118, n. 3–4, p. 264–269, 2007.

AN, K. *et al.* A highly selective catalyst of Co/La4Ga2O9 for CO2 hydrogenation to ethanol. **Journal of Energy Chemistry**, v. 56, p. 486–495, 2021.

AN, K. *et al.* Co0−Coδ+ active pairs tailored by Ga-Al-O spinel for CO2-to-ethanol synthesis. **Chemical Engineering Journal**, v. 433, p. 134606, 2022. Disponível em: https://linkinghub.elsevier.com/retrieve/pii/S1385894722001140.

ANDO, H. *et al.* Hydrocarbon synthesis from CO2 over Fe-Cu catalysts. **Catalysis Today**, v. 45, n. 1–4, p. 229–234, 1998.

AO, M. *et al.* Active Centers of Catalysts for Higher Alcohol Synthesis from Syngas: A Review. **ACS Catalysis**, v. 8, n. 8, p. 7025–7050, 2018.

AO, M. *et al.* Effects of alkali promoters on tri-metallic Co-Ni-Cu-based perovskite catalyst for higher alcohol synthesis from syngas. **Catalysis Today**, v. 355, n. June 2019, p. 26–34, 2020.

ARENA, F. *et al.* Synthesis, characterization and activity pattern of Cu-ZnO/ZrO2 catalysts in the hydrogenation of carbon dioxide to methanol. **Journal of Catalysis**, v. 249, n. 2, p. 185–194, 2007.

ARESTA, M.; DIBENEDETTO, A.; QUARANTA, E. State of the art and perspectives in catalytic processes for CO2 conversion into chemicals and fuels: The distinctive contribution of chemical catalysis and biotechnology. **Journal of Catalysis**, [*s. l.*], v. 343, p. 2–45, 2016.

ATSONIOS, K.; PANOPOULOS, K. D.; KAKARAS, E. Thermocatalytic CO2 hydrogenation for methanol and ethanol production: Process improvements. **International Journal of Hydrogen Energy**, v. 41, n. 2, p. 792–806, 2016.

BAI, S. *et al.* Highly Active and Selective Hydrogenation of CO 2 to Ethanol by Ordered Pd−Cu Nanoparticles. **Journal of the American Chemical Society**, v. 139, n. 20, p. 23–26, 2017.

BENHITI, R. *et al.* Synthesis, characterization, and comparative study of MgAl-LDHs prepared by standard coprecipitation and urea hydrolysis methods for phosphate removal. **Environmental Science and Pollution Research**, v. 27, n. 36, p. 45767–45774, 2020.

BERENGUER, R. *et al.* Electro-oxidation of cyanide on active and non-active anodes: Designing the electrocatalytic response of cobalt spinels. **Separation and Purification Technology**, v. 208, p. 42–50, 2019.

BIESINGER, M. C. Advanced analysis of copper X-ray photoelectron spectra. **Surface and Interface Analysis**, v. 49, n. 13, p. 1325–1334, 2017.

BIESINGER, M. C. *et al.* Analysis of mineral surface chemistry in flotation separation using imaging XPS. **Minerals Engineering**, v. 20, n. 2, p. 152–162, 2007.

BIESINGER, M. C. *et al.* Resolving surface chemical states in XPS analysis of first row transition metals, oxides and hydroxides: Cr, Mn, Fe, Co and Ni. **Applied Surface Science**, v. 257, n. 7, p. 2717–2730, 2011.

BIESINGER, M. C. *et al.* Resolving surface chemical states in XPS analysis of first row transition metals, oxides and hydroxides: Sc, Ti, V, Cu and Zn. **Applied Surface Science**, v. 257, n. 3, p. 887–898, 2010.

BIESINGER, M. C. *et al.* X-ray photoelectron spectroscopic chemical state quantification of mixed nickel metal, oxide and hydroxide systems. **Surface and Interface Analysis**, v. 41, n. 4, p. 324–332, 2009.

BLOOMBERG, F. L. P. **Clean Energy Ministerial - Energy Transition Factbook**, 2023.

BOYCE, J. K. Carbon Pricing: Effectiveness and Equity. **Ecological Economics**, v. 150, p. 52–61, 2018.

CAPARRÓS, F. J. *et al.* Remarkable Carbon Dioxide Hydrogenation to Ethanol on a Palladium/Iron Oxide Single-Atom Catalyst. **ChemCatChem**, v. 10, n. 11, p. 2365–2369, 2018.

CARBON ENGINEERING. **Carbon Engineering - Air-to-Fuel Technology**. 2023. Disponível em: https://carbonengineering.com/air-to-fuels/. Acesso em: 24 jul. 2023.

CARBON RECYCLING INTERNATIONAL. **Technology to Product Renewable or Recycled Carbon Methanol**. 2023. Disponível em: https://www.carbonrecycling.is/technology. Acesso em: 24 jul. 2023.

CENTI, G.; PERATHONER, S. Opportunities and prospects in the chemical recycling of carbon dioxide to fuels. **Catalysis Today**, v. 148, n. 3–4, p. 191–205, 2009.

CHAILLOT, D.; BENNICI, S.; BRENDLÉ, J. Layered double hydroxides and LDH-derived materials in chosen environmental applications: a review. **Environmental Science and Pollution Research**, v. 28, n. 19, p. 24375–24405, 2021.

CHAUVY, R. *et al.* Selecting emerging CO2 utilization products for short- to mid-term deployment. **Applied Energy**, v. 236, p. 662–680, 2019.

CHEN, C. *et al.* Insight into heterogeneous catalytic degradation of sulfamethazine by peroxymonosulfate activated with CuCo2O4 derived from bimetallic oxalate. **Chemical Engineering Journal** v. 384, p. 123257, 2020.

CHENG, K. *et al.* Direct and Highly Selective Conversion of Synthesis Gas into Lower Olefins: Design of a Bifunctional Catalyst Combining Methanol Synthesis and Carbon-Carbon Coupling. **Angewandte Chemie - International Edition**, v. 55, n. 15, p. 4725–4728, 2016.

CHENG, S.-Y. *et al.* Preparation of complexant-modified Cu/ZnO/Al2O3 catalysts via hydrotalcite-like precursors and its highly efficient application in direct synthesis

of isobutanol and ethanol from syngas. **Applied Catalysis A: General**, v. 556, p. 113–120, 2018.

CORRÊA, C. L. O. *et al.* Effect of composition and thermal treatment in catalysts derived from Cu-Al hydrotalcites-like compounds in the NO reduction by CO. **Catalysis Today**, v. 289, p. 133–142, 2017.

CUÉLLAR-FRANCA, R. M.; AZAPAGIC, A. Carbon capture, storage and utilisation technologies: A critical analysis and comparison of their life cycle environmental impacts. **Journal of CO2 Utilization**, v. 9, p. 82–102, 2015.

DELGADO, J. A. *et al.* Estimation of Adsorption Parameters from Temperature-Programmed Desorption Thermograms: Application to the Adsorption of Carbon Dioxide onto Alumina. **Adsorption Science & Technology**, v. 25, n. 3–4, p. 113–128, 2007. Disponível em: http://doi/10.1260/026361707782398146.

DELGADO, J. A.; GÓMEZ, J. M. Estimation of adsorption parameters from temperature-programed-desorption thermograms: Application to the adsorption of carbon dioxide onto Na-and H-mordenite. **Langmuir**, v. 21, n. 21, p. 9555–9561, 2005.

DIAS, Y. R.; PEREZ-LOPEZ, O. W. CO2 methanation over Ni-Al LDH-derived catalyst with variable Ni/Al ratio. **Journal of CO2 Utilization**, v. 68, p. 102381, 2023.

DORNER, R. W. *et al.* K and Mn doped iron-based CO2 hydrogenation catalysts: Detection of KAlH4 as part of the catalyst's active phase. **Applied Catalysis A: General**, v. 373, n. 1–2, p. 112–121, 2010.

FAN, G. *et al.* Catalytic applications of layered double hydroxides: recent advances and perspectives. **Chem. Soc. Rev.**, v. 43, n. 20, p. 7040–7066, 2014.

FAN, T. *et al.* Cobalt Catalysts Enable Selective Hydrogenation of CO2 toward Diverse Products: Recent Progress and Perspective. **The Journal of Physical Chemistry Letters**, v. 12, n. 43, p. 10486–10496, 2021.

FAN, W. K.; TAHIR, M. Recent trends in developments of active metals and heterogenous materials for catalytic CO2 hydrogenation to renewable methane: A review. **Journal of Environmental Chemical Engineering**, v. 9, n. 4, p. 105460, 2021.

FANG, X. *et al.* Progress in Adsorption-Enhanced Hydrogenation of CO2 on Layered Double Hydroxide (LDH) Derived Catalysts. **Journal of Industrial and Engineering Chemistry**, v. 95, p. 16–27, 2021.

FIERRO, J. L. G.; MELIÁN-CABRERA, I.; LÓPEZ GRANADOS, M. Pd-modified Cu-Zn catalysts for methanol synthesis from CO2/H2 mixtures: Catalytic structures and performance. **Journal of Catalysis**, v. 210, n. 2, p. 285–294, 2002a.

FIERRO, J. L. G.; MELIÁN-CABRERA, I.; LÓPEZ GRANADOS, M. Reverse topotactic transformation of a Cu-Zn-Al catalyst during wet Pd impregnation: Relevance for the performance in methanol synthesis from CO2/H2 mixtures. **Journal of Catalysis**, v. 210, n. 2, p. 273–284, 2002b.

FRIEDLINGSTEIN, P. *et al.* Global Carbon Budget 2022. **Earth System Science Data**, v. 14, n. 11, p. 4811–4900, 2022.

FUJIMOTO, K.; SHIKADA, T. Selective synthesis of C2-C5 hydrocarbons from carbon dioxide utilizing a hybrid catalyst composed of a methanol synthesis catalyst and zeolite. **Applied Catalysis**, v. 31, n. 1, p. 13–23, 1987.

FUJIWARA, M. *et al.* CO2 hydrogenation for C2+ hydrocarbon synthesis over composite catalyst using surface modified HB zeolite. **Applied Catalysis B: Environmental**, v. 179, p. 37–43, 2015a. Disponível em: http://doi.org/10.1016/j.apcatb.2015.05.004.

FUJIWARA, M. *et al.* Synthesis of C2+ hydrocarbons by CO2 hydrogenation over the composite catalyst of Cu-Zn-Al oxide and HB zeolite using two-stage reactor system under low pressure. **Catalysis Today**, v. 242, n. PB, p. 255–260, 2015b. Disponível em: http://doi.org/10.1016/j.cattod.2014.04.032.

GAO, J. *et al.* A thermodynamic analysis of methanation reactions of carbon oxides for the production of synthetic natural gas. **RSC Advances**, v. 2, n. 6, p. 2358–2368, 2012.

GAO, P. *et al.* Direct conversion of CO2 into liquid fuels with high selectivity over a bifunctional catalyst. **Nature Chemistry**, v. 9, n. 10, p. 1019–1024, 2017. Disponível em: http://dx.doi.org/10.1038/nchem.2794.

GARAFFA, R. *et al.* Distributional effects of carbon pricing in Brazil under the Paris Agreement. **Energy Economics**, v. 101, p. 105396, 2021.

GNANAMANI, M. K. *et al.* Hydrogenation of Carbon Dioxide over Co-Fe Bimetallic Catalysts. **ACS Catalysis**, v. 6, n. 2, p. 913–927, 2016.

GÖBEL, C. *et al.* Structural evolution of bimetallic Co-Cu catalysts in CO hydrogenation to higher alcohols at high pressure. **Journal of Catalysis**, v. 383, p. 33–41, 2020.

GORYACHEV, A. *et al.* A Multi-Parametric Catalyst Screening for CO2 Hydrogenation to Ethanol. **ChemCatChem**, v. 13, n. 14, p. 3324–3332, 2021.

GROSVENOR, A. P. *et al.* Examination of the Bonding in Binary Transition-Metal Monophosphides MP (M = Cr, Mn, Fe, Co) by X-Ray Photoelectron Spectroscopy. **Inorganic Chemistry**, v. 44, n. 24, p. 8988–8998, 2005.

GUO, X. *et al.* Combustion synthesis of CuO-ZnO-ZrO2 catalysts for the hydrogenation of carbon dioxide to methanol. **Catalysis Communications**, v. 10, n. 13, p. 1661–1664, 2009. Disponível em: http://doi.org/10.1016/j.catcom.2009.05.004.

GUO, W. *et al.* Higher Alcohols Synthesis from CO2 Hydrogenation over K2O-Modified CuZnFeZrO2 Catalysts. **Advanced Materials Research**, v. 827, p. 20–24, 2013.

HADDAD, N. *et al.* Benzaldehyde reduction over Cu–Al–O bimetallic oxide catalyst. Influence of pH during hydrothermal synthesis on the structural and catalytic properties. **Journal of Molecular Catalysis A: Chemical**, v. 396, p. 207–215, 2015.

HANNAH RITCHIE; MAX ROSER; PABLO ROSADO. **CO2 and Greenhouse Gas Emissions**. [*S. l.*], 2020. Disponível em: https://ourworldindata.org/co2-and-greenhouse-gas-emissions. Acesso em: 11 nov. 2023.

HASHIMOTO, K. *et al.* Materials for global carbon dioxide recycling. **Corrosion Science**, v. 44, n. 2, p. 371–386, 2002.

HAVE, I. C. ten *et al.* Uncovering the reaction mechanism behind CoO as active phase for CO2 hydrogenation. **Nature Communications**, v. 13, n. 1, p. 324, 2022.

HE, Y. *et al.* Assessing the efficiency of CO2 hydrogenation for emission reduction: Simulating ethanol synthesis process as a case study. **Chemical Engineering Research and Design**, v. 195, p. 106–115, 2023.

HE, Z. *et al.* Synthesis of higher alcohols from CO2 hydrogenation over a PtRu/Fe2O3 catalyst under supercritical condition. **Philosophical Transactions of the Royal Society A: Mathematical, Physical and Engineering Sciences**, v. 373, n. 20150006, p. 1–10, 2015. Disponível em: https:// doi/10.1098/rsta.2015.0006.

HE, Y. *et al.* Thermodynamic Analysis of CO2Hydrogenation to Higher Alcohols (C2-4OH): Effects of Isomers and Methane. **ACS Omega**, v.7, n. 19, p. 16502-16514, 2022.

HE, Z. *et al.* Water-Enhanced Synthesis of Higher Alcohols from CO2 Hydrogenation over a Pt/Co3O4 Catalyst under Milder Conditions. **Angewandte Chemie - International Edition**, v. 55, n. 2, p. 737–741, 2016.

HERRANZ, T. *et al.* Hydrogenation of carbon oxides over promoted Fe-Mn catalysts prepared by the microemulsion methodology. **Applied Catalysis A: General**, v. 311, n. 1–2, p. 66–75, 2006.

HIGUCHI, K. *et al.* A study for the durability of catalysts in ethanol synthesis by hydrogenation of carbon dioxide. **Studies in Surface Science and Catalysi**, , v. 114, p. 517–520, 1998.

IEA. **CO2 Emissions in 2022**. Paris: [*s. n.*], 2023a. Disponível em: https://www.iea.org/reports/co2-emissions-in-2022. Acesso em: 11 nov. 2023.

IEA. **World Energy Outlook 2023**. Paris: [*s. n.*], 2023b. Disponível em: https://www.iea.org/reports/world-energy-outlook-2023. Acesso em: 11 nov. 2023.

IRSHAD, M. *et al.* Synthesis of n-butanol-rich C3+ alcohols by direct CO2 hydrogenation over a stable Cu–Co tandem catalyst. **Applied Catalysis B: Environmental**, v. 340, p. 123201, 2024.

ISAHAK, W. N. R. W.; SHAKER, L. M.; AL-AMIERY, A. Oxygenated Hydrocarbons from Catalytic Hydrogenation of Carbon Dioxide. **Catalysts**, v. 13, n. 1, p. 115., 2023.

JIA, C. *et al.* The thermodynamics analysis and experimental validation for complicated systems in CO2 hydrogenation process. **Journal of Energy Chemistry**, v. 25, n. 6, p. 1027–1037, 2016.

JIRÁTOVÁ, K. *et al.* Total oxidation of ethanol over layered double hydroxide-related mixed oxide catalysts: Effect of cation composition. **Catalysis Today**, v. 277, p. 61–67, 2016.

KAMKENG, A. D. N. *et al.* Transformation technologies for CO2 utilisation: Current status, challenges and future prospects. **Chemical Engineering Journal**, v. 409, 2021.

KANURI, S. *et al.* An insight of CO2 hydrogenation to methanol synthesis: Thermodynamics, catalysts, operating parameters, and reaction mechanism. **International Journal of Energy Research**, v. 46, n. 5, p. 5503–5522, 2022.

KARÁSKOVÁ, K. *et al.* K-Modified Co–Mn–Al Mixed Oxide—Effect of Calcination Temperature on N2O Conversion in the Presence of H2O and NOx. **Catalysts**, v. 10, n. 10, p. 1134, 2020.

KATTEL, S. *et al.* Active sites for CO2 hydrogenation to methanol on Cu/ZnO catalysts. **Science**, v. 355, n. 6331, p. 1296–1299, 2017.

KATTEL, S. *et al.* Optimizing Binding Energies of Key Intermediates for CO2 Hydrogenation to Methanol over Oxide-Supported Copper. **Journal of the American Chemical Society**, v. 138, n. 38, p. 12440–12450, 2016.

KATTEL, S.; LIU, P.; CHEN, J. G. Tuning Selectivity of CO2 Hydrogenation Reactions at the Metal/Oxide Interface. **Journal of the American Chemical Society**, v. 139, n. 29, p. 9739–9754, 2017.

KEFIF, F. *et al.* Evans Blue dye removal from contaminated water on calcined and uncalcined Cu-Al-CO3 layered double hydroxide materials prepared by coprecipitation. **Bulletin of Materials Science**, v. 42, n. 1, 2019. Disponível em: https://doi.org/10.1007/s12034-018-1694-z.

KIM, W. *et al.* Methanol-steam reforming reaction over Cu-Al-based catalysts derived from layered double hydroxides. **International Journal of Hydrogen Energy**, v. 42, n. 4, p. 2081–2087, 2017.

KOMMOSS, B. *et al.* Heterogeneously Catalyzed Hydrogenation of Supercritical CO2to Methanol. **Chemical Engineering and Technology**, v. 40, n. 10, p. 1907–1915, 2017.

KOSCHANY, F.; SCHLERETH, D.; HINRICHSEN, O. On the kinetics of the methanation of carbon dioxide on coprecipitated NiAl(O)x. **Applied Catalysis B: Environmental**, v. 181, p. 504–516, 2016.

KREITZ, B. *et al.* Microkinetic Modeling of the CO2Desorption from Supported Multifaceted Ni Catalysts. **Journal of Physical Chemistry C**, v. 125, n. 5, p. 2984–3000, 2021.

KUMAR, S. *et al.* P25@CoAl layered double hydroxide heterojunction nanocomposites for CO 2 photocatalytic reduction. **Applied Catalysis B: Environmental**, v. 209, p. 394–404, 2017.

KUPKOVÁ, K. *et al.* Cobalt-Copper Oxide Catalysts for VOC Abatement: Effect of Co:Cu Ratio on Performance in Ethanol Oxidation. **Catalysts**, v. 13, n. 1, p. 107, 2023.

KUSAMA, H. *et al.* CO2 hydrogenation to ethanol over promoted Rh/SiO2 catalysts. **Catalysis Today**, v. 28, n. 3, p. 261–266, 1996.

LAGE, V. D. *et al.* Tuning Co-Cu-Al catalysts and their reaction conditions on the CO2 hydrogenation reaction to higher alcohols under mild conditions. **Chemical Engineering Science**, v. 281, p. 119208, 2023.

LATSIOU, A. I. *et al.* CO2 hydrogenation for the production of higher alcohols: Trends in catalyst developments, challenges and opportunities. **Catalysis Today**, v. 420, p. 114179, 2023.

LE, T. A. *et al.* CO and CO2 Methanation Over Supported Cobalt Catalysts. **Topics in Catalysis**, v. 60, n. 9–11, p. 714–720, 2017.

LEE, J. -F *et al.* Hydrogenation of carbon dioxide on iron catalysts doubly promoted with manganese and potassium. **The Canadian Journal of Chemical Engineering**, v. 70, n. 3, p. 511–515, 1992.

LI, W. *et al.* A short review of recent advances in CO 2 hydrogenation to hydrocarbons over heterogeneous catalysts. **RSC Advances**, v. 8, n. 14, p. 7651–7669, 2018a.

LI, S. *et al.* Effect of iron promoter on structure and performance of K/Cu-Zn catalyst for higher alcohols synthesis from CO2 hydrogenation. **Catalysis Letters**, v. 143, n. 4, p. 345–355, 2013.

LI, T. *et al.* Effect of manganese on an iron-based Fischer-Tropsch synthesis catalyst prepared from ferrous sulfate. **Fuel**, v. 86, n. 7–8, p. 921–928, 2007.

LI, K. *et al.* Nature of Catalytic Behavior of Cobalt Oxides for CO2 Hydrogenation. **JACS Au**, v. 3, n. 2, p. 508–515, 2023.

LI, H. *et al.* Ni/SBA-15 catalysts for CO methanation: effects of V, Ce, and Zr promoters. **RSC Advances**, v. 5, n. 117, p. 96504–96517, 2015.

LI, Z. *et al.* Oxygen vacancy mediated CuyCo3-yFe1Ox mixed oxide as highly active and stable toluene oxidation catalyst by multiple phase interfaces formation and metal doping effect. **Applied Catalysis B: Environmental**, v. 269, p. 118827, 2020.

LI, X. *et al.* Research progress of hydrogenation of carbon dioxide to ethanol. **Chemical Engineering Science**, v. 282, p. 119226, 2023. Disponível em: https://doi.org/10.1016/j.ces.2023.119226.

LI, S. *et al.* Tuning the Selectivity of Catalytic Carbon Dioxide Hydrogenation over Iridium/Cerium Oxide Catalysts with a Strong Metal–Support Interaction.

Angewandte Chemie - International Edition, v. 56, n. 36, p. 10761–10765, 2017.

LI, W. *et al.* ZrO2 support imparts superior activity and stability of Co catalysts for CO 2 methanation. **Applied Catalysis B: Environmental**, v. 220, p. 397–408, 2018b.

LI, Y.; LU, G.; MA, J. Highly active and stable nano NiO-MgO catalyst encapsulated by silica with a core-shell structure for CO2 methanation. **RSC Advances**, v. 4, n. 34, p. 17420–17428, 2014.

LIANG, B. *et al.* Effect of Na Promoter on Fe-Based Catalyst for CO2 Hydrogenation to Alkenes. **ACS Sustainable Chemical Engineering**, v. 7, n. 1, p. 925–932, 2018. Disponível em: https://doi.org/10.1021/acssuschemeng.8b04538.

LIANG, X. L. *et al.* Carbon nanotube-supported Pd-ZnO catalyst for hydrogenation of CO2 to methanol. **Applied Catalysis B: Environmental**, v. 88, n. 3–4, p. 315–322, 2009.

LIAW, B. J.; CHEN, Y. Z. Liquid-phase synthesis of methanol from CO2/H2 over ultrafine CuB catalysts. **Applied Catalysis A: General**, v. 206, n. 2, p. 245–256, 2001.

LIM, A. M. H.; YEO, J. W.; ZENG, H. C. Preparation of CuZn-Doped MgAl-Layered Double Hydroxide Catalysts through the Memory Effect of Hydrotalcite for Effective Hydrogenation of CO2 to Methanol. **ACS Applied Energy Materials**, v. 6, n. 2, p. 782–794, 2023.

LIMA DA SILVA, A.; MALFATTI, C. de F.; MÜLLER, I. L. Thermodynamic analysis of ethanol steam reforming using Gibbs energy minimization method: A detailed study of the conditions of carbon deposition. **International Journal of Hydrogen Energy**, v. 34, n. 10, p. 4321–4330, 2009.

LIMA, D. dos S.; DIAS, Y. R.; PEREZ-LOPEZ, O. W. CO2methanation over Ni-Al and Co-Al LDH-derived catalysts: The role of basicity. **Sustainable Energy and Fuels**, v. 4, n. 11, p. 5747–5756, 2020.

LIU, S. *et al.* Activated Carbon-Supported Mo-Co-K Sulfide Catalysts for Synthesizing Higher Alcohols from CO2. **Chemical Engineering & Technology**, v. 42, n. 5, p. 962–970, 2019.

LIU, B. *et al.* Effects of mesoporous structure and Pt promoter on the activity of Co-based catalysts in low-temperature CO2 hydrogenation for higher alcohol synthesis. **Journal of Catalysis**, v. 366, p. 91–97, 2018a. Disponível em: https://doi.org/10.1016/j.jcat.2018.07.019.

LIU, B. *et al.* Unravelling the New Roles of Na and Mn Promoter in CO2 Hydrogenation over Fe3O4-Based Catalysts for Enhanced Selectivity to Light α-Olefins. **ChemCatChem**, v. 10, n. 20, p. 4718–4732, 2018b. Disponível em: https://doi.org/10.1002/cctc.201800782.

LIU, S. *et al.* Hetero-site cobalt catalysts for higher alcohols synthesis by CO2 hydrogenation: A review. **Journal of CO2 Utilization**. v. 67, p. 102322, 2023. Disponível em: https://doi.org/10.1016/j.jcou.2022.102322

LIU, C. *et al.* Methanol synthesis from CO2 hydrogenation over copper catalysts supported on MgO-modified TiO2. **Journal of Molecular Catalysis A: Chemical**, v. 425, p. 86–93, 2016.

LIU, S. *et al.* Moderate Surface Segregation Promotes Selective Ethanol Production in CO2 Hydrogenation Reaction over CoCu Catalysts. **Angewandte Chemie - International Edition**, v. 61, n. 2, 2022.

LIU, X. M. *et al.* Recent Advances in Catalysts for Methanol Synthesis via Hydrogenation of CO and CO2. **Industrial and Engineering Chemistry Research**, v. 42, n. 25, p. 6518–6530, 2003.

LIU, X. *et al.* Selective transformation of carbon dioxide into lower olefins with a bifunctional catalyst composed of ZnGa2O4 and SAPO-34. **Chemical Communications**, v. 54, n. 2, p. 140–143, 2017.

LIU, L. *et al.* Sunlight-assisted hydrogenation of CO 2 into ethanol and C2+ hydrocarbons by sodium-promoted Co@C nanocomposites. **Applied Catalysis B: Environmental**, v. 235, p. 186–196, 2018.

LIU, J. *et al.* Surface active structure of ultra-fine Cu/ZrO2 catalysts used for the CO2+H2 to methanol reaction. **Applied Catalysis A: General**, v. 218, n. 1–2, p. 113–119, 2001.

LIU, S. *et al.* Synthesis of higher alcohols from CO 2 hydrogenation over Mo–Co–K sulfide-based catalysts. **Journal of the Taiwan Institute of Chemical Engineers**, v. 76, p. 18–26, 2017.

LIU, X. M.; LU, G. Q.; YAN, Z. F. Nanocrystalline zirconia as catalyst support in methanol synthesis. **Applied Catalysis A: General**, v. 279, n. 1–2, p. 241–245, 2005.

LIU, P.; YANG, Y.; WHITE, M. G. Theoretical perspective of alcohol decomposition and synthesis from CO 2 hydrogenation. **Surface Science Reports**, v. 68, n. 2, p. 233–272, 2013. Disponível em: http://dx.doi.org/10.1016/j.surfrep.2013.01.001.

LOU, Y. *et al.* CeO2 supported Pd dimers boosting CO2 hydrogenation to ethanol. **Applied Catalysis B: Environmental**, v. 291, 2021.

LUK, H. T. *et al.* Status and prospects in higher alcohols synthesis from syngas. **Chemical Society Reviews**, v. 46, n. 5, p. 1358–1426, 2017.

LYU, M. *et al.* Core–shell silica@CuxZnAl LDH catalysts for efficient CO2 hydrogenation to methanol. **Chemical Science**, v. 14, n. 36, p. 9814–9819, 2023.

MARTIN, O. *et al.* Indium oxide as a superior catalyst for methanol synthesis by CO2 hydrogenation. **Angewandte Chemie - International Edition**, v. 55, n. 21, p. 6261–6265, 2016.

MCCUSKER, L. B. *et al.* Rietveld refinement guidelines. **Journal of Applied Crystallography**, v. 32, n. 1, p. 36–50, 1999.

MOULDER, J. F. *et al.* **Handbook of X-ray Photoelectron Spectroscopy**. Eden Prairie: Perkin-Elmer Corp , 1992.

MULEJA, A. A. *et al.* Variation of the short-chain paraffin and olefin formation rates with time for a cobalt Fischer-Tropsch catalyst. **Industrial and Engineering Chemistry Research**, v. 56, n. 2, p. 469–478, 2017.

NAIMS, H. Economics of carbon dioxide capture and utilization—a supply and demand perspective. **Environmental Science and Pollution Research**, v. 23, n. 22, p. 22226–22241, 2016.

NGUYEN, T. H.; KIM, H. B.; PARK, E. D. CO and CO2 Methanation over CeO2-Supported Cobalt Catalysts. **Catalysts**, v. 12, n. 2, 2022.

NIE, X. *et al.* Mechanistic Insight into C-C Coupling over Fe-Cu Bimetallic Catalysts in CO2 Hydrogenation. **Journal of Physical Chemistry C**, v. 121, n. 24, p. 13164–13174, 2017.

NIESKENS, D. L. S. *et al.* The conversion of carbon dioxide and hydrogen into methanol and higher alcohols. **Catalysis Communications**, v. 14, n. 1, p. 111–113, 2011.

NING, W.; KOIZUMI, N.; YAMADA, M. Researching Fe catalyst suitable for CO2-containing syngas for Fischer-Tropsch synthesis. **Energy and Fuels**, v. 23, n. 9, p. 4696–4700, 2009.

NORHASYIMA, R. S.; MAHLIA, T. M. I. Advances in CO_2 utilization technology: A patent landscape review. **Journal of CO2 Utilization**, v. 26, p. 323–335, 2018.

OBALOVÁ, L. *et al.* Effect of potassium in calcined Co-Mn-Al layered double hydroxide on the catalytic decomposition of N2O. **Applied Catalysis B: Environmental**, [*s. l.*], v. 90, n. 1–2, p. 132–140, 2009.

OBEID, M. *et al.* CO2 methanation over LDH derived NiMgAl and NiMgAlFe oxides: Improving activity at lower temperatures via an ultrasound-assisted preparation. **Chemical Engineering Journal**, v. 474, p. 145460, 2023.

OJELADE, O. A.; ZAMAN, S. F. A review on CO2 hydrogenation to lower olefins: Understanding the structure-property relationships in heterogeneous catalytic systems. **Journal of CO2 Utilization**, v. 47, p. 101506, 2021.

OVESEN, C. V. *et al.* Kinetic implications of dynamical changes in catalyst morphology during methanol synthesis over Cu/ZnO catalysts. **Journal of Catalysis**, v. 168, n. 2, p. 133–142, 1997.

PAKNAHAD, P.; ASKARI, M.; GHORBANZADEH, M. Characterization of nanocrystalline CuCo2O4 spinel prepared by sol–gel technique applicable to the SOFC interconnect coating. **Applied Physics A**, v. 119, n. 2, p. 727–734, 2015.

PRAKRUTHI, H. R. *et al.* Hydrogenation efficiency of highly porous Cu-Al oxides derived from dealuminated LDH in the conversion of furfural to furfuryl alcohol. **Journal of Industrial and Engineering Chemistry**, v. 62, p. 96–105, 2018.

PRIETO, G. Carbon Dioxide Hydrogenation into Higher Hydrocarbons and Oxygenates: Thermodynamic and Kinetic Bounds and Progress with Heterogeneous and Homogeneous Catalysis. **ChemSusChem**, v. 10, n. 6, p. 1056–1070, 2017.

RAMOS, R. *et al.* Selective conversion of 5-hydroxymethylfurfural to cyclopentanone derivatives over Cu-Al2O3 and Co-Al2O3 catalysts in water. **Green Chemistry**, v. 19, n. 7, p. 1701–1713, 2017.

RAUDASKOSKI, R.; NIEMELÄ, M. V.; KEISKI, R. L. The effect of ageing time on co-precipitated Cu/ZnO/ZrO 2 catalysts used in methanol synthesis from CO 2 and H 2. **Topics in Catalysis**, v. 45, n. 1–4, p. 57–60, 2007.

RONDUDA, H. *et al.* A high performance barium-promoted cobalt catalyst supported on magnesium-lanthanum mixed oxide for ammonia synthesis. **RSC Advances**,.], v. 11, n. 23, p. 14218–14228, 2021.

RÖNSCH, S. *et al.* Review on methanation - From fundamentals to current projects. **Fuel**, v. 166, p. 276–296, 2016.

SAEIDI, S. *et al.* Recent advances in CO2 hydrogenation to value-added products — Current challenges and future directions. **Progress in Energy and Combustion Science**, v. 85, p. 100905, 2021.

SASOL. **Sasol and UCT researchers collaborate on the use of commercial iron catalysts to convert hydrogen and CO2 into green jet fuel and chemicals**, 2021. Disponível em: https://www.sasol.com/media-centre/media-releases/sasol-and-uct-researchers-collaborate-use-commercial-iron-catalysts. Acesso em: 24 jul. 2023.

SATTHAWONG, R. *et al.* Light olefin synthesis from CO2 hydrogenation over K-promoted Fe-Co bimetallic catalysts. **Catalysis Today**, v. 251, p. 34–40, 2015. Disponível em: http://dx.doi.org/10.1016/j.cattod.2015.01.011.

SCHEMME, S. *et al.* Promising catalytic synthesis pathways towards higher alcohols as suitable transport fuels based on H2 and CO2. **Journal of CO2 Utilization**, v. 27, p. 223–237, 2018.

SCHUBERT, M. *et al.* Highly active Co-Al2O3-based catalysts for CO2 methanation with very low platinum promotion prepared by double flame spray pyrolysis. **Catalysis Science and Technology**, v. 6, n. 20, p. 7449–7460, 2016.

SEEG. **Sistema de Estimativas de Emissões de Gases do Efeito Estufa**, 2022. Disponível em: https://plataforma.seeg.eco.br/map?cities=true#. Acesso em: 12 nov. 2023.

SEEO2 ENERGY. **What We Do - SeeO2 Energy**, 2023. Disponível em: https://www.seeo2energy.com/what-we-do/. Acesso em: 24 jul. 2023.

SHAO, F. *et al.* Effects of manganese on the catalytic performance of CuCo catalysts for direct conversion of CO/CO2 to higher alcohols. **Dalton Transactions**, v. 52, n. 2, p. 461–468, 2023.

SHI, Z. *et al.* Direct conversion of CO2 to long-chain hydrocarbon fuels over K-promoted CoCu/TiO2 catalysts. **Catalysis Today**, v. 311, p. 65–73, 2018.

SI, Z. *et al.* Synthesis of Alkene and Ethanol in CO2 Hydrogenation on a Highly Active Sputtering CuNaFe Catalyst. **ACS Sustainable Chemistry and Engineering**, v. 10, n. 45, p. 14972–14979, 2022.

SŁOCZYŃSKI, J. *et al.* Catalytic activity of the M/(3ZnO·ZrO2) system (M = Cu, Ag, Au) in the hydrogenation of CO2 to methanol. **Applied Catalysis A: General**, v. 278, n. 1, p. 11–23, 2004.

SŁOCZYŃSKI, J. *et al.* Effect of metal oxide additives on the activity and stability of Cu/ZnO/ZrO2 catalysts in the synthesis of methanol from CO2 and H2. **Applied Catalysis A: General**, v. 310, n. 1–2, p. 127–137, 2006.

STANGELAND, K.; LI, H.; YU, Z. Thermodynamic Analysis of Chemical and Phase Equilibria in CO2 Hydrogenation to Methanol, Dimethyl Ether, and Higher Alcohols. **Industrial & Engineering Chemistry Research**, v. 57, p. 11, p. 4081-4094, 2018.

SUBRAMANIAN, N. D. *et al.* Development of cobalt-copper nanoparticles as catalysts for higher alcohol synthesis from syngas. **Catalysis Today**, v. 147, n. 2, p. 100–106, 2009.

SULMONETTI, T. P. *et al.* Reduced Cu-Co-Al Mixed Metal Oxides for the Ring-Opening of Furfuryl Alcohol to Produce Renewable Diols. **ACS Sustainable Chemistry and Engineering**, v. 5, n. 10, p. 8959–8969, 2017.

SUN, K. *et al.* CO hydrogenation to ethanol and higher alcohols over ultrathin CuCoAl nanosheets derived from LDH precursor. **Fuel**, v. 333, p. 126308, 2023.

SUN, K. *et al.* Effect of Hydroxyl Groups on CuCoMg Nanosheets for Ethanol and Higher Alcohol Synthesis from Syngas. **Industrial & Engineering Chemistry Research**, v. 60, n. 6, p. 2388–2399, 2021. Disponível em: https://doi/10.1021/acs.iecr.0c05204.

SUN, K. *et al.* Synergetic catalysis of bimetallic copper-cobalt nanosheets for direct synthesis of ethanol and higher alcohols from syngas. **Catalysis Science and Technology**, v. 8, n. 15, p. 3936–3947, 2018.

SWAPNESH, A.; SRIVASTAVA, V. C.; MALL, I. D. Comparative study on thermodynamic analysis of co2 utilization reactions. **Chemical Engineering and Technology**, v. 37, n. 10, p. 1765–1777, 2014.

TAKAGAWA, M. *et al.* Ethanol synthesis from carbon dioxide and hydrogen. **Studies in Surface Science and Catalysis**, v. 114, p. 525–528, 1998.

TANG, H.; KITAGAWA, K. Supercritical water gasification of biomass: Thermodynamic analysis with direct Gibbs free energy minimization. **Chemical Engineering Journal**, v. 106, n. 3, p. 261–267, 2005.

TEIXEIRA, P. *et al.* The effect of preparation methods on the thermal and chemical reducibility of Cu in Cu-Al oxides. **Dalton Transactions**, v. 47, n. 32, p. 10989–11001, 2018.

TEODORESCU, F. *et al.* A comparative study on the catalytic activity of ZnAl, NiAl, and CoAl mixed oxides derived from LDH obtained by mechanochemical method in the synthesis of 2-methylpyrazine. **Catalysis Communications**, v. 133, 2020.

THAMPI, K. R.; KIWI, J.; GRÄTZEL, M. Methanation and photo-methanation of cabon dioxide at room temperature and atmospheric pressure. **Nature**, v. 327, p. 506–508, 1987.

THE HINDU BUSINESSLINE. **L&T evaluating tech for CO2-to-methanol plant**, 2022. Disponível em: https://www.thehindubusinessline.com/news/lt-evaluating-tech-for-co2-to-methanol-plant/article62199149.ece. Acesso em: 24 jul. 2023.

TURSUNOV, O.; KUSTOV, L.; TILYABAEV, Z. Methanol synthesis from the catalytic hydrogenation of CO2 over CuO–ZnO supported on aluminum and silicon oxides. **Journal of the Taiwan Institute of Chemical Engineers**, v. 78, p. 416–422, 2017.

WAN, C. *et al.* Hydrotalcite-derived aluminum-doped cobalt oxides for catalytic benzene combustion: Effect of calcination atmosphere. **Molecular Catalysis**, v. 520, 2022.

WANG, G. *et al.* Active sites in CO2 hydrogenation over confined VOx-Rh catalysts. **Science China Chemistry**, v. 62, n. 12, p. 1710–1719, 2019.

WANG, L. *et al.* Cobalt–Nickel Catalysts for Selective Hydrogenation of Carbon Dioxide into Ethanol. **ACS Catalysis**, v. 9, n. 12, p. 11335–11340, 2019.

WANG, W. *et al.* Recent advances in catalytic hydrogenation of carbon dioxide. **Chemical Society Reviews**, v. 40, n. 7, p. 3703–3727, 2011.

WANG, Lingxiang *et al.* Selective Hydrogenation of CO2 to Ethanol over Cobalt Catalysts. **Angewandte Chemie - International Edition**, v. 130, p. 6212–6216, 2018.

WANG, X. *et al.* Synthesis of isoalkanes over a core (Fe-Zn-Zr)-shell (zeolite) catalyst by CO2 hydrogenation. **Chemical Communications**, v. 52, n. 46, p. 7352–7355, 2016.

WANG, J. *et al.* Synthesis of lower olefins by hydrogenation of carbon dioxide over supported iron catalysts. **Catalysis Today**, v. 215, p. 186–193, 2013. Disponível em: http://.doi.org/10.1016/j.cattod.2013.03.031.

WANG, Z. *et al.* The role of CO2 dissociation in CO2 hydrogenation to ethanol on CoCu/silica catalysts. **Nano Research**, v. 16, n. 5, p. 6128–6133, 2023.

WANG, M. *et al.* Unraveling the tunable selectivity on cobalt oxide and metallic cobalt sites for CO2 hydrogenation. **Chemical Engineering Journal**, v. 446, 2022.

WEBER, D. *et al.* Recent Advances in the Mitigation of the Catalyst Deactivation of CO2 Hydrogenation to Light Olefins. **Catalysts**, v. 11, n. 12, p. 1447, 2021.

WEI, J. *et al.* Directly converting CO 2 into a gasoline fuel. **Nature Communications**, v. 8, p. 1–8, 2017.

WEI, Y. *et al.* Synthesis of Cu–Co Catalysts for Methanol Decomposition to Hydrogen Production via Deposition–Precipitation with Urea Method. **Catalysis Letters**, v. 149, n. 10, p. 2671–2682, 2019. Disponível em: http://doi.org/10.1007/s10562-019-02731-9.

WENK, R. **MAUD**, 2023. Disponível em: https://seismo.berkeley.edu/MAUD.htm. Acesso em: 19 nov. 2023.

WITOON, T. *et al.* Enhanced CO2 hydrogenation to higher alcohols over K-Co promoted In2O3 catalysts. **Chemical Engineering Journal**, v. 431, 2022.

WITOON, T. *et al.* Highly active Fe-Co-Zn/K-Al2O3 catalysts for CO2 hydrogenation to light olefins. **Chemical Engineering Science**, v. 233, p. 116428, 2021.

XU, D. *et al.* Advances in higher alcohol synthesis from CO2 hydrogenation. **Chem**, v. 7, n. 4, p. 849-881, 2021a.

XU, D. *et al.* Mechanistic aspects of the role of K promotion on Cu−Fe-based catalysts for higher alcohol synthesis from CO2 hydrogenation. **ACS Catalysis**, v. 10, n. 24, p. 14516–14526, 2020a.

XU, J. *et al.* Production of renewable fuel from CO2 by Co3O4/Cr doped MgAl–LDH p-n heterojunction catalyst. **Fuel Processing Technology**, v. 246, p. 107762, 2023.

XU, D. *et al.* Selective C2+ Alcohol Synthesis from Direct CO2 Hydrogenation over a Cs-Promoted Cu-Fe-Zn Catalyst. **ACS Catalysis**, v. 10, n. 9, p. 5250–5260, 2020b.

XU, D. *et al.* Tandem Catalysis of Direct CO2Hydrogenation to Higher Alcohols. **ACS Catalysis**, v. 11, n. 15, p. 8978–8984, 2021b.

XU, M.; IGLESIA, E. Readsorption and Adsorption-Assisted Desorption of CO2 on Basic Solids. **The Journal of Physical Chemistry B**, v. 102, n. 6, p. 961–966, 1998. Disponível em: https://doi/10.1021/jp972200b.

YAN, Z. *et al.* Unraveling the Role of H2O on Cu-Based Catalyst in CO2 Hydrogenation to Methanol. **Catalysis Letters**, v. 153, n. 4, p. 1046–1056, 2023.

YANG, C. *et al.* Hydroxyl-mediated ethanol selectivity of CO2 hydrogenation. **Chemical Science**, v. 10, n. 11, p. 3161–3167, 2019. Disponível em: http://doi.org/10.1039/C8SC05608K.

YOSHIHARA, J.; CAMPBELL, C. T. Methanol synthesis and reverse water-gas shift kinetics over Cu(110) model catalysts: Structural sensitivity. **Journal of Catalysis**, v. 161, n. 2, p. 776–782, 1996.

YOUNAS, M. *et al.* Recent Advancements, Fundamental Challenges, and Opportunities in Catalytic Methanation of CO2. **Energy and Fuels**, v. 30, n. 11, p. 8815–8831, 2016.

YUAN, F. *et al.* Boosting the Production of Light Olefins from CO2 Hydrogenation over Fe–Co Bimetallic Catalysts Derived from Layered Double Hydroxide. **Industrial & Engineering Chemistry Research**, v. 62, n. 21, p. 8210–8221, 2023.

ZENG, F. *et al.* Catalysts design for higher alcohols synthesis by CO2 hydrogenation: Trends and future perspectives. **Applied Catalysis B: Environmental**, v. 291, p. 120073, 2021.

ZHANG, S. *et al.* Direct CO2 hydrogenation to ethanol over supported Co2C catalysts: Studies on support effects and mechanism. **Journal of Catalysis**, v. 382, p. 86–96, 2020.

ZHANG, G. *et al.* Ga-Promoted CuCo-Based Catalysts for Efficient CO2 Hydrogenation to Ethanol: The Key Synergistic Role of Cu-CoGaOx Interfacial Sites. **ACS Applied Materials & Interfaces**, v. 14, n. 31, p. 35569–35580, 2022. Disponível em: https://doi/10.1021/acsami.2c07252.

ZHANG, Z. *et al.* LDH derived Co-Al nanosheet for lipid hydrotreatment to produce green diesel. **Fuel**, v. 333, p. 126341, 2023.

ZHANG, S. *et al.* Revealing and Regulating the Complex Reaction Mechanism of CO2 Hydrogenation to Higher Alcohols on Multifunctional Tandem Catalysts. **ACS Catalysis**, v. 13, n. 5, p. 3055–3065, 2023.

ZHANG, J. *et al.* Selective formation of light olefins from CO2 hydrogenation over Fe–Zn–K catalysts. **Journal of CO2 Utilization**, v. 12, p. 95–100, 2015.

ZHANG, S. *et al.* Tuning the interaction between Na and Co2C to promote selective CO2 hydrogenation to ethanol. **Applied Catalysis B: Environmental**, v. 293, 2021.

ZHANG, Q.; KANG, J.; WANG, Y. Development of Novel Catalysts for Fischer-Tropsch Synthesis: Tuning the Product Selectivity. **ChemCatChem**, v. 2, n. 9, p. 1030–1058, 2010.

ZHAO, Q. *et al.* Oxidation of acetone over Co-based catalysts derived from hierarchical layer hydrotalcite: Influence of Co/Al molar ratios and calcination temperatures. **Chemosphere**, v. 204, p. 257–266, 2018.

ZHAO, K. *et al.* Unraveling and optimizing the metal-metal oxide synergistic effect in a highly active Cox(CoO)1–x catalyst for CO2 hydrogenation. **Journal of Energy Chemistry**, v. 53, p. 241–250, 2020.

ZHENG, J. *et al.* Direct synthesis of ethanol via CO2 hydrogenation over the Co/La-Ga-O composite oxide catalyst. **Journal of Fuel Chemistry and Technology**, v. 47, n. 6, p. 697–708, 2019.

ZHENG, Y. *et al.* Energy related CO2 conversion and utilization: Advanced materials/nanomaterials, reaction mechanisms and technologies. **Nano Energy**, v. 40, p. 512–539, 2017.

ZHONG, J. *et al.* State of the art and perspectives in heterogeneous catalysis of CO2 hydrogenation to methanol. **Chemical Society Reviews**, v. 49, n. 5, p. 1385–1413, 2020.

ZHOU, G. *et al.* Methanation of carbon dioxide over Ni/CeO2 catalysts: Effects of support CeO2 structure. **International Journal of Hydrogen Energy**, v. 42, n. 25, p. 16108–16117, 2017.

ZHOU, G. *et al.* Role of surface Ni and Ce species of Ni/CeO 2 catalyst in CO 2 methanation. **Applied Surface Science**, v. 383, p. 248–252, 2016.

Appendix A

Supplementary Data: Methodology

A.1 Modifications in Catalyst Synthesis Methodology

During the sample preparation, several challenges were encountered, including obtaining materials with very low surface area, difficulty in achieving desired ratios, and elevated sodium content, as illustrated by **Figure A.1**.

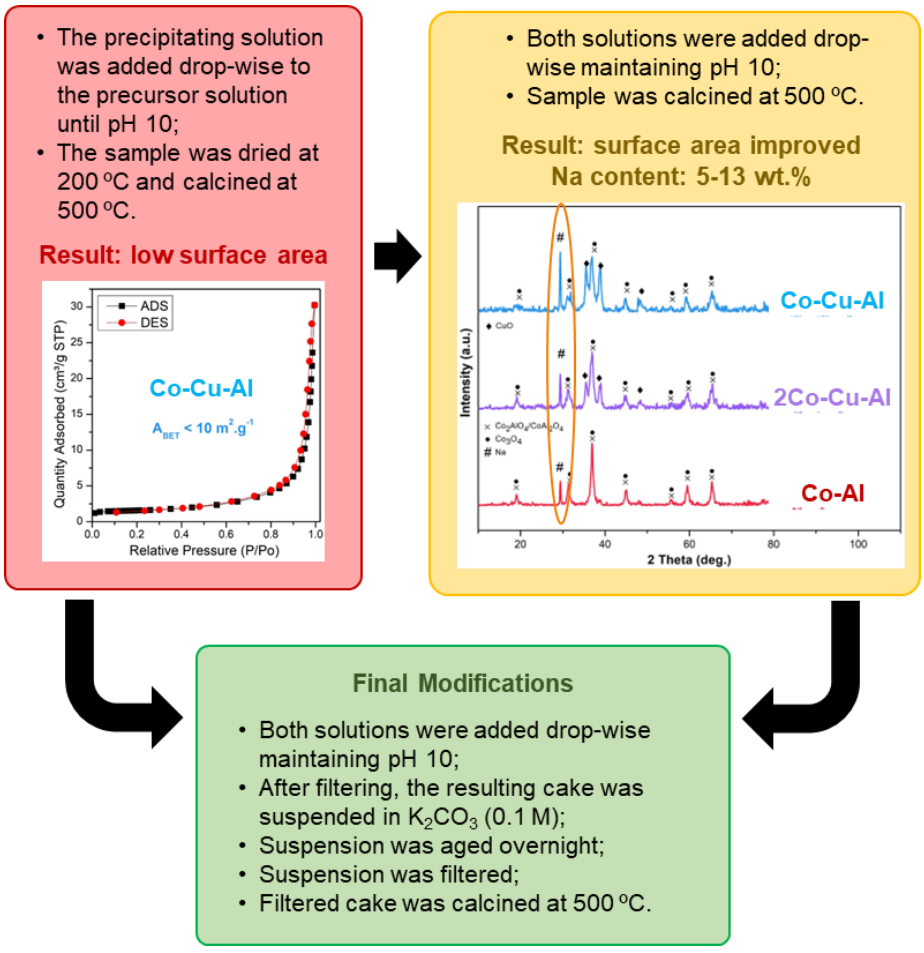

Figure A.1 - *Process of modifying preparation method*.

To address the low surface area issue, adjustments were made to the dry and calcination procedures to impact the decomposition of carbonates in interplanar spaces (KEFIF *et al.*, 2019). The challenge of achieving desired ratios was mitigated by controlling the addition of precursor solutions to promote the formation of LDHs (BENHITI *et al.*, 2020; GÖBEL *et al.*, 2020). Despite attempts to improve the washing and filtering processes, the persistence of high sodium content led to the utilization of a potassium carbonate solution for sodium removal through ionic exchange (AO *et al.*, 2020; KARÁSKOVÁ *et al.*, 2020; OBALOVÁ *et al.*, 2009).

A.2 Catalyst Bulk Density

For each sample, a random amount of sieved powder was placed inside a cylinder container with an internal diameter of 10 mm. Then, the container was then gently tapped against the lab counter to ensure uniform settling of the powder. The height of the catalyst column formed after settling was measured using a vernier caliper. Mass measurements were performed using an analytical balance. These measurements were performed in triplicate. The bulk or apparent density was calculated by dividing the mass by the volume occupied by the sample. The volume was determined using the formula for the volume of a cylinder, considering the measured diameter and height. The average density resulting of the three measurements for each sample is displayed on **Table A.1**.

Table A.1 – Bulk density of prepared catalysts after sieving.

Catalyst Samples	**Average Density ($g \cdot cm^{-3}$)**
$Cu_{2.6}AlO_x$	0.49
$Co_{1.3}Cu_{1.3}AlO_x$	0.73
$Co_{1.8}Cu_{0.9}AlO_x$	0.81
$Co_{2.6}AlO_x$	0.75

Appendix B

Supplementary Data: Catalytic Tests

In this section, all data obtained from catalytic tests are presented comprehensively. More specifically, **Table B1** provides general catalytic performance information discussed in Chapter 04. **Table B2** and **Table B3** details the selectivity and yield, respectively, of C_{2+} hydrocarbons (HCs) by carbon number (n = 1-5) and further categorize them into olefins (C_n=) and paraffins (C_n).

Table B1. Reaction data for all presented catalysts and reaction conditions. All catalytic tests were conducted at 30 bar.

	Catalyst	T_R [a] (ºC)	T [a] (ºC)	R [b]	GHSV ([c])	X_{CO_2} (%)	Selectivity (%)						Yield ($mmol.g_{cat}^{-1}.h^{-1}$)			
							CO	CH_4	HCs (C_{2-5})	ROH			HCs (C_{2-5})	ROH		
										C_1	C_2	C_{3+}		C_1	C_2	C_{3+}
1	$Cu_{2.6}AlO_x$	250	250	3:1	14200	8.8	78.8	0	0	21	0	0	0	2.78	0	0
2	$Co_{1.3}Cu_{1.3}AlO_x$	250	250	3:1	14200	14.6	0	68.9	19.6	1.6	5.4	4.5	1.77	0.34	0.59	0.32
3	$Co_{1.8}Cu_{0.9}AlO_x$	250	250	3:1	14200	11.3	0	52.5	31.0	0.4	8.4	7.7	2.12	0.07	0.71	0.43
4	$Co_{2.6}AlO_x$	250	250	3:1	14200	5.3	0	59	18.8	7.2	6.7	8.3	0.63	0.56	0.26	0.21
5	$Co_{2.6}AlO_x$	300	250	3:1	14200	6.9	0	53.4	28.9	2.0	6.3	9.4	1.11	0.2	0.32	0.33
6	$Co_{2.6}AlO_x$	400	250	3:1	14200	9.8	0	44.1	35.4	0.3	10.6	9.6	2.03	0.04	0.77	0.46
7	$Co_{2.6}AlO_x$	500	250	3:1	14200	51.8	0	90.1	5.6	0.0	2.1	2.2	1.74	0	0.79	0.57
8	$Co_{1.8}Cu_{0.9}AlO_x$	300	250	3:1	14200	12.6	0	45.1	30.5	0.7	10.6	13.1	2.18	0.13	0.97	0.79
9	$Co_{1.8}Cu_{0.9}AlO_x$	400	250	3:1	14200	17.1	0	39.5	31.3	0.7	12.0	16.5	3	0.18	1.55	1.35
9	$Co_{1.8}Cu_{0.9}AlO_x$	500	250	3:1	14200	12.0	0	47.8	34.9	0.6	8.6	8.1	2.35	0.11	0.78	0.51
10	$Co_{1.8}Cu_{0.9}AlO_x$	400	200	3:1	14200	7.1	0	53.4	21.8	0.4	12.3	12.1	0.95	0.04	0.65	0.43
11	$Co_{1.8}Cu_{0.9}AlO_x$	400	300	3:1	14200	30.1	9.4	45	31.2	3.4	4.1	6.9	4.84	1.52	0.91	1.03
12	$Co_{2.6}AlO_x$	400	200	3:1	14200	3.0	0	49	19.3	2.3	16.5	12.9	0.34	0.1	0.37	0.19
13	$Co_{2.6}AlO_x$	400	300	3:1	14200	19.5	14.2	40.6	28.7	5.1	5.5	5.9	3.25	1.49	0.81	0.6
14	$Co_{1.8}Cu_{0.9}AlO_x$	400	250	3:1	10625	24.4	0	28.4	31.6	0.3	17.3	22.4	3.24	0.08	2.39	2.15
15	$Co_{1.8}Cu_{0.9}AlO_x$	400	250	3:2	14200	12.2	0	22.5	32.3	0.4	20.8	24.0	3.54	0.12	3.08	2.46

[a] T_R: reduction temperature; and T: reaction temperature.

[b] R: H_2/CO_2 ratio.

[c] GHSV expressed in $mL.g_{cat}^{-1}.h^{-1}$.

Table B2. Hydrocarbons selectivity distribution for all presented catalysts and reaction conditions. All catalytic tests were conducted at 30 bar.

	Catalyst	T_R [a] (ºC)	T [a] (ºC)	R [b]	GHSV ([c])	XCO_2 (%)	Selectivity (%) [d]							
							C_2=	C_2	C_3=	C_3	C_4=	C_4	C_5=	C_5
1	$Cu_{2.6}AlO_x$	250	250	3:1	14200	8.8	0	0	0	0	0	0	0	0
2	$Co_{1.3}Cu_{1.3}AlO_x$	250	250	3:1	14200	14.6	0.0	9.7	0.1	9.7	0.0	0.0	0.0	0.0
3	$Co_{1.8}Cu_{0.9}AlO_x$	250	250	3:1	14200	11.3	0.2	13.6	3.7	13.5	0	0	0	0
4	$Co_{2.6}AlO_x$	250	250	3:1	14200	5.3	0	10.8	0	8	0	0	0	0
5	$Co_{2.6}AlO_x$	300	250	3:1	14200	6.9	1.8	8.3	7.6	5.4	3.3	0.7	0.3	1.5
6	$Co_{2.6}AlO_x$	400	250	3:1	14200	9.8	0	14.1	4.3	14.9	1.1	1	0	0
7	$Co_{2.6}AlO_x$	500	250	3:1	14200	51.8	0.1	2.8	0.6	1.4	0.3	0.1	0.1	0.2
8	$Co_{1.8}Cu_{0.9}AlO_x$	300	250	3:1	14200	12.6	0.3	12.1	5.2	10.5	1.6	0.8	0	0
9	$Co_{1.8}Cu_{0.9}AlO_x$	400	250	3:1	14200	17.1	0.9	10.9	6.8	8.9	2.7	0.9	0.1	0.1
9	$Co_{1.8}Cu_{0.9}AlO_x$	500	250	3:1	14200	12.0	1.2	11.9	6.1	11.1	1.7	1.9	0.3	0.7
10	$Co_{1.8}Cu_{0.9}AlO_x$	400	200	3:1	14200	7.1	0.6	10.2	0.5	9.9	0.1	0.5	0	0
11	$Co_{1.8}Cu_{0.9}AlO_x$	400	300	3:1	14200	30.1	2.1	7.8	6.8	6.4	3.1	2.7	0.6	1.7
12	$Co_{2.6}AlO_x$	400	200	3:1	14200	3.0	0	7.2	0	9.8	0	2.2	0	0
13	$Co_{2.6}AlO_x$	400	300	3:1	14200	19.5	3.6	8.8	3.5	8.4	2.2	1.7	0.2	0.3
14	$Co_{1.8}Cu_{0.9}AlO_x$	400	250	3:1	10625	24.4	1.2	8.2	8.8	6.3	3.6	2.3	0.5	0.7
15	$Co_{1.8}Cu_{0.9}AlO_x$	400	250	3:2	14200	12.2	2.1	8.6	8.3	6.2	3.9	1.2	0.7	1.3

[a] T_R: reduction temperature; and T: reaction temperature.

[b] R: H_2/CO_2 ratio.

[c] GHSV expressed in $mL.g_{cat}^{-1}.h^{-1}$.

[d] HCs are separated by the number of carbons and whether they are paraffins (C2, C3) or olefins (C2=, C3=).

Table B3. Hydrocarbons yield distribution for all presented catalysts and reaction conditions. All catalytic tests were conducted at 30 bar.

	Catalyst	T_R [a] (ºC)	T [a] (ºC)	R [b]	GHSV ([c])	XCO_2 (%)	HCs Yield (mmol.g_{cat}^{-1}.h^{-1}) [d]							
							C_2=	C_2	C_3=	C_3	C_4=	C_4	C_5=	C_5
1	$Cu_{2.6}AlO_x$	250	250	3:1	14200	8.8	0	0	0	0	0	0	0	0
2	$Co_{1.3}Cu_{1.3}AlO_x$	250	250	3:1	14200	14.6	0.00	1.06	0.01	0.70	0	0	0	0
3	$Co_{1.8}Cu_{0.9}AlO_x$	250	250	3:1	14200	11.3	0.02	1.14	0.21	0.76	0	0	0	0
4	$Co_{2.6}AlO_x$	250	250	3:1	14200	5.3	0	0.42	0	0.21	0	0	0	0
5	$Co_{2.6}AlO_x$	300	250	3:1	14200	6.9	0.1	0.43	0.27	0.18	0.07	0.02	0.01	0.03
6	$Co_{2.6}AlO_x$	400	250	3:1	14200	9.8	0	1.02	0.21	0.72	0.04	0.04	0	0
7	$Co_{2.6}AlO_x$	500	250	3:1	14200	51.8	0.03	1.06	0.15	0.37	0.06	0.02	0.02	0.03
8	$Co_{1.8}Cu_{0.9}AlO_x$	300	250	3:1	14200	12.6	0.03	1.09	0.31	0.64	0.07	0.04	0	0
9	$Co_{1.8}Cu_{0.9}AlO_x$	400	250	3:1	14200	17.1	0.13	1.3	0.56	0.73	0.19	0.07	0.01	0.01
9	$Co_{1.8}Cu_{0.9}AlO_x$	500	250	3:1	14200	12.0	0.12	1	0.36	0.63	0.09	0.1	0.02	0.03
10	$Co_{1.8}Cu_{0.9}AlO_x$	400	200	3:1	14200	7.1	0.03	0.51	0.04	0.33	0.01	0.03	0	0
11	$Co_{1.8}Cu_{0.9}AlO_x$	400	300	3:1	14200	30.1	0.45	1.68	0.95	0.91	0.33	0.28	0.06	0.18
12	$Co_{2.6}AlO_x$	400	200	3:1	14200	3.0	0	0.17	0	0.15	0	0.02	0	0
13	$Co_{2.6}AlO_x$	400	300	3:1	14200	19.5	0.52	1.19	0.36	0.89	0.15	0.12	0.01	0.01
14	$Co_{1.8}Cu_{0.9}AlO_x$	400	250	3:1	10625	24.4	0.17	1.16	0.83	0.59	0.25	0.17	0.03	0.04
15	$Co_{1.8}Cu_{0.9}AlO_x$	400	250	3:2	14200	12.2	0.29	1.29	0.85	0.63	0.29	0.09	0.04	0.06

[a] T_R: reduction temperature; and T: reaction temperature.

[b] R: H_2/CO_2 ratio.

[c] GHSV expressed in mL.g_{cat}^{-1}.h^{-1}.

[d] HCs are separated by the number of carbons and whether they are paraffins (C2, C3) or olefins (C2=, C3=).

Appendix C

Supplementary Data: Characterization

C.1 Reference Material for XRD - *Rietveld refinement*

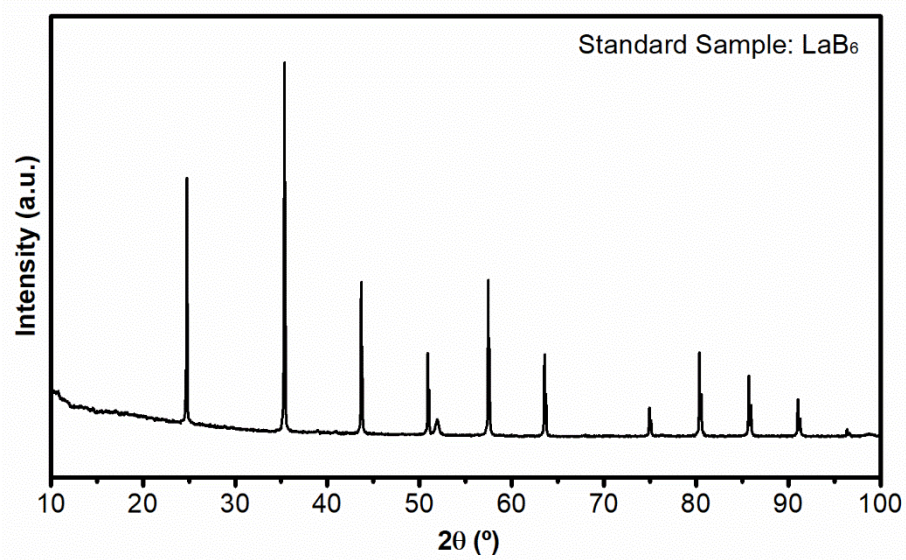

Figure C.1 - *XRD pattern for LaB_6, reference material for Rietveld refinement*.

C.2 Different iterations during refinement - MAUD

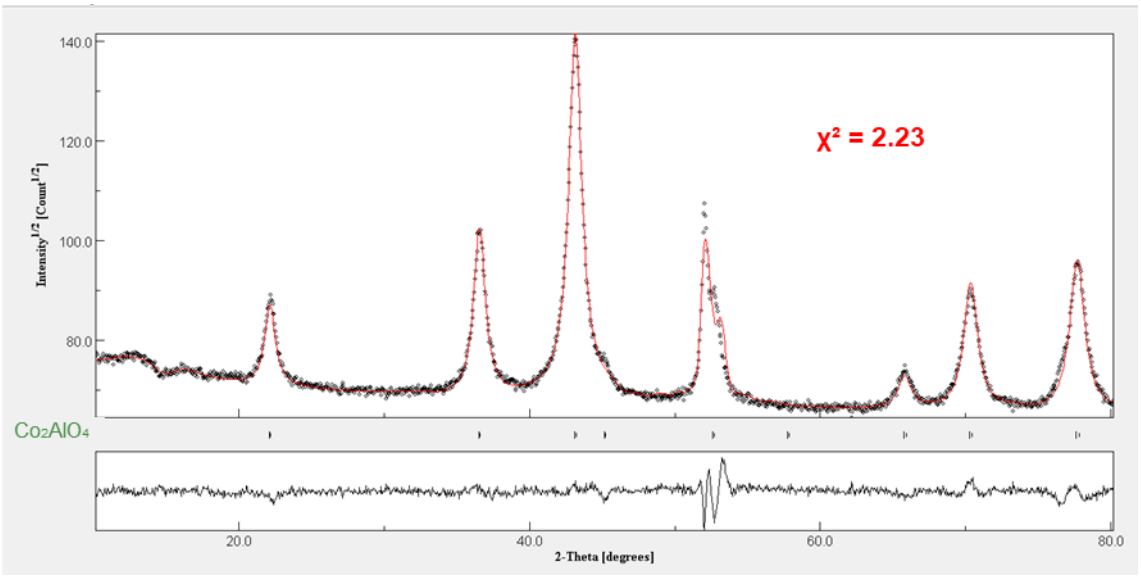

Figure C.2 - *Rietveld refinement iteration on MAUD for $Co_{2.6}AlO_x$ considering Co2AlO4 (38-0814) phase.*

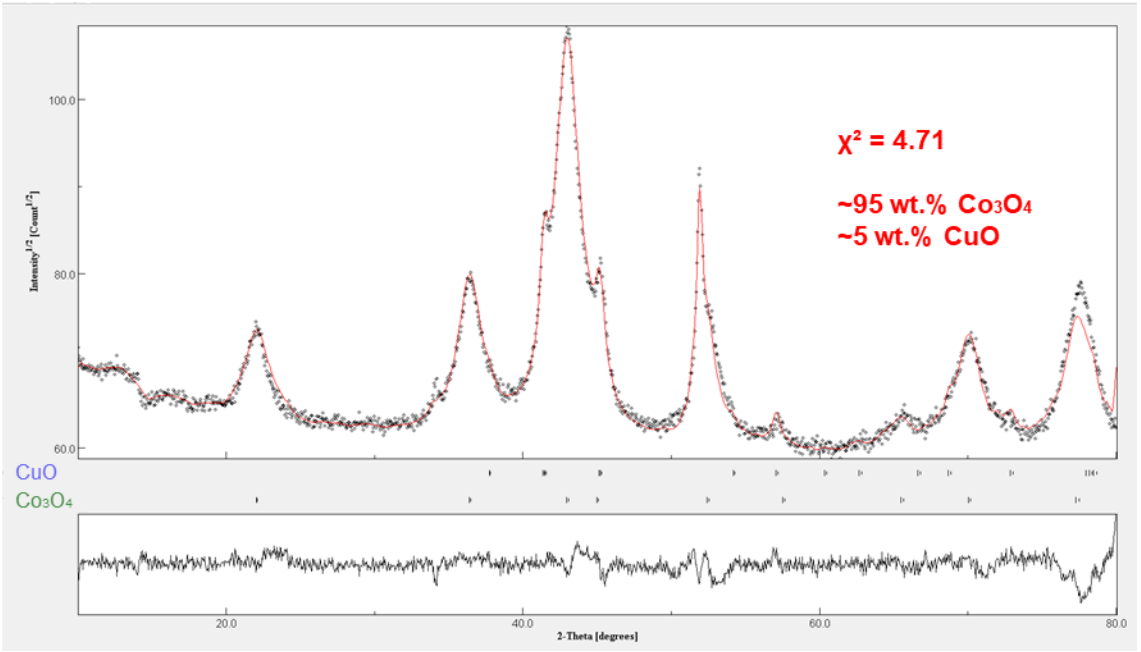

Figure C.3 - *Rietveld refinement iteration on MAUD for $Co_{1.8}Cu_{0.9}AlO_x$ considering CuO (45-0937) and Co_3O_4 (36-1189) phases.*

C.3 Scanning Transmission Electron Microcopy

The STEM-in-TEM images, while informative, did not offer a comprehensive understanding of the catalysts' surface morphology before and after reduction. Nevertheless, it is apparent that after calcination, remnants of the lamellar structure from the LDH precursor are discernible. After reduction, these materials appear to lose this characteristic lamellar appearance. Notably, in the images of $Co_{2.6}AlO_x$ and $Co_{1.8}Cu_{0.9}AlO_x$ reduced at 400 °C, no discernible lamellae were identified. STEM images for calcined $Cu_{2.6}AlO_x$, $Co_{2.6}AlO_x$ and $Co_{1.8}Cu_{0.9}AlO_x$ are presented in **Figure C.4**, **Figure C.6** and **Figure C.8**, respectively, and for the reduced samples are presented in **Figure C.5**, **Figure C.7** and **Figure C.9**.

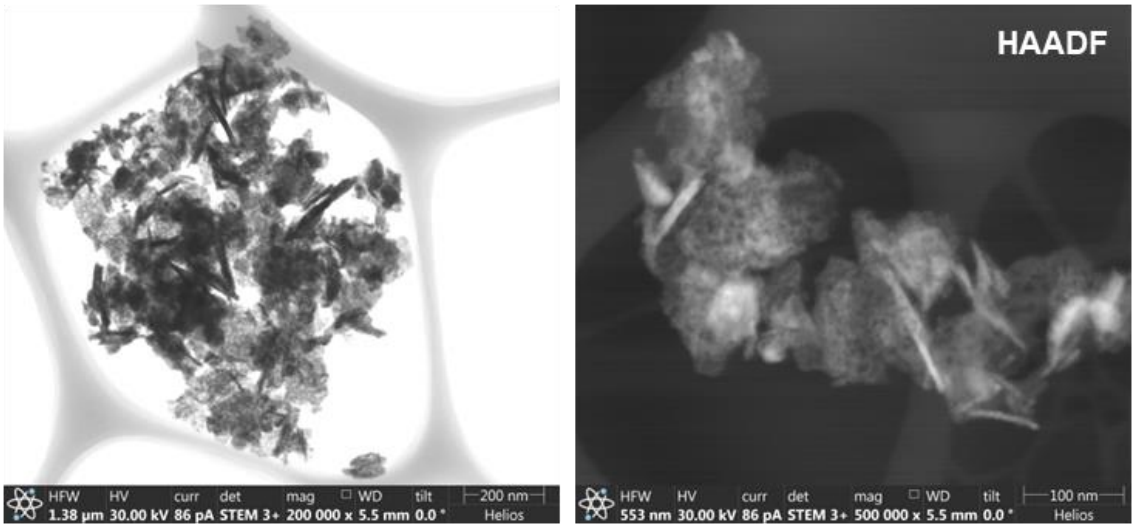

Figure C.4 - *STEM images for $Cu_{2.6}AlO_x$ calcined.*

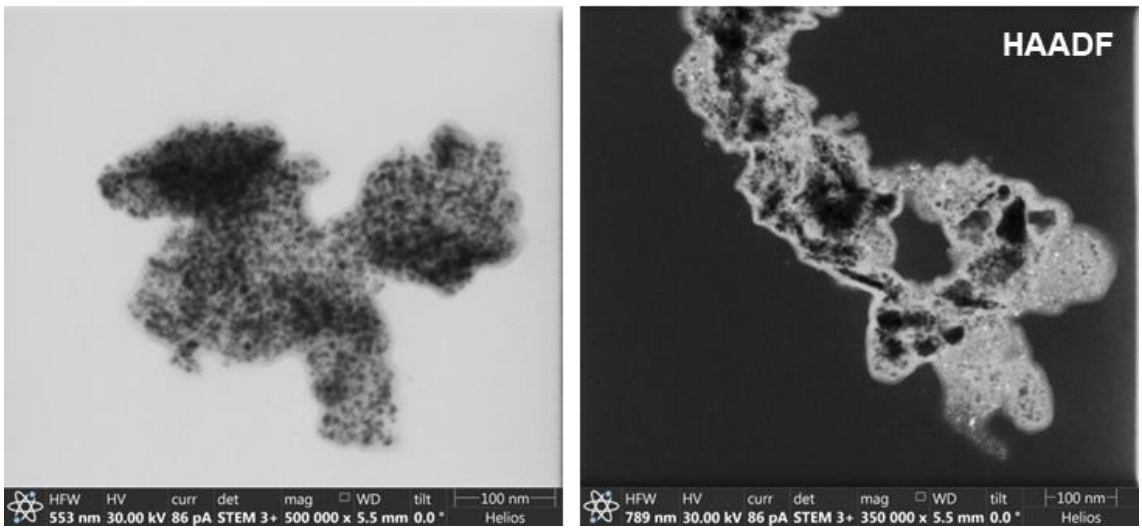

Figure C.5 – *STEM images for $Cu_{2.6}AlO_x$ reduced at 250 °C.*

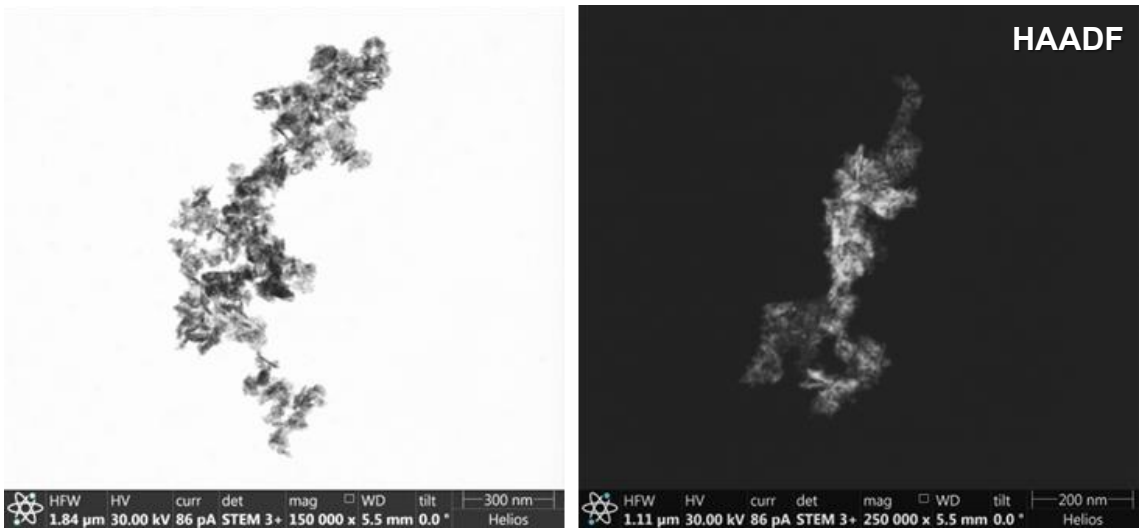

Figure C.6 - *STEM images for $Co_{2.6}AlO_x$ calcined.*

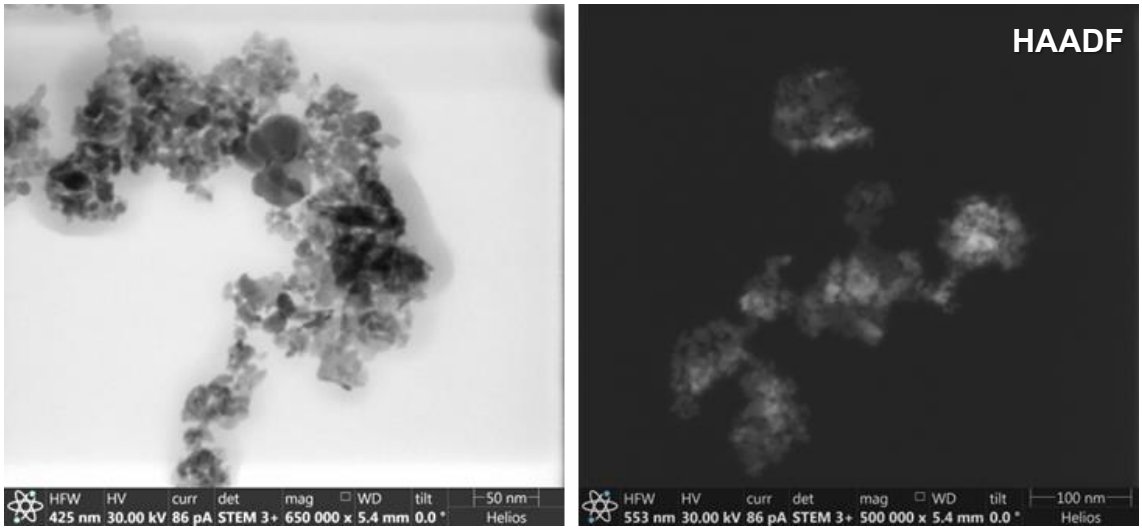

Figure C.7 – *STEM images for $Co_{2.6}AlO_x$ reduced at 400 °C.*

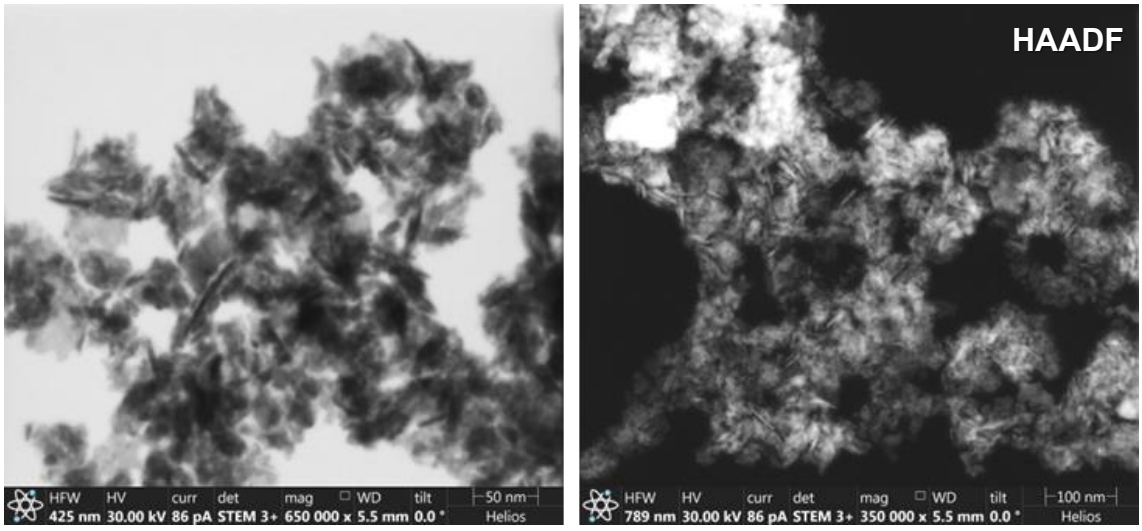

Figure C.8 - *STEM images for $Co_{1.8}Cu_{0.9}AlO_x$ calcined.*

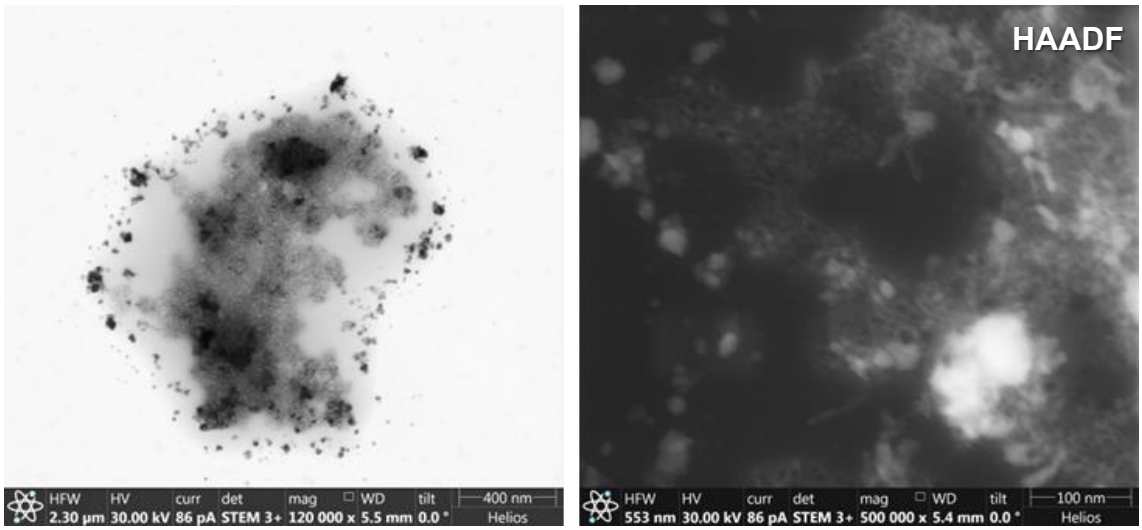

Figure C.9 - *STEM images for* $Co_{1.8}Cu_{0.9}AlO_x$ *reduced at 400 °C.*

C.4 High-Resolution Transmission Electron Microcopy

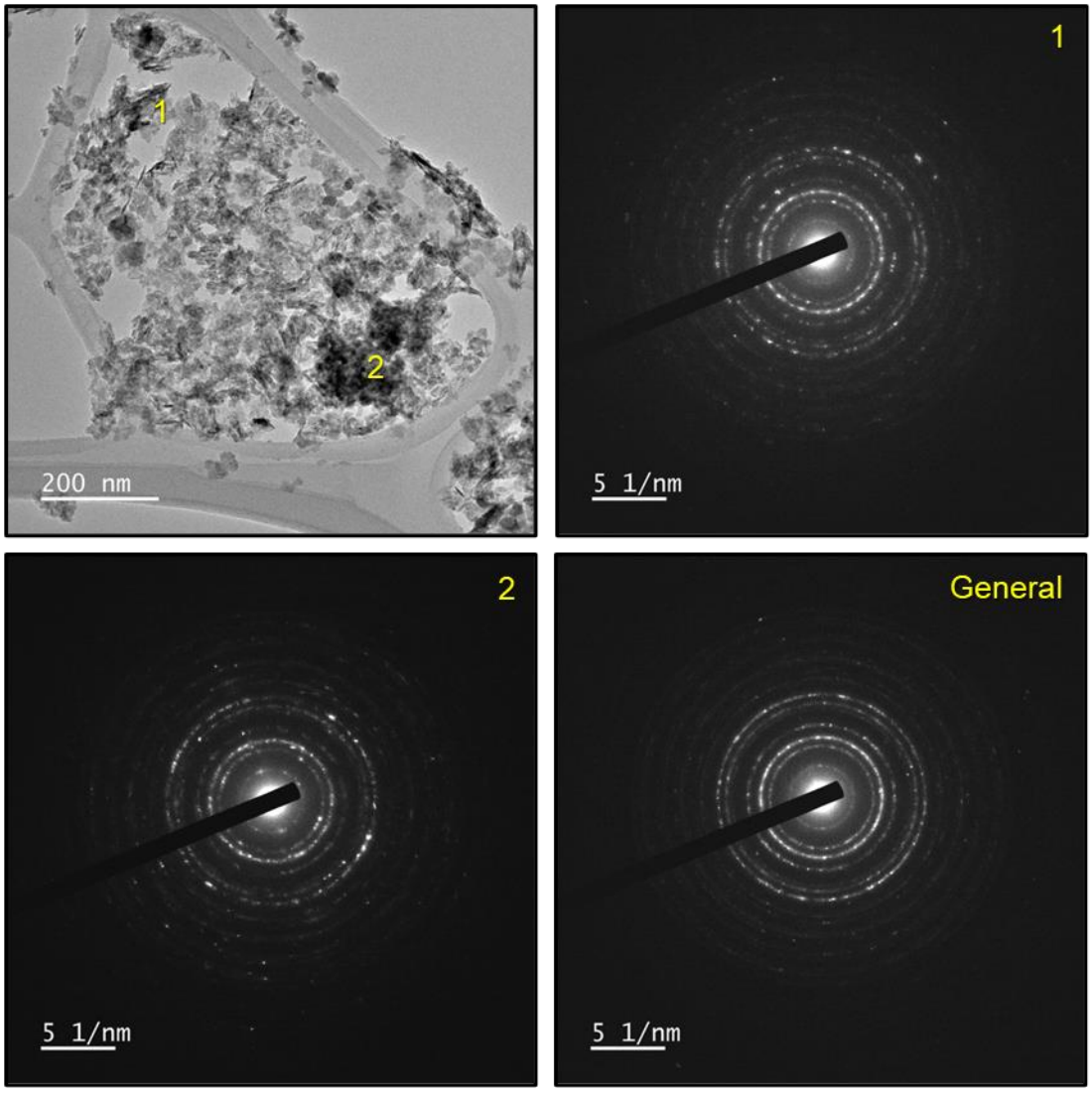

Figure C.10 - *HRTEM images and SAED patterns for* $Co_{1.8}Cu_{0.9}AlO_x$ *calcined.*

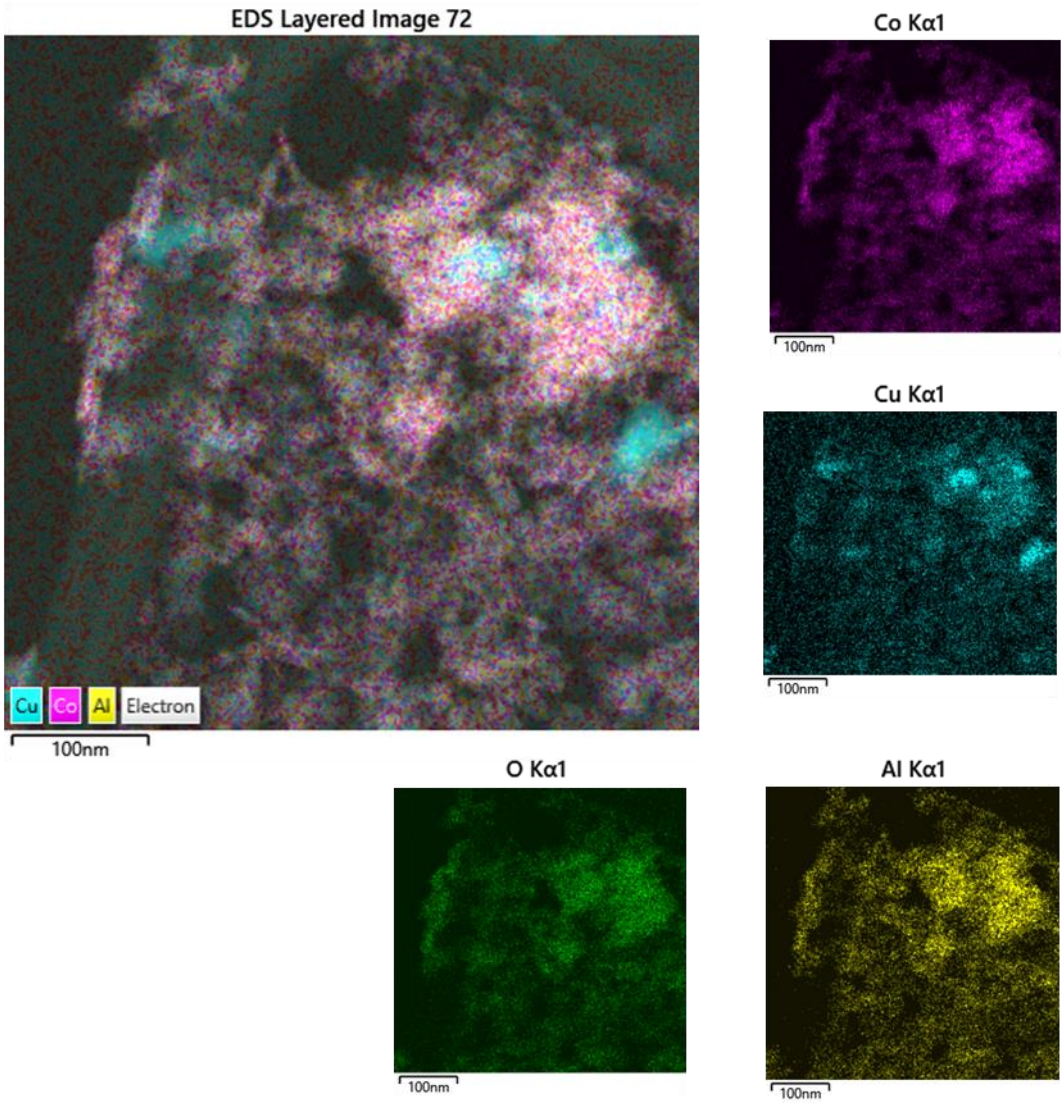

Figure C.11 - *EDS mapping for* $Co_{1.8}Cu_{0.9}AlO_x$ *calcined.*

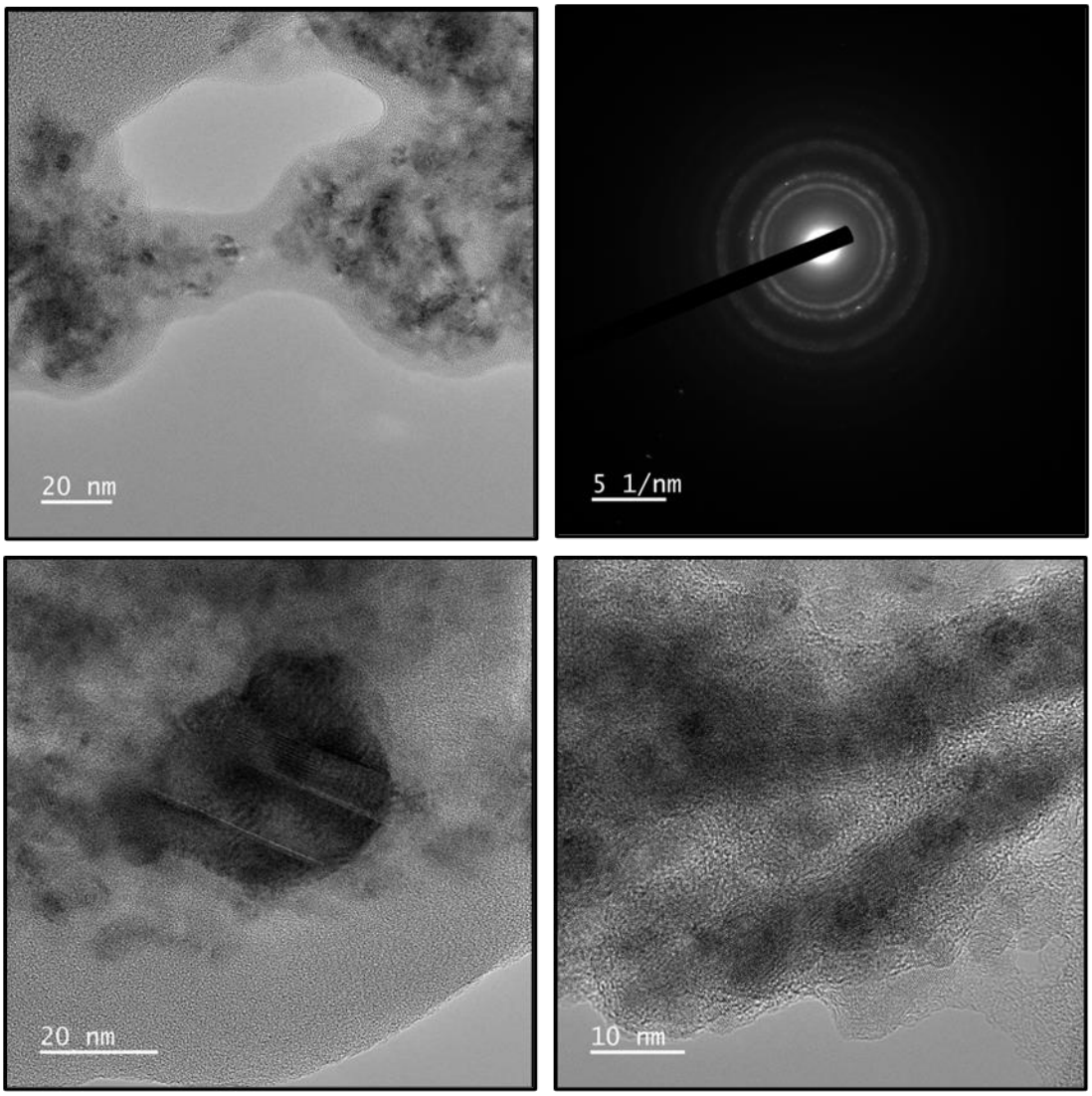

Figure C.12 - *HRTEM images and SAED patterns for* $Co_{1.8}Cu_{0.9}AlO_x$ *reduced at 400 °C.*

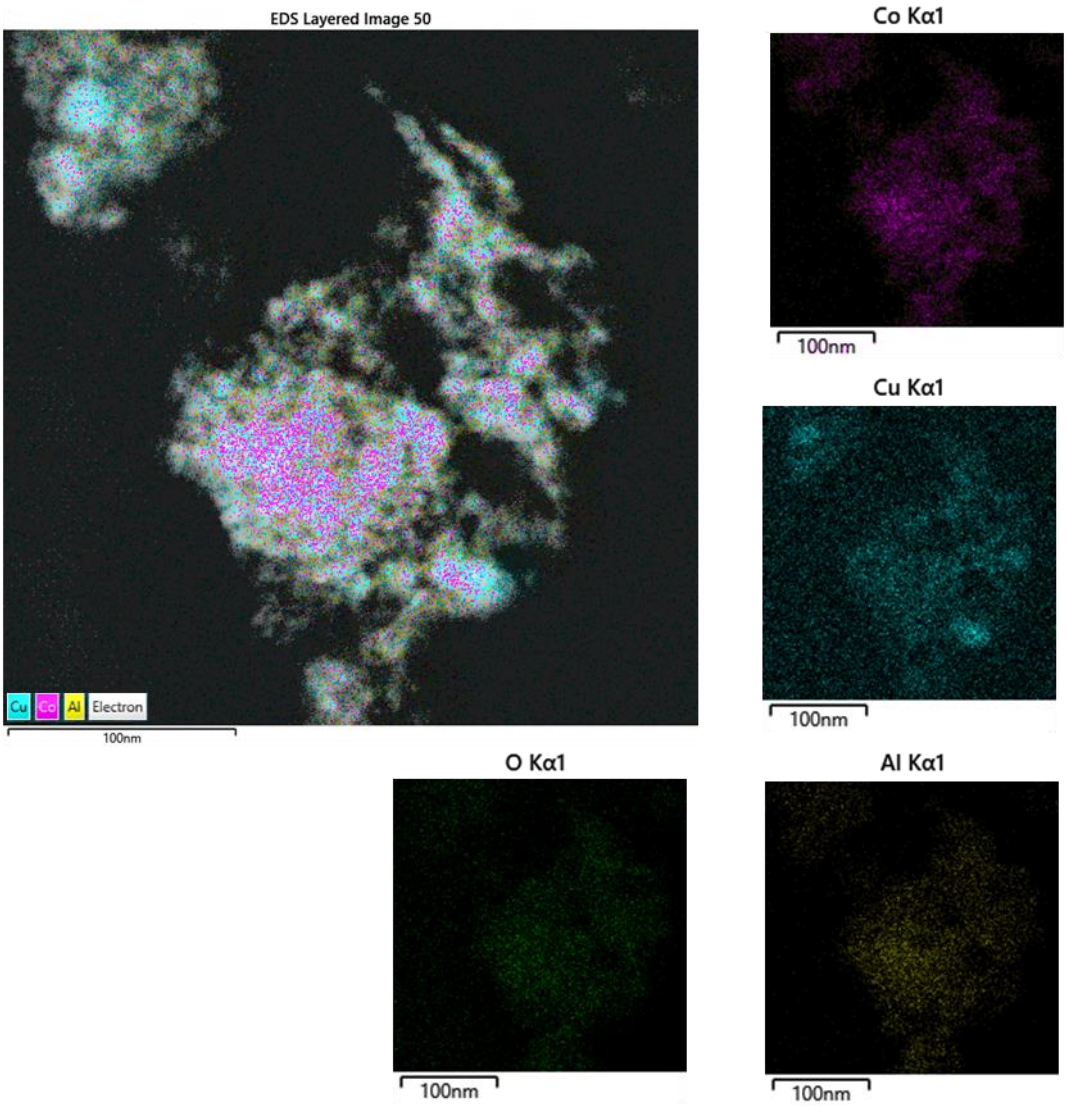

Figure C.13 - *EDS mapping for* $Co_{1.8}Cu_{0.9}AlO_x$ *reduced at 400 °C.*

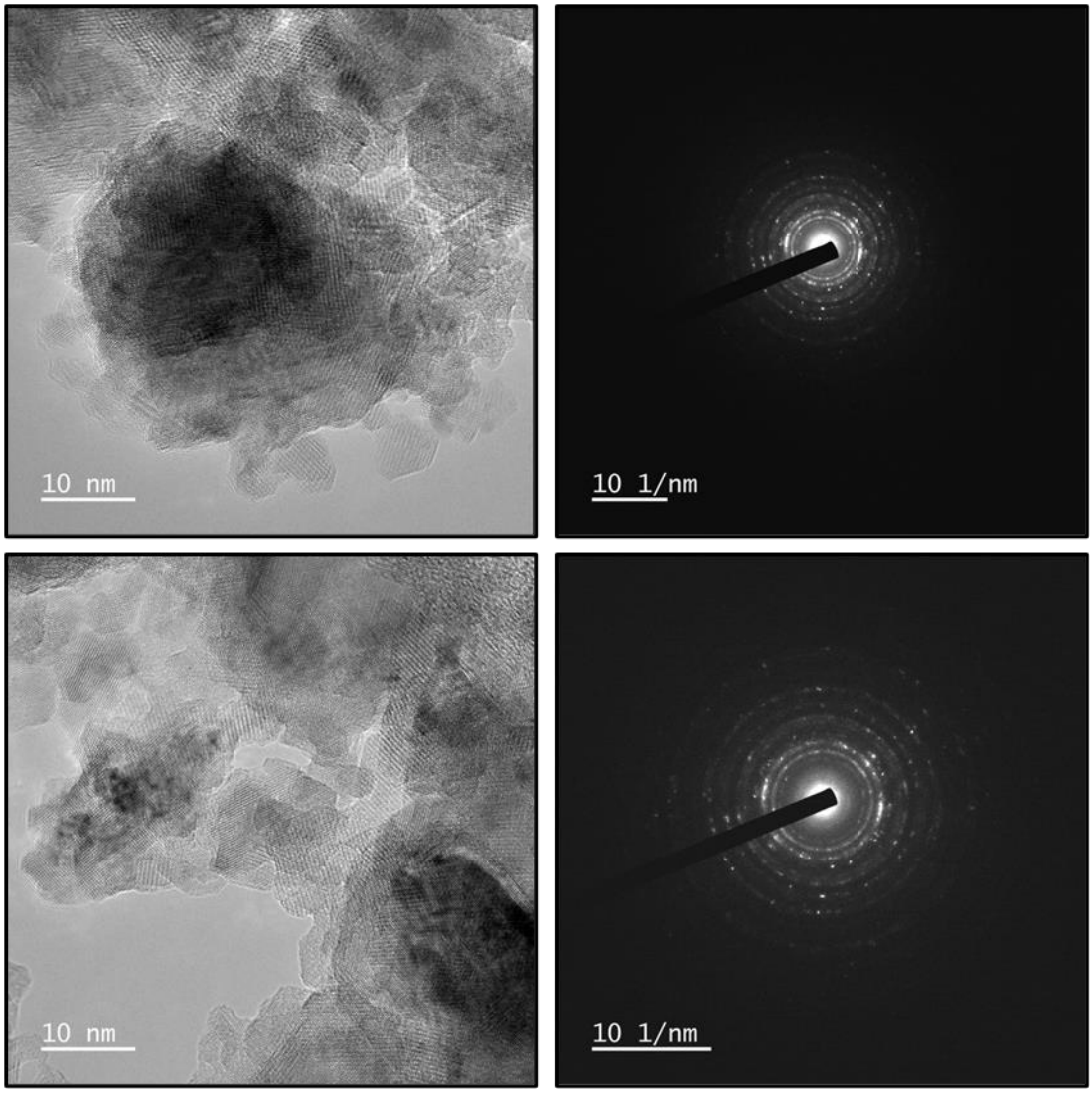

Figure C.14 - *HRTEM images and SAED patterns for* $Co_{1.8}Cu_{0.9}AlO_x$ *after reaction.*

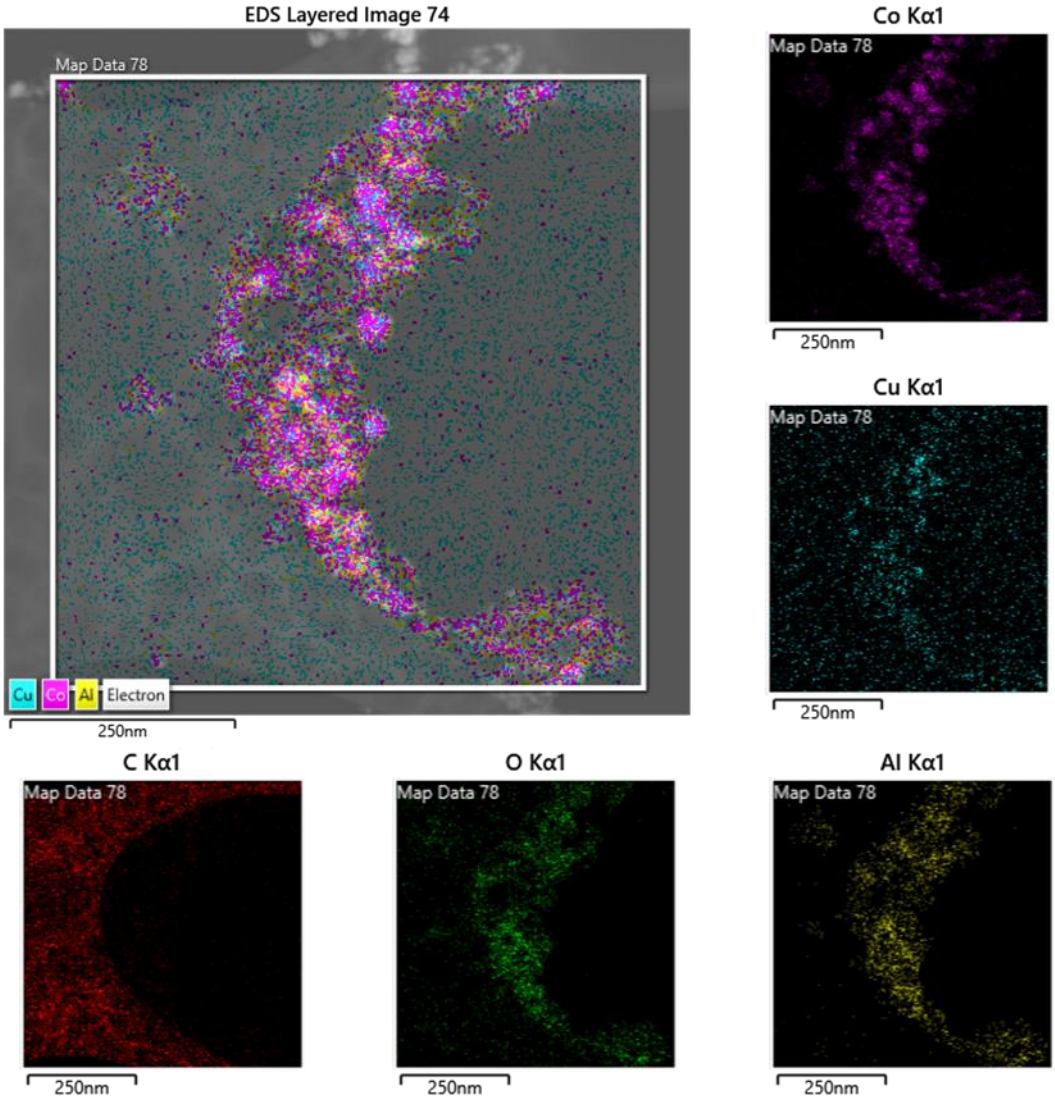

Figure C.15 – *EDS mapping for* $Co_{1.8}Cu_{0.9}AlO_x$ *after reaction.*

C.5 X-Ray Photoelectron Spectroscopy

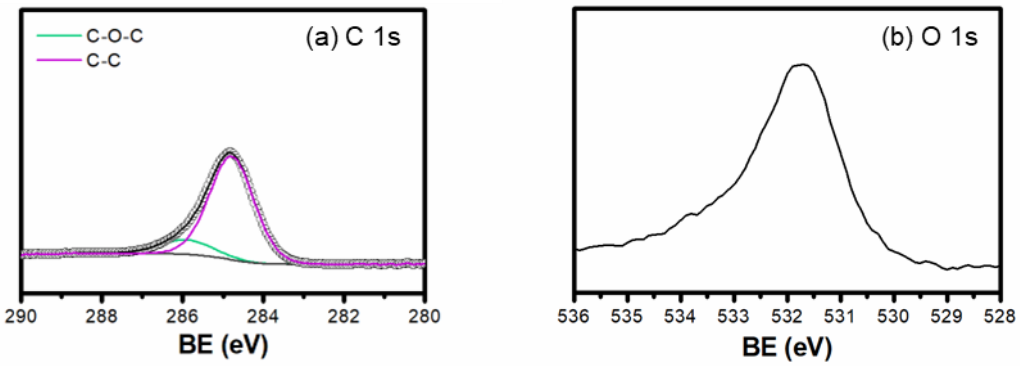

Figure C.16 - *XPS C 1s and O 1s spectra for calcined* $Co_{1.8}Cu_{0.9}AlO_x$.

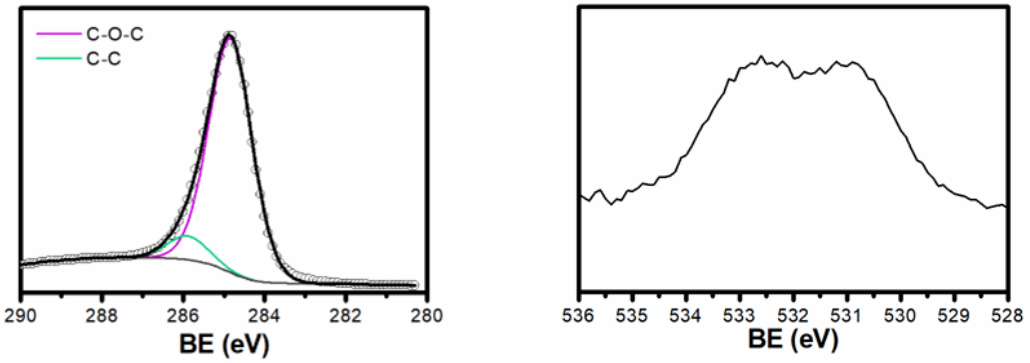

Figure C.17 - *XPS C 1s and O 1s spectra for* $Co_{1.8}Cu_{0.9}AlO_x$ *after reaction.*

Annex A

Published Work

Chemical Engineering Science 281 (2023) 119208

Contents lists available at ScienceDirect

Chemical Engineering Science

journal homepage: www.elsevier.com/locate/ces

Tuning Co-Cu-Al catalysts and their reaction conditions on the CO_2 hydrogenation reaction to higher alcohols under mild conditions

Vitor Duarte Lage [a,*], Anthony Le Valant [b], Nicolas Bion [b], Fabio Souza Toniolo [a,*]

[a] Chemical Engineering Program – PEQ/COPPE – Universidade Federal do Rio de Janeiro, Cidade Universitária, Rio de Janeiro CEP 21941-972, RJ, Brazil
[b] Institut de Chimie des Milieux et Matériaux de Poitiers (IC2MP)/Université de Poitiers - CNRS, Poitiers, France

ARTICLE INFO

Keywords:
CO_2 hydrogenation
Ethanol production
CO_2 conversion
Co-based catalyst
Cu-based catalyst
Bimetallic catalyst

ABSTRACT

The catalytic conversion of CO_2 and H_2 into valuable chemicals is a promising alternative to the recent energy and environmental challenges. However, designing an earth-abundant catalyst capable of actively and selectively converting CO_2 into desirable products is yet a challenge. Herein, we report on a facile K-Co-Cu-Al catalyst prepared by a coprecipitation method for CO_2 hydrogenation to higher alcohols (HAs). We investigated different Co:Cu ratios, reduction temperatures, and reaction conditions (temperature, space velocity, and H_2/CO_2 ratio) to tune it, enhancing the selectivity and yield of higher alcohols. $Co_{1.8}Cu_{0.9}AlO_x$ (1 wt% K), reduced at 400 °C, exhibits a high HAs selectivity of 44.8% (20.8% for ethanol) and space–time yield of 5.54 $mmol \cdot h^{-1} \cdot g_{cat}^{-1}$ (3.08 $mmol \cdot h^{-1} \cdot g_{cat}^{-1}$ of ethanol), under mild conditions (250 °C, 30 bar, H_2/CO_2 ratio of 1.5, and 14200 $mL \cdot g_{cat}^{-1} \cdot h^{-1}$), which represents one of the best performances among related studies, especially among Co-based catalysts.

https://doi.org/10.1016/j.ces.2023.119208

Received 9 June 2023, Revised 25 July 2023, Accepted 20 August 2023

Available online 22 August 2023, Version of Record 28 August 2023

Annex B

Supporting Information - XPS

The information provided below serves as reference for the interpretation of XPS data concerning Co 2p and Cu 2p spectra. These summaries consolidate interpretation data extracted from research papers conducted by Biesinger and Grosvenor's research group (BIESINGER, 2017; BIESINGER *et al.*, 2007, 2009, 2010, 2011).

Visual reference and deconvolution data for Co 2p interpretation.

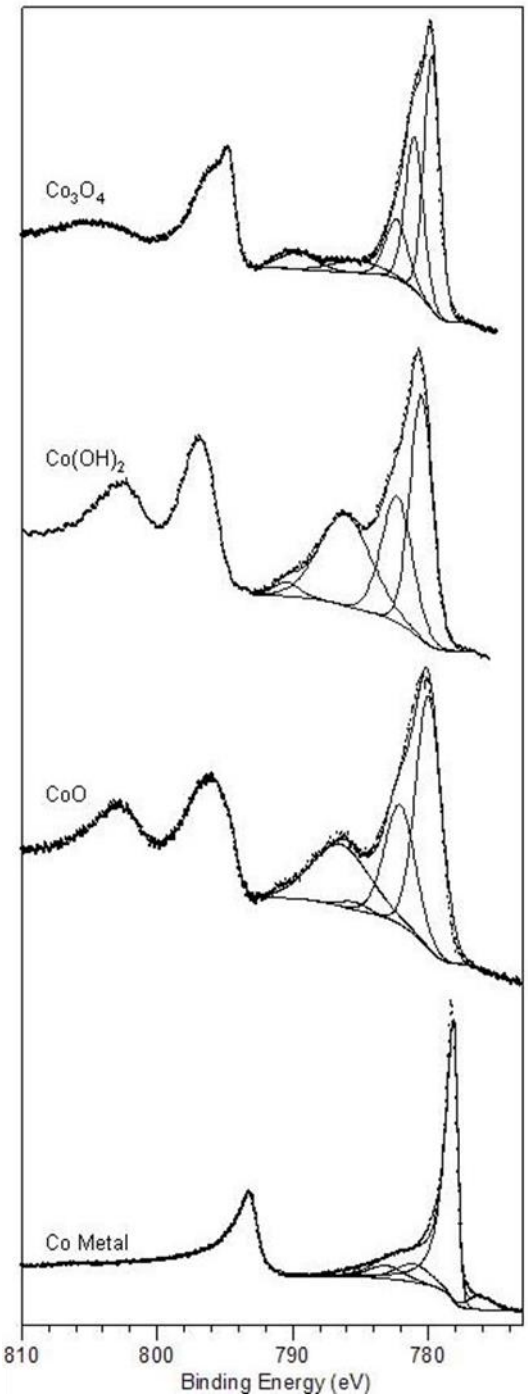

Compound	Peak 1 (eV)	%	Peak 1 FWHM, 10 eV Pass Energy	Peak 1 FWHM, 20 eV Pass Energy	Peak 2 (eV)	Δ Peak2 - Peak1 (eV) a)	%	Peak 2 FWHM, 10 eV Pass Energy	Peak 2 FWHM, 20 eV Pass Energy	Peak 3 (eV)	Δ Peak3 - Peak2 (eV)	%	Peak 3 FWHM, 10 eV Pass Energy	Peak 3 FWHM, 20 eV Pass Energy	Peak 4 (eV)	Δ Peak4 - Peak3 (eV)	%	Peak 4 FWHM, 10 eV Pass Energy	Peak 4 FWHM, 20 eV Pass Energy	Peak 5 (eV)	Δ Peak5 - Peak4 (eV)	%	Peak 5 FWHM, 10 eV Pass Energy	Peak 5 FWHM, 20 eV Pass Energy
Co(0)	778.1	81.0	0.70	0.75	781.1	3.00	11.0	3.00	3.00	783.1	2.00	8.0	3.00	3.00										
CoO	780.0	46.6	2.23	2.24	782.1	2.10	25.7	2.59	2.66	785.5	3.40	1.6	2.42	2.29	786.5	1.00	26	5.28	4.98					
Co(OH)2	780.4	38.1	2.01	2.04	782.2	1.80	26.6	2.60	2.55	786.0	3.79	33.0	4.47	4.47	790.4	4.40	2.4	2.33	2.33					
CoOOH	780.1	61.4		1.48	781.4	1.32	24.5		1.48	783.1	1.68	5.2		1.48	790.1	7.07	8.9		3.30					
Co3O4	779.6	40.5	1.38	1.39	780.9	1.30	29.1	1.55	1.62	782.2	1.30	15.2	1.94	2.18	785.2	3.00	8.1	4.28	4.44	789.5	4.30	7.2	3.15	3.29
	c)																b)							

a) Binding energies are significant to 0.1eV but an additional figure is added because energy splittings are much more accurate than the absolute binding energies.
b) Asymmetric peakshape (Peak 1) and FWHM defined by standard cobalt metal sample LA(1.2,5.5), LMM B Auger peak seen at 766.2 eV, 2.2 eV FWHM

Publicly available at:

https://www.harwellxps.guru/knowledgebase

https://www.xpsfitting.com/

https://xpslibrary.com/

https://xpsdatabase.net/

Visual reference and deconvolution data for Cu 2p interpretation.

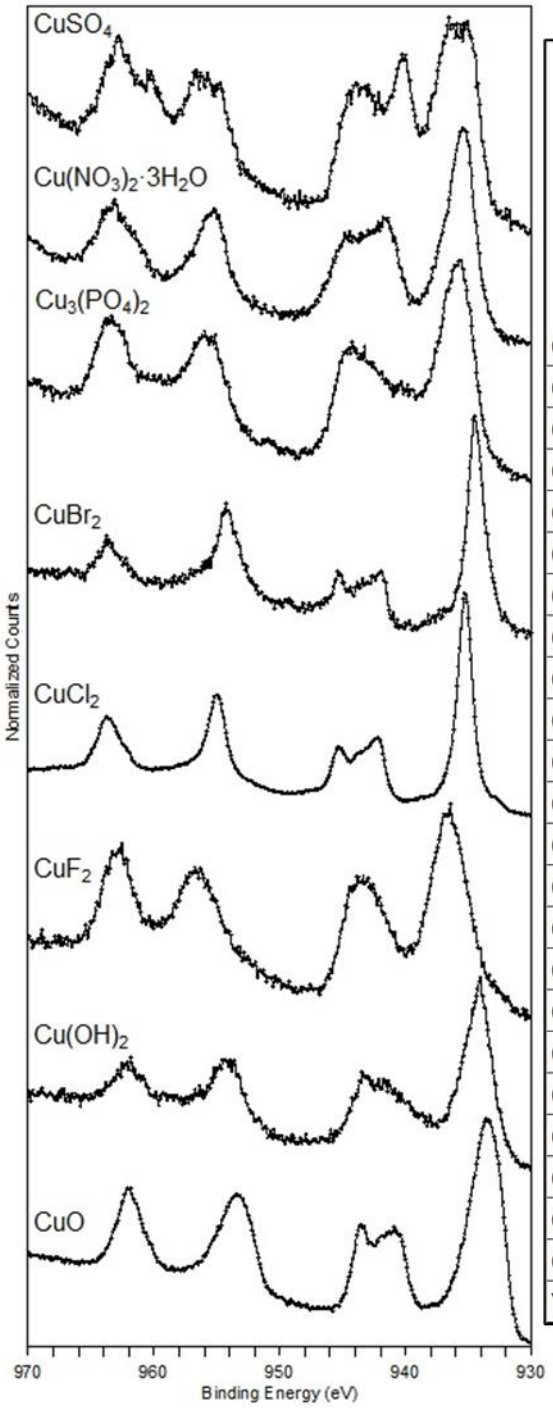

Compound	Cu 2p3/2 (eV) (Lit. Ave)	Std. Dev. (+/- eV)	# of Citations
Cu(0) a)	932.6	0.2	27
Cu2O	932.4	0.2	18
CuO	933.6	0.4	18
Cu(OH)2	934.8	0.5	2
CuF2	936.4	0.4	12
CuCl	932.4	0.2	6
CuCl2	934.8	0.7	8
CuBr	932.3	0.2	2
CuBr2	934.3	0.7	8
CuI	932.2	0.4	2
CuCO3	935.0		1
CuCN	933.0	0.2	2
Cu2Se	932.1	0.3	3
CuInSe2	932.2	0.4	4
CuInS2	932.6	0.4	3
CuSe	932.0		2
Cu(NO3)2	935.5		2
CuSO4	935.3	0.5	4
CuS	932.2	0.2	8
Cu2S	932.5	0.3	10
CuFeS2	932.2	0.2	3
Cu3AsS3	932.3		2
YBa2Cu3O	934.7	1.2	5

Publicly available at:

https://www.harwellxps.guru/knowledgebase

https://www.xpsfitting.com/

https://xpslibrary.com/

https://xpsdatabase.net/